Two thousand years of temperature variability on the lower East Antarctic Plateau inferred from the analysis of stable isotopes of water and inert gases in the Aurora Basin North ice core

Aymeric Servettaz

Thèse de doctorat

NNT : 2021UPASJ005

université PARIS-SACLAY

Two thousand years of temperature variability on the lower East Antarctic Plateau inferred from the analysis of stable isotopes of water and inert gases in the Aurora Basin North ice core

Deux mille ans d'évolution de la température sur le plateau Est-Antarctique reconstruits à partir des isotopes stables de l'eau et des gaz inertes de la carotte de glace d'Aurora Basin North

Thèse de doctorat de l'université Paris-Saclay

École doctorale n° 129, Sciences de l'Environnement d'Île-de-France (SEIF)

Spécialité de doctorat : Météorologie, océanographie physique et physique de l'environnement

Unité de recherche : Université Paris-Saclay, CNRS, CEA, UVSQ, Laboratoire des sciences du climat et de l'environnement, 91191, Gif-sur-Yvette, France.

Référent : Université de Versailles -Saint-Quentin-en-Yvelines

Thèse présentée et soutenue à Paris-Saclay, le 11 mars 2021, par

Aymeric SERVETTAZ

Composition du Jury

Valérie DAUX Professeure des Universités, UVSQ, Université Paris-Saclay	Présidente
Vincent FAVIER Physicien adjoint, HDR, Université Grenoble-Alpes	Rapporteur
Barbara STENNI Professeure, Université de Venise	Rapporteur
Emilie CAPRON Post-doctorante, Université Grenoble-Alpes	Examinatrice

Direction de la thèse

Amaëlle LANDAIS Directrice de recherche, CNRS, Université Paris-Saclay	Directrice de thèse
Anaïs ORSI Chercheure, CEA, Université Paris-Saclay	Co-encadrante

université PARIS-SACLAY
ÉCOLE DOCTORALE
Sciences de l'Environnement d'Île-de-France (SEIF)

Titre : Deux mille ans d'évolution de la température sur le plateau Est-Antarctique reconstruits à partir des isotopes stables de l'eau et des gaz inertes de la carotte de glace d'Aurora Basin North

Mots clés : Antarctique, climat, température, isotopes stables, carotte de glace

Résumé : L'Antarctique joue un rôle majeur dans le climat de la Terre, car le gradient de température entre l'équateur et les pôles contrôlent la circulation atmosphérique. L'Antarctique est également utile pour comprendre la variabilité du climat, puisque les informations préservées dans la glace peuvent complémenter les observations récentes. Cependant, l'emplacement des forages de carotte de glace sont irrégulièrement répartis sur le continent, et les reconstructions de température sur le plateau Est-Antarctique sont entravées par la faible résolution temporelle résultant d'une trop faible accumulation de neige à haute altitude. Nous présentons ici de nouvelles reconstructions de température à partir de la carotte de glace d'Aurora Basin North (ABN, 77°S, 111°E, 2700 m d'altitude). D'abord, nous utilisons le Modèle Atmosphérique Régional (MAR) pour caractériser le climat récent à ABN, et montrons que les événements de précipitation sont intermittents, et sont marqués par une température 2°C supérieure à la moyenne. Les événements de fortes précipitations sont enregistrés dans les isotopes de l'eau, avec des valeurs de $\delta^{18}O$ avoisinant les valeurs estivales, même en hiver, comme l'attestent des mesures dans la neige et le modèle atmosphérique ECHAM5-wiso, qui est équipé avec les isotopes de l'eau. Les précipitations sont systématiquement associées avec un blocage atmosphérique sur la côte de Wilkes Land, au nord-est d'ABN, et ces blocages sont favorisés par les phases négatives du Southern Annular Mode (SAM), le principal mode de variabilité dans le climat de l'hémisphère Sud. Par conséquent, les phases positives du SAM sont marquées par des température froides à ABN, mais pas nécessairement par un $\delta^{18}O$ faible, car les précipitations peuvent être réduites. La température reconstruite à partir de la carotte forée à ABN, qui fait 300 m et couvre 2000 ans, reste relativement stable, à ± 1°C de la température moyenne. Nous détaillons une deuxième reconstruction de température faite sur la même carotte, basée sur l'inversion de la température de trou de forage et des anciens gradients de température dans le névé, estimés avec les isotopes stables des gaz Ar et N_2 piégés dans les bulles. Cette seconde reconstruction de température révèle deux périodes environ 3°C plus froides à ABN au cours des 2000 dernières années : de 300 à 550 EC, et de 1000 à 1400 EC. Cette anomalie froide médiévale est synchrone avec une phase positive du SAM, et n'a pas pu être identifiée à partir du $\delta^{18}O$ seul. Cette étude souligne l'importance d'utiliser plusieurs indicateurs pour déterminer les variations passées de température, car le $\delta^{18}O$ pourrait surreprésenter les événements chauds à forte précipitation.

Title: Two thousand years of temperature variability on the lower East Antarctic Plateau inferred from the analysis of stable isotopes of water and inert gases in the Aurora Basin North ice core

Keywords: Antarctica, climate, temperature, stable isotopes, ice core

Abstract: Antarctica is a major component in Earth's climate system, as the equator to pole temperature gradient controls the characteristics of the general circulation of the atmosphere. Antarctica is also very useful to understand climate variability, as past climate information preserved in the ice may help extend the short observational records. However, the ice core drilling locations are unevenly spread across the glaciated continent, and the temperature reconstructions from the high elevation East Antarctic plateau suffer from poor temporal resolution, because low snow accumulation hampers our interpretation of water isotopes. Here, we present new temperature reconstructions from the Aurora Basin North (ABN, 77°S, 111°E, 2700 masl) ice core. First, we use the regional atmospheric model MAR to characterize the recent climate at ABN, and show that precipitation events are intermittent, and occur under temperature 2°C warmer than average. The large precipitation events are marked in the snow isotopes with $\delta^{18}O$ values on par with summer levels, even during the winter, as attested by snow measurements and the isotope-enabled atmospheric model ECHAM5-wiso. Precipitations are consistently associated with a blocking on the Wilkes Land coast, North-East of ABN, and the blockings are more likely to occur during negative phases of the Southern Annular Mode (SAM), the main mode of variability in the southern hemisphere climate. Consequently, SAM positive phases are marked by cold temperatures at ABN, but not necessarily low $\delta^{18}O$, as precipitations may be weakened. The temperature reconstructed from the $\delta^{18}O$ in the 300-m-deep, 2000-year ice core drilled at ABN supports stable conditions, with a temperature remaining within a ± 1°C range. We present a second temperature reconstruction from the same core, based on the inversion of borehole temperature and past firn temperature gradients, estimated with the stable isotope composition of Ar and N_2 gases trapped in bubbles. This second temperature reconstruction, representative of changes in the snow, suggests that temperature at ABN was about 3°C colder during two periods of the last 2000 years: from 300 to 550 CE, and from 1000 to 1400 CE. This medieval cold anomaly is concurrent with a positive SAM phase, and could not be identified from the $\delta^{18}O$ alone. This work highlights the importance of using multiple proxies to determine past temperature variability in Antarctica, as $\delta^{18}O$ may be biased towards warm precipitation events.

Maison du doctorat de l'Université Paris-Saclay
2ème étage aile ouest, Ecole normale supérieure Paris-Saclay
4 avenue des Sciences,
91190 Gif sur Yvette, France

Preface

I owe my interest to climate and science to my grandfather Bernard and my aunt Manou.

First, I am thankful to all the teachers that I could meet during my education, most of whom have been superbly supportive. I remember Anne Woehrle introducing me to ice cores, and Valérie Masson-Delmotte who advised me going to Boulder as part of the Master. This thesis marks the end of a long road since I first came to LSCE to work with Nicolas Vuichard. I would like to thank the many people I met, and especially the people who supervised me: Valerie Morris, Bruce Vaughn, Fabrice Minoletti, Pierre Sabatier, Fabien Arnaud, Guillemette Ménot, Vincent Grossi, Yusuke Yokoyama, Amaëlle Landais and Anaïs Orsi.

I am extremely grateful to Anaïs, who shared her knowledge both and scientific and life topics, with on-point insights whenever I asked. I always felt supported in my choices and she was available anytime I had a question.

Special thanks go to my private python teacher Cécile. I enjoyed talking with the former and current students in the Glaccios team: Sentia, Thomas, Margaux, Christophe, Ilaria, Antoine, Soren, Clémence. Thanks Ji-Woong for staying late in the lab with me, and Fred for selecting the best coffee for us all. Thanks to Bénédicte for helping me prepare some standards, and together with Elise for replacing our already-missed former team head.

Finally, thanks to my old friends who kept me entertained: Mickaël, Jérémie, Lina, Félicien, Roxanne, Sarah, Baptiste, Joann, Julien. Thanks to the one who waited for three years for me to head back to Japan, Ayaka.

Thanks to my brothers for keeping the family house lively, and to my parents, who supported me all along the way.

Table of contents

Chapter 1

Past and present Antarctic Climate, a search for temperature changes

1.1 Importance of Antarctic temperature in the global climate

Antarctica is a major component in Earth's climate system. Indeed, this mostly ice-covered continent, located at the south pole, acts as a cold end for the temperature gradient between the warm tropics and the cold pole. Variations of temperature in the Antarctic region thus influence the atmospheric circulation of the southern hemisphere, dominated by jet streams and the resulting meteorological events (Gill, 1982). Moreover, the large quantity of water stored in the Antarctic ice cap raises concern for future sea level rise in the actual context of global warming, as it could contribute to elevate the sea level by 3 to 7 m by the year 2300 (Edwards et al., 2019). Therefore, understanding precisely the variation of temperature in Antarctica and the associated changes in the region is critical for improving meteorological and climatological predictions that could have global impacts.

Because of its late discovery in the beginning of the 19th century, and due to its inhospitable conditions preventing the settling on the continent, observational records in Antarctica only began in 1957 (Jones et al., 2016). Additionally, the sparse measurements cannot fully represent the climate in the vast continent that is Antarctica. The observations greatly benefit from remote sensing with satellite based instruments, starting in 1979. With almost 40 years of data, Jones et al. (2016) showed that it was difficult to examine the full range of climate variability: to put the recent observations of temperature, sea ice extent and sea surface temperature in hindsight, the values and trends can only be compared to reconstructions based on proxies in natural archives. Jones et al. (2016) evaluated the ability of climate models to

reproduce the observed trends, and concluded that the difference in model results and the measurements may be due to the model not being able to fully account for the large natural variability in this region. This highlights that we still do not completely understand the processes involved in the natural variability of temperature, with periodicities longer than 10 years; and cannot implement them in models. Additionally, these timescales cannot be evaluated with observational series as short as 40 years.

1.2 Use of paleoclimate records to understand the natural variability

To better understand the long-term climate variability, we rely on the estimation of climate parameters based on the measurement of proxies. Indeed, the physical, chemical composition or ecological assemblage in an archive – a lake, ice, coral or any natural material that was made at a given time – depends on the conditions during its formation. By analogy to what we observe today, under the uniformitarian principle, the composition of the archive may be used to infer the past conditions during the formation of the archive: its composition acts as a proxy. Archives that contain information about past climate are named paleoclimate archives. The Intergovernmental Panel on Climate Change (IPCC) summarized the knowledge acquired from paleoclimate in the 2013 report (Masson-Delmotte et al., 2013). They exposed the forcings that drive climate changes, such as solar irradiance, volcanic aerosol, and greenhouse gases. These parameters are important because they determine the total amount of energy the Earth exchanges with the Sun and space, by absorbing or reflecting short-waved electromagnetic radiation, or emitting and reabsorbing long-waved radiation. Masson-Delmotte et al. (2013) also point out the importance of internal variability, as energy

redistribution may change due to restructuration of atmospheric and oceanic circulation, such as in El-Niño events.

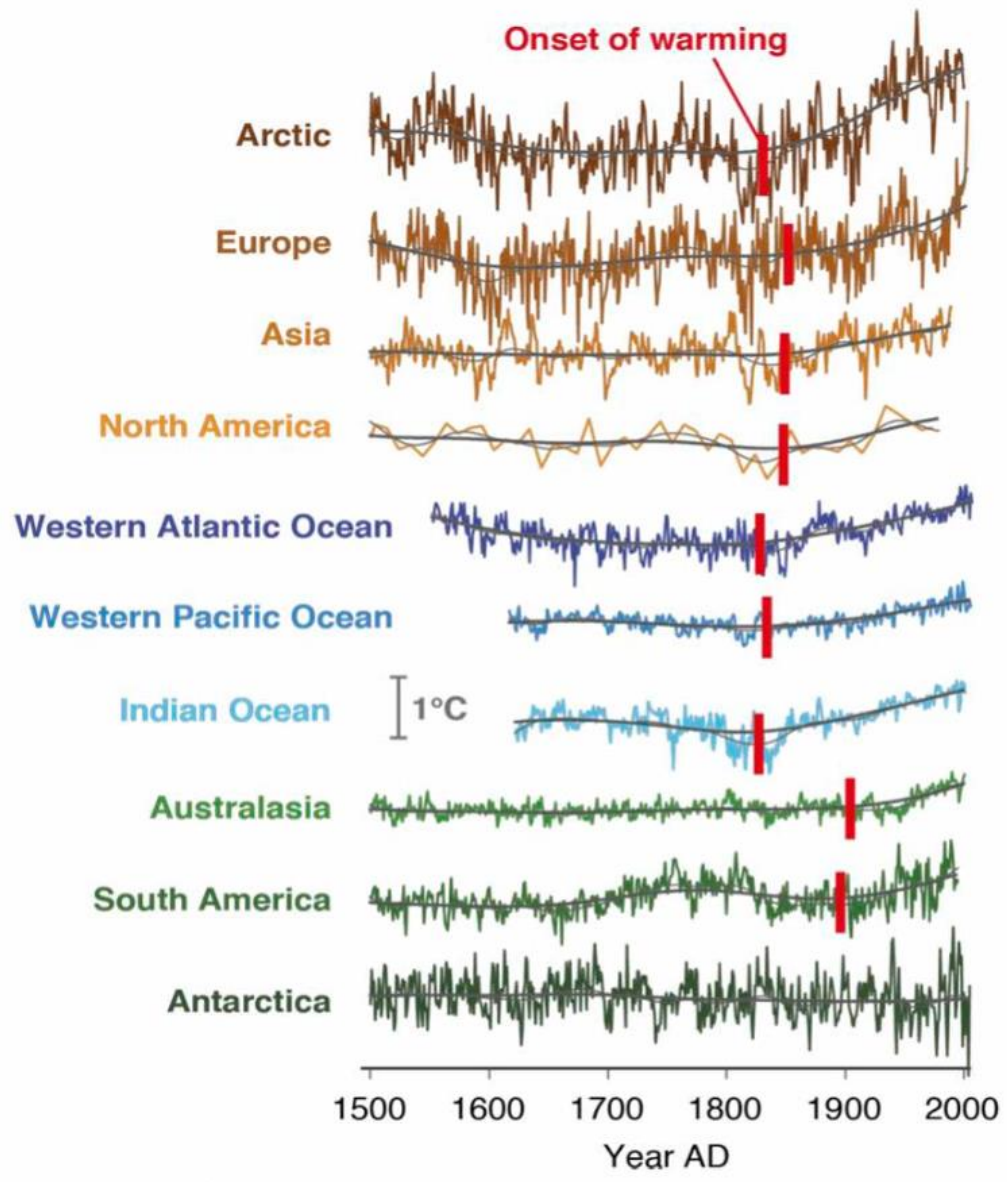

Figure 1.1 Regional reconstructions since 1500 CE (colored lines) with 15-year (thin black lines) and 50-year (thick black lines) Gaussian smoothing, shown alongside the median time of onset for sustained, significant industrial-era warming assessed across 15–50-year filter widths (vertical black bars). Grey 1°C scale bar denotes the y-axis scale of each regional temperature reconstruction. Figure from Abram et al. (2016)

The last 2000 years are especially important as it provides a context of climate variability to better understand the range of natural variability and the contribution of anthropogenic forcing to the recent warming. This timescale is relevant for our society, and relatively well preserved in a wide variety of archives around the world. The Past Global Changes 2k Network was specifically created to respond to the raising interest around this time-frame of 2000 years. Climate scientists in this network create new records and gather existing ones to build a database of past climate changes. Temperature is one of the most important parameter of the climate system and was reviewed in detail on land (PAGES 2k Consortium, 2013) and oceans (Tierney et al., 2015). Abram et al. (2016) used this database to provide insight on the recent warming in different regions of the globe: they showed that the onset of recent warming was not simultaneous in all regions, with an early response of tropical oceans and Northern Hemisphere continents, but a warming starting later in the Southern Hemisphere (figure 1.1). Of all the regions presented, Antarctica is the only region where a warming trend during the 20th century is not detected at a continental scale.

1.3 Regional differences in Antarctic temperature records

Stenni et al. (2017) present in further detail the temperature reconstructions of the past 2000 years in Antarctica, with a division of this continent into seven regions. Stenni et al. (2017) show that the Antarctic continent was generally cooling from 0 to 1900 CE (Common Era), but that no common trend is standing out for the last 100 years. While the Antarctic Peninsula, West Antarctica and the coastal Dronning Maud Land show a recent warming trend, other regions and among which the large East Antarctic Plateau show no significant trend, resulting in the absence of consistent trend for the most recent 100 years at the continental scale (figure 1.2). The database used by Stenni et al. (2017) relies largely on the measurement

of water stable isotopes in ice cores, as a proxy for temperature (the measurement and interpretation of water stable isotopes will be detailed in Chapter 2 of this work). There are two limitations to this: (1) ice cores included in this database are unevenly spatially distributed, especially the records covering the full 2000-year window, as ice cores are often drilled on domes or divides to avoid the glaciological advection of ice, leaving the vast areas between coastal domes and the plateau summits untouched and (2) the temperature reconstruction relies almost only on water-stable isotopes, which also depend on other parameters, particularly the conditions at the moisture source during evaporation (Jouzel et al., 2003; further details in Chapter 2). The existing isotope data would benefit from a better understanding of processes influencing the recorded signal. The regional climate would be better understood with temperature records from new locations, to increase the spatial coverage (Christiansen & Ljungqvist, 2017). Finally, the temperature reconstructions in the Antarctic continent could include more diverse temperature proxies, here borehole temperature inversion was only used to calibrate the water isotope-temperature reconstruction in West Antarctica.

The work of Stenni et al. (2017) has shown differing temperature trends between the subregions, based on water stable isotope analysis. The spatial heterogeneity of water stable isotopes was detailed by Masson-Delmotte et al. (2008): they used a database of surface snow analyses to discuss the changes of isotopic composition with elevation, and local average temperature. Masson-Delmotte et al. (2008) highlight the difference between coastal and inland sites, for which the moisture paths are very different, with a more local source supplying water for the coastal precipitations compared to plateau sites for which the precipitation comes from the free-tropospheric flow. This work shows the importance of understanding

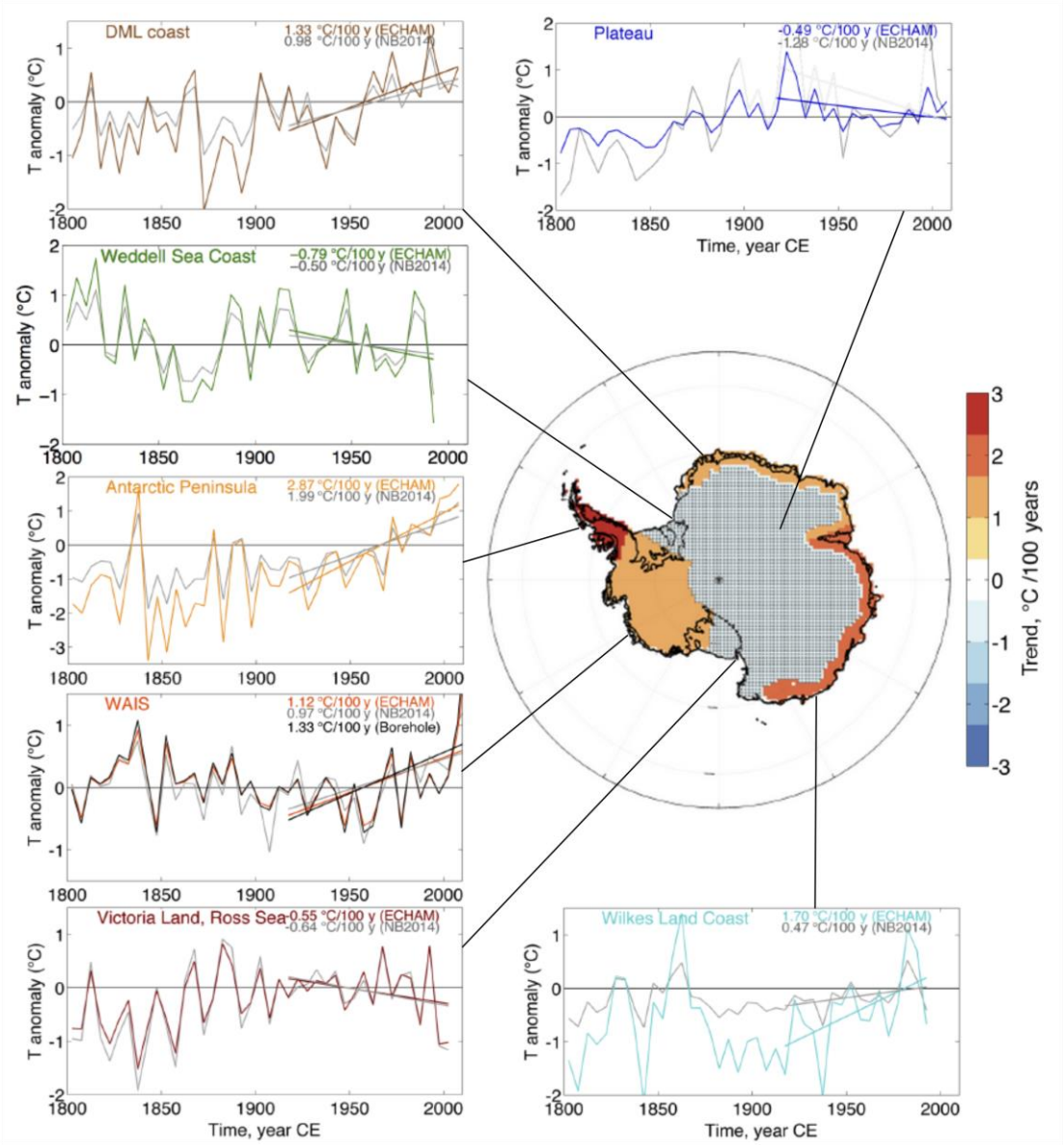

Figure 1.2 Regional temperature anomalies (°C, relative to the 1960–1990 CE interval) reconstructions. Three temperature reconstructions are shown: (i) based on the correlation between annual mean regional ^{18}O and regional T from ECHAM5-wiso forced by ERA-interim (colored lines), (ii) scaled on the Nicolas & Bromwich (2014) target over 1960 – 1990 CE, based on the correlation between site T and regional T (grey lines), and (iii) adjusted to match the temperature trend between 1000 and 1600 CE based on borehole temperature measurements in WAIS (black line; Orsi et al., 2012). Linear trends are calculated over the last 100 years of the reconstructions. The map at the center reports regional trends based on the ECHAM method (adjusted to borehole data for WAIS). Grey areas are not significant ($p > 0.05$). DML – Dronning Maud Land, WAIS – West Antarctic Ice Sheet. Figure modified from Stenni et al. (2017).

the atmospheric circulation which may explain some spatial discrepancies, because the specific atmospheric processes that can influence a given site differ between regions. To fully capture the atmospheric variability and its influence on local climate, we should study a variety of locations representative of their regions. The database used by Masson-Delmotte et al. (2008) covers many areas in the Antarctic continent, but there is no equivalent coverage for paleoclimate records, because the logistics are much heavier to retrieve ice cores. Increasing the spatial coverage of paleoclimate records seems essential to capture the past variability of atmospheric processes across Antarctica.

1.4 Sensitivity of Antarctic climate to atmospheric modes of variability

Ice core water stable isotopes are proxies of temperature initially formed by snow precipitations. For Antarctica, the sensitivity of temperature and precipitation to atmospheric variability has been described by Marshall & Thompson (2016), and Marshall et al. (2017). They define the main modes of variability in the southern hemisphere south of 30°S, as the empirical orthogonal functions (EOF) of atmospheric parameters (eddy kinetic energy and geopotential height). EOF are principal component analysis technique applied to geographically weighted mapped variables, and help understand the most influent sources of variance. The most described mode in the literature on the Southern Hemisphere is the Southern Annular Mode (SAM), sometimes named as Antarctic Oscillation. Marshall & Thompson (2016) define the SAM as the first EOF of geopotential height, an analog of pressure variability. In a positive SAM phase, the latitudinal pressure gradient is strengthened, pushing the westerly jet poleward, with enhanced zonal circulation and reduced meridional flow. Consequently, the Antarctic continent is colder and more isolated as the advection of warm air from

mid latitude ocean is reduced (Van Den Broeke & Van Lipzig, 2003). Because of these two effects, a SAM positive phase has a cold signature in most of Antarctic surface temperature (figure 1.3, Marshall & Thompson, 2016), and is associated with reduced precipitation especially on the East Antarctic Plateau (Marshall et al., 2017). As the SAM influences both temperature and precipitations simultaneously, a detailed impact assessment is necessary for a better understanding of how water isotopes in Antarctica respond to the main variability mode in the Southern Hemisphere.

Turner et al. (2019) described the precipitation variability in Antarctica. They evidenced that just a few extreme precipitation events dominate the annual precipitation budget, and they also contribute to most of the interannual variability. There is a spatial diversity in the relative contribution of extreme precipitation events. The highest parts of the plateau are less affected by precipitation caused by marine air intrusions, which are responsible for the extreme precipitations, and receive a substantial contribution from clear-sky precipitation (Stenni et al., 2016). Conversely, coastal areas are much more sensitive to precipitation caused by synoptic events, and extreme precipitation events contribute largely to the total. Therefore, Turner et al. (2019) show that locations in between the coast and the summit display a range of sensitivity to extreme precipitations. This study further demonstrates that precipitations, in which the initial isotopic composition of snow is acquired, are not necessarily representative of the average conditions, and precipitation events may bias temperature reconstructions based on water isotope proxies. The direct impact of precipitation intermittency on water isotopes was presented by Persson et al. (2011) for Greenland, but the diversity of precipitation regimes and contribution of extreme events at each site calls for careful

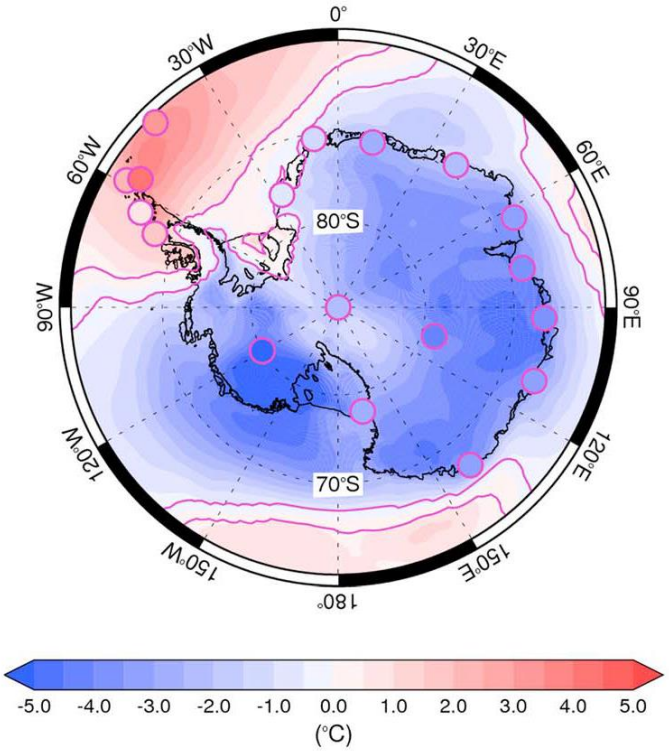

Figure 1.3 Differences in mean daily Surface Air Temperature anomalies across all seasons between the positive and negative polarities of the SAM. The purple contour represents regions where the difference is significant at the $p < 0.05$ level. Similarly, stations where the difference is significant at the $p < 0.05$ level are represented as a purple circle. Figure from Marshall & Thompson (2016)

evaluation of the impacts at each ice coring location, in order to estimate the potential biases in the water stable isotope record.

1.5 Diversity of temperature proxies

We discussed the limits of the precipitation-borne proxy that is the isotopic composition of water, related to the variability of precipitation. In addition, the snow deposition is associated with processes of wind mixing, redeposition, patchy accumulation, and vapor-ice exchanges, resulting in further changes in the measured isotopes (Casado et al., 2018; Jones et al., 2017; Picard et al., 2019). The added variability is superimposed on the climate signal in the isotopes, and can be considered as noise. The deposition noise modifies the isotopic signal at a short spatial scale of a few meters, even though the climatic influence is the same (Münch et al., 2016), and is particularly important in low accumulation areas (Casado et al., 2020). Consequently, it is difficult to evaluate the climate variability from the water isotopic signal of a single core, and averaging multiple cores helps to smooth out the deposition noise

(Münch & Laepple, 2018). However, drilling the long ice-cores needed to assess past climate variability is technically costly and difficult: even in the areas with low resolution and high time span, the 2000-year-old ice is buried at a depth of about 100 m, and coastal areas with high accumulation would require cores of several hundred meters. As a result, drilling multiple cores at a single location is not always feasible. For instance, the 3,400 m core retrieved from the West Antarctic ice sheet divide took five seasons to complete drilling (WAIS Divide Ice Core, 2011), as most of the field work is restricted to summer months. In the absence of replicated time series, the limitations on water stable isotopes can be mitigated by complementing water isotope data with other proxies for temperature reconstruction in Antarctica.

The temperature of the ice sheet itself is controlled by the diffusion and advection of heat in the polar ice sheet, with the ground temperature and the atmospheric surface temperature as boundary conditions (Ritz, 1987). Changes in annual average surface temperature, and advection of ice by accumulation of new snow are the main sources of variability as the ground temperature is controlled primarily by the geothermal heat flux, which is stable under ice sheets. Using a model of ice advection and heat diffusion, Dahl-Jensen et al. (1998) produced temperature profiles in the ice sheet, from different history scenarios for the temperature. They then used a Monte-Carlo method to match the modelled temperature profiles with measurements of temperature in the borehole left after drilling the GRIP ice core in Greenland, and have a range of compatible temperature histories. Dahl-Jensen et al. (1998) used the temperature in ice to quantify past changes in annual surface temperature in the snow over the last 50,000 years, with a low resolution. This method uses the diffusion properties of temperature in the ice, which can provide a direct quantification of temperature. However, the estimate quickly loses in temporal resolution as the diffusion smears the variations over time. In general, the glacial-interglacial temperature change can be accurately retrieved by this method, at sites with high enough accumulation (Cuffey et al., 1995, 2016; D. Dahl-

Jensen et al., 1998). Large features of the late Holocene, like the “little ice age” temperature minima can also be reconstructed (Dahl-Jensen et al., 1998; Orsi et al., 2012), and the most recent 50 year changes in temperature trends can be retrieved at more locations, because it is less diffused. For instance, Muto et al. (2011) reconstructed the recent trends at four sites in Dronning Maud Land, East Antarctica. They found both warming and cooling trends, and attributed the divergence of the results to the different altitude and surface slope of their sites, with warming temperature trends on the crest and cooling or no trend in the slope. This method can be very useful to estimate the stability of the local temperature in recent decades, and provide an absolute reference for the temperature calibration of other proxies. It is also precious to establish longer term trends that may be too weak to be captured by other methods.

In addition to the borehole temperature proxy, another temperature estimate can be derived from the gases that diffuse in the porous snow at the top of an ice cap (Severinghaus et al., 1998). The porous snow layer is named the firn and is usually 60 to 100 m deep, at which depth the pressure of the snow loaded above forces the closure of porosity and traps gases in bubbles within the ice matrix. Severinghaus et al. (1998) have shown that the isotopic composition of gases in the firn not only depends on the gravitational settling of heavy isotopes, but is also sensitive to the temperature gradient in the firn. Severinghaus et al. (2001) precisely quantified the thermal fractionation of isotopes for different gases in the firn, allowing Kobashi et al. (2008) to reconstruct past temperature changes in Greenland. Kobashi et al. (2008) used series of nitrogen and argon isotopes to produce a temperature signal independent of the gravitational fractionation. Improving from this study, Orsi et al. (2014) used the same isotope pairs and a temperature diffusion model in the ice, to reconstruct a temperature history, similarly to what has been done from borehole temperature (figure 1.4). Contrary to

borehole temperature inversion, the gases isotope inversion allows for a much higher temporal resolution, and is useful to quantify changes of temperature at a decadal to centennial scale. Orsi (2013) combined the information from gases and from borehole temperature, and used an ice-advection temperature diffusion model to fit both datasets to provide information on the past temperature in West Antarctica. This method has not yet been used to reconstruct millennial-length temperature records in East Antarctica.

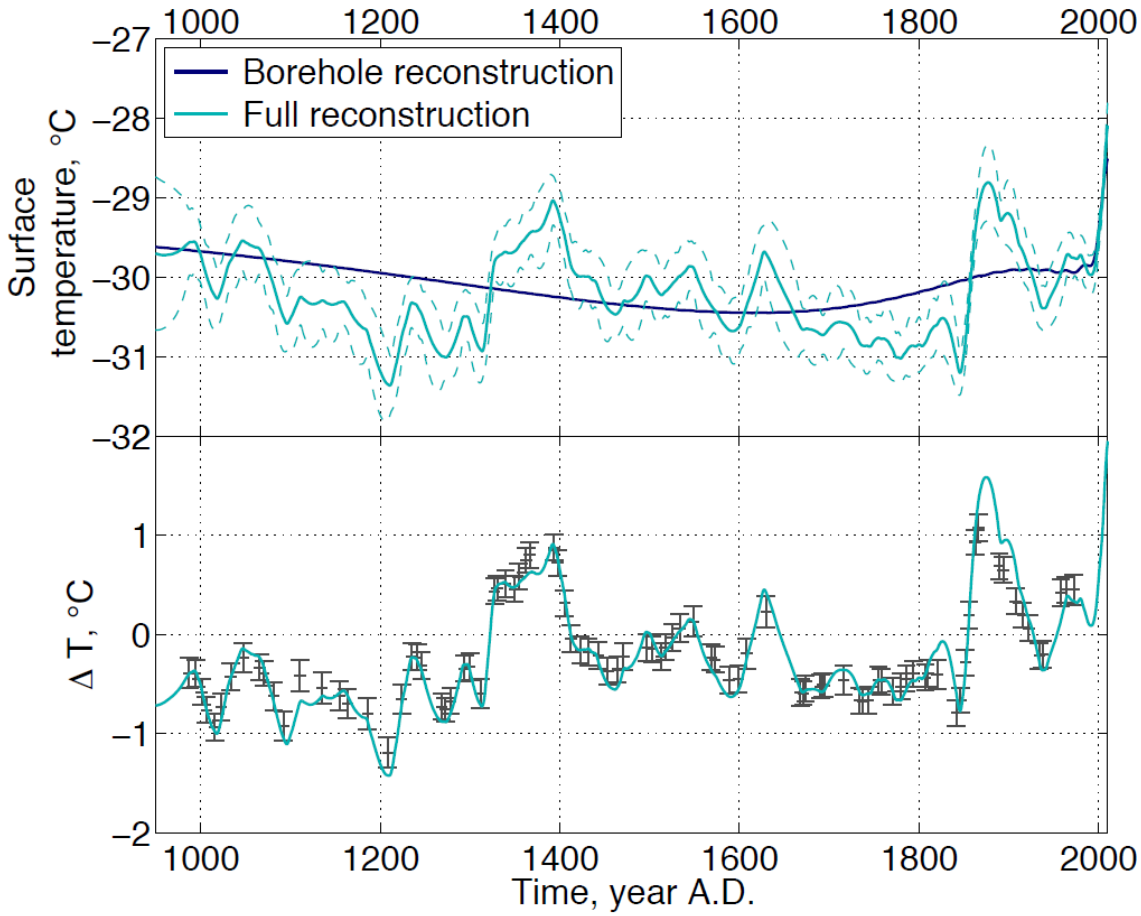

Figure 1.4 West Antarctic Ice Sheet surface temperature reconstruction, from the borehole temperature data (dark blue), and from the dual inversion of borehole temperature and ΔT (teal). The dashed line shows the uncertainty estimation in the reconstruction. Bottom: ΔT data (error-bars), and forward model output for the temperature history shown above (teal line). Figure from Orsi (2013).

Previous works have highlighted the uniqueness of Antarctic climate. While the climate in most regions has warmed as a response to anthropogenic forcing, the high variability of Antarctic surface temperature does not allow us to distinguish a general trend for Antarctica (Abram et al., 2016). The different regions of Antarctica respond differently to changes in Southern Hemisphere climate, owing to atmospheric pathways that are specific to each region. Paleoclimate reconstructions, and especially high resolution temperature records covering the last 2000 years, are needed to complement the sparse records available in Antarctica. So far, ice cores have been preferentially drilled near the coast or at high elevation, and the few ice cores in between usually cover a much shorter time span.

When drilling ice cores with the aim to reconstruct temperature, the main proxy used is traditionally the water isotopic composition of the ice. However, it is highly sensitive to precipitation regimes. It is thus necessary to evaluate the sensitivity of the water isotopes to the climate where the core is drilled.

Finally, temperature reconstructions are mostly reliant on the water stable isotopes. Other existing proxies such as borehole temperature and gases isotopes should be further applied, as they could complement the water isotopes and provide a quantitative estimate of temperature changes.

Here we propose to study the last 2000 years of temperature variability on the lower East Antarctic Plateau, using both water stable isotopes and inert gases stable isotopes in the Aurora Basin North ice core. This core was recently drilled in East Antarctica to increase the spatial coverage of paleo-temperature records, at a site midway between the coast and the summits.

1.6 Organization of the manuscript

After detailing the commonly used methods (Chapter 2), we will determine the local climate conditions at Aurora Basin North, with a focus on the temperature and precipitation (Chapter 3). We will evaluate the impacts of the precipitation regimes on the water stable isotopes in recent snow (Chapter 4). Then we will describe the main core that was drilled, and how we used the measurements made by our collaborators to reconstruct the temperature from water stable isotopes (Chapter 5). We will detail the measurements of stable isotopes in gases and how they were used to produce a second temperature record (Chapter 6). Finally, we discuss the temperature records and how they inform us on the climate evolution of Antarctica in the last 2000 years (Chapter 7), and give our conclusions (Chapter 8).

Chapter 2

Tools for understanding temperature and climate from ice core records

A variety of methods have been used to understand the temperature variability in the Antarctic region. Ice core can provide long-term information for the location at which they were drilled, with the most common temperature proxy being the water stable isotopes. Other methods, relying on borehole temperature inversion or gases stable isotopes were also implemented in some locations. Atmospheric models can also help understand the interaction between the different regions at a shorter timescale. In this chapter, we review and detail the existing methods to study the temperature in polar regions.

2.1 Characteristics of ice sheets allowing for ice coring

Greenland and Antarctica are currently covered by large continental ice sheets: glacier ice covering more than 50,000 km^2. Their location, respectively near the north pole and at the south pole, limits the amount of energy received by sunlight because the incident light is at a very low angle. This allows for the sustained cold conditions necessary for the ice to remain over summer.

The Antarctic continent in particular was at its south pole location for the last 70 million years (Ma), and the Antarctic ice sheet appeared as early as 36 Ma ago, stabilizing into a permanent ice sheet around 14 Ma ago (Zachos et al., 2001). The changes in oceanic currents associated with opening of Drake and Tasmanian passages, and closing of the Tethys Ocean caused the isolation and subsequent cooling of Antarctic continent, mainly due to the intensification of circumpolar currents (Woodruff & Savin, 1989).

Cold surface temperature that remains below freezing year-round allows for preservation of the snow deposited, as it does not melt in summer. Consequently, the ice deposited on the surface accumulates over time (figure 2.1). Upon loading more ice, the old ice underneath is squeezed out and pushed to the sides of the ice sheet. Ice slowly thins and flows towards the sides of the ice sheet, and can either reach places where surface conditions cause loss of ice by melt or sublimation, or reach the sea, and the floating ice is broken down and ablated in icebergs.

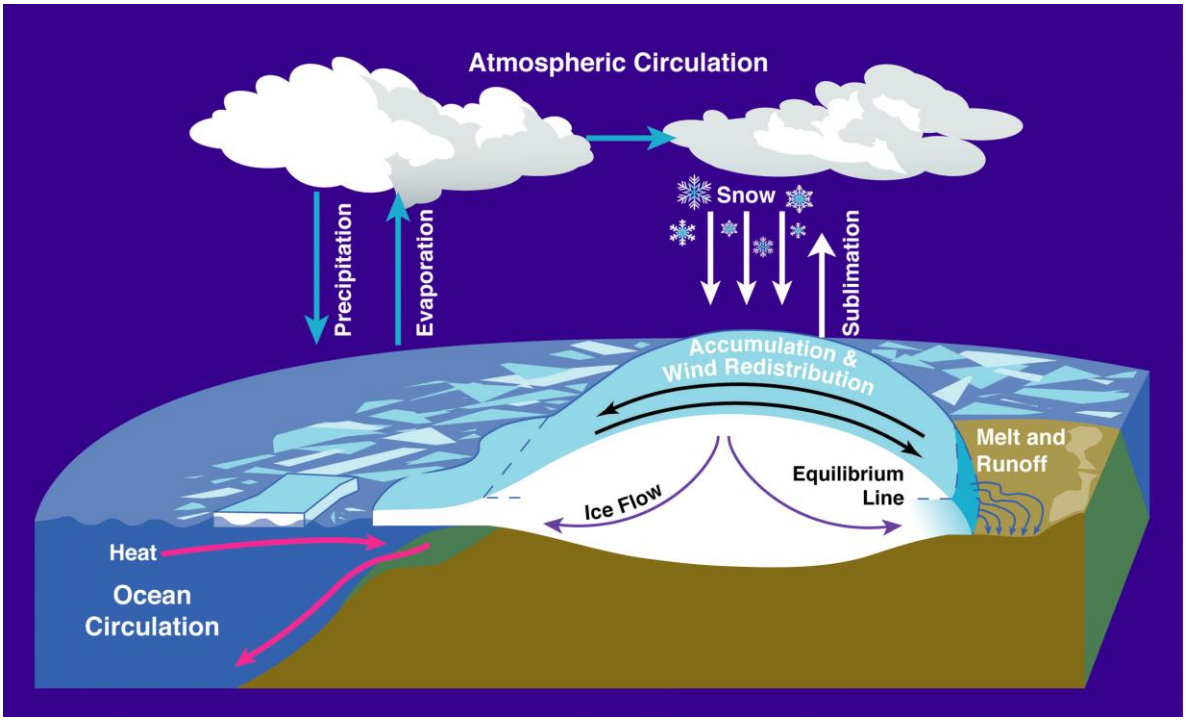

Figure 2.1 Diagram of the hydrological cycle in the Antarctic region (credits: NASA).

When the ice accumulates during each deposition event, it adds up on top of the ice sheet. As more layers of ice accumulate, the older deposition events are buried down under the snow deposited above. By drilling down in the ice cap, we access older layers of ice that are preserved: this is the principle of ice coring.

Polar ice sheets are composed mostly of pure ice – frozen water – but also include dust and aerosols that are transported in the atmosphere and can either deposit directly on the surface (dry deposition), or be caught in a water or snow particle before being deposited with the precipitation event. Most droplets and snowflakes form on an aerosol nucleus on which saturated vapor in the atmosphere will condensate. Finally, the complex forms of snowflakes are quickly broken down into round grains on the surface, but arrangement of round grains leaves space for air to diffuse in an open porosity. With time, and as more ice is loaded on top, the grains will merge together, gradually lowering the porosity to a point where the gas is trapped in bubbles, enclosed in the ice matrix.

Ice core archives are analyzed for their ice, gases and dust contents, which can indicate changes in the environment during the formation, transport and deposition. In this thesis, we will focus on water and gases, by measuring their isotopic composition.

2.2 General information on stable isotopes

Stable isotopes are described extensively by Criss (1999). Here we briefly summarize the general information that is necessary to understand the processes responsible for the signal in isotopic composition of water and gases.

2.2.1 Definition of stable isotopes

Atoms composing the matter are classified in elements depending on the number of protons in the nucleus. The nucleus can also include neutrons, that largely contribute to the mass of the atom. Isotopes are two versions of the same element (identical number of protons) with differing masses, due to a change in the number of neutrons. We qualify as stable the isotopes that do not decay with nuclear reactions. A single element may have several stable isotopes (e.g. argon has three stable isotopes: ^{36}Ar, ^{38}Ar, ^{40}Ar), or none (e.g. promethium). Heavy

isotopes denote the isotopes with more neutrons, responsible for a greater mass. By extension, we call isotopologues the versions of the same molecule with different isotopes in their atomic composition.

We note the isotopic composition of a reservoir as the ratio of the heavy isotope over the light isotope:

$$R = \frac{^{A_1}X}{^{A_2}X} \tag{2.1}$$

where X is the element and A_1 or A_2 the mass numbers.

2.2.2 Partitioning of stable isotopes during fractionating processes

The difference of mass between two isotopes is associated with a change in thermodynamic and kinetic properties. Consequently, chemico-physical processes in which at least two phases (or two parts of a system) co-exist often concentrate an isotope in one phase and deplete it elsewhere: this process is named fractionation.

$$Phase_A \rightleftharpoons Phase_B \tag{2.2}$$

In a process where two phases are involved (equation 2.2), the $Phase_B$ may have an isotopic composition R_B that differs from R_A in $Phase_A$. We note the fraction coefficient associated with this process

$$\alpha_{A \to B} = \frac{R_A}{R_B} \tag{2.3}$$

As fractionation processes induce very small variations of the R ratio of two isotopes, we use the δ notation, where the ratio is given as the difference relative to a standard (equation 2.4).

$$\delta = \frac{R_{sample} - R_{standard}}{R_{standard}} \times 1000 \tag{2.4}$$

The values for δ are given in permil (‰). Most standards were defined during the consultants meeting held in Vienna, 1-3 December 1993 (IAEA, 1995).

2.2.2.1 Equilibrium fractionation

If the chemico-physical process is under thermodynamical conditions where the two phases may co-exist, it may eventually reach an equilibrium where the exchanges $A \rightarrow B$ and $B \rightarrow A$ occur at an equal rate, so the net flux is null. In that case, the partitioning of isotopes is conditioned by the thermodynamical properties alone. The fractionation between the two phases is then named equilibrium fractionation. The equilibrium fraction coefficient is often temperature-dependent, as in the exchange of oxygen isotopes between calcite and water (Tiwari et al., 2015).

2.2.2.2 Kinetic fractionation

When the exchanges between the two phases (or two parts of a system) are not at equilibrium, one of the exchanges occurs at a greater rate than the other, resulting in a net flux. Non-equilibrium systems include fast, incomplete or unidirectional processes. The availability of different isotopes to be exchanged depends on their kinetic properties, which differ from the thermodynamic properties. Consequently, an additional fractionation occurs in non-equilibrium systems.

2.3 Water stable isotopes

Water molecular composition is H_2O, and can thus be composed by a combination of ^{1}H, D (for deuterium, alternative notation of ^{2}H), ^{16}O, ^{17}O, and ^{18}O. The relative abundances of each stable isotope are given in Table 2.1

Table 2.1 Relative abundances of stable isotopes of Hydrogen and Oxygen

Element	Hydrogen		Oxygen		
Number of mass (A)	1	2	16	17	18
Number of neutrons	0	1	8	9	10
Symbol	^{1}H	^{2}H, D	^{16}O	^{17}O	^{18}O
Abundance (%)	99.985	0.0155	99.759	0.037	0.204

It is very rare to have a combination of two heavy isotopes in the same molecule, because of the low relative abundance of heavy isotopes of both hydrogen and oxygen. For example, $D_2{}^{16}O$ and $H_2{}^{18}O$ have the same molecular mass (20), but the relative abundance of $D_2{}^{16}O$ is nearly 5 orders of magnitude lower than the relative abundance of $H_2{}^{18}O$. Therefore, the measurements are usually approximated to the detection of the most abundant isotopologues: $H_2{}^{16}O$, HDO, $H_2{}^{17}O$, and $H_2{}^{18}O$. We approximate the isotopic ratios by the ratios of the most abundant isotopologues $R_D = \frac{HD^{16}O}{H_2{}^{16}O}$, $R_{17} = \frac{H_2{}^{17}O}{H_2{}^{16}O}$, and $R_{18} = \frac{H_2{}^{18}O}{H_2{}^{16}O}$.

For water isotopes, the standard to which isotopic ratios are usually compared to is the Vienna Standard Mean Ocean Water (V-SMOW; given by IAEA, 1995). It is convenient to place the ocean as the starting point of hydrological processes, because it is the largest and most stable water reservoir on Earth. We thus use $\delta^{18}O$, $\delta^{17}O$, and δD to describe the isotopic composition of water.

2.3.1 Isotopes in polar precipitation

In this section, we describe the processes affecting the water and altering its isotopic composition, starting from the ocean to the precipitation in polar regions.

2.3.1.1 Evaporation at moisture source

Water feeding Antarctic precipitation evaporates from the Oceans surrounding Antarctica (Sodemann & Stohl, 2009). Because evaporation – precipitation regimes vary with latitude, the mean isotopic composition of ocean surface water depends primarily on its latitude (Bigg & Rohling, 2000). The $\delta^{18}O$ of surface water varies from +0.6‰ in tropical latitudes (around 30°S), where evaporation is the dominant process, to – 0.3‰ in the Southern Ocean, south of the polar front (around 50°S). As moisture pathways differ for air masses bringing moisture to high elevation continental sites and coastal sites (Masson-Delmotte et al., 2008), the evaporative sources reaching high-altitude continental sites are located at lower latitude in the open ocean, as opposition to coastal sites that have local moisture sources (Sodemann & Stohl, 2009). Therefore, the initial composition of the water evaporating may differ between sites, depending on elevation and source location, but this effect is relatively low.

Evaporation is a physical process where strong fractionation can occur. The winds over the ocean causes the evaporated moisture to be quickly removed from the surface as it is formed, resulting in non-equilibrium kinetic fractionation as one phase is consistently removed from the transformation. Craig & Gordon (1965) described the evaporation as a first equilibrium between ocean water and a laminar surface layer, from which the diffusion of a saturated vapor to under-saturated atmosphere accounts for the kinetic fractionation.

Water fractionating processes at thermodynamic equilibrium are about 8 times stronger in δD than $\delta^{18}O$. The number 8 results from the equilibrium fractionation coefficients for the hydrogen and oxygen isotopes. Kinetic fractionation results in an additional fractionation, deviating from this equilibrium, resulting in same magnitude changes for δD and $\delta^{18}O$. Consequently, we use the excess notation by quantifying the deuterium in excess compared to

this equilibrium: $d_{excess} = \delta D - 8\delta^{18}O$ (Dansgaard, 1964). By analogy, the $^{17}O_{excess}$ was defined as the difference to the $\delta^{17}O$ – $\delta^{18}O$ thermodynamic equilibrium, with a ratio of 0.528 in logarithmic form (equation 2.5, Barkan & Luz, 2005).

$$^{17}O_{excess} = \ln(\delta^{17}O + 1) - 0.528 \ln(\delta^{18}O + 1) \quad (2.5)$$

Note that because changes in $^{17}O_{excess}$ are usually very small, we use the permeg notation (1000 permeg = 1 ‰)

Uemura et al. (2008) measured the isotopic composition of water vapor over the ocean. The temperature, humidity and wind speed play a role in the fractionation during evaporation (Uemura et al., 2008). These parameters determine the isotopic composition of the vapor in the air mass, and especially influence its d_{excess}. Uemura et al. (2008) found relative depletions in the vapor of the order of -15‰ for $\delta^{18}O$ and -110‰ for δD, resulting in a d_{excess} of about 10‰.

More recently, Bonne et al. (2019) argued that wind speed was less influent, and that d_{excess} was most sensitive to sea surface temperature and relative humidity. They give the following multivariable regression for d_{excess} with field measurements on the North Atlantic Ocean (Bonne et al., 2019):

$$d_{excess} = -0.33RH_{sea} + 0.27SST + 25.01 \quad (2.5)$$

where RH_{sea} is the relative humidity of the air at sea temperature, from observations of relative humidity 29 m above the surface, adjusted for variation of the vapor saturation pressure with temperature. SST is the sea surface temperature, measured 5 m below sea level. In other terms, an increase of 10% in relative humidity will cause a decrease of 3.3‰ in d_{excess}. Alternatively, an increase of 10°C in SST will cause an increase of 2.7‰ in d_{excess}.

On the other hand, $^{17}O_{excess}$ is primarily sensitive to changes in humidity at the moisture source, but less sensitive to temperature than d_{excess} (Barkan & Luz, 2005; Uechi & Uemura, 2019; Uemura et al., 2010). Indeed, the ratio between equilibrium fractionations coefficients

for $^{17}O/^{16}O$ and $^{18}O/^{16}O$ do not depend on temperature (Angert et al., 2004). Uemura et al. (2010) measured the $^{17}O_{excess}$ composition of vapor collected over the South Indian Ocean, and give a linear regression slope against relative humidity of –0.64 permeg/%. An increase of 10% in relative humidity causes a decrease of 6.4 permeg in $^{17}O_{excess}$. The $^{17}O_{excess}$ is also particularly convenient as it is less sensitive to continental temperature changes and will therefore better preserve the moisture source signal in ice cores (Landais et al., 2008; Touzeau et al., 2016).

In summary, a change in the location of the moisture source has an influence on both meteorological conditions at the moisture source and the isotopic composition of the surface water available to evaporate, therefore resulting in a significant change in the water stable isotopes (Markle et al., 2017).

2.3.1.2 Transport and condensation of precipitation

After evaporation, the vapor is, on average, advected towards the pole by the atmospheric general circulation. The simplest hydrological model consists in a one-directional longitudinal transport of oceanic air masses with newly evaporated water. As the air mass cools with increasing latitude, the saturation vapor pressure decreases. Upon reaching saturation, the vapor condensates onto aerosol nuclei, and grow droplets that form the cloud. Largest droplets are washed out in precipitation, removing a part of the air mass water content. The isotopic composition of droplets is enriched in heavy isotopes D and ^{18}O, because the vapor saturation pressure of heavy isotopologues is lower. Consequently, the transport toward colder polar regions is associated with gradual washout of the heavy isotopes, because water vapor saturation pressure decreases with temperature. This process is a Rayleigh distillation.

With the assumption that droplets are at equilibrium with water vapor in the cloud, Dansgaard (1964) detailed the evolution of isotopic content of water vapor during a Rayleigh

distillation where cloud temperature decreases. The slope for $\delta^{18}O$ to temperature in newly formed droplets varies on the initial temperature of the air mass. Under average conditions for temperature, Rayleigh distillation at equilibrium gives a slope of $\delta^{18}O$ – T of 0.45‰/°C. In summary, the Rayleigh distillation and gradual removal of heavy isotopes with cooling temperature causes the temperature signal in the isotopes in precipitations.

The Rayleigh distillation gives a slope of δD – $\delta^{18}O$ that matches well with the isotopes measured in precipitations. Craig (1961) found a slope of $\delta D = 8\delta^{18}O + 10$ in meteoric waters, where the slope of 8 mostly reflects equilibrium processes during Rayleigh distillation and the excess of 10 originates from kinetic fractionation at evaporation. However, the equilibrium model fails to explain d_{excess} signature in polar regions.

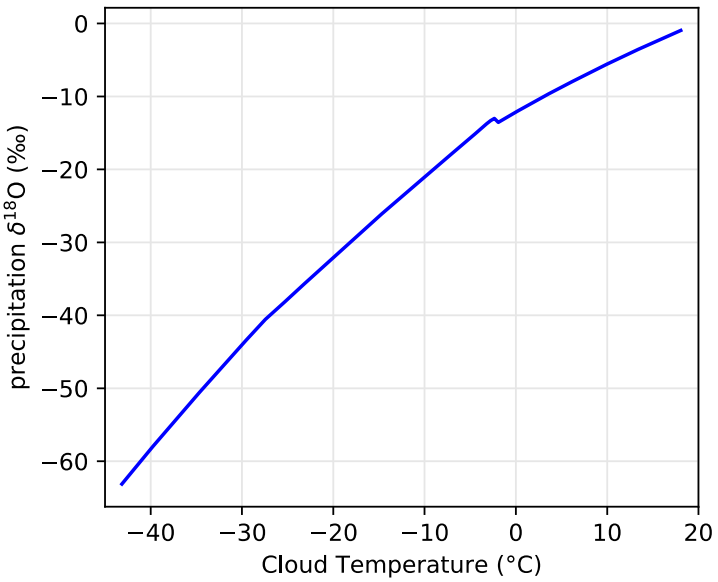

Figure 2.2. Example of the evolution of $\delta^{18}O$ and temperature in the precipitations in the Mixed Cloud Isotopic Model (Ciais & Jouzel, 1994).

Jouzel & Merlivat (1984) refined the one-dimensional distillation model by implementing kinetic fractionation in the cloud as the vapor is often in an oversaturated state when droplets or ice form in the cloud, causing out-of-equilibrium fractionation. In addition, Ciais & Jouzel (1994) improved the model for cold environments by implementing the isotopic fractionation in a mixed cloud where ice and liquid coexist (a $\delta^{18}O$ – T evolution is shown in

figure 2.2). In mixed clouds, the saturation pressure over ice and over liquid are different, resulting in an additional fractionation. The $\delta^{18}O$ – T slopes given by the mixed cloud model remain similar to a simple Rayleigh distillation model. The d_{excess}, strongly affected by kinetic fractionation, gives values similar to the meteoric water line, and matches the observations in Antarctica.

One-dimensional distillation models give a good understanding of how the water isotopic composition varies in a single air mass moving poleward. However, the reality is much more complex, with mixing of air masses that causes non-linear effects on the secondary parameters d_{excess} and $^{17}O_{excess}$. Recent improvements in atmospheric global circulation models that account for realistic atmospheric transport and mixing may help understand the isotope – temperature relationship (Galewsky et al., 2016). More detail on atmospheric circulation models will be given later in this chapter (section 2.6).

2.3.2 Mitigation of the climate signal related to snow deposition

The formation of precipitation does not mark the end of isotopic exchanges, and the initial climate signal present in precipitation isotopes may be significantly altered from the cloud to archival in the ice.

2.3.2.1 Deposition

Patterns of deposition can alter the signal recorded in ice core, by controlling the quantity of snow at a given location. Picard et al. (2019) analyzed accumulation patterns at Dome C, a low accumulation plateau site. They showed that large variation of accumulation occurred at a meter scale. They also showed that nonconsolidated snow may be eroded and redeposited several times before definitively settling, and surface winds causing the erosion reshape the surface frequently with a surface roughness of the order of 10 cm. Consequently, Picard et

al. (2019) show that the day from which the snow was present at the surface varies horizontally, and snow older than a year may be found at the surface despite several deposition events in the near surroundings (few meters).

This horizontal heterogeneity in snow translates into the isotopic composition of surface snow. Ritter et al. (2016) found variations of up to 20‰ in δD of surface snow sampled in a 100-m-transect near Kohnen station, on the East Antarctic Plateau. Münch et al. (2016) show that in a 50-m long trench dug at Kohnen station, the isotopic composition varies horizontally with stratigraphic noise. Münch et al. (2016) measured the correlation between profiles of isotopes in the trench, which decreases to 0.5 within 10 m, and plateaus at a correlation of 0.5 with more distant profiles. These profiles were however affected by additional processes that occur after deposition, thus named post-deposition effects. Changes in isotopic composition do not reflect only a stratigraphic noise. We describe the post-deposition effects on isotopes in the next sections.

2.3.2.2 Snow-vapor exchanges

When snow or water precipitate from the cloud, it often passes through under-saturated air masses between the cloud and the surface (Agosta et al., 2019; Jullien et al., 2020). Although the quantity of precipitation re-evaporated is difficult to evaluate, it is likely associated with isotopic fractionation during the fall (Bony et al., 2008; Dansgaard, 1964).

Even after deposition, the snow is porous and keeps exchanging with the atmosphere. Steen-Larsen et al. (2014) monitored the isotopic content of surface snow and near surface vapor. They reported fluxes of vapor between air and snow affecting the isotopic composition of the snow by increasing $\delta^{18}O$ by up to 7‰, and decreasing d_{excess} by 6‰. Ritter et al. (2016) evidenced diurnal cycles of water isotopes in near surface vapor and surface snow, which

result from evaporation-condensation processes with changes in surface temperature and saturation vapor pressure. Warming of 10°C with the diurnal cycle causes evaporation of the snow, resulting in an increase of about +0.4‰ in $\delta^{18}O$ (or 3‰ in δD). A simple condensation evaporation box-model with snow at equilibrium with surface air gives an amplitude of the isotopic changes in vapor twice as large as observations, that are probably overestimated as the model does not account for advection of air masses or modification of the boundary layer (Ritter et al., 2016).

The isotopic effect of evaporation-condensation was also evaluated from surface snow collected near Dome C. Casado et al. (2018) evaluated the $\delta^{18}O$ – temperature slope in surface snow and compared it to values from fresh precipitation for the same site (Stenni et al., 2016), and found that the slope was lower in surface snow. Moreover, the Pearson correlation coefficient between temperature and $\delta^{18}O$ in the snow is only of $r^2 = 0.29$, much lower than the $r^2 = 0.65$ with $\delta^{18}O$ in the fresh precipitations (Casado et al., 2018). This evidences the loss of the condensation temperature signal in the snow due to post-deposition processes. Touzeau et al. (2016) presented a database of surface snow isotopic measurements in Antarctica, including snow pits. They reported positive slopes of $\delta^{18}O$ – temperature, even in locations with no precipitation, suggesting that post deposition effects maintain a relationship between snow isotopes and local temperature, despite the changes in slope values and correlation coefficients.

2.3.2.3 Diffusion

Evaporation and recondensation of snow in contact with the atmosphere circulating in the open porosity keep exchanging water molecules, as they sublimate and condensate, especially during diurnal temperature cycle (Ritter et al., 2016). The molecules do not necessarily condensate at the same depth from where they evaporated, resulting in an apparent diffusion

of the isotopic signal. The diffusion smooths out the high frequencies of the snow isotopic signal (e.g. Jones et al., 2017). Generally, it tends to homogenize the snow isotopic composition.

Johnsen et al. (2000) presented a quantitative diffusion model for isotopes in the snow, and compared it to measurements from East Antarctica and Greenland. They discuss how smoothing of high frequencies may alter the $\delta^{18}O$ – temperature slope by decreasing the apparent variance of isotopes. Furthermore, a faster diffusion rate for $\delta^{18}O$ than δD may cause changes in the d_{excess}.

Laepple et al. (2018) showed that the diffusion of noise-dominated isotope signal in the snow could create cycles of about 20 cm unrelated to climate. Their results highlight that low accumulation regions (under 100 kg m^{-2} yr^{-1}) are not suited for high resolution climate reconstructions, at annual to decadal scale.

In conclusion, deposition and post-deposition processes may alter the climate signal acquired during precipitation formation, by inducing spatial heterogeneities and smoothing of high frequencies. However, the temperature – snow isotope relationship can still be observed in most locations, in longer periodicities or using averages of several cores to overcome spatial heterogeneities and the noise masking the high frequencies (Graf et al., 2002). Therefore, we expect ice cores to record a temperature signal.

2.3.3 Calibration of isotope – temperature slope

Water isotopes in the snow scale with temperature due to the Rayleigh distillation with preferential removal of heavy isotopes. Several approaches were taken to quantify the isotope – temperature slope that could then be used to infer past temperature from the measurement of isotopes in ice cores. We describe here the different definitions of slopes.

A first approach is to use measurements of isotopes in snow at different locations in a range of annual mean temperature, which determine a "spatial" slope of 0.80‰/°C for $\delta^{18}O$ in Antarctica (0.77‰/°C in Lorius & Merlivat, 1975; slope value of 0.80‰/°C from Masson-Delmotte et al., 2008). However, sites at different locations receive moisture from many different sources, so the initial isotopic composition varies for each location. This influences the final isotopic composition, and thus the spatial slope may significantly differ from temporal variability of isotope and temperature at a given site (Boyle, 1997; Casado et al., 2017). Consequently, spatial slopes are not the best option when trying to reconstruct temporal temperature changes from ice cores.

The isotope – temperature slope can be estimated with models. The one-dimension model including the most realistic micro-physical processes, the Mixed Cloud Isotopic Model, gives a δD – temperature slope of 6.5‰/°C (Ciais & Jouzel, 1994, equivalent to 0.81‰/°C for $\delta^{18}O$). This value also does not account for changes in the moisture source, and best explains spatial variations. It is indeed very close to the spatial slope. More complex isotopic enabled Global Circulation Model still poorly reproduce the amplitude of isotope and temperature (Galewsky et al., 2016; Goursaud et al., 2018), and cannot be used to quantify the isotope – temperature slope. They remain very useful to investigate the relative influence of large scale climate variability on the isotopes.

Site specific calibrations are preferred, as they describe the temporal relationship between isotope and temperature, and account for all the processes specific to this site that may alter the precipitation signal: moisture source, post-deposition changes in isotopic composition will be included in the isotope variability measured on-site. Borehole temperature inversions give a good estimate of the temperature range, but with low resolution. Cuffey et al. (1995) used the isotope signal averaged over extended cold periods and warm periods to estimate a range for both isotope and temperature for the Greenland Ice Sheet Project II site.

They obtained a slope of 0.33‰/°C for $\delta^{18}O$, much lower than the spatial slope. This slope was defined over a period covering 40,000 years, covering the warm Holocene (most recent 11,850 years) and an important part of the last glacial period. The slope given by Cuffey et al. (1995) is representative of long term changes in atmospheric conditions over Greenland.

Lastly, we can use temperature from observations in monitored locations, or estimated from atmospheric climate models to have a recent history of temperature variability, which can then be compared to high resolution isotopic records covering the recent period. The simplest way to compute a slope is to compute the linear regression of isotope to temperature, but it heavily depends on the resolution: the seasonal temperature signal has a much lower $\delta^{18}O$ – temperature slope (Casado et al., 2017), which may bias reconstructions aiming at longer timescale. In that case, it is preferable to average annually at least, and preferably a few years, to remove the seasonal variability. The difficulty is then to have a record long enough to produce a robust calibration, with sufficient number of data point. For example, Stenni et al. (2017) calibrated ice cores in Antarctica using a temperature product from (Nicolas & Bromwich, 2014) covering the 1957-2013 period. They used a ratio of variance in 5 to 10-years windows to scale the detla18O – temperature slope. However, using the ratio of variances may cause underestimation of temperature variations if some of the ^{18}O variance is caused by other processes such as deposition noise (Stenni et al., 2017). They reported $\delta^{18}O$ – temperature slopes ranging from 0.40 to 1.21‰/°C, with a weighted average of 0.98‰/°C for the entire Antarctic continent.

The calibration of isotope – temperature for temporal reconstructions is complex as it varies depending on the timescale (Jouzel et al., 2003). As the climate variability strongly depends on the location, a thorough investigation of isotope – temperature relationship is required before trying to infer past temperature from isotope measurements.

2.3.4 Analytical methods

Formation of the snow is accompanied with the record of climate signal in the water isotopes. In this section, we describe how we measure water stable isotopes.

2.3.4.1 Cavity Ring-Down Spectroscopy

Preparation

A small amount of water is enough for the analysis, because it is the main component in an ice core. Usually a few microliters are analyzed, but we prefer larger samples of the order of milliliters to minimize the effect of fractionation during handling and storage. Spectroscopy measures the composition of vapor, so the ice is preemptively melted, filtered and vaporized before injection into the spectrometer.

General principle of the spectrometer

Recent improvements on spectroscopy allowed for rapid determination of isotopic ratios in water vapor, with little loss on precision, and reduced costs. Consequently, most laboratories interested in water isotopic composition are now equipped with water isotope-specific spectrometers. Cavity Ring-Down Spectrometry (CRDS) instruments measure the composition of vapor injected into a cavity walled by high reflectivity mirrors (*Picarro*, website). A single wavelength laser pulse is emitted and bounces off the mirrors with an effective travel length of several km. A photo-sensor measures the decay of light due to absorption by the water vapor molecules in the cavity. The rate of absorption and thus the shape of decay depend on the isotopic composition of the water, because the energy of resonance in covalent bounds differs with the mass of the atoms involved. Laboratory tests showed that the precision of this technique was 0.5‰ for δD and 0.1‰ for $\delta^{18}O$ (Gupta et al., 2009).

2.3.4.2 Fluorination and mass spectrometry

Although recent spectrometers are able to measure $^{17}O_{excess}$ with a decent precision (15 permeg), the natural changes in $^{17}O_{excess}$ are often of the order of 10 to 20 permeg (Landais et al., 2008; Winkler et al., 2013). More precise measurements are required for the oxygen isotopes.

Barkan & Luz (2005) optimized a fluorination method to isolate oxygen from the water molecule, which is transformed in dioxygen gas. The dioxygen can then be analyzed on mass spectrometer, and the count of masses 32, 33 and 34 give the isotopic ratios for oxygen, under the approximation that we can neglect clumped isotopes (combination of two heavy isotopes in the same molecule, that are several orders of magnitude less frequent – see Table 2.1).

Measurements of gases are often performed on dual inlet Isotope Ratio Mass Spectrometers (IRMS), which give excellent analytical precision thanks to frequent measurements of a working standard (first inlet) compared directly to the sample (second inlet), measured under the same conditions. The mass spectrometer, comports three main parts: (1) a source, where gases are ionized, and accelerated in an electric field, (2) a magnet that deviates the trajectory of charged particles, where heavier isotopes take a larger curve due to their greater inertia, and (3) a collector, with multiple cups to count the ions in the mass-separated beams and compute isotopic ratios.

This method, is used mostly for $^{17}O_{excess}$ as it requires the transformation of water molecules into oxygen. The $\delta^{18}O$ values are also measured and compare well with other methods. This method is also the most precise for $^{17}O_{excess}$, and we can reach replicated precision of about 6 permeg (Touzeau et al., 2016).

2.3.4.3 Working standards

Officially calibrated standard material is expensive, and V-SMOW has a fixed isotopic composition at 0‰ for δD, $\delta^{17}O$ and $\delta^{18}O$. We calibrate working standards to reduce costs and have as assortment of standards with isotopic composition closer to the samples we analyze. Most ice samples present $\delta^{18}O$ values ranging from -25 to -55‰. Using working standards, we can indirectly calibrate samples to V-SMOW. Additionally, two working standards allow for calibration of the sensitivity of the spectrometer: we measure the range between two working standards with known values.

2.3.5 Summary of water isotope signal in ice cores

In conclusion, δD and $\delta^{18}O$ in snow and ice scale with temperature during their formation due to distillation of heavy isotopes during the transport (Ciais & Jouzel, 1994; Dansgaard, 1964). Second order parameters d_{excess} and $^{17}O_{excess}$, defined as the difference to equilibrium processes record history of kinetic fractionation (Dansgaard, 1964; Jouzel & Merlivat, 1984), and depend mostly on source relative humidity, while d_{excess} is also sensitive to sea surface temperature (Bonne et al., 2019; Uemura et al., 2008, 2010).

Using these properties, ice core studies evidenced past temperature changes. For example, Masson et al. (2000) showed millennial variability in Antarctic ice cores during the Holocene. They suggested the influence of oceanic forcings, with internal oscillations causing decadal to centennial periodicities observed in all ice cores. Jouzel et al., (2007) presented the δD record from EPICA Dome C, from which they inferred temperature changes in Antarctica during the last 800,000 years. They evidenced eight glacial-interglacial cycles with variable amplitude in response to orbital forcings, and identified oceanic-driven millennial variability within all the glacial periods. As described in chapter 1, Stenni et al. (2017) contributed to understand trends in Antarctic temperature during the last 2000 years. Markle et

al. (2017) used the d_{excess} to track changes in the moisture source for the West Antarctic Ice Sheet divide ice core, and showed the influence of rapid atmospheric circulation changes on moisture source location.

2.4 Gases Stable isotopes

In this section, we detail the gases isotopes, and the mechanisms leading to a recording of temperature signal in gases trapped in ice cores. Our analysis focuses on two elements: nitrogen (N) with isotopes ^{14}N and ^{15}N, and argon (Ar) with isotopes ^{36}Ar, ^{38}Ar, and ^{40}Ar, which relative abundances are given in Table 2.2.

Argon is a mono-atomic gas, so the ratio of the two most abundant stable isotopes can be measured directly as $R_{40} = \frac{^{40}Ar}{^{36}Ar}$. Nitrogen is mostly found under the dinitrogen (N_2) form in the atmosphere. As described previously for water isotopes, the occurrence of clumped isotopes (several heavy isotopes in a same molecule) is orders of magnitude less frequent, hence we approximate $R_{15} = \frac{^{15}N^{14}N}{^{14}N_2}$. For purposes of the analysis of gases in firn and ice core, we use the free atmosphere as the standard (Mariotti, 1983), because it is the largest reservoir of gases. Additionally, the atmosphere is globally mixed in about a year, and the isotopic composition of N_2 and Ar remained stable during the last 2000 years, the period of interest in our study.

Table 2.2 Relative abundances of isotopes of Nitrogen and Argon

Element	Nitrogen		Argon		
Number of mass (A)	14	15	36	38	40
Number of neutrons	7	8	18	20	22
Symbol	^{14}N	^{15}N	^{36}Ar	^{38}Ar	^{40}Ar
Abundance (%)	99.636%	0.364%	0.334%	0.063%	99.604%

2.4.1 Structure of the firn

The firn describes the porous layer formed as the snow accumulate on ice sheets (figure 2.3). Initial snowflakes shape are broken down into round grains within days, due to rolling of snow on the surface with wind, and evaporation – condensation processes (Colbeck, 1982). In deeper layers, evaporation – condensation processes causes the growth of larger ice crystals at the expense of smaller grains because of tensile strength, resulting in a general increase in grain size (Colbeck, 1982). With increasing pressure, ice crystals also merge together into larger grains. Compression due to the snow load causes increased density and decreased porosity as we move further down the firn (e.g. Fourteau et al., 2019).

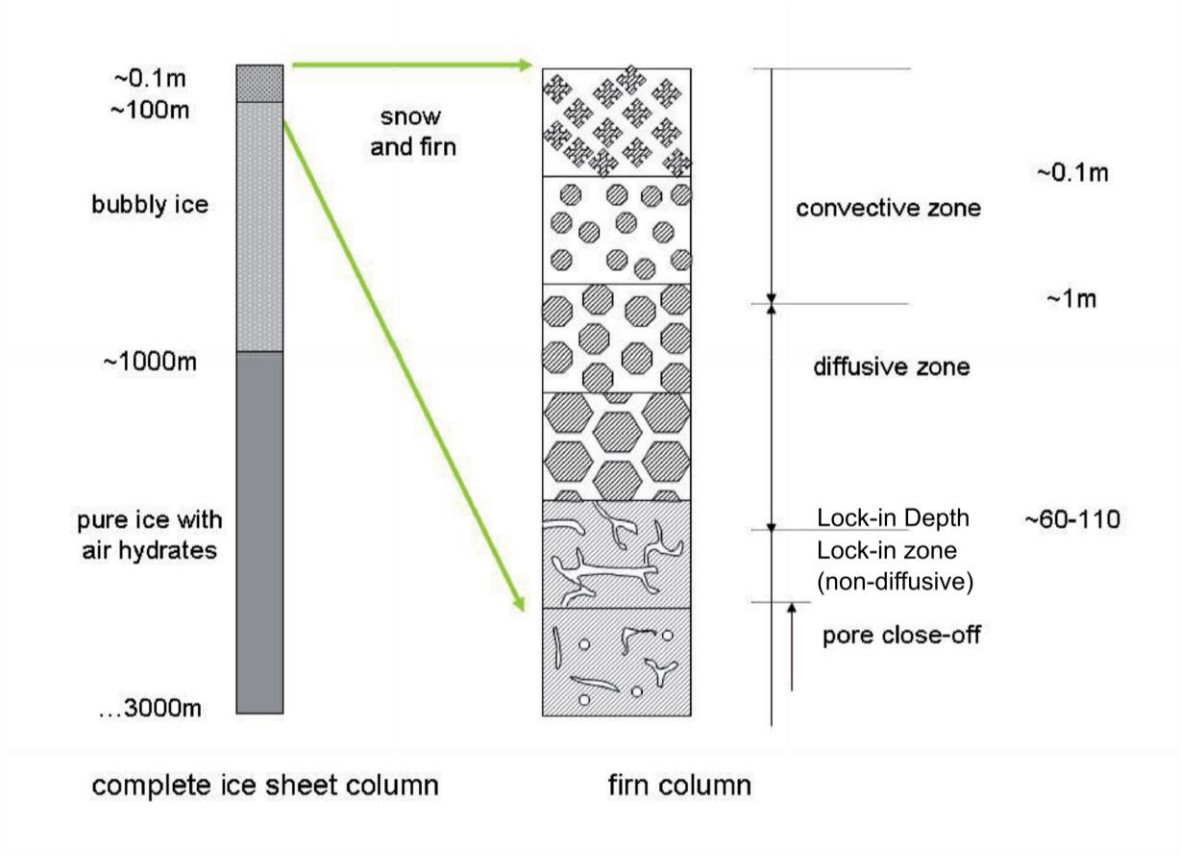

Figure 2.3. Vertical structure of the ice sheet column (left) and detailed firn column (right). Original figure from Maria Hörholdt.

Air circulates in the open porosity. While the top meters can be actively mixed with changes in winds, the movement of air in the deeper layers is regulated by diffusion. The lock-in zone describes a zone where the gases diffuse so slowly that it is negligible. In this zone, there is no gas exchange with the atmosphere, yet bubbles are not fully formed. We name lock-in depth the deepest point where gases can diffuse from the free atmosphere, and is at the top of the lock-in zone. At the bottom of the lock-in zone, bubbles are closed and we have bubbly ice below the close-off depth. Because the lock-in zone is about ten meters vertically, the bubbles are formed progressively with ages spanning several years, depending on local accumulation (Buizert et al., 2012).

2.4.2 Firn fractionation processes

The gases in the diffusive column of the firn can move slowly and reach an equilibrium. Gases are subject to varying conditions along the column: first the gravity pulls gases down, second there may be different temperature conditions at the top and at the bottom of the firn, and third the top of the firn may be mixed due to convection. We detail here the effects on gases isotopes.

2.4.2.1 Gravitational fractionation

In the firn diffusive column, the equilibrium conditions are dictated by gravity. Craig et al. (1988) showed that the gas isotopic composition in ice bubbles was enriched in heavy isotopes and heavy elements relative to the atmosphere. This enrichment is proportional to the mass difference of the two gases compared, be it two isotopes or two elements with different masses, and scales with the depth of the diffusive column (Craig et al., 1988). Indeed, the proportion of heavy gases increases with depth in the firn as predicted by the barometric equation (Craig et al., 1988; Sowers et al., 1992; given in equation 2.6), and as measured in

firn air sampled from Greenland (Schwander et al., 1993) and Antarctica (Severinghaus et al., 2001). The simplified barometric equation in delta notation gives:

$$\delta_{gravitational} = \frac{\Delta m g z}{R^* T} \tag{2.6}$$

where Δm is the mass difference in the two isotopes involved, g the gravitational acceleration, z the depth, R^* the gas constant and T the temperature in Kelvin (Severinghaus et al., 2001).

2.4.2.2 Thermal Fractionation

In addition to the gravitational settling of isotopes, differences of temperature between the two ends of the diffusive column is accompanied with fractionation. Indeed, lighter isotopes diffuse more easily, and the diffusive molecular transport that occurs in presence of temperature gradient tends to enrich the cold phase in heavy isotopes (Severinghaus et al., 1998). By analogy with gravitational fractionation, the thermal fractionation $\delta_{thermal}$ will modify the isotopic composition of the gases in the firn depending on a diffusivity coefficient Ω:

$$\delta_{thermal} = \Omega \Delta T \tag{2.7}$$

where ΔT is the temperature difference between the bottom and the top of the diffusive column, (Severinghaus et al., 2001). Diffusivity coefficients Ω do not proportionally depend on the mass, but are different for each couple of isotopes of a gas (Severinghaus et al., 2001). Diffusivity coefficients at cold temperature were measured in laboratory for N_2 (Grachev & Severinghaus, 2003a) and Ar (Grachev & Severinghaus, 2003b).

In the firn, the two effects add up, and the apparent isotopic compositions $\delta^{15}N$ and $\delta^{40}Ar$ can be approximated by

$$\begin{cases} \delta^{15}\mathrm{N} = \dfrac{1 \cdot \mathrm{gz}}{\mathrm{R^*T}} + \Omega_{15} \cdot \Delta\mathrm{T} \\ \delta^{40}\mathrm{Ar} = \dfrac{4 \cdot \mathrm{gz}}{\mathrm{R^*T}} + \Omega_{40} \cdot \Delta\mathrm{T} \end{cases} \tag{2.8}$$

We can isolate the thermal fractionation signal to

$$\Delta T = \frac{\delta^{15}N - \frac{1}{4} \cdot \delta^{40}Ar}{\Omega_{15} - \frac{1}{4} \cdot \Omega_{40}} = \frac{^{15}N_{excess}}{\Omega_{15} - \frac{1}{4} \cdot \Omega_{40}} \quad (2.9)$$

Where $^{15}N_{excess}$ describes the non-gravitational fractionation of $\delta^{15}N$ (Kobashi et al., 2008). Kobashi et al. (2008) used the measurement of $\delta^{15}N$ and $\delta^{40}Ar$ in a Greenland ice core to evaluate temperature changes during the last 11,500 years, using $^{15}N_{excess}$. They also introduce a separation method for N_2 and Ar that we will reuse in this Ph.D., and will precisely detail in Chapter 6 of this work. Similarly, Orsi et al. (2014) combined the measurements of $^{15}N_{excess}$ with a model of temperature and gas diffusion to estimate temperature changes with an inverse method, as it had been done for borehole temperature inversion.

2.4.2.3 Convective disequilibrium

Gravitational and thermal fractionation were described for a steady diffusive column, where equilibrium conditions are met. However, the diffusive zone does not reach the surface, because the air in the top meters of the firn can be actively mixed by wind. Severinghaus et al. (2010) measured the firn isotopic composition of gases in the firn at Megadunes, a low accumulation site in Antarctica. They showed that deep convection of several meters occurred at this site, lowering the heavy isotope enrichment in the firn because of the reduction in the diffusive column height. On the first meters, there is a gradual transition between convection (no isotope enrichment) and diffusion profiles (barometric enrichment). Kawamura et al. (2013) shows from measurement on the same site that diffusion and convection compete in the transitional area, resulting in additional fractionation related to kinetics of diffusion for each gas and isotope: gases that diffuse faster reach the diffusion-dominated equilibrium faster, resulting in an increase in their heavy isotopes relative to other gases. In the case of

Ar and N_2, this may lead to an overestimation of $\delta^{15}N_{excess}$, as Ar diffuses slightly slower than N_2.

2.4.3 Fractionation during close-off

Formation of bubbles may be accompanied with additional fractionation. Severinghaus & Battle (2006) show that firn is enriched in small-sized gases compared to the content of ice bubbles. They suggest that the thin layers of ice walling the newly formed bubbles could let some gases out depending on their size, as the pressure increases with compression. Severinghaus & Battle (2006) show that this process may cause elemental depletion of Ar in ice relative to N_2. Additionally, comparison of isotopic compositions of Ar and N_2 in firn and in ice shows consistently enriched $\delta^{40}Ar$ in the ice, while the $\delta^{15}N$ does not vary, causing decreased $\delta^{15}N_{excess}$ (Kobashi et al., 2008; Orsi, 2013). Even if processes leading to this enrichment are not fully understood yet, it has significant impact on the record of temperature gradient and firn to ice changes in $\delta^{40}Ar$ should be quantified and taken into consideration.

2.4.4 Analytical methods

The stable isotopic composition of gases is usually measured on gas isotope ratio mass spectrometers. For the determination of $\delta^{15}N_{excess}$, it is better to measure isotope ratios of argon and dinitrogen from the same sample. We use the method introduced by Kobashi et al. (2008), where both gases are measured from the same sample in which oxygen was removed, because $^{18}O_2$ interfere with the measurement of ^{36}Ar. Full methods from ice preparation to mass spectrometry will be thoroughly detailed in chapter 6 of this work, as they cover work realized during the thesis.

2.5 Firn model and temperature reconstructions

2.5.1 Forward diffusion-advection model

Firn diffusion models have been used to estimate the temperature profile in the firn given the surface temperature. The firn is not static, with fresh snow accumulating on top: this causes downward advection of snow, in addition to diffusion in porous snow with varying density. Alley & Koci (1990) rewrote the temperature diffusion and advection model from Johnsen (1977), adding a term to account for heat generation from ice deformation. This model can be written as

$$\rho c_p \frac{\partial T}{\partial t} = \frac{\partial}{\partial z}\left(k \frac{\partial T}{\partial z}\right) - \rho c_p w \frac{\partial T}{\partial z} + Q \tag{2.10}$$

where ρ is the density of firn/ice, k the thermal conductivity, c_p the heat capacity, T the temperature, t the time, z the depth, w the downward velocity of the firn/ice due to accumulation, and Q the heat production term, taking into account ice deformation and firn compaction (Orsi et al., 2012). This model thus accounts for diffusion with $\frac{\partial}{\partial z}\left(k \frac{\partial T}{\partial z}\right)$, advection with $\rho c_p w \frac{\partial T}{\partial z}$, and heat production with Q. The inputs of the model are (1) the surface temperature history, (2) the accumulation rate, and (3) the geothermal heat flux. It can be used to produce temperature profiles at a given time and compare it with temperature gradient in the firn estimated from other methods.

2.5.2 Inversion of the model for temperature reconstruction

With several simulations of temperature diffusion with different scenarios on surface temperature history, we have multitude of temperature profiles resulting from the diffusion model. An inverse method is then used to reconstruct the real temperature history from the

observations, either with Monte-Carlo methods (Dahl-Jensen et al., 1999), least-squares inversion (Orsi et al., 2012) or Tikhonov regularization (Roberts et al., 2013). The temperature can be inversed from temperature gradients estimated in the firn at different times (Orsi et al., 2014) or present-day temperature profile measured in the borehole, or a combination of the two as we will use in this work.

2.6 Borehole temperature

Borehole temperature is the measurement of the temperature in the ice sheet, from a borehole left over by an ice core drilling. This method relies on the fact that snow and ice conduct temperature relatively slowly, and retains information about past temperatures. The temperature profile in an ice sheet is an advection-diffusion problem, with surface temperature being one of the boundary conditions, and geothermal heat flux the second boundary condition. The information retrieved from a borehole temperature profile depends on site characteristics, principally the thickness of the ice sheet (thinner ice will be more heavily influenced by the geothermal heat flux), and the accumulation rate, which advects the surface temperature signal downward faster. Thick ice sheets with high accumulation rate are thus the best sites to use this method, and in these conditions, the temperature change from the last glacial period to the present can be retrieved, as well as major Holocene variations like the “Little Ice Age” temperature minimum, and the recent warming trend (e.g. Cuffey et al., 2016; Dahl-Jensen et al., 1998).

Measurements of borehole temperature are typically done by lowering a thermistor down the borehole with a 4-wire circuit, and recording of the resistance as a function of depth with a precise multimeter. The calibration of the thermistor is done in a controlled laboratory, and precision of 2-5 mK can be achieved (Clow, 2008). The ice core drilling perturbs the measurements by creating heat, and advecting warm air and drilling fluid down the borehole. It is

best to wait two years or more for the borehole temperature to relax to the ice sheet temperature. When this is impossible, a thermistor string is sometimes lowered in the borehole and data retrieved a year later by telemetry. Platinum Resistant Thermometers are sometimes used instead of thermistors, because although the precision is not as good (10 mK), they are less susceptible to drift with time (Muto et al., 2011). Recently, fiber-optic cables are being developed for this purpose (Law et al., 2020).

The borehole data is analyzed using a model of temperature diffusion in the ice sheet, as described in the previous section. Borehole temperature reconstructions have the advantage of providing an absolute temperature measurement that does not need a complex scaling to a proxy, but they are limited by the loss of information by diffusion. The recent warming trend of the last 50 years has been reconstructed successfully at several locations in Antarctica (Muto et al., 2011; Orsi et al., 2012; Roberts et al., 2013). Temporal temperature variability reconstructed from boreholes aid the calibration of other proxies, but longer records are rare: The Larissa record on the Antarctic peninsula goes back to 1800 (Zagorodnov et al., 2012), and WAIS-Divide is the only published record that provides a glacial-interglacial temperature estimate (Cuffey et al., 2016).

2.7 Atmospheric models and reanalysis

Direct monitoring of atmospheric parameters is limited to the locations where instruments are present. In Antarctica, the instrument network is especially sparse, and many locations are not directly documented. Remote sensing with satellite-mounted instruments help increase the spatial coverage of measurements, but is restricted to a few passes in a day, therefore resulting in discontinuous monitoring.

Atmospheric climate models solve the physical equations for fluid and gases in a discretized atmosphere (*Climate Models | NOAA Climate.gov*). Given initial conditions and boundary conditions, models simulate the evolution of climate in their domain. Atmospheric climate models thus help us understand the evolution of conditions at locations and time where we do not have direct observations. They let us compare atmospheric parameter and understand atmospheric processes where we would otherwise have no information. However, models can drift away from real conditions if the simulations are long. Initial and boundary conditions are primordial when setting up the model. For an atmospheric model, boundary conditions include the surface conditions on land and sea. Models are thus best used with good initial conditions, when we have observations to constrain the boundary conditions, *i.e.* in the recent period.

Climate reanalyses are built by running forecast models, and adjusting the results to the next set of observational data, in a process named data assimilation (Keeley, 2013). Consequently, the climate reanalysis gives parameters as close to reality as possible, by limiting the drift. For example, ERA-interim assimilates data from the satellite era (1979 onwards) to produce high fidelity global atmospheric variations (Dee et al., 2011). ERA-interim is particularly suited to study the Antarctic hydrological cycle, with the most realistic variability compared to other reanalyses (Bromwich et al., 2011). Reanalyses can be used to increase the skills of other models with nudging: some of the model parameters are interpolated and assimilated, which sensibly reduces the drift of the model (Telford & Dalvi, 2010). Contrary to boundary conditions, nudging can prescribe atmospheric conditions in the entire domain of the model (e.g. Radu et al., 2008). Climate reanalyses are thus useful to assimilate observational data that will be passed to other models with nudging for more realistic simulations.

Atmospheric circulation models can also include modelling of water isotope, because water isotopes grew important as a tracer of hydrological cycle. These models are especially

useful to better understand the climate information registered in the proxies. For example, ECHAM5-wiso is equipped with water isotopes δD and $\delta^{18}O$, allowing for direct comparison of isotope and temperature (Werner et al., 2011). This model, with good performance in Antarctica (Goursaud et al., 2018), was used to evaluate temperature variability in Antarctica from ice cores, by defining local slopes of isotope temperature (Stenni et al., 2017). However, isotopic-enabled atmospheric models are associated with isotopic biases (Steen-Larsen et al., 2017) that hamper our ability to use the isotope – temperature slope to interpret paleoclimate variability (Galewsky et al., 2016). They remain useful to understand the processes controlling the isotope and understand the relative variability of the isotope in direct comparison with atmospheric parameters.

2.8 Conclusion

We have at our disposal different tools to study the Antarctic temperature. It is possible to understand the daily interactions between different parameters and regional variability thanks to reanalyses-nudged atmospheric models, while ice cores can provide critical information on past temperature to describe the decadal to millennial variability at a given location. The combination of all available information will help us get a deep understanding of the mechanisms responsible for temperature variability at different timescales.

Chapter 3

Evaluation of the climate variability at Aurora Basin North, using atmospheric climate models

For a better understanding of past climate variability in East Antarctica, we need to increase the spatial coverage and temporal resolution of paleo-climate records (Chapter 1). Ice cores covering the past thousand years drilled on the East Antarctic Plateau (Dome C, Vostok, Dome F) all suffer from very low snow accumulation and related low temporal resolution, and specific biases related to low snow accumulation. Here we aim to improve our understanding of East Antarctic climate variability by finding an ice core site that allows annual layer counting, and still represents broadly the East Antarctic climate. The Aurora Basin North (ABN) site was chosen for this purpose (figure 3.1, Curran, 2015). It is located at equal distance between two deep ice coring locations: Law Dome near the coast and Dome C on the higher part of the East Antarctic Plateau. To better understand the climate record in the ABN core, and especially the precipitation sensitive proxies, we first need to understand the climate variability at the ABN location. This chapter relies on the analysis of a regional climate model to describe the recent temperature and precipitation variability at ABN and in East Antarctica. Contents of this chapter were published in a peer-reviewed journal (Servettaz et al., 2020) and were adapted for the chapter format.

3.1 Introduction

Understanding the climate of Antarctica is essential for the interpretation of ice cores. The calibration of proxy records during the instrumental period allows us to interpret ice core records over the last few millennia or under conditions similar to present day – when the calibration has been made. Recent climate is known from meteorological observations and extensive snow studies that overlap with satellite era data since 1979 (Fogt et al., 2017).

Given the brevity and sparsity of observational data, it remains difficult to assess the climate variability and trends in Antarctica (Jones et al., 2016) at decadal and longer timescales. Paleoclimate data such as ice-core records help to evaluate changes in atmospheric conditions over longer timescales, with the assumption that we understand how climate information is expressed in the climate proxy.

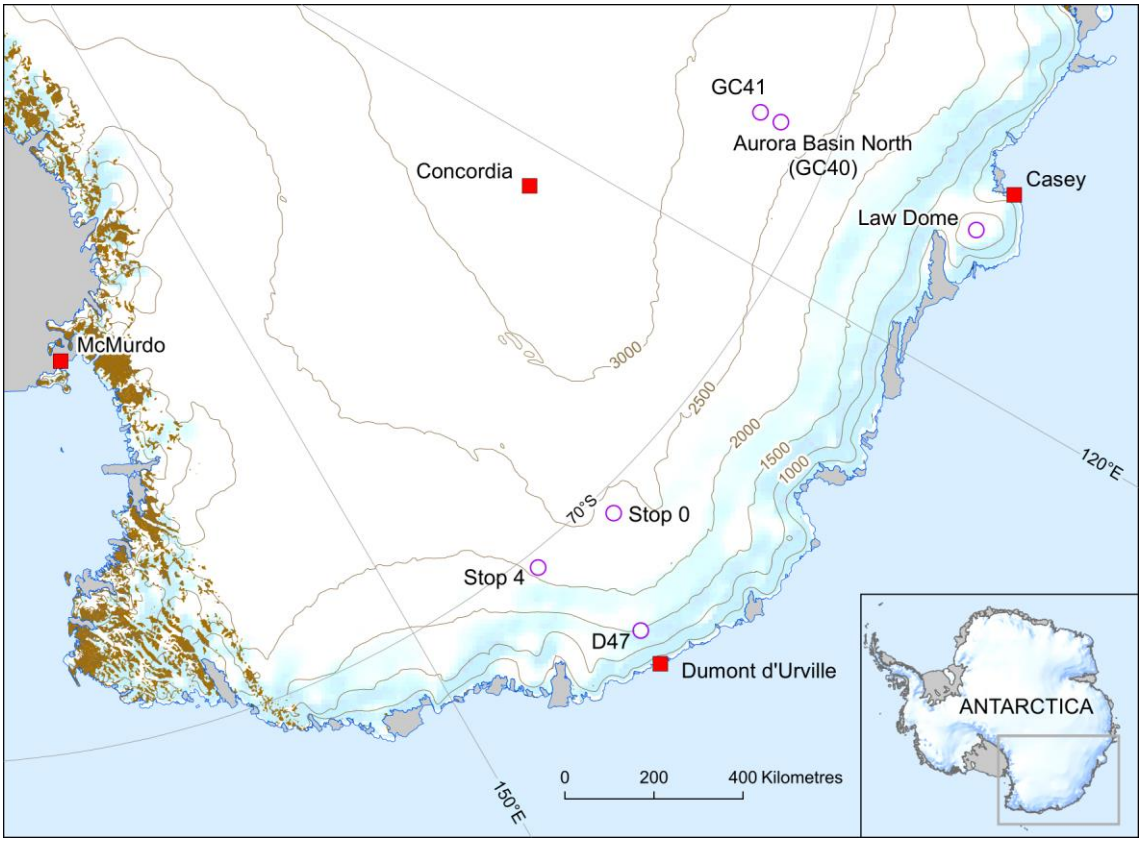

Figure 3.1. Map of the Aurora Basin North site and a selection of Antarctic stations and coring locations. Adapted from a production of the Australian Antarctic Data Centre, September 2013 (Map Catalogue No. 14254 – data.aad.gov.au © Commonwealth of Australia 2013).

Ice cores provide a variety of proxy records that can be used to reconstruct past climatic conditions. One of these proxies, water isotope ratio in snow and ice, can be used to trace past temperatures. The isotope ratios of oxygen and hydrogen scale with temperature due to preferential removal of heavy isotopes by the partial precipitation of water in the air masses

when they move poleward and cool down (Dansgaard, 1964; Jouzel & Merlivat, 1984; Masson-Delmotte et al., 2008). The most common water isotope ratios are given relative to standard mean ocean water, and noted $\delta^{18}O$ and δD (Craig, 1961; Dansgaard, 1964). In Antarctica, water isotopes have been widely used in ice cores across the continent to infer past temperatures (Jouzel, 2003; Stenni et al., 2017), with the oldest continuous ice core drilled to this day dating back to 800,000 year before 1950 (EPICA community members, 2004).

Advances in analytical methods and introduction of Cavity Ring-Down Spectroscopy have allowed precise measurements of $\delta^{18}O$ and δD with a decreased analysis time, leading to a substantial increase in resolution (Gupta et al., 2009). However, archival limitations due to intermittency of precipitation events, and loss of short periodicity signal due to post-deposition processes are particularly important in low accumulation areas, such as the East Antarctic Plateau (Casado et al., 2018, 2020). Deep ice cores drilled on the East Antarctic Plateau provide climate information over long timescales with a low (>50 year) resolution, complementing the short instrumental record (Ekaykin et al., 2017). Decadal to centennial variability, however, is not fully understood, although it is of increasing interest for secular projections (Jones et al., 2016). While coastal ice cores have a much higher resolution, they often record oceanic signals such as changes in sea ice conditions (Bertler et al., 2011; 2018; Rhodes et al., 2012; Thomas et al., 2019) and are not representative of the continental landmass (Altnau et al., 2015). This gap of data could benefit from ice cores drilled in higher accumulation areas on the plateau's edges, such as the recently drilled Aurora Basin North (ABN) ice core, with the aim clarifying the last 2000 years of climate variability in East Antarctica. Because water isotopes constitute a precipitation-dependent proxy for temperature, we must first understand the local variability of temperature and precipitations. The main objective of this chapter is to provide a framework for the interpretation of the ice core record.

We use the polar-oriented regional climate model MAR (Modèle Atmosphérique Régional) which performs well in Antarctica (Agosta et al., 2019) to describe the precipitation climatology and estimate the biases due to (1) seasonality and (2) warming associated with the air masses responsible for precipitation. We investigate the regional significance of ABN climate (section 3.2.2) and the conditions in which precipitation events occur (section 3.4). We discuss possible implications for other east Antarctic Plateau sites where the precipitation mechanisms are similar.

3.2 Methods

3.2.1 Site description

Aurora Basin North (71.17°S, 111.37°E at 2690 m elevation) is the site selected for the single summer drilling campaign conducted in the 2013–2014 season by the Australian Antarctic Science Program. The drilling site is located on the lower elevation edge of the East Antarctic Plateau, ~500 km inland of the coastal station Casey, approximately halfway to Concordia station on Dome C (figure 3.1).

Annual surface temperature from the nearby automatic weather station GC41 (71.60°S, 111.26°E, 2191 m elevation, located 50 km south of ABN; operation period 1985 to 1992) averages -43.7°C. This value is consistent with the borehole temperature measured at ABN, of -43.4 ± 0.3°C (with 3 measures downward and 3 measures upward from 16.5 to 31.5 m), although this value needs to be taken with caution because the temperature was measured shortly after the core was drilled.

Accumulation estimated with annually dated snow records (discussed in Chapter 4) averages 119 mm water equivalent (hereafter abbreviated mm w.eq.) yearly. Accumulation at ABN is much higher than deep ice core drilling sites on the East Antarctic Plateau: the yearly

accumulation at Kohnen station (EPICA Dronning Maud Land ice core) is just more than half that of ABN with 64 mm w.eq. (Münch et al., 2016), and even lower at Dome C with only 25 mm w.eq. (Stenni et al., 2016).

3.2.2 The regional climate model MAR

To assess the climate at ABN, which is hundreds of kilometers away from the nearest permanent meteorological station, we use the regional atmospheric climate model Modèle Atmosphérique Régional (MAR) forced by ERA-interim climate re-analysis (European Centre for Medium-Range Weather Forecast re-analysis interim dataset; Dee et al., 2011). The model simulation with MAR for Antarctica covering the period 1979 to 2015 was performed and evaluated by Agosta et al. (2019). We chose to use the MAR model because this model was developed with implementation of specific physical parameterizations for polar regions

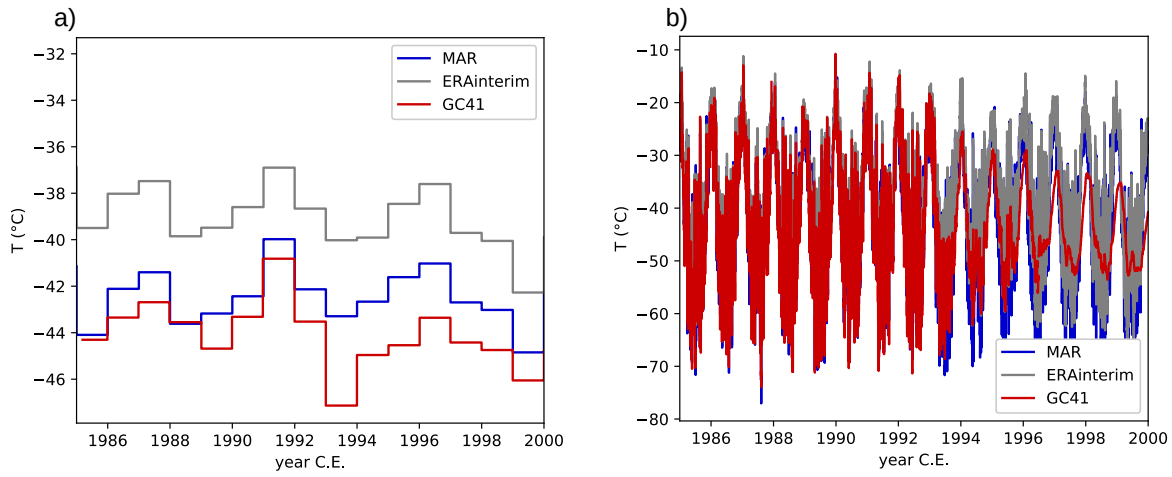

Figure 3.2. Comparison of temperatures from automatic weather station GC41 (71.60°S, 111.26°E) and 2 m temperature of corresponding grid points in MAR and ERA-interim. (**a**) annual averages (**b**) daily resolution. The automatic weather GC41 station gets buried in snow from 1993, causing the smoothing of temperatures on the red curve (GC41, **b**). Besides, the gradual burial of the GC41 station causes the captor to move closer to the surface where inversion is stronger and temperature is colder than the model output at 2 m.

(Agosta et al., 2019), with a high resolution of 35 x 35 km. The MAR turbulent scheme is adapted for stable conditions of the Antarctic Plateau (Gallée et al., 2015) and has a high vertical resolution near the surface (5 levels in the first 10 m above the surface), which enables a better representation of temperature inversion conditions compared to other models, and atmospheric reanalyses. MAR shows a strong correlation with observations ($r^2 = 0.83$ for all Antarctica) and has low surface mass balance (SMB, defined as precipitation minus evaporation) bias over inland East Antarctica (Agosta et al. 2019). The yearly SMB simulated by MAR at ABN averages 118 mm w.eq. for the 1979–2013 period, with an interannual variability of ± 22 mm w.eq. (1σ), in agreement with the estimated accumulation of 119 mm w.eq. Snow drift after deposition is not modelled in the MAR simulations we used, and it is known to significantly affect the surface mass balance of windy areas (Agosta et al., 2019). Because ABN is on the lower elevation edge of the Antarctic Plateau, katabatic winds usually occur, with a mean summer wind speed of 6.0 $m \cdot s^{-1}$ at 4 m above ground level with prevailing southerly winds (wind speed and direction data availability restricted to summers for 2014–2017, from Automatic Weather Station AuroraBN, aws.acecrc.org.au/AuroraBN.html).

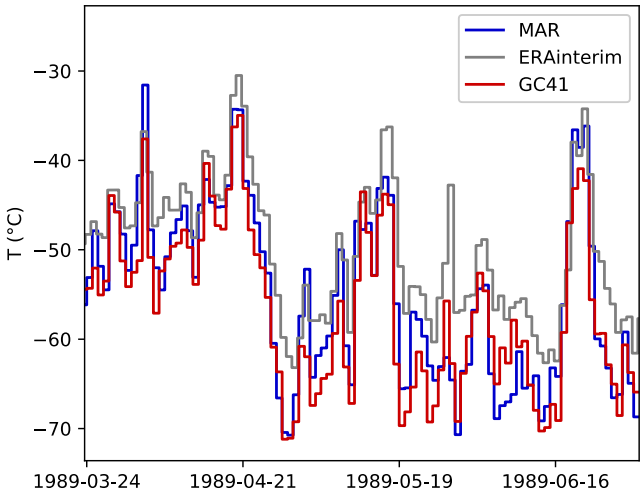

Figure 3.3. Comparison of daily mean temperatures from automatic weather station GC41 (71.60°S, 111.26°E) and 2 m temperature of corresponding grid points in MAR, and ERA-interim zoom on a part of the winter of 1989.

MAR performs well in simulating the 2 m temperature at the automatic weather station GC41 with a mean bias of +0.9°C (for the period 1985–1992), whereas the bias is of +4.7°C in ERA-Interim (figures 3.2 and 3.3). The warm bias in ERA-Interim is due to an overestimate of the surface turbulent fluxes in very stable conditions (Fréville et al., 2014). The day-to-day temperature variability is also more accurate with MAR than ERA-interim, yet some low temperatures in winter are not represented fully, causing a slight underestimation of the seasonal range.

3.3 ABN as a tracer of East Antarctic Climate

The ABN site was chosen to increase the spatial coverage of ice core records spanning the last 2000 years in East Antarctica (*Aurora Basin*, webpage). Here we evaluate whether this site is representative of East Antarctica, using temperature and SMB correlation maps.

The first maps show that at interannual scale, the temperature at ABN is highly correlated ($r > 0.9$, $n=35$, $p < 0.01$) with a large part of Wilkes Land (100°E to 136°E; figure 3.4b). The

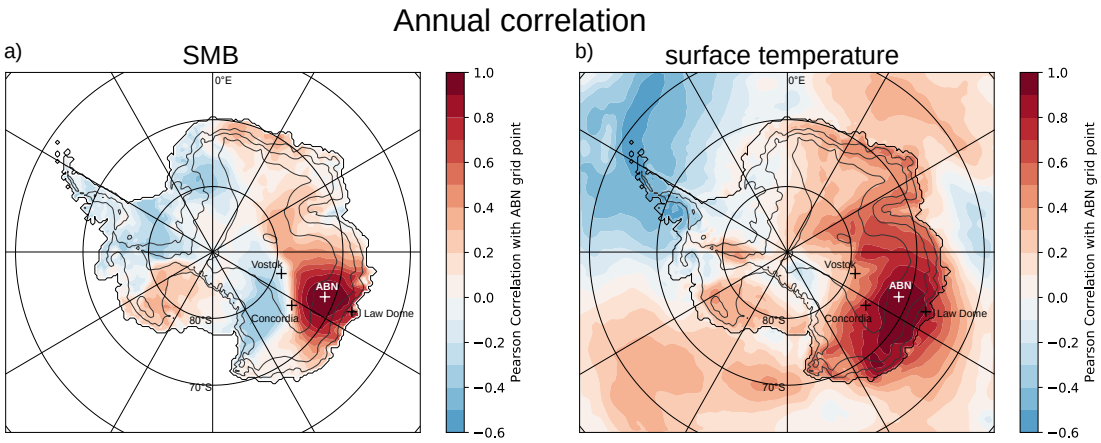

Figure 3.4. (a) Yearly summed Surface Mass Balance (Precipitation – Evaporation) correlation map with Aurora Basin North (white cross). **(b)** Yearly averaged surface (2 m) Temperature correlation map with Aurora Basin North (white cross). The statistics have been computed from MAR outputs on the 1979-2015 period.

annual SMB at ABN is highly correlated to a more restricted area, yet larger than 100,000 km^2 (figure 3.4a). Years with high temperature at ABN were mostly years with high temperature in most of Wilkes Land, except for the high plateau locations (above 3000 m, e.g. Concordia and Vostok), and the coastal regions (e.g. Law Dome). Climate reconstructions at interannual scale from ABN are therefore likely to represent the variability of a large part of Wilkes Land.

We can also note lower positive correlations for both SMB and temperature with more distant regions: most of Indian-Ocean-facing East Antarctica, and Ross Sea side of West Antarctica are positively correlated with ABN. Conversely, the Antarctic peninsula and Weddell Sea slightly negatively correlated. This highlights the influence of modes of variability of temperature and SMB at annual scale in Antarctica, which will be discussed later.

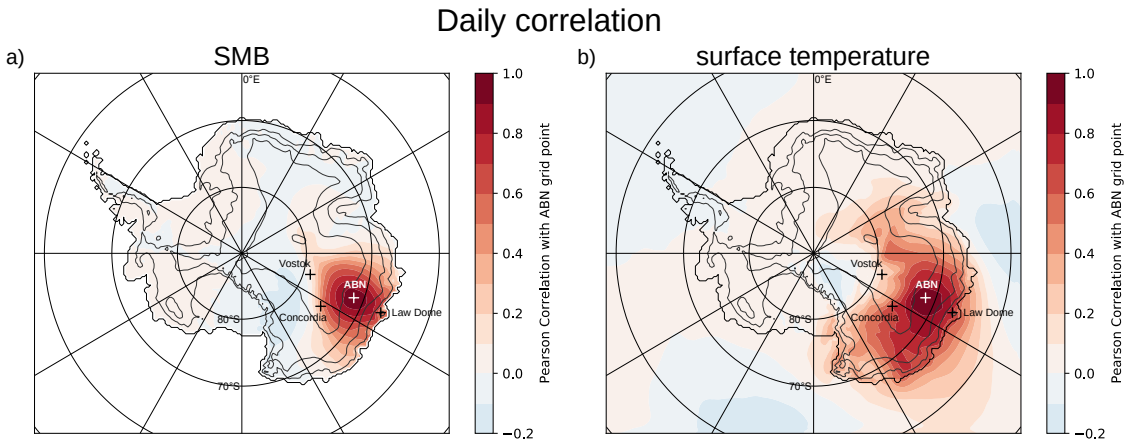

Figure 3.5. (a) Daily Surface Mass Balance (Precipitation – Evaporation) correlation map with Aurora Basin North (white cross). **(b)** Daily surface (2 m) Temperature anomaly correlation map with Aurora Basin North (white cross). Temperature anomalies have been computed as the difference to a 30-day rolling mean of seasonal temperatures. The statistics have been computed from MAR outputs on the 1979-2015 period.

At daily scale (figure 3.5), the highly correlated area is much more local, and the long-range correlations fade. Daily variability is regulated by meteorological phenomena that have a spatially restricted influence. Diminution of spatial extent of the correlated area at higher temporal resolution is a known feature of climate variability (Christiansen & Ljungqvist, 2017).

While daily correlation maps show the reach of synoptic meteorological events, the long term climate changes (more than one year) reconstructed from an ice core at ABN are likely to represent a large part of Wilkes land, except for high plateau and coastal sites.

3.4 Climatology of the precipitation in the MAR model

Ice core records are not comprised of continuously deposited snow. Rather, the intermittent precipitation causes unevenness of the climate recorded in the ice core. Water stable isotope ratios in precipitation are closely related to condensation temperature, often considered as linearly dependent (Dansgaard, 1964), and form the parameter that we measure in snow and ice. In order to investigate the ability of water isotopes to record temperature, an understanding of how the isotopic signal is formed and then preserved in precipitation is required. In this section, we demonstrate that extreme precipitation events are over-represented in deposited snow, and we quantify the associated bias in temperature and seasonality, using outputs from the MAR model forced by ERA-interim.

3.4.1 Distribution of precipitation events

Snowfall events vary in size and are unevenly distributed throughout the year in Antarctica. We investigate the distribution of cumulated daily surface mass balance (SMB, defined as precipitation minus evaporation) using MAR over the 1979–2015 period at Aurora Basin North.

Figure 3.6 shows the cumulative day count, and the cumulative SMB of days, sorted by daily SMB. In the MAR model, daily SMB at ABN ranges from – 0.2 to + 8 mm w.eq. day^{-1} in the 1979 to 2015 period. About 30% of the days have negative daily SMB (loss of mass), and less than 10% of the days have an accumulation greater than 1 mm w.eq. day^{-1}.

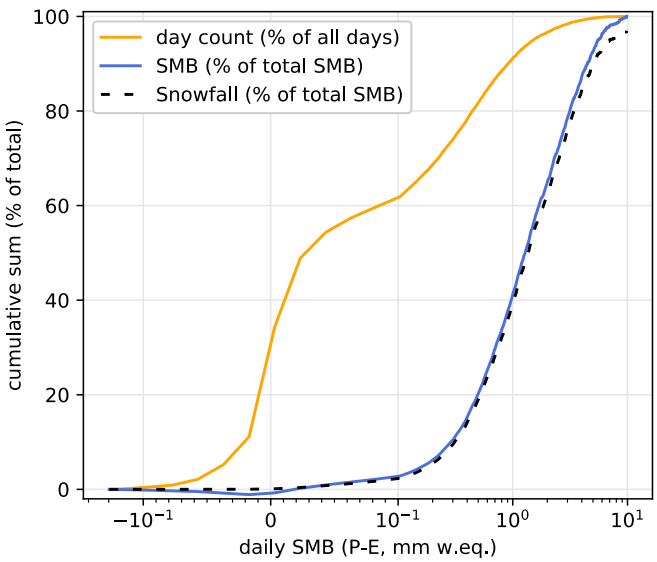

Figure 3.6. Cumulative sum of number of days (orange line), SMB (blue line, defined as precipitation minus evaporation), and snowfall (as percent of total SMB), with days sorted by daily SMB in MAR outputs for ABN site. Note that x-axis is linear between -10^{-1} and 10^{-1} mm w.eq. day^{-1}, and logarithmic outside of this range.

We find that the snowfall accounts for 95% of the total SMB while evaporation – condensation processes are responsible for less than 5 % of the total SMB, although hoar frost and clear-sky precipitation might be underestimated in the models (Agosta et al., 2019; Stenni et al., 2016). This indicates that precipitation is controlling the SMB record.

Half of the yearly precipitation is deposited during less than 10% of the days, corresponding to 24 days per year on average. This means that the ice is not accumulated evenly throughout a year, and will be mostly due to a few large events. Consequently, large precipitation events significantly bias the recorded signal towards the conditions under which they occur. In the next sections, we analyze the specificities and variability of precipitation events. For simplicity, we distinguish the days with high (> 1 mm w.eq. day^{-1}) and low SMB, which represents 58% and 42% of the total SMB, respectively.

3.4.2 Seasonality and variability of precipitation

The SMB is higher in winter months, with a mean monthly SMB above 11 mm w.eq. month^{-1} in May through August (MJJA), compared to 5.8 mm w.eq. month^{-1} in December or 7.2 mm w.eq. month^{-1} in January (figure 3.7a). The winter monthly SMB is variable compared to summer SMB, with interquartile ranges higher than 8 mm w.eq. month^{-1} in MJJA compared with 4.5 mm w.eq. month^{-1} in December and January. However, if we consider the inter-quartile range relative to the mean SMB, the variability is constant throughout the year, with highest relative variability in October and November, due to low mean SMB. Slightly more snow is deposited in winter, with 64% of total SMB in April through September, so the winter signal will be enhanced in snowfall-dependent proxies such as water isotopes, which could affect reconstructed temperatures (Persson et al., 2011). That is, if water isotopes were only sensitive to condensation temperature above the site, the annual mean temperature as recorded by the water isotopes in the snow would be 0.86°C lower than the true annual mean temperature.

The distinction between monthly SMB resulting from low (<1 mm w.eq. day^{-1}, white) and high (>1 mm w.eq. day^{-1}, blue) daily SMB is shown in figure 3.7b. High SMB are characterized by a large spread of monthly means, with interquartile-ranges of at least 3.3 mm w.eq. month^{-1} and up to 11.1 mm w.eq. month^{-1}, twice as large as interquartile-ranges of the SMB during small rates that range from 1.5 to 2.7 mm w.eq. month^{-1}. This shows that most of the variability in the SMB is due to the large events with high daily precipitation rates. The importance of high precipitation events on inter-annual variability of SMB is relevant for most of Antarctica, when considering the largest 10% of daily total SMB, defined locally (Turner et al., 2019)

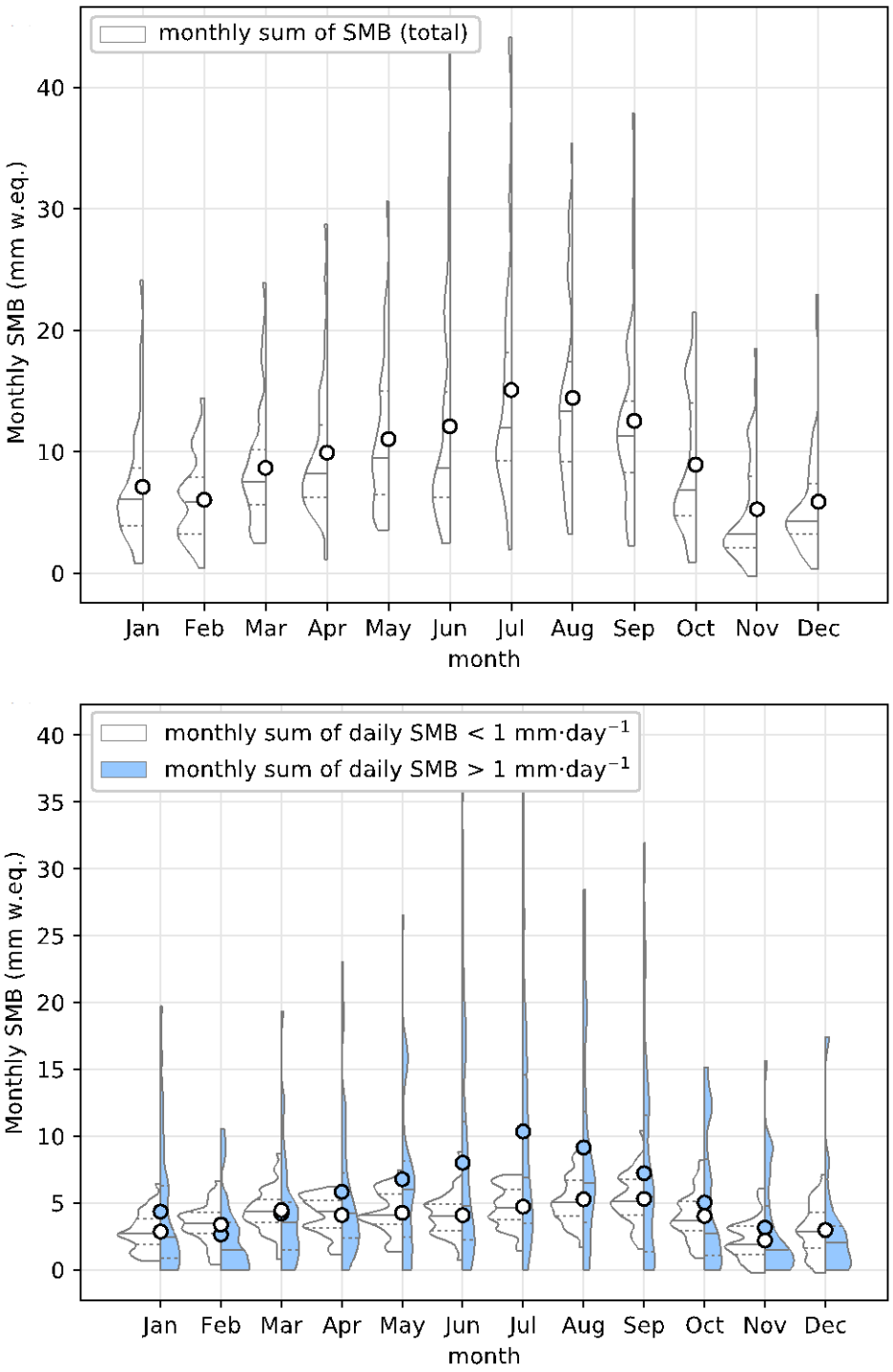

Figure 3.7. Probability density function of **(a)** monthly SMB, and **(b)** monthly SMB due to low (<1 mm w.eq. day^{-1}, white) and high (>1 mm w.eq. day^{-1}, blue) daily SMB rates. Mean (colored circles), median (plain lines) and quartiles (dashed lines) are indicated for each monthly distribution.

To sum up, low (< 1 mm w.eq. day^{-1}) precipitation events happen regularly during the year, and provide a baseline of SMB, without specific seasonality. In addition, high precipitation events can happen throughout the year, but with a larger prevalence in winter. These high precipitation events are responsible for the interannual variability in precipitation (Turner et al., 2019), and drive the seasonal cycle, possibly causing a bias in the distribution of water isotopes in the snow. In the next section, we investigate the meteorological conditions occurring during these high precipitation events.

3.4.3 Synoptic conditions driving snowfall

While most of the precipitation falls on the coastal areas of Antarctica, occasional poleward flow brings moisture to continental sites. Figure 3.8 shows the 500 hPa geopotential height anomaly relative to the seasonal average (30-days rolling mean of the climatology calculated on 1979 – 2015), for the days with high snowfall at ABN. Large precipitation events (SMB > 1 mm day^{-1}) on the East Antarctic Plateau are consistently associated with positive geopotential height anomalies corresponding to high pressure over Wilkes Land and Adélie Land (located in 60~75°S, 120~150°E), northeast of ABN. These high-pressure anomalies channel warm and moist air inland, causing the precipitation.

The influence of blocking on snowfall has been shown for Dome C, where high pressure anomalies forces air masses inland from the Indian Ocean (Scarchilli et al., 2011). The blocking is located at lower latitudes, and funnels the air masses from the Indian Ocean over the East Antarctic Plateau. We therefore expect blocking events to have a regional footprint on the plateau, as the moisture precipitates along the air mass transport path when it moves inland, up the plateau slope, and cools down (see figure 5 – temporal correlation maps of daily SMB and temperatures). Although the spatial representativeness of ABN is limited to a few hundreds of kilometers, the mechanisms involved in high precipitation events are consistent

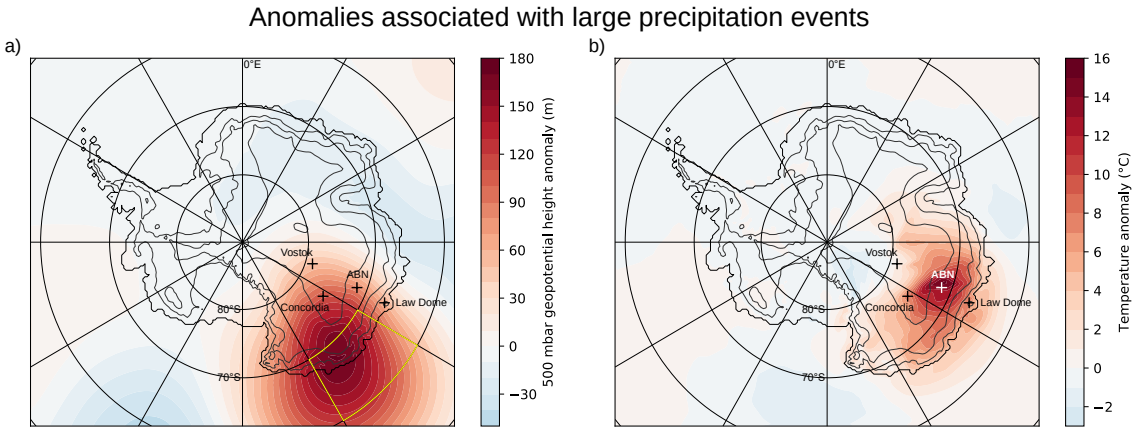

Figure 3.8. (a) Mean 500 hPa geopotential height anomaly, and **(b)** mean 2 m temperature anomaly, when daily SMB at ABN is larger than 1 mm w.eq. day^{-1} (1,217 days on a total of 13,514, on the 1979 – 2015 period). We define a blocking index for the region in the yellow box as a geopotential height anomaly greater than 100 m lasting for at least 5 days (see text for detail on computation).

across the East Antarctic Plateau at comparable altitudes, and therefore responsible for a similar part of interannual variability (Turner et al., 2019). Schlosser et al. (2010) also showed that a few synoptic events were responsible for most of the precipitation at Kohnen Station, another East Antarctic Plateau site. Consequently, the findings at ABN site may be valid for other regions of Antarctica.

To assess the influence of blocking on precipitation at ABN, a blocking index is defined in the area of high geopotential anomalies associated with precipitation (figure 8a, yellow box): the index is the ratio of grid points with a 500 hPa geopotential height anomaly larger than +100 m lasting for at least 5 days in the 60°S to 70°S, 120°E to 150°E area (Wilkes and Adélie Coasts). The blocking index values range from 0 (no blocking: no grid point with persistent +100 m geopotential anomaly) to 1 (all grid points with a blocking). This ratio is

defined daily, taking the past 5 days for the computation, and is averaged to monthly resolution. There is a positive correlation of the blocking with monthly snowfall at ABN ($r = 0.37$, p value < 0.01), which supports the role of blocking in East Antarctic precipitations.

In the Southern Hemisphere, the prevalent atmospheric modes are the Baroclinic Annular Mode (BAM) and the Southern Annular Mode (SAM), which are defined as the first empirical orthogonal functions of eddy kinetic energy and atmospheric surface pressure, respectively, between 20°S and 70°S (Marshall & Thompson, 2016). BAM and SAM both influence Antarctic precipitation (Marshall et al., 2017): BAM positive phases are associated with an enhanced poleward moisture flux, and thus results in increased precipitation in most of Antarctica. On the other hand, SAM positive phases imply a strong latitudinal gradient of atmospheric pressures that enhances zonal flow and prevents blockings that favors moisture transport to inland Antarctica, and results in reduced precipitation on East Antarctic Plateau. These patterns are observed year-round, but are weakest in austral summer. The annual SAM Marshall index (Marshall, 2003) is indeed negatively correlated with the blocking index ($r = -0.77$) and annual precipitations at ABN ($r = -0.35$) from 1979 to 2015. Because the SAM is responsible for most of the variability in the southern hemisphere, and because it is a zonal feature, changes in precipitation and temperature associated with SAM affect homogeneously most of the East Antarctic Plateau at longer timescales, which explains why SMB and temperature at ABN are positively correlated with a large part of the plateau at annual resolution (figure 3.4). The precipitation at inland East Antarctica responds to large-scale atmospheric patterns via the blocking over the coast.

3.4.4 Temperature anomaly associated with precipitation events.

As we have shown, large precipitation events are associated with meridional airflow, due to a high-pressure system forcing oceanic air masses inland. In this section, we quantify the temperature anomalies induced by the specific atmospheric conditions during snowfall.

Air masses forced inland cause a warming of air temperature at ABN, both due to the advection of air from the warmer ocean and due to the latent heat released by condensation. Moreover, the pressure dipole counters the usual surface winds from south to north, and breaks the temperature inversion that is settled especially in winter months. By comparing surface temperatures, we would see both warm air intrusion and breaking of temperature inversion. In order to focus only on the air temperature at which condensation happens, we hereafter discuss the temperatures at a vertical level where pressure is 90% of surface pressure (P_{90}), which is above inversion year-round (figure 3.9), thus more representative of the condensation level at which isotopic signal is acquired (Jouzel & Merlivat, 1984).

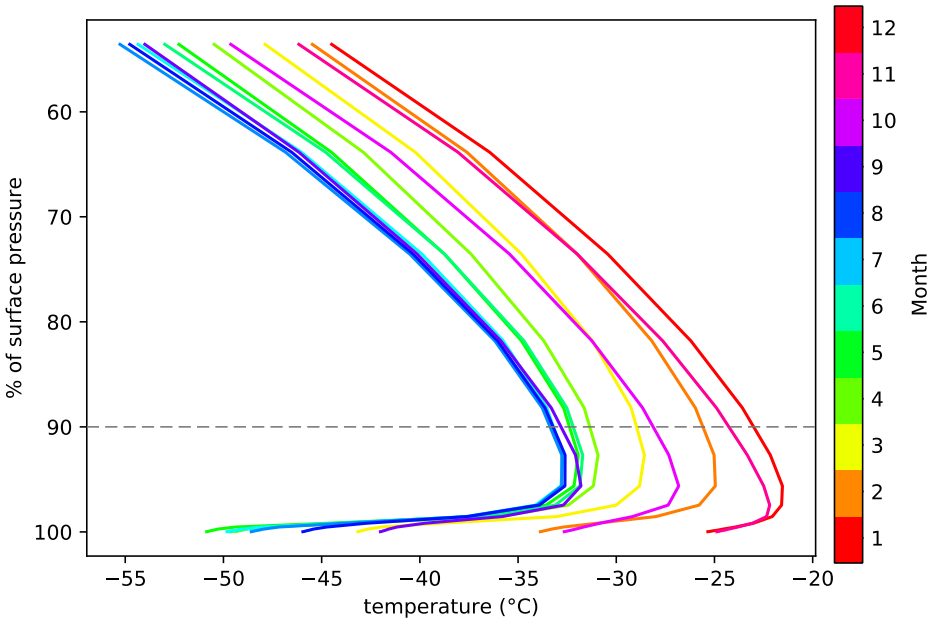

Figure 3.9. Monthly vertical profiles of temperature in MAR. The dashed line at 90% of surface pressure indicates the level used in the main article to compute temperature biases.

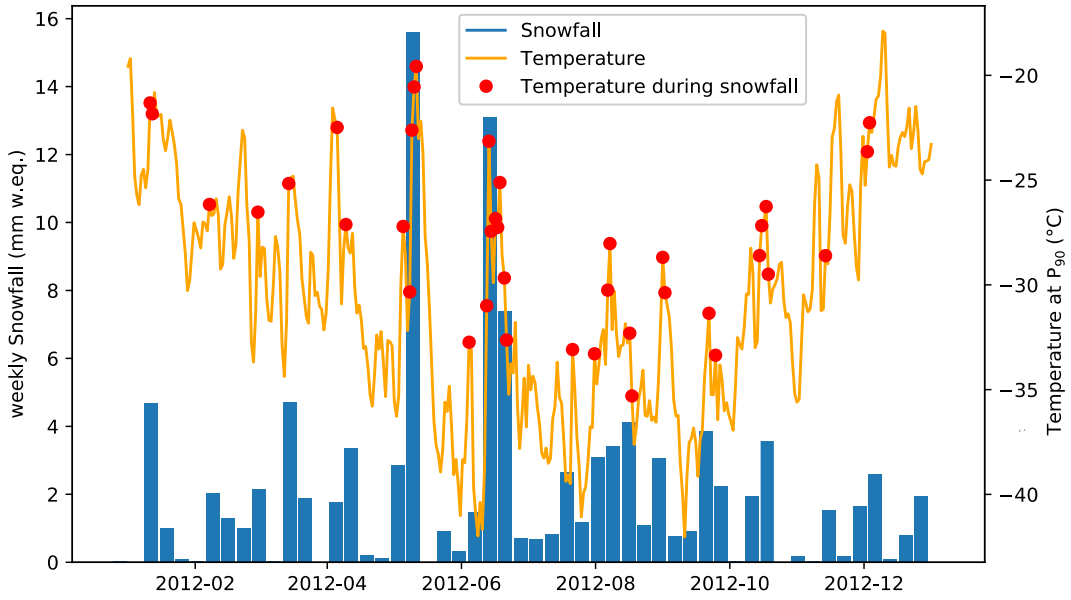

Figure 3.10. MAR temperature (orange), and weekly snowfall (blue) during the year 2012. Temperature *when daily* SMB *at ABN is larger than 1 mm w.eq. day*$^{-1}$ is highlighted with red dots.

A time series of daily temperature and weekly snowfall for the year 2012 illustrates the variability of the climate at ABN (figure 3.10). It appears that precipitation events are consistently associated with high temperature, even above inversion. The two weeks with most precipitations, in May and in June, reach summer-like temperature of above -25°C. The fact that the largest precipitation events have a very particular warm signature may alter the accuracy of precipitation-based proxies, which may not represent average conditions.

To evaluate the impact of warm events on precipitation-based records, we compare the probability of density functions of monthly mean temperatures, with monthly snowfall-weighted mean temperatures (figure 11). The latter are representative of the temperature of snowy days weighted for the amount of precipitation each day, as would be recorded in snow isotopes in ideal conditions, ignoring post-deposition effects. Monthly snowfall-weighted

mean temperature (m_w) is defined as the mean of daily temperatures (T_{day}) weighted by the snowfall (P_{day}) on the corresponding day:

$$m_w = \frac{\sum_{day=1}^{31} T_{day} * P_{day}}{\sum_{day=1}^{31} P_{day}} \quad (3.1)$$

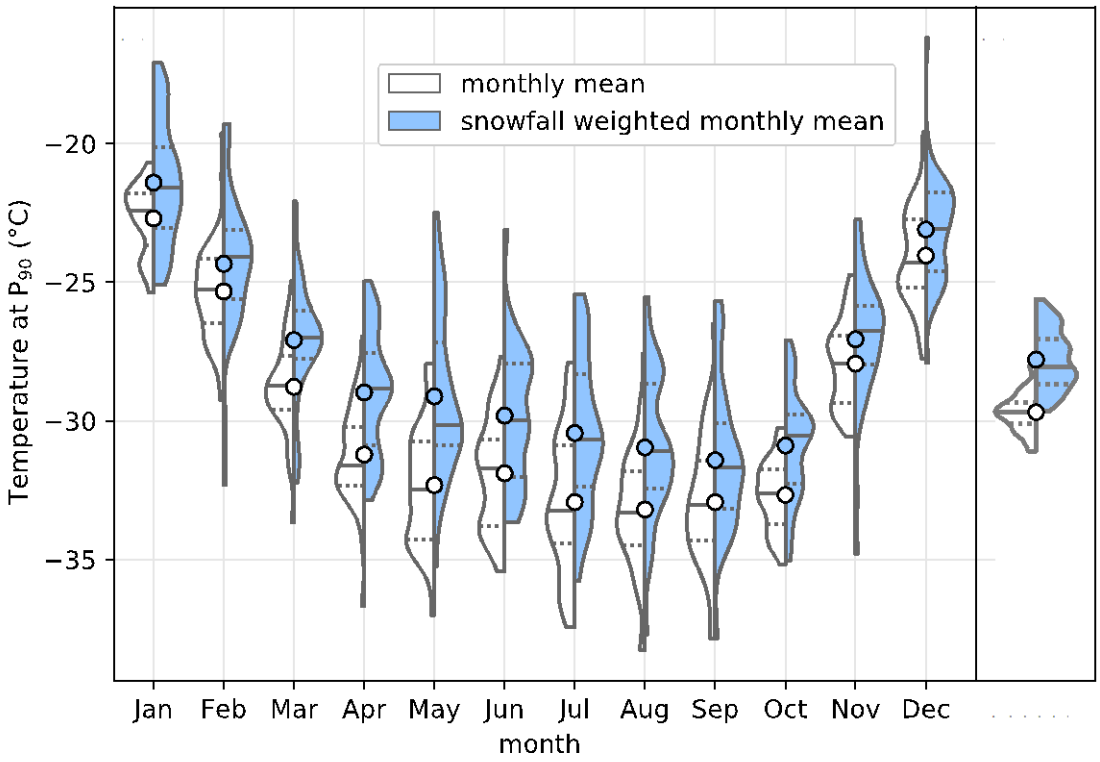

Figure 3.11. (**a**) Probability density function of monthly mean temperatures (white) and snow-fall-weighted mean temperatures (blue). Mean (colored circles), median (plain lines) and quar-tiles (dashed lines) are indicated for each month distribution. P_{90} refers to the vertical level where pressure equals 90% of the surface pressure, and is above inversion year-round. (**b**) same as (**a**) but for annual temperatures distribution.

Monthly mean temperatures (white, non-weighted) are characterized by an average of -24 ± 4°C in December and January. In winter, the monthly mean temperatures decrease to -80

33 ± 5°C. The interquartile range is lower in summer (~2°C in DJ) than in winter (~3°C in MJJA). Interquartile-ranges are slightly larger (+0.4°C) for snowfall-weighted monthly means, and they also evidence a greater variability in the winter months with interquartile ranges up to 4.1°C. The monthly snowfall-weighted temperatures (blue) are warmer than mean temperatures (white) of the corresponding month by an average difference of +1.82°C, because large precipitations coincide with warm temperature anomalies (the 1-year time-series of temperature and precipitation illustrates this in figure 3.10). However, months with higher SMB have a significantly larger temperature bias, so the snowfall-weighted difference increases to +2.83°C when accounting for the snowfall of each month relative to the total snowfall of the study period (1979–2015). Combined with the cold bias due to the seasonality of precipitation of -0.86°C (given in section 3.1), the resulting bias associated with snowfall is +1.97°C, and is equivalent to the difference between the mean temperature and the snowfall-weighted mean temperature for the 1979–2015 period.

Because the continental temperatures drop very low in the winter, the arrival of precipitating warm oceanic air masses contrasts even more in the coldest months, so the warm bias is larger. Consequently, the total amplitude of the annual cycle of temperature is lowered in the precipitation-weighted mean. Increased variability in the winter dominates the average signal, so the temperature record will reflect the occurrence (or absence) of warm events in the winter months.

3.5 Conclusions

Paleoclimate reconstructions covering the last 2000 years in Antarctica are sparse, which hampers our understanding of the climate in this region. Aurora Basin North (ABN) is a side located halfway from the coast and the summits, and was targeted to drill an ice core covering the last 2000 years, therefore increasing our spatial resolution.

We show that this site is highly correlated at interannual scale with a large part of Wilkes Land, and will thus represent temperature and surface mass balance (SMB) in this region. Because the main temperature proxy in ice core, the water isotopes, are precipitation-dependent, we want to understand the mechanisms associated with precipitations at ABN, to be able to interpret the proxy.

Consistently with Turner et al. (2019), we show that half of the annual SMB is accumulated in under 24 days, so precipitation-based proxies may poorly represent average conditions. The SMB is highly variable from year to year, but shows a seasonality with a maximum in winter. This maximum is due to the large precipitation events that bring more precipitation in winter. Because of this seasonality with more precipitation in the cold months, precipitation-dependent proxies of temperature are biased by an average -0.86°C.

High SMB are related to synoptic events bringing intense snowfall at ABN, with a blocking over Wilkes Land coast. Blocking events respond to large scale patterns of pressure variability, with negative correlation with the Southern Annular Mode. The synoptic events causing snowfall are consistently associated with warm anomalies due to advection of warm and moist air from the ocean. This causes an average warm bias of +2.83°C compared to seasonal temperature.

The overall temperature bias associated with precipitation is +1.97°C. This may significantly alter our interpretation of water stable isotopes, the main temperature proxy in ice cores. We will evaluate the sensibility of stable isotopes at ABN to precipitation and temperature in the next chapter.

Chapter 4

Warm synoptic event control of the snow isotope variability in East Antarctic Plateau evidenced from snow record and isotope-enabled atmospheric circulation model

4.1 Introduction

Snow precipitation at the ice core drilling site Aurora Basin North is associated with consistent warm anomalies, which may cause a bias in the precipitation-dependent water stable isotopes in snow and ice, used as a proxy for past temperature. In this chapter, we precisely date recent snow isotopic records using classical chemistry annual layer counting and improved with sub-seasonal comparison with climate models. Then, we assess how climate information is passed to $\delta^{18}O$ using the isotope-enabled model ECHAM5-wiso (Werner et al., 2011), which is suited for isotope studies in Antarctica (e.g. Goursaud et al., 2018). We demonstrate that seasonal-long anomalies are recorded in the $\delta^{18}O$ by comparing the modelled temperature and atmospheric modes with high-resolution snow pit isotope measurements. We calibrate the of isotope – temperature slope for the Aurora Basin North site, and discuss the limits of this calibration. This chapter was adapted from the results presented in Servettaz et al. (2020).

4.2 Material and methods

4.2.1 The isotope-enabled general circulation model ECHAM5-wiso

In addition to the MAR model, introduced in Chapter 3, we use the general circulation model ECHAM5-wiso, which simulates water isotopologues $H_2{}^{16}O$, $H_2{}^{18}O$ and $HD^{16}O$,

hence it is able to trace $\delta^{18}O$ and δD in water vapor and precipitations (Werner et al., 2011). The use of ECHAM5-wiso gives a detailed view of how the isotopic signal is recorded in precipitation in response to changes in temperature and atmospheric conditions. We present results of a simulation with a horizontal spatial resolution of 1.1° by 1.1°, where ECHAM5-wiso has been nudged to ERA-interim for the period 1979–2015.

ECHAM5-wiso performance in Antarctica has been evaluated by Goursaud et al. (2018) and shows a warm bias on East Antarctic Plateau stations: the computed mean temperature is higher than observations by 1.1°C at Concordia and by 4.7°C at GC41, because winter temperatures are not cold enough in the model. There is also a much larger cold bias for coastal stations, with mean temperature at Casey 7.3°C colder than observed. This is likely due to the coarse resolution of the model that inaccurately represent the steep changing topography of coastal areas. Similarly, mean $\delta^{18}O$ is generally higher than observed in the interior and lower on the coast. ECHAM5-wiso underestimates the seasonal temperature range on the plateau. Furthermore, ECHAM5-wiso overestimates the amplitude of $\delta^{18}O$ annual cycles (Goursaud et al., 2018), and introduces very light and extremely ^{18}O-depleted precipitations in winter on the East Antarctic Plateau, which are probably an artefact caused by the calculation of delta values for very low precipitation rates in ECHAM5-wiso model. Therefore, the computed isotope – temperature slope is too large. With all these caveats in mind, we restrict our interpretation of the model output to the study of isotope sensitivity to temperature changes, and its link with atmospheric conditions.

4.2.2 Snow isotope records

Recent snow was recovered from the Aurora Basin North (ABN) site. Samples for water isotopes (δD and $\delta^{18}O$) analysis include: a shallow 12 m firn core analyzed on a Picarro

L2130-i isotopic water analyzer using a continuous flow analysis (CFA) - melt system at Desert Research Institute (DRI), Reno, Nevada (Maselli et al., 2013; McConnell et al., 2002), and discrete snow samples were collected from two parallel profiles in a 2.5 m deep snow pit located in a designed clean area ~1 km from the main camp (71°10.003' S, 110°22.401' E). Sampling took place between 7-9 January 2014. One profile of the snow pit was analyzed by the Australian Antarctic Division (AAD) at 2.5 cm resolution on a Picarro L2130-i isotopic water analyzer, and the other was analyzed at Laboratoire des Sciences du Climat et de l'Environnement (LSCE; measurements performed by Alexandra Touzeau) at a 3 cm resolution on a Picarro L2130-i. Isotopic values are expressed as per mil (‰) and relative to the Vienna Standard Mean Oceanic Water (V-SMOW) standard. The standard deviation for repeated measurements of laboratory reference water samples was less than 0.05‰ for $\delta^{18}O$ and less than 0.5‰ for δD for this series of measurements.

4.3 Annual dating of snow

The sampling resolution of the snow-pits and short cores allows us to identify a seasonal cycle in water isotopes and impurities. In this section, we describe the dating method for each dataset, and discuss the implications for the reconstruction of the snow accumulation rate.

4.3.1 Snow record age models

The first step in the construction of the age model is to identify yearly horizons, shown in figure 4.1. Snow pits and the short core are dated annually using seasonally varying signal of non-sea-salt sulfate or sulfur (peaking in spring) and sodium (peaking in late winter; Sigl et al., 2016). Yearly horizons are counted up from the sulfur fallout of Pinatubo eruption, which peaked in 1993 in Antarctica (Cole-Dai and Mosley-Thompson, 1999).

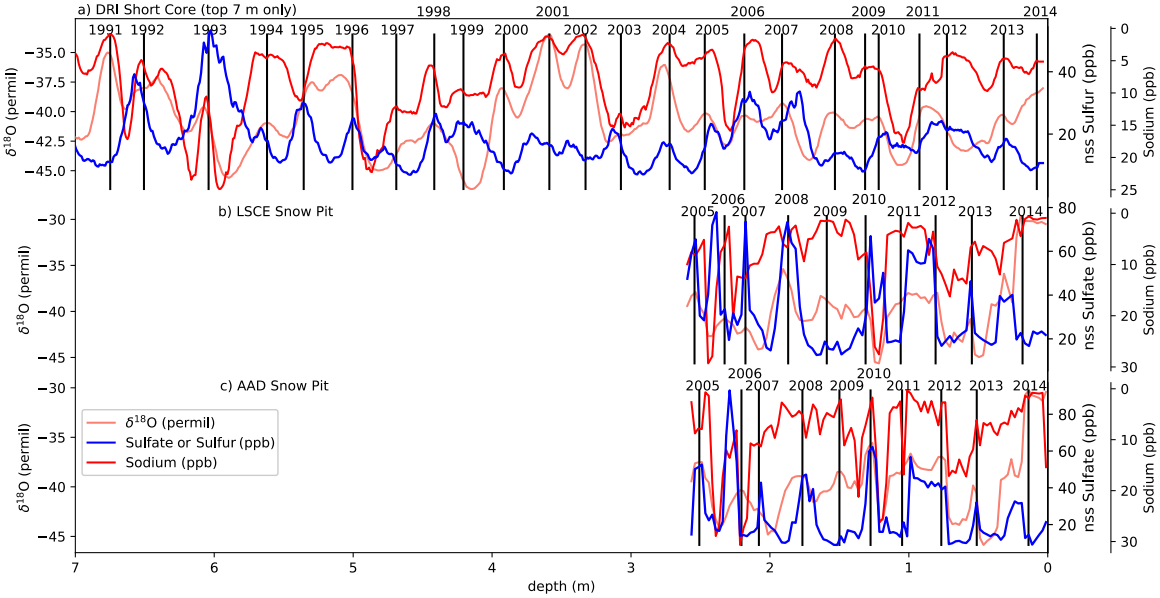

Figure 4.1. Series of $\delta^{18}O$, non-sea-salt sulfur or sulfate and sodium for (a) the top 7 m of the DRI Short Core (including Pinatubo eruption deposit), (b) the LSCE snow pit and (c) the AAD snow pit. Year horizons are shown with vertical black bars. For the LSCE snow pit profile, the sulfate concentration has been measured by ion chromatography at the Institut des Geosciences de l'Environnement (Ginot et al., 2014). Sulfur is shown for the DRI short core instead of sulfates because of the measurement was done with ICP-MS (McConnell et al., 2002).

We then use the $\delta^{18}O$ series to refine the chronology at the seasonal scale, *i.e.* we do not modify the chronology at the yearly scale but better adjust the seasonal thickness within the different years. The identified year horizons cannot be moved by more than one year in the following process.

With the assumption that the snow pit $\delta^{18}O$ can be modelled using the $\delta^{18}O$ of precipitation, daily precipitation rates and water vapor diffusion within the snow, we refined our dating by a method of peak and mid-slope matching between the measured $\delta^{18}O$ and modelled temperature from MAR or modelled $\delta^{18}O$ from ECHAM5-wiso. In this exercise, temperatures from MAR were converted into $\delta^{18}O$ using a linear transformation of $\delta^{18}O = a \times T -$

b, even if we are aware that site differences are expected. Actually, the exact $\delta^{18}O$ values do not matter, as only the relative amplitude of the peaks will influence the diffusion and matching process. We detail hereafter the matching of LSCE snow pit $\delta^{18}O$ to ECHAM5-wiso $\delta^{18}O$.

Because isotopic diffusion smoothens and broadens annual peaks, we simulated a diffusion in the modelled series. We convert the time series to depth using the ECHAM model snowfall rates adjusted to virtual snow depth using a Herron-Langway densification (Herron & Langway, 1980). We then apply a simple vertical diffusion model

$$\frac{\partial \delta^{18}O}{\partial t} = \frac{\partial}{\partial \mathrm{z}}\left(D_f(z) \cdot \frac{\partial \delta^{18}O}{\partial \mathrm{z}}\right) \tag{4.1}$$

that we simplified to

$$\frac{\partial \delta^{18}O}{\partial t} = D_f(z) \cdot \frac{\partial^2 (\delta^{18}O)}{\partial \mathrm{z}^2} \tag{4.2}$$

with D_f given by Johnsen et al. (2000):

$$D_f(z) = \frac{m \cdot p \cdot D_a}{R \cdot T \cdot \alpha \cdot \tau(z)}\left(\frac{1}{\rho(z)} - \frac{1}{\rho_{ice}}\right) \tag{4.3}$$

where m is water molar weight in $kg \cdot mol^{-1}$, p is the saturation vapor pressure over ice in Pa, D_a is the normal diffusivity in air of water vapor in $m^2 \cdot s^{-1}$, R the ideal gas constant, T the temperature in K, α the fractionation factor in water vapor for ^{18}O, τ the tortuosity defined as $\tau = \frac{1}{\left(1-1.3\times\left(\frac{\rho}{\rho_{ice}}\right)^2\right)}$, ρ the density of the snow in a Herron & Langway (1980) densification model and ρ_{ice} the density of the ice.

The depths were converted back into dates using the model dates. Results of the diffusion are shown for $\delta^{18}O$ from ECHAM5-wiso in figure 4.2. Next, we seek to match the extrema and mid-slope points of the measured $\delta^{18}O$ to the diffused $\delta^{18}O$ from models, as shown in figure 4.3.

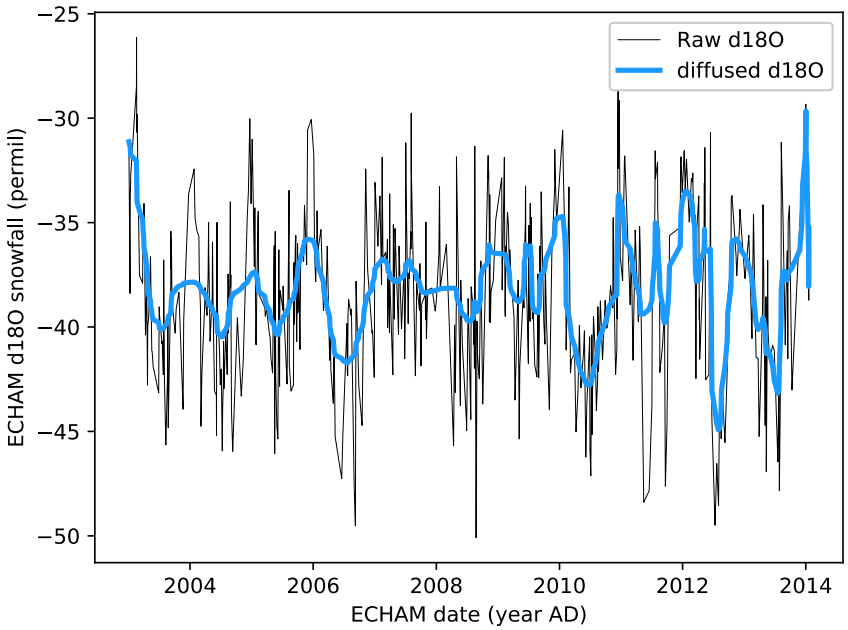

Figure 4.2. Original $\delta^{18}O$ in the precipitation from ECHAM5-wiso (thin black line) and diffused $\delta^{18}O$ (thick blue line). Note that the recent layers are less affected by diffusion than older layers.

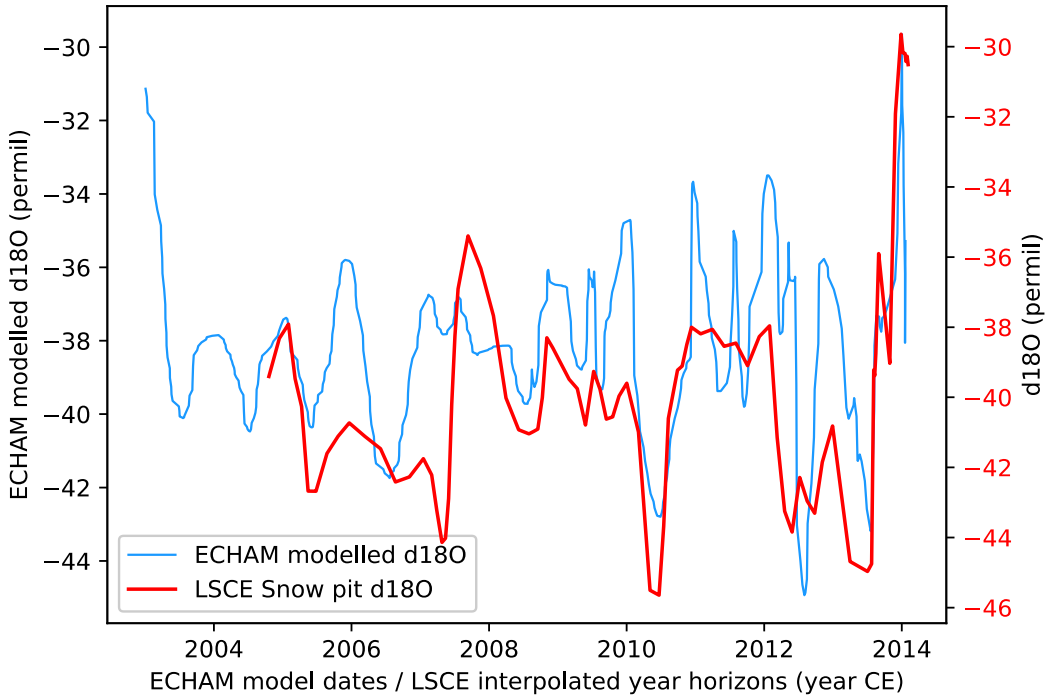

Figure 4.3. Diffused precipitation $\delta^{18}O$ from ECHAM5-wiso, with model dates (blue) and measured $\delta^{18}O$ from the LSCE snow pit, with year-horizon interpolation as the age-model (red).

To better match within a year, we apply a 1-year high-pass filter, by removing the 1-year running mean signal to each $\delta^{18}O$ series. We then detect maximum, minimum, and 0-value crossings for each year, and tie the LSCE $\delta^{18}O$ to the ECHAM $\delta^{18}O$. The tie points on the high-passed filtered series are shown in figure 4.4. LSCE age values are interpolated between the tie points.

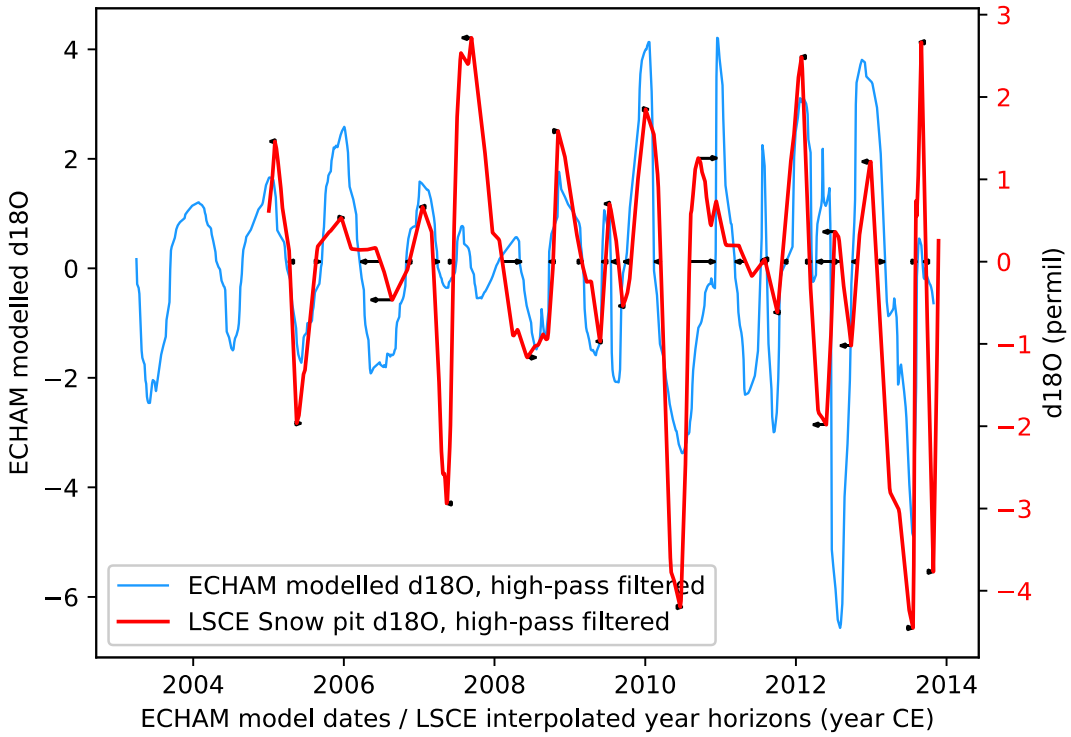

Figure 4.4. One-year high-passed diffused precipitation δ18O from ECHAM5-wiso, with model dates (blue) and one-year high-passed measured δ18O from the LSCE snow pit, with year-horizon interpolation as the age-model (red). Peak and 0-value crossings matching is represented by black arrows, pointing where the LSCE snow pit dates were shifted to match the ECHAM5-wiso δ18O.

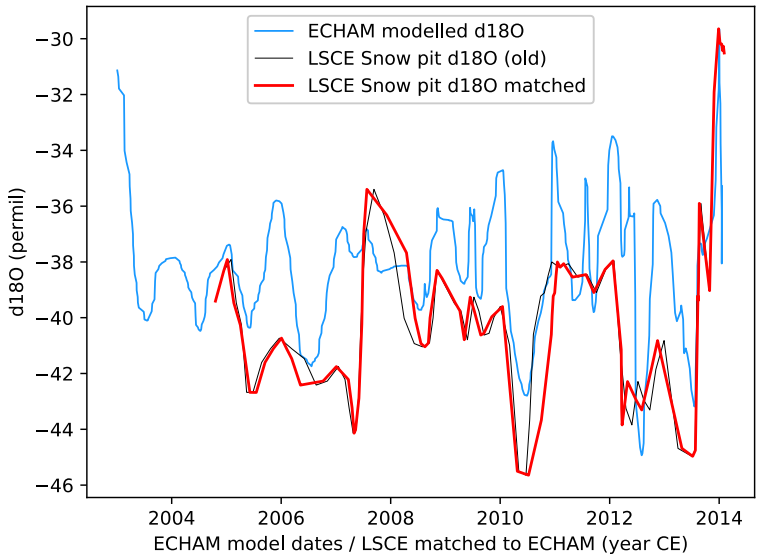

Figure 4.5. Diffused precipitation $\delta^{18}O$ from ECHAM5-wiso, with model dates (blue) and measured $\delta^{18}O$ from the LSCE snow pit, on the year-horizon interpolation age-model (thin black line), and on the newly created age model from the matching (red).

LSCE Snow Pit $\delta^{18}O$ original values are shown on their old age scale and new age scale in figure 4.5.

We repeat the same process with MAR temperatures converted to $\delta^{18}O$, resulting in a slightly different age model. The two matched age models are shown in figure 4.6, alongside the former age model resulting from year-horizon interpolation.

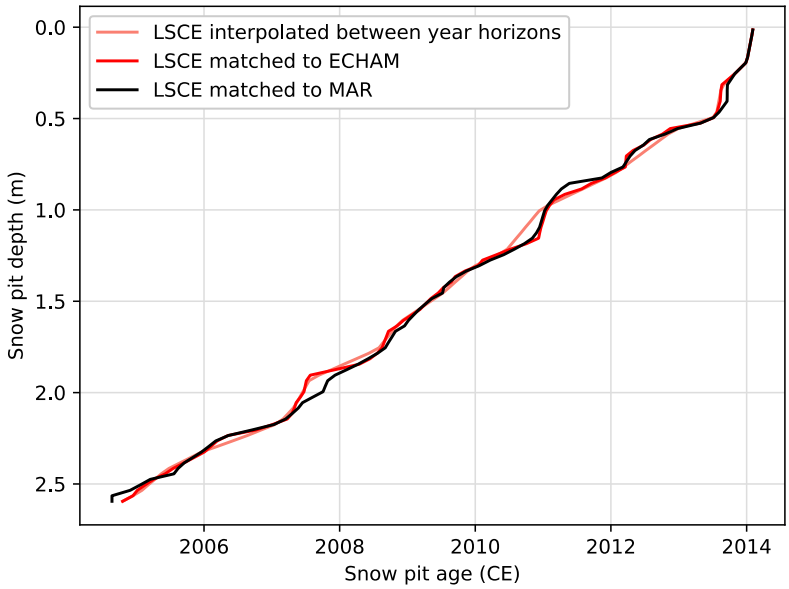

Figure 4.6. Three age models for the LSCE snow pit: interpolated between year horizons (salmon), matched to ECHAM5-wiso (red), and matched to MAR (black).

The differences between the age models are shown in figures 4.7 and 4.8.

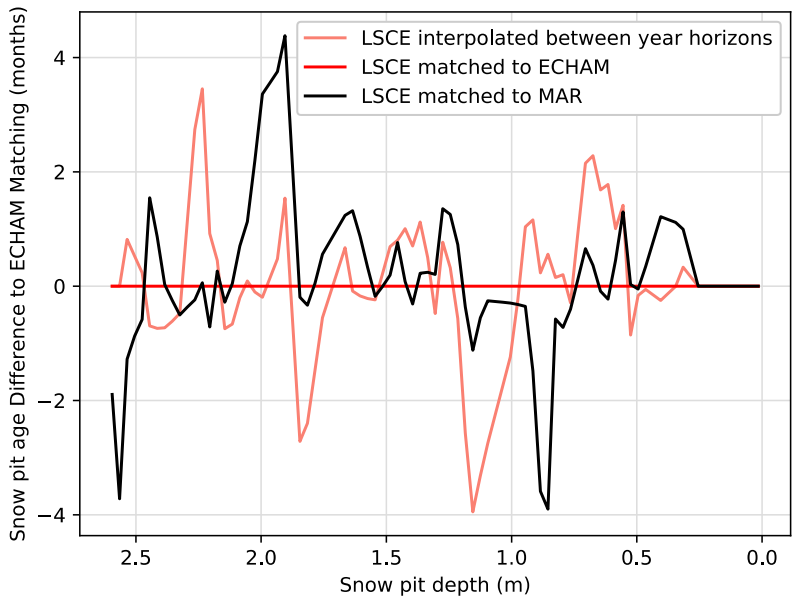

Figure 4.7. Differences between the LSCE age model matched to ECHAM5-wiso and LSCE interpolated between year horizons (salmon), and LSCE matched to MAR (black).

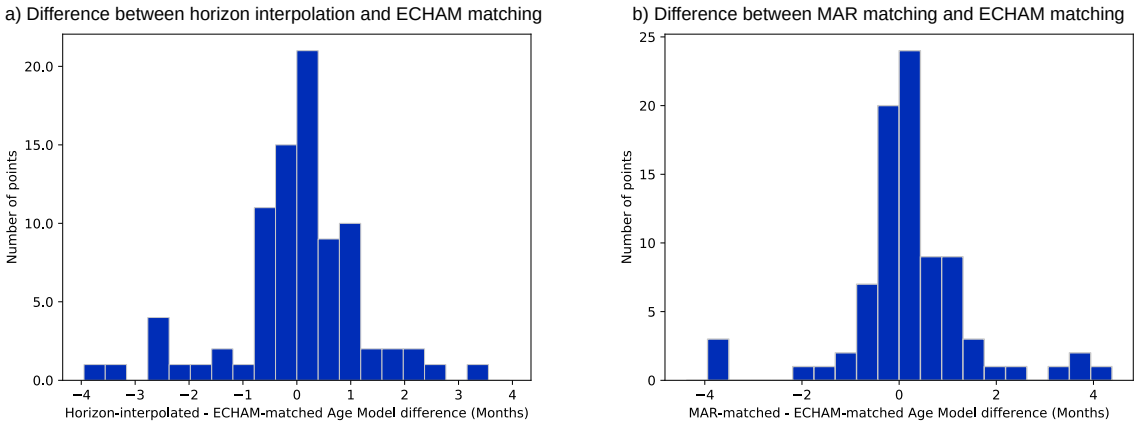

Figure 4.8. Distribution of differences between the LSCE age model matched to ECHAM5-wiso and **(a)** LSCE interpolated between year horizons, and **(b)** LSCE matched to MAR.

We chose to retain the ECHAM5-wiso matched age model, as ECHAM specifically models the $\delta^{18}O$. The other dating attempts results in age-differences of up to 4 months, but the difference is mostly lower than 1 month. The uncertainties due to the surface roughness, estimated to 4 months, exceed the difference introduced here with the matching.

Dating of the DRI short core $\delta^{18}O$ was matched to ECHAM5-wiso with the same method, for the 1979-2014 period. Points pre-dating 1979 kept their original dating based on year horizon interpolation, but are not discussed in this article. Because AAD Snow pit $\delta^{18}O$ is very similar to LSCE snow pit $\delta^{18}O$, we tied AAD snow pit to LSCE snow pit using the matching method, rather than tying AAD Snow pit to ECHAM5-wiso outputs. By doing so, we avoid the risk of tying unclear transitions to two different events of ECHAM5-wiso $\delta^{18}O$, and preserve the consistency between the two snow pits.

Globally, the matching process forces measured extrema of $\delta^{18}O$ to be simultaneous to those of the model, in addition to matching the duration of the warm and cold seasons, within the uncertainty of the dating caused by surface roughness. It results in higher correlation with the models, and clarifies the identification of large synoptic events in the snow $\delta^{18}O$.

4.3.2 Comparison of accumulation records

Based on the dating of the snow records and local density measurements, we estimate the mean annual accumulation, and compare the values with modelled SMB from MAR model (Table 4.1). The longest overlapping period between data and model is restricted to the DRI short core, as snow pits only date back to 2005. The DRI short core averages 119 mm water equivalent (hereafter abbreviated mm w.eq.) for the 1979–2013 period, with an interannual variability of ± 33 mm w.eq. (1σ).

The model MAR simulates a SMB of 118 mm w.eq. calculated for the period 1979-2013, and is in agreement with our accumulation from the short core of 119 mm w.eq. calculated over the same 1979-2013 period. On a multi-year average, the accumulation is very consistent between model SMB and snow accumulation records. However, in a year-to-year comparison, the accumulation can differ largely between our record (DRI short core) and the

Table 4.1. Comparison of snow accumulation for the three snow records, and MAR surface mass balance (SMB). All values are given in mm w.eq. year^{-1}. The first part features averages on given periods, and the second part of the table gives annual accumulation from each record. A relative data-model comparison and a relative cross-site comparison are given.

values in mm w.eq.yr^{-1}	**Snow Accumulation Data**				**Model**	**Model-Data difference**		**Cross-site difference**	
Average on period:	DRI	LSCE	AAD	Stack	MAR SMB	(DRI-MAR) /DRI	(Stack-MAR) /Stack	(LSCE-DRI) /LSCE	(LSCE-AAD) /LSCE
2005-2013 mean	102.2	100.4	100.5	101.1	110.0	-7.6%	-8.9%	-1.8%	-0.1%
2005-2013 std	± 34.3	± 19.	± 22.5	± 18.3	± 19.8				
1992-2013 mean	120.9				115.7	4.3%			
1992-2013 std	± 37.4				± 22.7				
1979-2013 mean	118.7				118.1	0.5%			
1979-2013 std	± 33.1				± 21.9				
1969-2013 mean	119.8								
1969-2013 std	± 33.2								
Yearly Accumulation									
2015					107.9				
2014					88.8				
2013	90.5	119.6	136.1	115.4	99.8	-10%	13%	24%	-14%
2012	148.8	110.5	96.1	118.5	111.9	25%	6%	-35%	13%
2011	74.9	95.7	103.5	91.4	89.4	-19%	2%	22%	-8%
2010	113.5	96.2	89.8	99.8	102.1	10%	-2%	-18%	7%
2009	37.3	105.1	86.2	76.2	155.9	-318%	-105%	65%	18%
2008	81.5	103.9	103.7	96.4	104.1	-28%	-8%	22%	0%
2007	153.4	128.5	114.2	132.0	111.1	28%	16%	-19%	11%
2006	107.2	59.6	53.0	73.3	88.0	18%	-20%	-80%	11%
2005	113.1	84.8	122.3	106.7	128.0	-13%	-20%	-33%	-44%
2004	102.3				117.3	-15%			
2003	143.0				105.6	26%			
2002	104.5				117.9	-13%			
2001	107.9				166.5	-54%			
2000	137.4				113.6	17%			
1999	123.4				77.0	38%			
1998	89.9				120.3	-34%			
1997	117.6				86.7	26%			
1996	137.4				147.3	-7%			
1995	154.6				121.3	22%			
1994	118.1				112.8	5%			
1993	189.7				115.6	39%			
1992	212.7				153.1	28%			
1991	111.9				126.0	-13%			
1990	147.2				98.7	33%			

Table 4.1. (continued)

values in mm w.eq.yr^{-1} Yearly Accumulation	**Snow Accumulation Data**				**Model**	**Model-Data difference**		**Cross-site difference**	
	DRI	LSCE	AAD	Stack	MAR SMB	(DRI-MAR) /DRI	(Stack-MAR) /Stack	(LSCE-DRI) /LSCE	(LSCE-AAD) /LSCE
1989	119.4				109.0	9%			
1988	101.3				111.0	-10%			
1987	77.6				117.2	-51%			
1986	88.9				114.6	-29%			
1985	141.7				106.9	25%			
1984	127.4				131.8	-3%			
1983	97.5				112.1	-15%			
1982	153.4				143.0	7%			
1981	93.5				170.8	-83%			
1980	138.6				144.2	-4%			
1979	97.0				102.5	-6%			
1978	119.6								
1977	118.4								
1976	121.7								
1975	179.9								
1974	74.8								
1973	96.4								
1972	96.6								
1971	115.9								
1970	184.3								
1969	130.3								

MAR model, but also between the DRI short core and the snow pit, taken at a ~200 m distance. This suggest that interannual variability of accumulation is much higher in the snow than in the models, because a single location may be affected by thickness changes due to erosion-redeposition processes and spatial heterogeneities. These processes occur at the meter-scale and cannot be represented in a regional model.

Consequently, the spatial variability in snow accumulation is so large that it does not allow us to interpret lack of snow in a record as a lack of snowfall. It is extremely difficult to assess annual variability of precipitation, even from annually resolved records, as deposition and surface reworking processes create heterogeneities of up to 10 cm in fresh snow (40 mm w.eq.), which are 4 months' worth of accumulation. This does not hamper the capacity of

MAR model to very accurately model the average accumulation, as shown for multi-year averages.

4.4 Water stable isotopes in ECHAM5-wiso

4.4.1 Sensitivity to temperature and precipitation

We discussed in the previous chapter how snowfall coincide with temperatures warmer than average conditions. Here we show how this bias can be transmitted to water isotopes using precipitation values from the ECHAM5-wiso model.

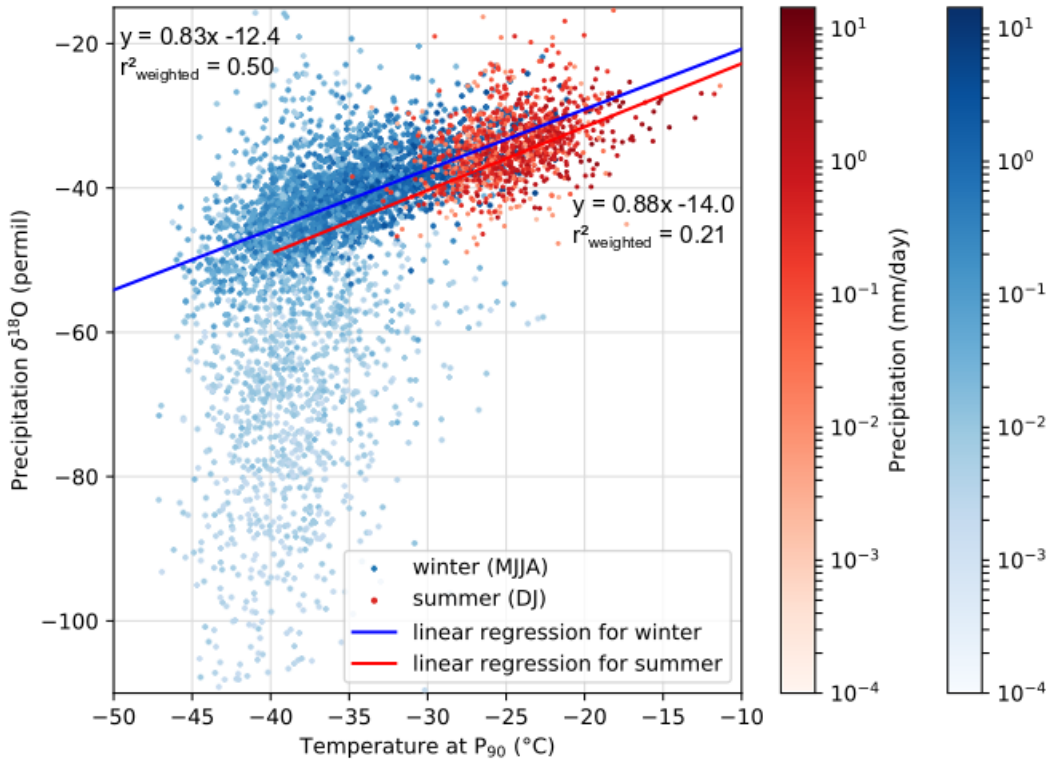

Figure 4.9. Scatter-plot of daily $\delta^{18}O$ in precipitation and temperature at P_{90} at the ABN grid point, for summer (December – January, red) and winter (May – August, blue). The color scales indicate the daily precipitation amount. Linear regressions are computed for both summer and winter with an orthogonal distance least mean squares with each point weighted with its daily precipitation. P_{90} refers to the vertical level where pressure equals 90% of the surface pressure, and is above inversion year-round. Equation of weighted regressions are indicated along with the Pearson weighted correlation coefficient (e.g. Pozzi et al. 2012).

Figure 4.9 illustrates the relationship between precipitation $\delta^{18}O$ and the daily temperature at P_{90} in the ECHAM5-wiso model at the ABN grid point. Each point also shows the daily precipitation amount on a color scale, and the linear regression was computed using the points weighted by the precipitation amount, so that points with larger precipitation will have proportionally greater influence on the isotope-temperature slope, following a weighted orthogonal distance regression (Boggs et al., 1992, Appendix 4.A). This method is roughly equivalent to using monthly weighted means to compute the linear regression, but here we show the larger spread provided by daily values compared to monthly means. Additionally, we distinguish winter points in blue (May, June, July, August) from summer points in red (December, January). We chose to limit the summer months to December and January as the temperature quickly decreases at the end of summer, whereas the winter months follow a more similar distribution.

The temperature during precipitation events ranges from *ca.* -45°C to -20°C in winter, and -30°C to -10°C in summer. The modelled $\delta^{18}O$ ranges from -50‰ to -20‰ in summer and from -110‰ to -25‰ in winter, with most of the points above -60‰. Precipitation events with $\delta^{18}O$ below -60‰ have precipitation rates lower than 0.01 mm w.eq. day^{-1}, and therefore barely influence the total snow $\delta^{18}O$ record. The very-depleted $\delta^{18}O$ of low snowfall events are probably an artifact caused by the calculation of $\delta^{18}O$ in ECHAM5-wiso, which is computed from the division of absolute quantities of $H_2{}^{16}O$ and $H_2{}^{18}O$ isotopologues. Despite a large spread of data points, especially in low precipitation events (lighter colors), there is a clear temperature – isotope relationship. The weighted regressions give slopes of 0.81 to 0.86‰ $°C^{-1}$ for winter and 0.81 to 0.95‰ $°C^{-1}$ for summer (95% confidence intervals) consistent with the 0.84 ± 0.05‰ $°C^{-1}$ slope found in precipitation $\delta^{18}O$ over inversion temperature at Dome C (Stenni et al., 2016). The variability, both in isotopes and temperature, is

larger in the winter season, but the linear regressions computed for each seasons (figure 4.10) have the same slope within the margin of error. This indicates that processes responsible for the isotopic signature in the snow are similar year-round, despite seasonal changes in moisture source and air mass transport (Sodemann & Stohl, 2009).

Changes in temperature will also affect the snow $\delta^{18}O$, as the temperature and $\delta^{18}O$ are strongly correlated. Even without the low snowfall events, the high winter variability evidenced for temperature in section 3.4 is also present in $\delta^{18}O$, and should drive the annual variability in isotopes as well. Therefore, we can use $\delta^{18}O$ as a proxy of temperature and atmospheric conditions described in section 3.3. Additionally, the +1.97°C mean bias will be translated in a *ca.* +1.7‰ bias in $\delta^{18}O$.

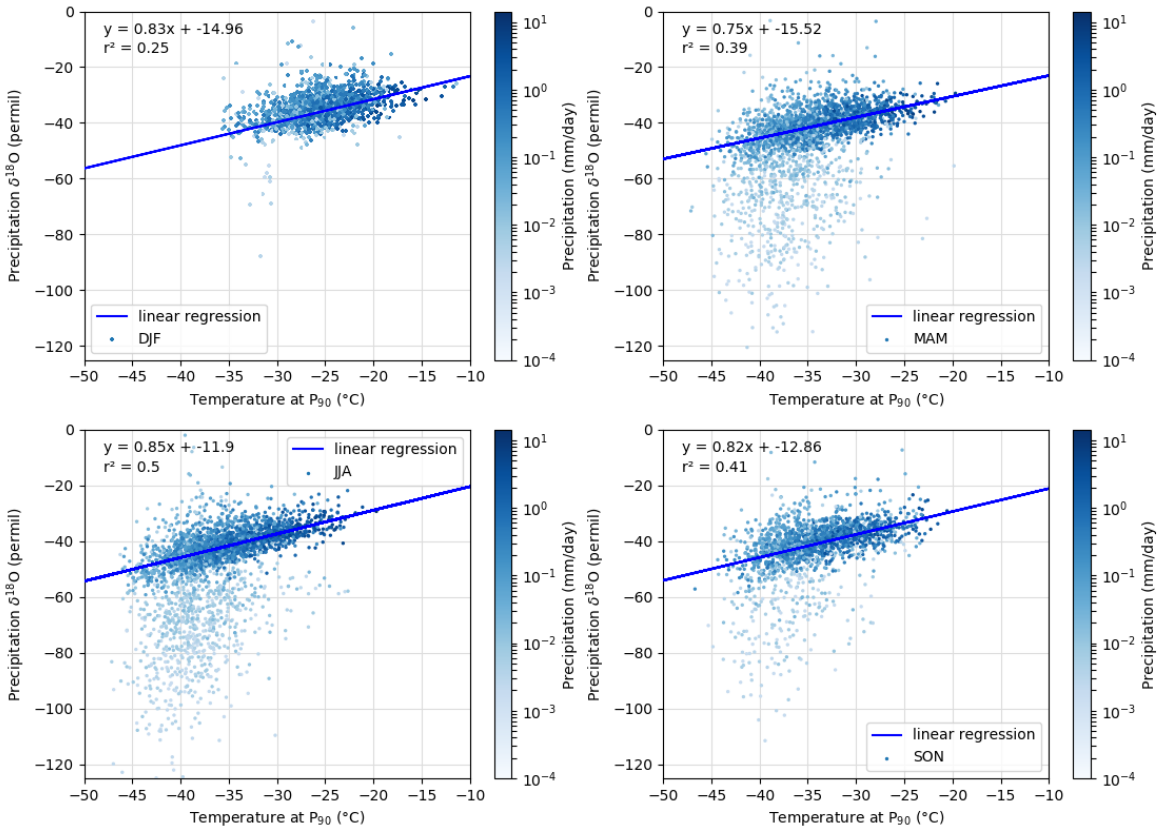

Figure 4.10. Same as figure 4.9, but for each of the four seasons: (**a**) DJF, (**b**) MAM, (**c**) JJA, (**d**) SON.

4.4.2 Spatial correlation of isotope signal

In Chapter 3, we discussed the spatial representativeness of the temperature at ABN, which is highly correlated with a large area on Wilkes Land. The maps of correlation for $\delta^{18}O$ (figure 4.11) show that this spatial correlation for the temperature, especially on annual averages, does not translate into spatial correlation of isotopes. Indeed, the $\delta^{18}O$ map looks more similar to the correlation map of SMB, suggesting that the spatial variability in precipitation and evaporation leads to heterogeneities in the $\delta^{18}O$. Consequently, areas with the same temperature variability do not necessarily record the same $\delta^{18}O$ signal.

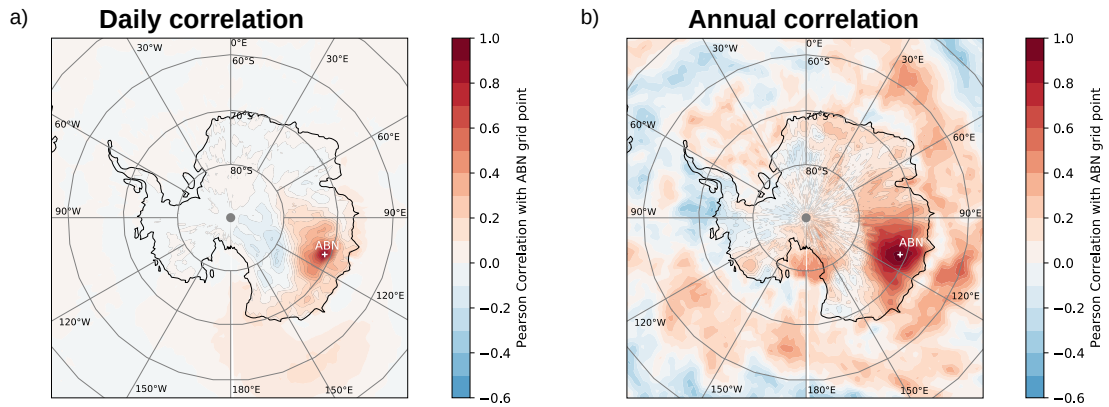

Figure 4.11. (a) Daily precipitation $\delta^{18}O$ correlation map with Aurora Basin North (white cross). **(b)** Yearly snowfall-weighted mean $\delta^{18}O$ correlation map with Aurora Basin North (white cross). The statistics have been computed from ECHAM5-wiso outputs on the 1979-2015 period. $\delta^{18}O$ of the precipitation only takes non-null value when there is precipitation on the site, so the correlation is constrained by the occurrence of precipitations.

4.5 Comparison of isotope records and climate from 2005 to 2014

We characterized the $\delta^{18}O$ seasonality in the previous section, showing that $\delta^{18}O$ – temperature slope remained similar for all seasons, but with a larger range of variability in winter.

In this section, we compare snow pit $\delta^{18}O$ measurements with modelled temperature (MAR) and isotopes (ECHAM), and discuss the climate features that get recorded in the $\delta^{18}O$ record.

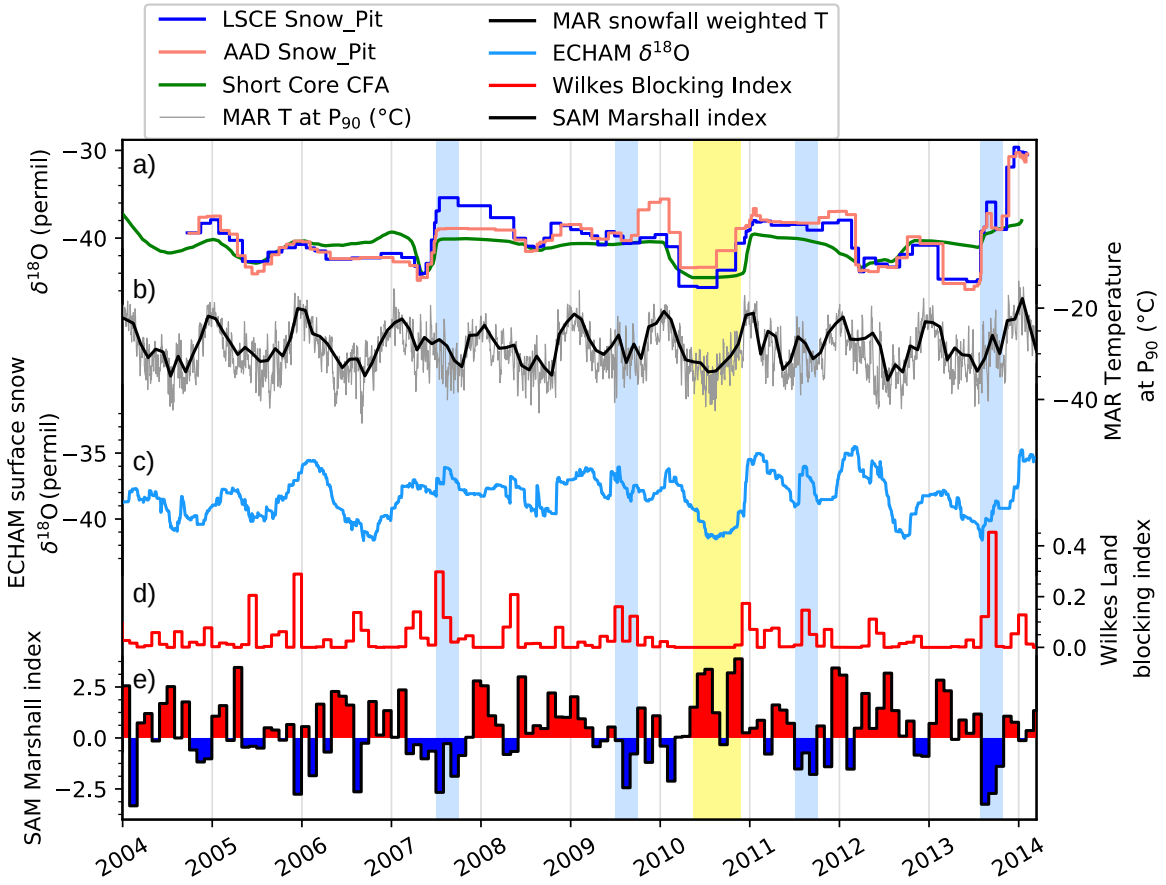

Figure 4.12. Comparison of (**a**) three high resolution records: 2 snow pit profiles and a short core, with (**b**) temperature at P_{90} at daily resolution (thin grey line) and monthly snowfall-weighted mean temperature (thick black line), (**c**) modelled surface snow $\delta^{18}O$ (buffer averaging the $\delta^{18}O$ in the last 10 mm w.eq. of precipitations), (**d**) Wilkes Land blocking index, and (**e**) SAM Marshall monthly index, (Marshall, 2003). Some periods with particularly negative (resp. positive) SAM index are highlighted with blue (yellow) shading.

We compare the measurements of $\delta^{18}O$ from samples collected from two snow pit profiles, $\delta^{18}O$ from a shallow firn core, temperature from the MAR model, $\delta^{18}O$ in ECHAM5-wiso model, and two atmospheric indices: the blocking index introduced in section 3.3 and the SAM Marshall index (Marshall, 2003), all shown on figure 4.12. The surface snow $\delta^{18}O$

parameter given by ECHAM5-wiso is a simple buffer where the $\delta^{18}O$ of the last 10 mm w.eq. of precipitation is averaged, with respect to the quantity of precipitation. Consequently, this $\delta^{18}O$ value is precipitation-weighted. We illustrate the average in the surface snow buffer of ECHAM5-wiso in figure 4.13. We describe hereafter the relationships between measured $\delta^{18}O$, modelled $\delta^{18}O$ and atmospheric conditions.

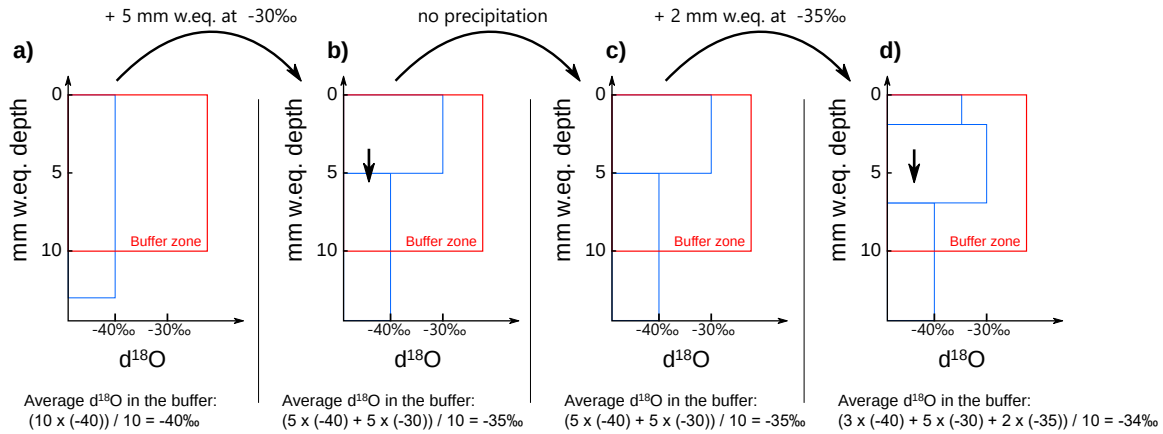

Figure 4.13. Diagram illustrating the average in the surface snow buffer in ECHAM5-wiso. The $\delta^{18}O$ in the buffer zone, which corresponds to the last 10 mm w.eq. of snowfall, is averaged and gives the value of the surface snow $\delta^{18}O$. In case of a snowfall event, e.g. between **(a)** and **(b)**, a layer of thickness equivalent to the snowfall in mm w.eq. is added to the snow surface, with its $\delta^{18}O$ value, and the rest of the snow is pushed downwards. If there is no snowfall, e.g. between **(b)** and **(c)**, the average value remains the same as previously.

We give the Pearson correlation coefficients of the different series in figure 4.14: the correlation for annually averaged (figure 4.14b) series are significant if they are higher than 0.67 (p-value < 0.05). Dating uncertainties and low interannual variabilities over a period as short as 9 years should call for caution when interpreting the statistics computed on annual averages. The seasonal signal drives the correlation for non-averaged series (figure 4.14a) and there might be auto-correlation within series.

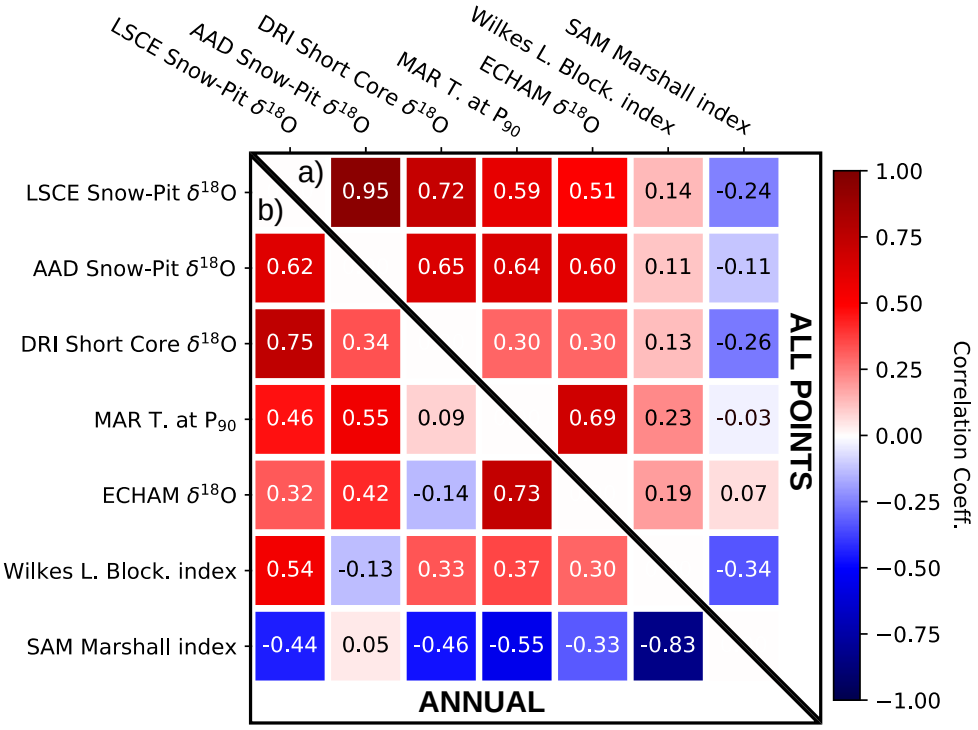

Figure 4.14. Pearson correlation coefficients table between the series shown in figure 4.12: snow pits measured at LSCE and AAD, short core measured at DRI, MAR-modelled temperature at P_{90}, ECHAM5-wiso modelled surface snow $\delta^{18}O$ (buffer averaging the $\delta^{18}O$ in the last 10 mm w.eq. of precipitations), Wilkes Land blocking index, and SAM Marshall monthly index. Correlations are shown for (a) the maximum resolution signal (all series were re-sampled on LSCE snow pit resolution, with an average of 8 points $year^{-1}$), and (b) the annually averaged signal.

4.5.1 Effect of post-deposition processes

The two snow pit records have near-identical $\delta^{18}O$ content (r = 0.95), because the samples were taken with similar resolution (2.5 cm for AAD, 3 cm for LSCE) at 1 m distance from each other. The short core $\delta^{18}O$ also shows similar features with a good correlation with both snow pit measurements (r = 0.72 and r = 0.65), but significantly lower than between the two snow pits. The lower correlation value might be due to: (1) the smoothing of high frequencies caused by the continuous flow analysis technique used to measure this core (Gkinis et al.,

2011; Holme et al., 2018), and/or (2) difference in snow deposition, as the short core was taken ~ 200 m away from the snow pits. Snow at low accumulation plateau sites exchanges isotopes with underlying snow through diffusion (Casado et al., 2018), and can be deposited in patches inducing differences in layer thicknesses related to surface roughness (Picard et al., 2019). These processes increase horizontal variability and influence the mean $\delta^{18}O$. Münch et al. (2016) also show that stratigraphic noise lowers the correlation of two $\delta^{18}O$ series in a few meters at Kohnen Station in Dronning Maud Land (dropping from r = 1.0 to r = 0.5 in 10 m, then plateauing at 0.5 correlation), albeit the accumulation at Kohnen Station (64 mm w.eq. $year^{-1}$) is lower than at ABN (119 mm w.eq. $year^{-1}$), so the ABN records show higher correlations (minimum r = 0.65) and will better record the decadal climate signal than plateau sites with lower accumulation. The high spatial variability is further evidenced by the large differences in annual accumulation between the three snow records (Table 4.1). An approach to overcome spatial variability, and increase signal to noise ratio, is to stack multiple records (e.g. Graf et al., 2002). In our case, stacking the three $\delta^{18}O$ records did not improve our understanding of how the climate signal is recorded in the snow. More studies would be needed to quantify the variability of the lower East Antarctic Plateau. Despite the uncertainties, $\delta^{18}O$ of all three snow records show large changes within a single winter season, from -45‰ to -35‰ (e.g. 2007, or 2013), highlighting the large variability of winter signals.

4.5.2 Isotopic signature of the winters with warm events

The modelled temperatures from MAR and modelled $\delta^{18}O$ from ECHAM5-wiso, which are in good agreement (r = 0.69 for the period 2005 to 2014), both show positive correlations with snow pit $\delta^{18}O$ at sub-annual resolution (r = 0.51 to 0.64), although the correlation is slightly lower with the DRI short core (r = 0.30). The absence of surface and post-deposition processes in ECHAM5-wiso,

which basically gives the precipitation $\delta^{18}O$, may partly explain why the modelled $\delta^{18}O$ is not better correlated to measured $\delta^{18}O$ than the modelled temperature is. ECHAM5-wiso or other isotope-enabled atmospheric models would highly benefit from being coupled with glaciological models that account for surface and post-deposition processes to give a range of values comparable to $\delta^{18}O$ recorded in ice cores, within a confidence interval. The standard deviation of interpolated ECHAM5-wiso $\delta^{18}O$ values is twice as large as the standard deviation of $\delta^{18}O$ measured in snow pits, due to the overestimation of $\delta^{18}O$ variability in the model, and lack of smoothing from post-depositional processes. Despite the different amplitude, the $\delta^{18}O$ measurements and modelled $\delta^{18}O$ exhibit strong consistent signals especially in the winters 2007, 2009, 2010, 2011 and 2013, that are related to temperature anomalies (Fig. 7, shaded in blue and yellow), arguing that atmospheric signals remain after post-deposition.

4.5.3 Influence of the Southern Annular Mode

As shown in Chapter 3, a blocking in the Wilkes and Adélie Land favors the meridional transport of moisture and warmth inland East Antarctica, thus the blocking index is moderately positively correlated with most $\delta^{18}O$ records and temperature at ABN ($r = 0.11$ to 0.23, figure 4.14a). The SAM, that enhances zonal flow in its positive phase, isolates the Antarctic continent and reduces the probability of blocking (Parsons et al., 2016), which explains why its index is negatively correlated with annual temperature ($r = -0.55$) and $\delta^{18}O$ ($r = -0.33$ with ECHAM $\delta^{18}O$) at ABN on annual means.

We highlight in figure 4.12 some remarkable positive (yellow shading) and negative (blue shading) phases of SAM that occurred during winter or spring. Extended positive SAM phase such as the winter 2010 prevents the intrusion of marine air masses, so the average winter temperature and isotopic signals remains very low. On the other hand, intense negative

SAM phases allow for strong blocking and thus warm anomalies at ABN and high $\delta^{18}O$ values. For example, the winter $\delta^{18}O$ in 2011 in snow pit records is almost as high as previous and following summers. This relationship between SAM and isotopes at ABN is however not

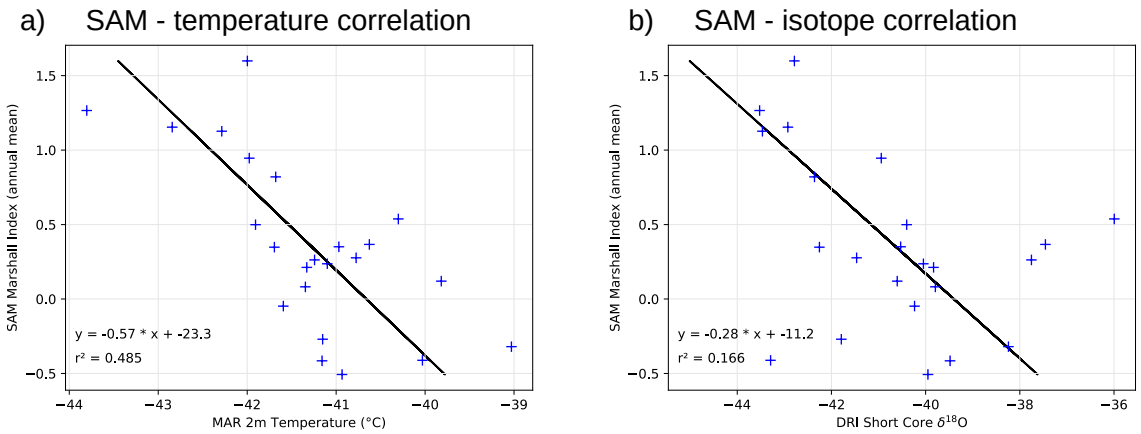

Figure 4.15. Scatter plots and linear regressions of (**a**) SAM and temperature and (**b**) SAM and $\delta^{18}O$ in the DRI short core, for the years 1991 – 2013.

valid for every year, because it depends on (1) persistent conditions throughout a season, (2) the occurrence of precipitation to capture the anomaly in $\delta^{18}O$, that are all the more unlikely given that SAM positive phases prevent snowfall, and (3) other atmospheric patterns may play a role, especially since SAM is defined at a hemispheric scale and is poorly suited to describe the meridional flow at a specific longitude. The multi-year average temperature signal is driven by the winter variability. The average will depend primarily on the frequency and intensity of high precipitation events; atmospheric modes (SAM or Pacific-South American patterns) play an important role in the control of the occurrence of such events on long timescales (Marshall et al., 2017).

The influence of the SAM on $\delta^{18}O$ and temperature at ABN is further illustrated with scatter plots and linear regression (figure 4.15). Both $\delta^{18}O$ and temperature have a negative

correlation with the SAM Marshall index, hence the negative slopes. The SAM is better correlated with temperature ($r^2 = 0.485$, $p < 0.05$) than with $\delta^{18}O$ ($r^2 = 0.166$, $p = 0.06$). The lower correlation value with $\delta^{18}O$ could result from increased variability induced by precipitation events, or noise caused by post-deposition processes. In particular, the less frequent blockings and large precipitation events associated with a positive SAM phase could lead to the lack of "cold" signal in the snow $\delta^{18}O$ at ABN. While $\delta^{18}O$ is representative of temperature changes, the SAM-related variability might be underestimated.

The recent trend in SAM, with a strengthening of positive phases (Marshall, 2004), may prevent the coastal blockings necessary to channel precipitating systems inland East Antarctica. This trend, associated with global warming and poleward shifts of atmospheric circulation, may induce a lowering in apparent temperature on the plateau, by reducing the number and intensity of warm precipitation events reaching the high altitude sites. This could explain why no significant warming has been observed yet on East Antarctic Plateau (Marshall, 2007; Stenni et al., 2017). The study of isotopes in the ABN ice core will help clarify the recent trend on the lower part of the East Antarctic Plateau between 110°E and 140°E.

4.5 Calibration of the isotope – temperature slope

We have shown that the $\delta^{18}O$ in the snow reflects atmospheric changes at the seasonal scale at ABN, and is especially sensitive to changes in winter conditions. Annual average values are consequently driven by the winter variability. In order to reconstruct past temperatures, we may rely on this relationship between isotopes and temperature.

We choose to use the longest record available to provide a more robust calibration of $\delta^{18}O$ versus temperature: the DRI Short Core was dated back to 1968, with great confidence on the annual dating after 1991. The $\delta^{18}O$ in the short core has undergone diffusion and surface reworking processes and is a direct measurement of the ice $\delta^{18}O$ which we aim to calibrate.

It overlaps with the MAR modelled temperature on the 1979-2013 period, and MAR was shown to model the surface temperature most accurately when compared with Automatic Weather Station (AWS) observations (Chapter 3). MAR will thus be used as the temperature reference, because the AWS temperature data record (1985 – 1993) is too short to capture the interannual variability of temperature, and we have lower confidence in the Short Core dating before 1991. We will calibrate a temperature – $\delta^{18}O$ slope for ABN using linear regression on the 1991 to 2013 period, where we are confident on the dating and have a decent number of years.

Time series of surface temperature, temperature at P_{90} from the MAR, and the DRI Short core $\delta^{18}O$ are shown in figure 4.16. Although we have discussed temperature at the cloud level to emphasize the effect of precipitation intermittency on the isotopes and ignore the effects of the inversion layer, we find that in the end the snow $\delta^{18}O$ is best correlated with surface temperatures ($r^2 = 0.316$, figure 4.16b) than with temperature at P_{90} ($r^2 = 0.216$, figure 4.16c). This may result from (1) temperature variability that is exacerbated by the surface inversion, resulting in a better correlation and/or (2) post deposition processes that depend on surface temperature may affect the snow isotopic composition (Touzeau et al., 2016). The estimated slope of 2 m temperature to $\delta^{18}O$ is of $\alpha = 2.01‰\ °C^{-1}$, given with a 95% confidence interval of $1.16 < \alpha < 2.87\ ‰\ °C^{-1}$. According to this slope, a change of 1°C in the mean annual temperature would be recorded in the snow by a 2‰ change in $\delta^{18}O$.

The $2.01‰\ °C^{-1}$ slope described here is relatively high compared with other values in East Antarctica, which average $1.00‰\ °C^{-1}$ (Stenni et al., 2017). It is also much larger than the $\sim 0.85\ ‰\ °C^{-1}$ slope estimated with ECHAM5-wiso, although this model tends to underestimate the inter-annual variability of isotopes (Goursaud et al., 2018).

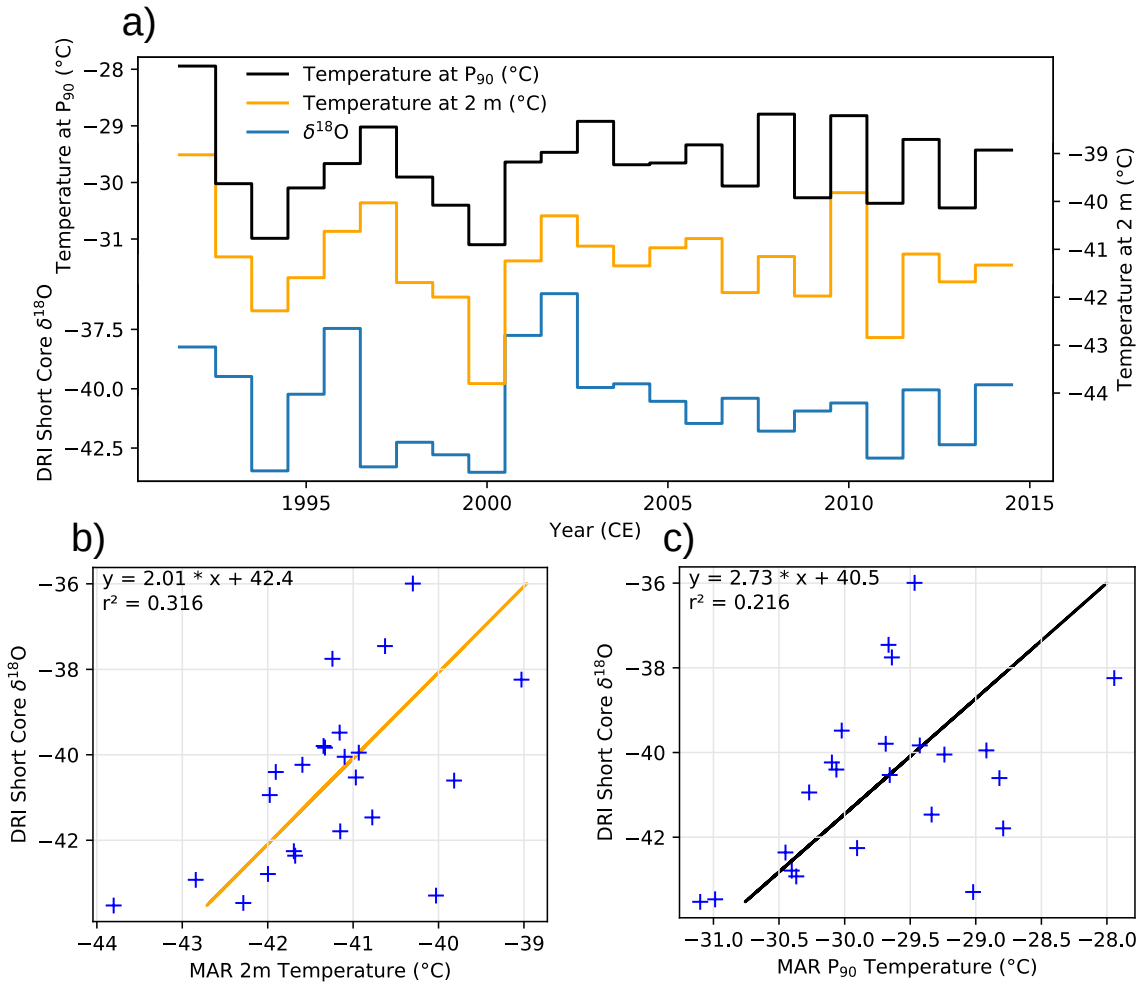

Figure 4.16. Correlation of the Short Core $\delta^{18}O$ with the temperature at P_{90} and the temperature at 2 m on the 1991-2013 period.

We use the inter-annual variability of temperature and $\delta^{18}O$ in precisely dated snow records to compute the slope, because it accounts for all the processes including post-deposition effects. We use a simple linear regression because is not possible to correct for the overrepresentation of warm phases in variability, but must keep in mind that this proxy might be biased, as precipitations occur consistently during warm phases.

4.6 Conclusions

We used the isotope-enabled model ECHAM5-wiso to study the isotopic signature of precipitation at East Antarctic site Aurora Basin North (ABN) and their potential effect on water isotopes, which are commonly used as a temperature proxy in ice cores.

Because of larger variability in both isotopes and temperature during the winter season, the interannual signal will depend primarily on the winter conditions, which in turn depend on whether synoptic events can reach the plateau or not. The blocking favoring precipitation at ABN are themselves conditioned by atmospheric circulation patterns, and are more likely to happen with a negative phase of the Southern Annular Mode. The results presented for ABN may apply for other sites, because mechanisms responsible for high precipitation events are comparable across the East Antarctic Plateau.

As isotopes reflect temperature changes, we can use the isotopes in ice core to trace past changes in atmosphere circulation conditions. Over the short timescale presented here, different series of $\delta^{18}O$ from snow pits and a short core clearly record large anomalies in Southern Annular Mode and atmospheric blocking happening in the winter, which supports the use of $\delta^{18}O$ (or its equivalent) as a tracer of atmospheric circulation in East Antarctic Plateau ice cores, at annual to decadal scale. An isotope – temperature slope for interannual variability was determined from precisely dated snow measurements and could be used to infer temperature from the isotopes at ABN, but we need to keep in mind that this record is biased towards conditions during precipitation, and might miss out cold periods with little to no accumulation.

Appendix 4.A – Computation of weighted statistics

For the dataset (*x*, *y*) of length *n* and weight coefficients *w*, we use:

Weighted mean: $m_w(x,w) = \frac{\sum_{i=1}^{n} w_i x_i}{\sum_{i=1}^{n} w_i}$

Weighted covariance: $cov_w(x,y,w) = \frac{\sum_{i=1}^{n} w_i (x_i - m_w(x,w))(y_i - m_w(y,w))}{\sum_{i=1}^{n} w_i}$

Weighted correlation: $r_w(x,y,w) = \frac{cov_w(x,y,w)}{\sqrt{cov_w(x,x,w) cov_w(y,y,w)}}$

Regression estimate: $\hat{y}_i = ax_i + b$ where a and b were obtained using Weighted Orthogonal Distance Regression (Boggs et al., 1992).

Weighted standard error of the slope: $\sigma_w(a) = \sqrt{\frac{\frac{1}{n-2}\sum_{i=1}^{n} w_i (\hat{y}_i - y_i)^2}{\sum_{i=1}^{n} w_i (x_i - m_w(x,w))^2}}$

Student's t-distribution threshold: $t_{\alpha,n}$ with α the confidence threshold, and *n* degrees of freedom

Confidence intervals: $a - t_{\frac{\alpha}{2},n-2}\sigma_w < a < a + t_{\frac{\alpha}{2},n-2}\sigma_w$

Chapter 5

The Aurora Basin North main core

This chapter describes the intermediate length ice core drilled at Aurora Basin North, known as the Aurora Basin North 2013 – 2014 core (ABN1314) and the information captured in this ice core record: we will analyze the snow accumulation, water isotopes, borehole temperature and methane concentration, and discuss the influence of horizontal displacement of ice on this ice core that was drilled on the slope of the East Antarctic Plateau. We propose a correction for the horizontal ice advection effect on water stable isotopes, based on an estimation of the ice flow rate and regional present-day gradients of isotopes and temperature. The ice core observations will lead to a 2000-year temperature reconstruction at the site that will provide new constraints on Antarctic climate variability.

5.1 Motivation for ice coring in Aurora Basin North

A 303 m core was retrieved in summer 2013 – 2014 by the project team led by Mark Curran (2014). International laboratories are associated with this project, covering a wide range of ice core science, including chemistry, greenhouse gases concentrations, water and gas isotopes. As described in Chapter 1, the purpose for retrieving an intermediate length ice core in this region of Antarctica is to obtain an unprecedented high accumulation record of climate variability at a site inland in East Antarctica, at annual resolution. Many questions regarding the climate of the last two millennia in East Antarctica remain unanswered, among which why the temperature warming observed all around the globe cannot be distinguished from natural variability in this region.

This Chapter is centered on the methods used, and we introduce the different records that will be described in later chapters to discuss the climate history, from ice dating to measurement of gases and isotopes.

5.2 Dating the ice

Producing a well-constrained age model is a necessary step in the analysis of a paleoclimate record. The ABN1314 core was dated by Annual Layer Counting (ALC) and tied to volcanic events using sulfate aerosols from other well dated ice core records. The age model presented here was established by Christopher Plummer and Mark Curran. This age model is preliminary (unpublished) and referred to as ALC01112018 (for Annual Layer Counting, 01 November 2018).

The concentration of various aerosol species shows a seasonal cycle. For example, sea-salts (Na^+, Cl^-) are mostly deposited in winter, while sulfur concentrations reach a maximum in spring (figure 5.1). Provided that the ice core has sufficient resolution, the seasonal cycles can be used to count years (e.g. Winstrup et al., 2012). Similarly, the water stable isotopes follow the seasonal temperature cycle with a maximum in summer and minima in winter. The water stable isotope is also influenced by diffusion because of ice-vapor exchanges. Chemical species, electro-conductivity, and water stable isotopes were measured at high resolution with Continuous Flow Analysis (CFA) at the Desert Research Institute (Maselli et al., 2013; McConnell et al., 2002), allowing identification of annual cycles in the ABN1314 ice core. Annual Layers were manually identified and counted on the entire ice core. A section of the annual horizon identification is shown in figure 5.1. In addition to the annual layer counting, the sulfur record was compared to other records from Antarctica, with the aim to synchronize and tie the volcanic events. Sulfate aerosols originating from the transformation

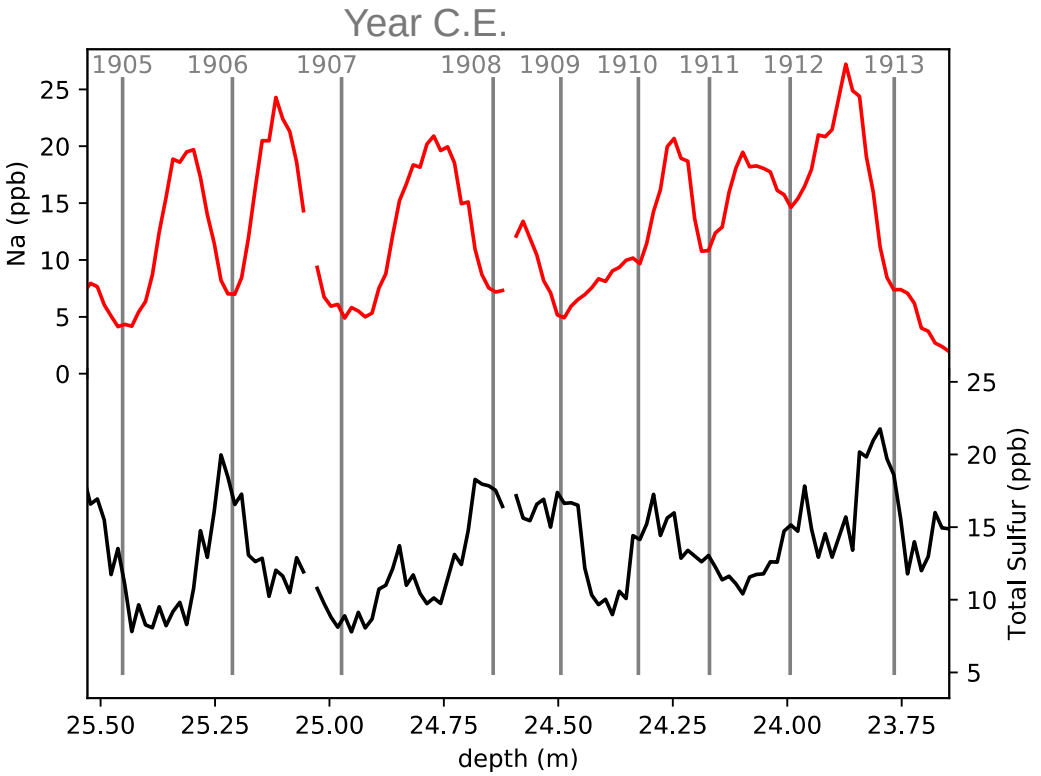

Figure 5.1. High resolution measurements of Sodium and Sulfur in a section of ABN1314 core, between 23.5 and 25.5 m depth. Year-horizons are shown with vertical grey bands.

of sulfur emitted by stratospheric volcanic eruptions have a larger concentration than biogenic sulfates and result in the deposition of high concentrations of sulfur. They occur as concentrated spikes as strong volcanic events are relatively short-lived. Sulphur records can be used to match age models from different ice core records (Sigl et al., 2013). In this case, the ABN1314 total sulfur record was tied to the Plateau Remote (Cole-Dai et al., 2000) and West Antarctic Ice Sheet Divide (Sigl et al., 2013) ice cores, as all sites are inland Antarctica and have similar backgrounds for sulfur. Even though Law Dome is the nearest site with high resolution sulfur record, the background is very different, probably because Law Dome is close to the coast.

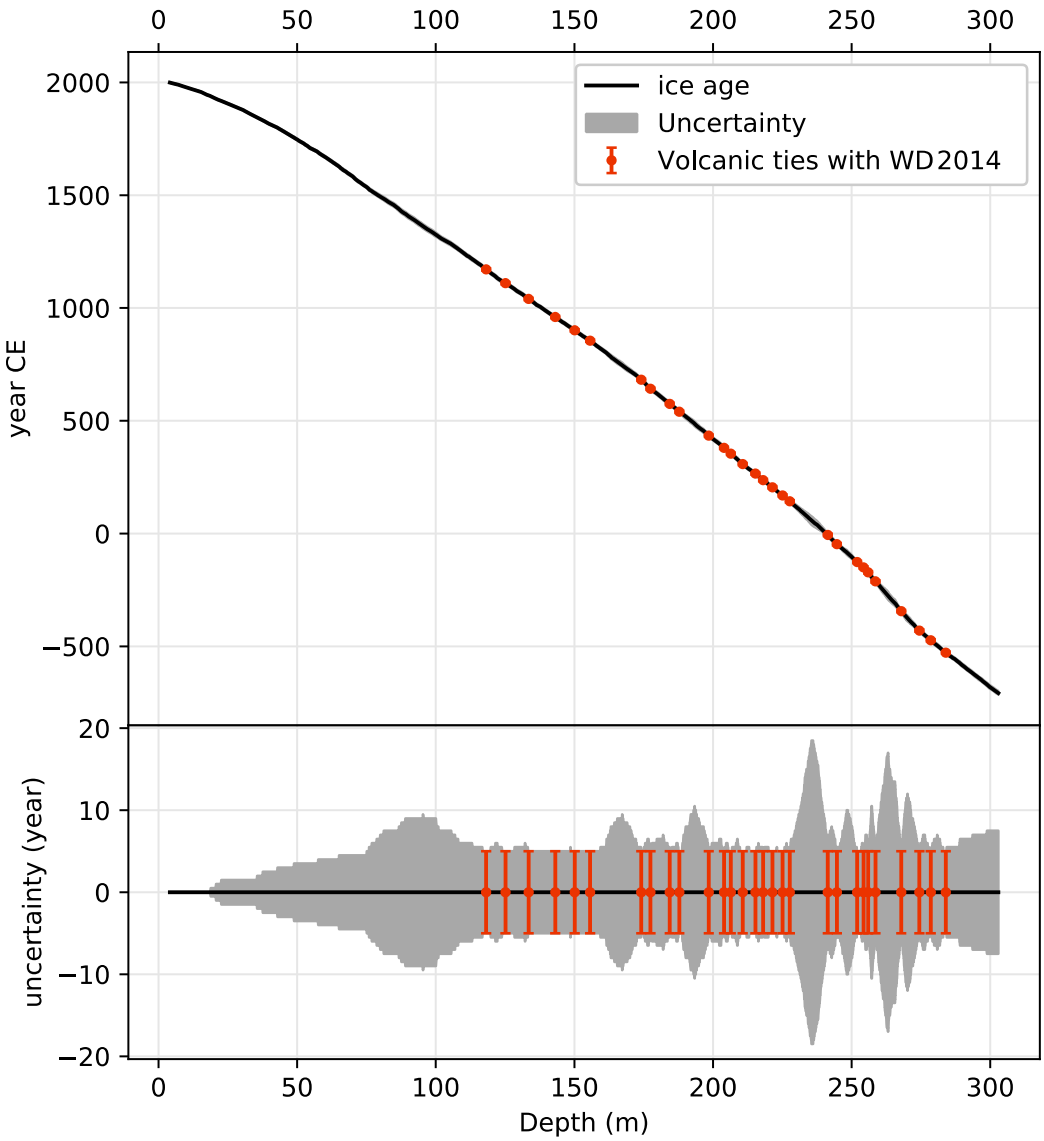

Figure 5.2. Age model for the ABN1314 core. The shading indicates cumulated uncertainties on annual layer counting, with half a year uncertainty for each uncertain year counted. Volcanic horizons were identified on the sulfur record and were tied to the ages of volcanic events on WD2014 timescale (Sigl et al., 2015; Sigl et al., 2016).

ABN1314 ALC was adjusted using the volcanic ties that were matched to the WD2014 chronology (Sigl et al., 2016), which has uncertainties of less than ±5 years for the last 2700 years. For example, the number of ALC years was lower compared to the WD2014 chronology, suggesting that years were missed during the counting. As described for the snow pit in

Chapter 4, the surface snow at Aurora Basin North presents a roughness with variations of up to 40 cm of snow (160 mm water equivalent), so it is likely that spatial inhomogeneities in accumulation and snow reworking resulted in the absence of an annual layer – or at least a seasonal extremum, making the annual layer in this case impossible to observe. Therefore, further ALC was performed to include "missing" annual layers, so that the identified volcanic ties at ABN1314 had ages matching the WD2014 chronology.

The 303 m core covers the last 2700 years (figure 5.2). Dating uncertainties result from the uncertainty of ALC: if an annual layer was counted but it is not on a clear seasonal extremum, it is flagged as uncertain, and a half-year uncertainty is added. Below 100 m, the ALC was not sufficient and many annual layers were not clear. Therefore, the sulfur record was used and 29 volcanic horizons were identified, and tied to ages of known volcanic events from the West Antarctic Ice Sheet Divide (WD) ice core chronology (Sigl et al., 2015; Sigl et al., 2016). Volcanic events at ABN1314 were tied to WD instead of the nearer record from Dome Summit South (Law Dome), because the background of sulfur was similar at WD. Indeed, Law Dome is a coastal site, probably more sensitive to local marine sulfur emissions, and shows a much noisier sulfur record. The uncertainty for the age of volcanic events on WD2014 timescale is less than ±5 years for the last 2500 years (Sigl et al., 2016). The ABN1314 age model consequently has low uncertainties of less than ±20 years, constrained by the volcanic tie points.

5.3 Accumulation history

Snow deposited on ice sheets gradually compacts under the weight of newly precipitated and preserved snow. Consequently, the density increases with depth, and can result in density variations in the top 100 meters. The thickness of annual layers is thus not representative of accumulation variations only. To account for the compaction effect, we convert the annual

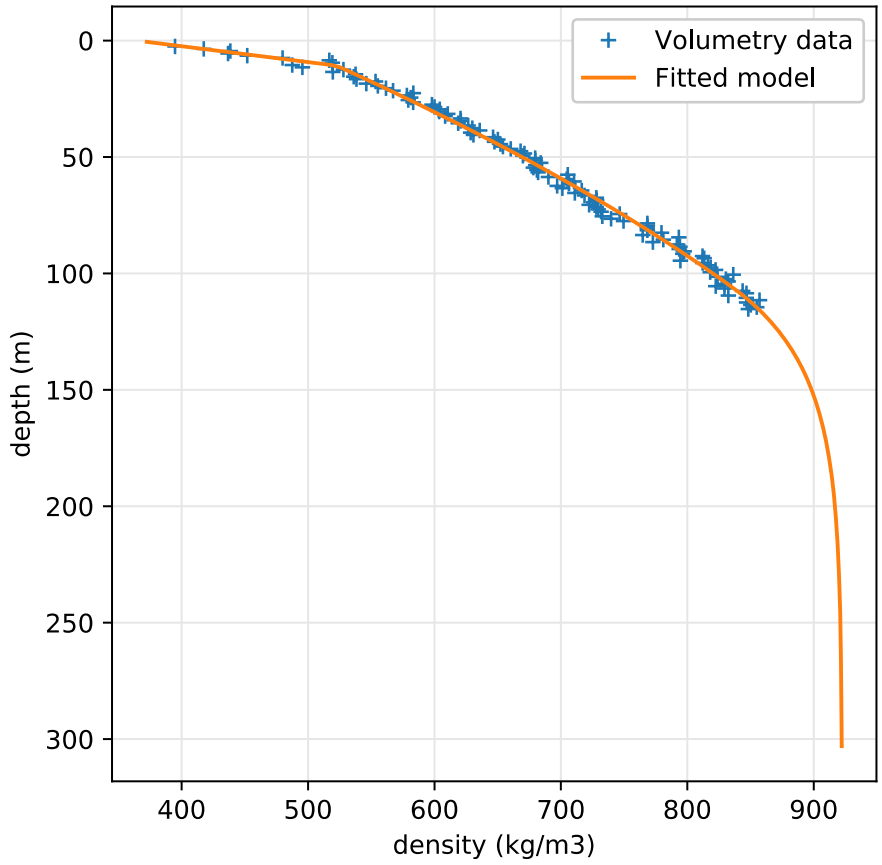

Figure 5.3. Density profile at Aurora Basin North.

accumulation height to mass equivalent accumulation (mm w.eq. yr^{-1}, identical to $kg \cdot m^{-2} \cdot yr^{-1}$), using the densities measured on ABN1314 (figure 5.3).

The density was measured by Tas van Ommen by weighing known volumes of the ice core. We then fitted a three-stage model (equation 5.1) to the density measurements to smooth the values, and extended the data to the total length of the core (figure 5.3). The density model and its separation in three stages is inspired from the firn densification model of Herron & Langway (1980). The first two stages are fitted to the measurements, and reflect rapid densification of snow by packing and grain transformation to a critical density for the first stage, and then densification of the firn until the porosity closes in the second stage. The third stage corresponds to the densification of ice with closed porosity, with compression of bubbles, and gaps filled between the deepest density measurement and the theoretical ice density value at a given temperature.

$$\begin{cases} \rho(z) = a_0 + a_1 z + a_2 \exp\left(a_3 (z - z_{critical})\right) & for\ z < z_{critical} \\ \rho(z) = b_0 + b_1 z + b_2 z^2 & for\ z_{critical} < z < z_{closeoff} \\ \rho(z) = \rho_{ice} - (\rho_{ice} - \rho_{closeoff}) \exp\left(\dfrac{(z_{closeoff} - z)(b_0 + 2 b_1 z_{closeoff})}{\rho_{ice} - \rho_{closeoff}}\right) & for\ z_{closeoff} < z \end{cases} \quad (5.1)$$

The values for coefficients a_0, a_1, b_0, b_1 and b_2 were obtained with least mean square error polynomial regressions on the corresponding depth sections, while a_2 and a_3 were adjusted so ρ(z) and $\frac{\partial \rho}{\partial z}$ were continuous at $z_{critical}$. The values are given in table 5.1.

Table 5.1 Coefficients used in the ice density model

a_0	a_1	a_2	a_3	$z_{critcal}$	b_0	b_1	b_2	$z_{closeoff}$
364.6886	14.64428	-2.34914	-4.51	11	477.9089	4.226257	-0.00803	106

The ice density model was adjusted for continuity of values and derivatives at close-off. In most firn density studies, the ice density is considered incompressible, at 917 kg·m^{-3} (Arthern et al., 2010; Herron & Langway, 1980). Here, we approximate the ice density at the deepest point by the ice density at 1000 hPa and a temperature T (Bader, 1964):

$$\rho_{ice} = 916.5\,[\,1 - 10^{-6}\,T\,(157.556 + 0.2779\,T + 0.00885\,T^2 + 0.0001778\,T^3)] \quad (5.2)$$

Where T is the annual average temperature in °C, and the density is in kg·m^{-3}. For a temperature of -43.4°C, corresponding to the annual mean temperature observed at ABN (Chapter 3), the ice density is 922.4 kg·m^{-3}. This value is used for ρ_{ice} in the model, although it does not account for increasing pressure with depth, nor for the bubbles in the ice that would lower the ice density, but is expected to be more realistic than the value of 917 kg·m^{-3}, which corresponds to ice at 1000 hPa and 0°C. Using the density profile, we convert the annual layer thickness determined from layer counting to annual layer mass, *i.e.* mass accumulation (figure 5.4).

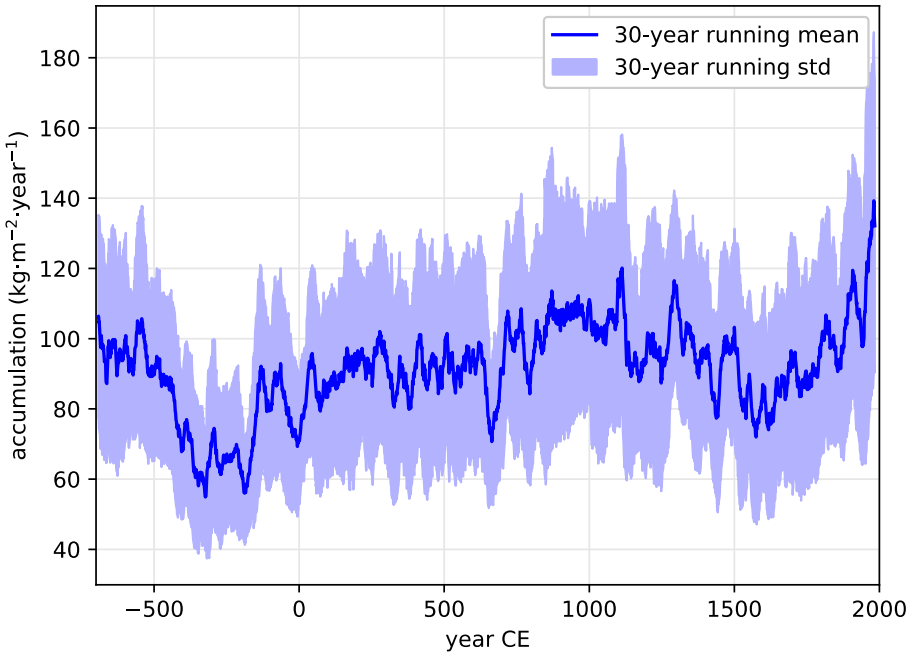

Figure 5.4. The ABN1314 accumulation record where annual layer thickness was converted to annual layer mass.

To account for uncertainties in the annual layer thickness, the accumulation was smoothed by applying a 30-year running mean. The full range of variability is shown by the shading, corresponding to ± 1σ, the standard deviation in the 30-year window (figure 5.4). Despite the smoothing, the accumulation record shows distinct variations, ranging from a minimum of 60 kg·m^{-2}·year^{-1} around 400 to 200 Before Common Era (year BCE, or negative year CE on the figure 5.4), to a recent maximum of 130 kg·m^{-2}·year^{-1}. The average accumulation for the entire record is 92 kg·m^{-2}·year^{-1}. This accumulation is representative of the ABN site, which location varied over time as the site is not on a divide. The influence of spatial variation will be determined later in this chapter (section 5.5).

5.4 Borehole temperature

Temperature is a fundamental climate parameter that we aim to obtain for the time frame covered by the ice core. It is also a physical quantity that can be measured in the environment. Taking advantage of the borehole that remains after the ice core was drilled, it is possible to measure the temperature at depth within the ice sheet, for as deep as the core was drilled. The

vertical temperature profile can then be used to infer past temperature changes using the heat diffusion properties in the ice (Johnsen et al., 1995; Orsi et al., 2012).

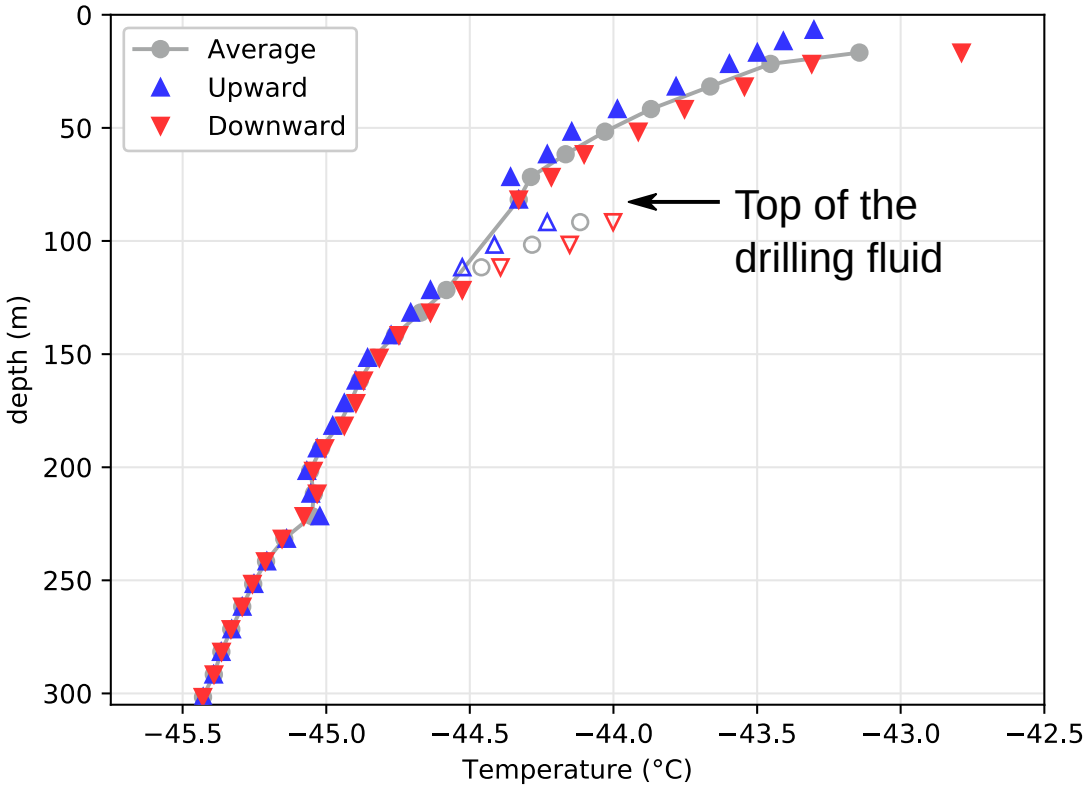

Figure 5.5. Temperature profile in the Aurora Basin North main core Borehole. The uppermost drilling fluid was added more recently and may have biased the borehole temperature, because the drilling fluid was stored at the surface at a warmer temperature of about -20°C. Open markers indicate points that will not be considered for this reason

At Aurora Basin North, Trevor Popp and Simon Sheldon measured the borehole temperature with two series: when the temperature probe was descending into the borehole (Downward) and when it was ascending (Upward, figure 5.5). The probe was stopped at each target depth to equilibrate the temperature probe with the temperature of surrounding ice. Friction during the drilling can heat the walls of the borehole, and because the ABN drilling campaign was completed in a single field season, it was not possible to wait and return in later years to

allow for more favorable equilibrium conditions. Repeated borehole temperature measurements at NEEM (North Greenland Eemian Ice Drilling Project, 51°W, 77°N) showed that heating caused by the drilling fades after a few years, and the estimated heating can be up to ~0.1°C (Orsi et al., 2017). This heating effect is lower than the difference between downward and upward temperature measurements and reaches 0.2°C for the top 100 m at ABN. The difference between upward and downward measurements likely results from the short equilibrium time between each measurement, and where the probe to retains temperature from the previous location, *i.e.* due to a memory effect. Because of the memory effect and a strong gradient in the temperature profile (figure 5.5), the temperature is likely overestimated in the downward series and underestimated in the upward series. To avoid any bias, the average of the two measurements at corresponding depths is used.

The most striking feature of the temperature profile is the decrease of temperature at depth, suggesting a warming of the surface. The temperature gradient is approximately $1°C \cdot 100\ m^{-1}$, on the shallow part of the profile, which is very strong considering that a similar temperature gradient at NEEM was attributed to a 2.7°C warming over the last 30 years. The ABN borehole temperature profile is in contrast with recent temperature records on the East Antarctic Plateau where no warming trend was evidenced (Nicolas & Bromwich, 2014). It is also possible that a portion of the warming of the ABN site and temperature gradient in the ice may result from ice rheology displacing the ABN ice to a warmer location over time, rather than climate forcing.

5.5 Ice rheology

Aurora Basin North is located in a basin, in opposition to many ice core drill sites that target a dome or a divide. Therefore, in a basin setting, ice slowly flows from the continent

interior, and the ABN drilling location moves closer to the coast. In this section, the ice velocity at ABN is estimated and we demonstrate how it affects the climate history preserved in the ice record.

5.5.1 Ground penetrating radar

Ground penetrating radar relies on the difference of physical properties at depth in the ice sheet to reflect radar waves emitted at the surface by an electromagnetic source. The reflected waves are recorded with a receiver, and the depth of the reflecting layer is estimated from the time elapsed between emission and reception, along with the propagation velocity of radar wave in the ice.

At ABN, Emmanuel Le Meur performed ground penetrating radar measurements from the ABN ice core site and up to 64 km upstream the ABN core drilling location. The goal was to identify and clarify flow lines, and to trace the origin location of the ice buried at ABN drilling location. The ground penetrating radar methods used are detailed in Meur et al. (2018), which are the same methods used for the Dome C – Vostok traverse. For ABN, Le Meur identified reflecting layers down to a depth of 175 m. It is hypothesized that reflecting layers spatially distributed were formed simultaneously due to variations in surface conditions, and known as isochrons. From tracing the isochrons upstream on the ABN transect, we interpret the depth variations as variation of accumulation. Reduced vertical distance between isochrons indicate a lower accumulation, and conversely larger distances between isochrons result from higher accumulation. With the assumption that the density profile measured at the coring location can be extrapolated to the 64 km transect, Le Meur was able to quantify the accumulation in a 2D field at different depths for the upstream transect. The results are shown in figure 5.6, along with the accumulation record that we estimated from the ice core. The depth of the most recent and shallowest isochron at the ABN ice core site is used to

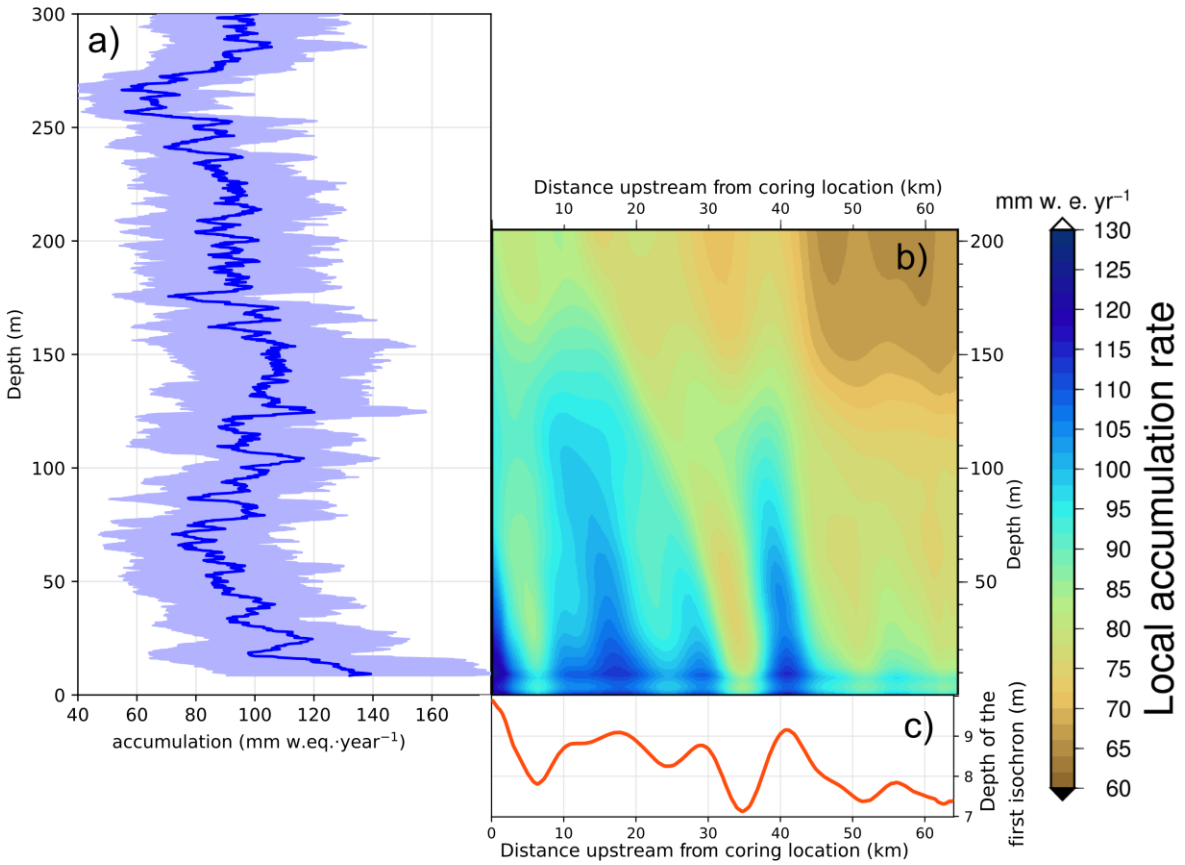

Figure 5.6. Propagation of dunes in the accumulation record at ABN. **(a)** Accumulation profile from the ABN1314 core, **(b)** local accumulation rate from radar reflectance survey and identification of isochrons (original sub-figure produced by Emmanuel Le Meur), and **(c)** depth of the first isochron along the upstream radar transect of 64 km.

estimate the local accumulation rate and traced along from ABN ice core site and along the 64 km upstream transect from real measurements.

The radar profile shows that regions with low accumulation were sustained for an extended amount of time, as the low accumulation features are propagated at depths when buried under more recent snow. The low accumulation feature is tilted at depth towards the ABN coring location, showing the displacement of the ice. Consequently, we are able determine the regional variability of accumulation to have an influence at different depths, in the ABN1314 core, because of the ice origin.

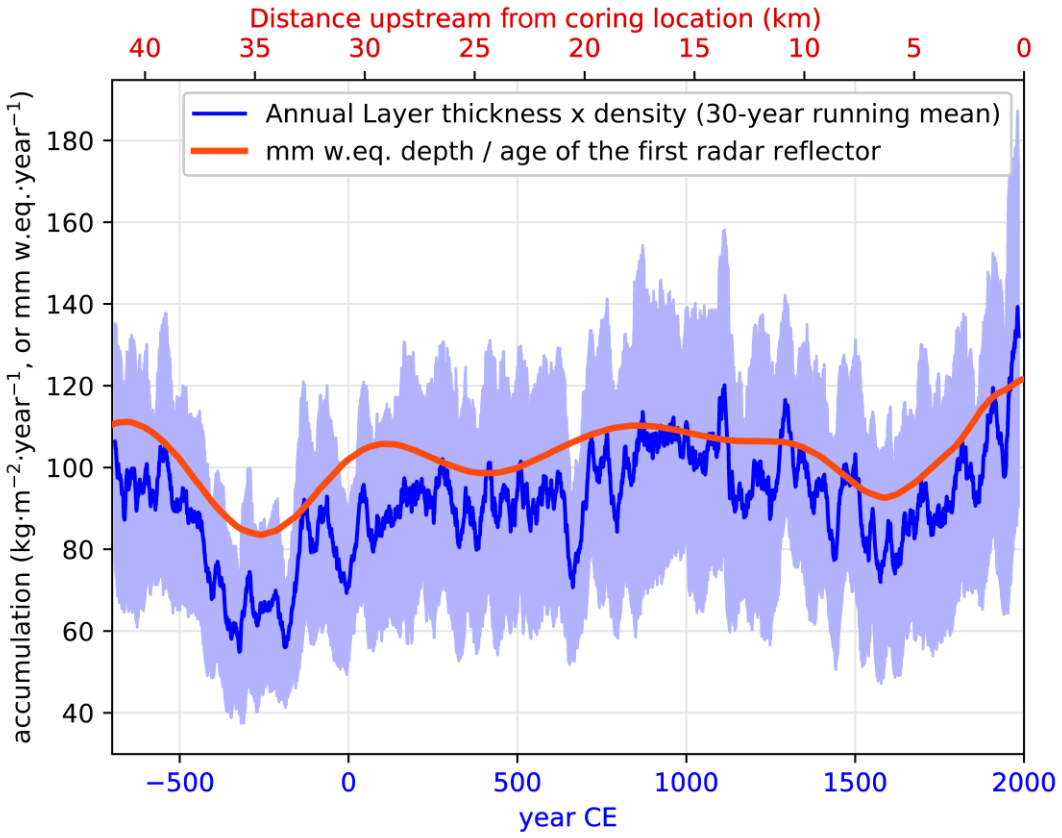

Figure 5.7. (blue) Temporal variation of accumulation in the ABN1314 ice core and (red) spatial accumulation estimated from the age and depth of the first reflecting layer. The distance axis (red) was manually adjusted to match the variations of accumulation in the time axis (blue).

A more direct comparison of accumulation from ABN1314 (temporal evolution) and from the average accumulation above the first isochron (spatial variation) reveals striking similarities (figure 5.7), supporting that (1) the long-term accumulation is at a steady state and (2) that the variation of accumulation in the core is due to the spatial heterogeneities in accumulation rates, at the first order. Climate-induced changes in the accumulation may superimpose on these low-frequency changes, but deposition noise may also create high-frequency variability that is related to surface roughness. This allows us to calculate a mean ice velocity, of 41.5 km in 2700 years, or 15.4 m·year^{-1}. This value is in agreement with satellite-

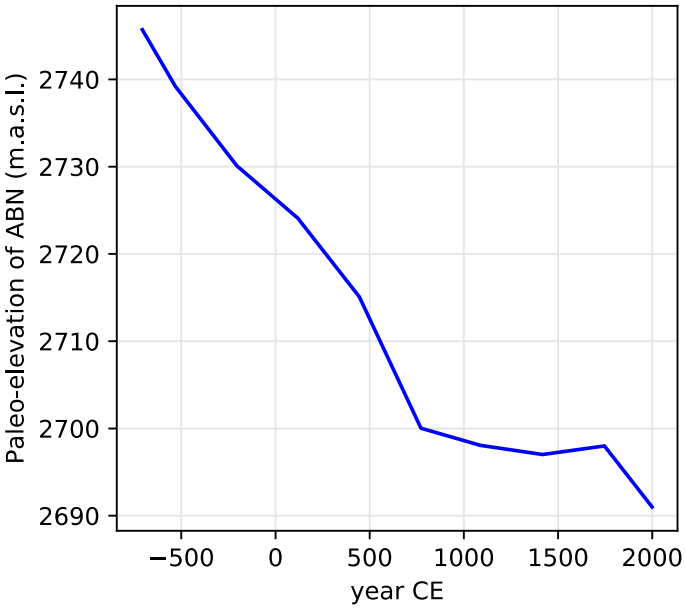

Figure 5.8. Paleo elevation of ABN drilling site

based estimation of 16.2 m·year^{-1} at ABN for the 1996-2018 period (Mouginot et al., 2019). Consequently, it is likely that other ice core proxy parameters are affected by the ice flow. Because accumulation depends on horizontal advection and was probably affected by topographic slope changes, we chose not to discuss the accumulation record in terms of climate changes. Further work would be needed to interpret this record.

5.5.2 Elevation changes

Although the East Antarctic Plateau has very little changes in elevation, the substantial distance over which the ice was advected over the last 2700 years is associated with a decrease of 60 m in the surface elevation (figure 5.8). The paleo-elevation of ABN site decreased from an initial altitude of 2745 m between 700 BCE and 700 CE, then it plateaued at about 2700 m for 1000 years. The elevation decrease resumed around 1750 and continued until reaching the present elevation of 2690 m.

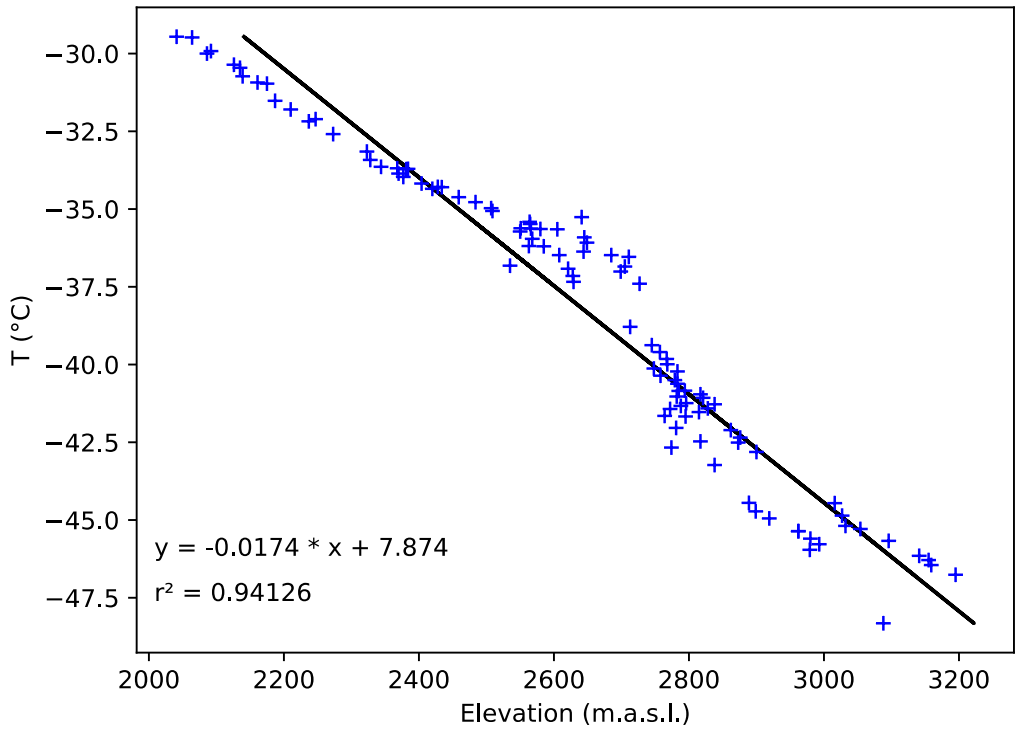

Figure 5.9. Annual average temperatures interpolated with kriging from Automatic Weather Stations and borehole temperature measurements for two traverses in Princess Elizabeth Land, East Antarctica (Pang et al., 2015; Xiao et al., 2013). The regression was performed on a subset of the traverse between 2000 and 3250 m.a.s.l., corresponding to the lower plateau.

5.5.3 Temperature changes

The change in elevation and advection of ice closer to the coast is associated with a warming, as the site gets further away from the cold summits of the East Antarctic Plateau. The change in temperature caused by the decrease in elevation can be estimated from Antarctic traverse expeditions, which reveal the spatial variability of conditions along a route between two points. Xiao et al. (2013) show the evolution of surface conditions in a traverse in Princess Elizabeth Land, from Zongshan Station (Princess Elizabeth Land) to Dome A, roughly following the longitude 77°E. Using their annual average temperature data, we estimate the relationship between temperature and elevation on the lower East Antarctic

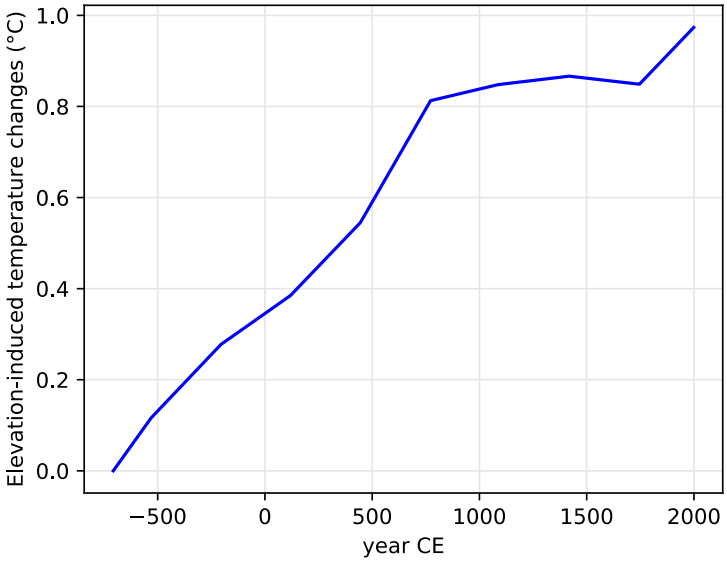

Figure 5.10. Temperature changes caused by the variation of elevation associated with ice flow.

Plateau (figure 5.9). The results show that temperature decreases by 1.8°C for every 100 m of elevation gained. We restricted our calibration area to the lower plateau by using only the points with elevations from 2000 to 3250 m.a.s.l.

Because the East Antarctic Plateau is zonally symmetric, we assume that the temperature slope at Aurora Basin North is similar, and use the relationship from the Zongshan to Dome A traverse to infer temperature changes on the drilling location, from the changes in elevation (figure 5.10). We assume that the temperature gradient relationship with elevation was stable throughout time, and this is supported by the relatively stable conditions in Antarctica during the late Holocene (Masson et al., 2000). The elevation decrease of 60 m of the ABN site results in a warming of about 1°C over the last 2700 years, mainly on the early half of the record when elevation changes were the fastest. The borheole temperature gradient in the top 300 m was roughly 2°C, so a portion of this gradient cannot be explained by advection and must be due to a climatic warming trend. The influence of colder ice advected at depth will be discussed in the chapter 6, with a temperature diffusion model.

5.6 Water stable isotopes

The water stable isotopes measured in ice cores are used to infer past temperatures, due to the relationship between cloud temperature and isotope composition of the precipitation (Ciais & Jouzel, 1994; Dansgaard, 1964 detailed in Chapter 2). Water stable isotopes are routinely measured and used as a proxy for temperature, because it is widely available to measure in ice, and is relatively well understood, owing to the numerous studies describing the connection between the isotopes and climate parameters (Jouzel & Masson-Delmotte, 2010), as well as its archival in ice cores (Casado et al., 2018).

5.6.1 Measurements of $\delta^{18}O$ and δD

The ABN1314 core was subsampled at 20 cm resolution for water stable isotope analysis at the Australian Antarctic Division. The measurements were performed on a Picarro L2130-i isotopic water analyzer. With a total of 1522 measurements for the 2707 years spanned by the record, the temporal resolution is slightly above 2 points per year (figure 5.11). However,

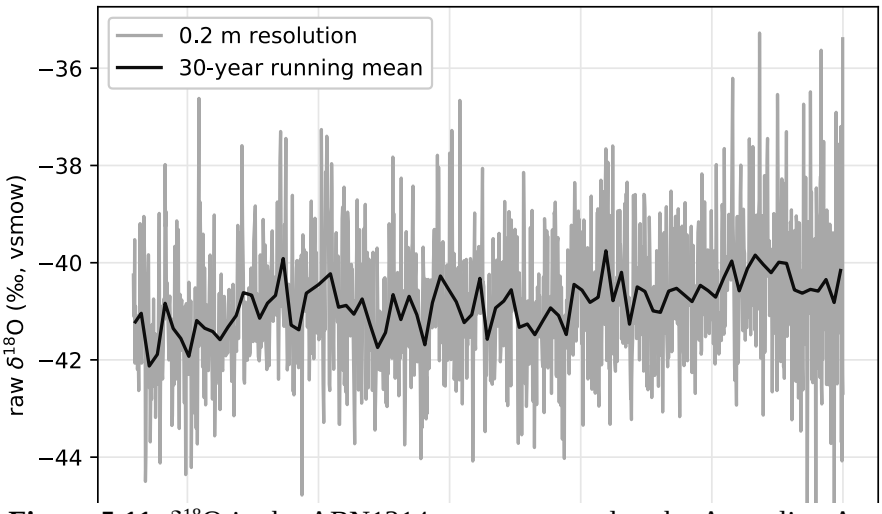

Figure 5.11. $\delta^{18}O$ in the ABN1314 core, measured at the Australian Antarctic Division.

the water isotopes are strongly affected by non-climatic factors that may mask the climate signal at high resolution, especially for low accumulation regions such as the East Antarctic Plateau (Casado et al., 2020; Münch & Laepple, 2018). Therefore, a 30-year average is used to better represent the signal affected by climate factors. The 30-year averaged $\delta^{18}O$ series has a mean value of -40.8 ± 0.5‰ (1σ) and shows minimal variation over time. The δD was also measured, and bears the same information on the first order (Dansgaard, 1964). Similar to the temperature, this trend includes the effect of ice flow and lowering site elevation.

5.6.2 Flow-correction with spatial $\delta^{18}O$ calibration

Similar to temperature, the $\delta^{18}O$ values of the snow varies with the location of the site, because of the increased elevation and continentality – distance from the ocean (Goursaud et al., 2018; Masson-Delmotte et al., 2008). Here, we use two different snow surface datasets to estimate the slope of $\delta^{18}O$ versus elevation (figure 5.12): data from two traverses from Zongshan to Dome A (Pang et al., 2015; Xiao et al., 2013) that we used previously for the

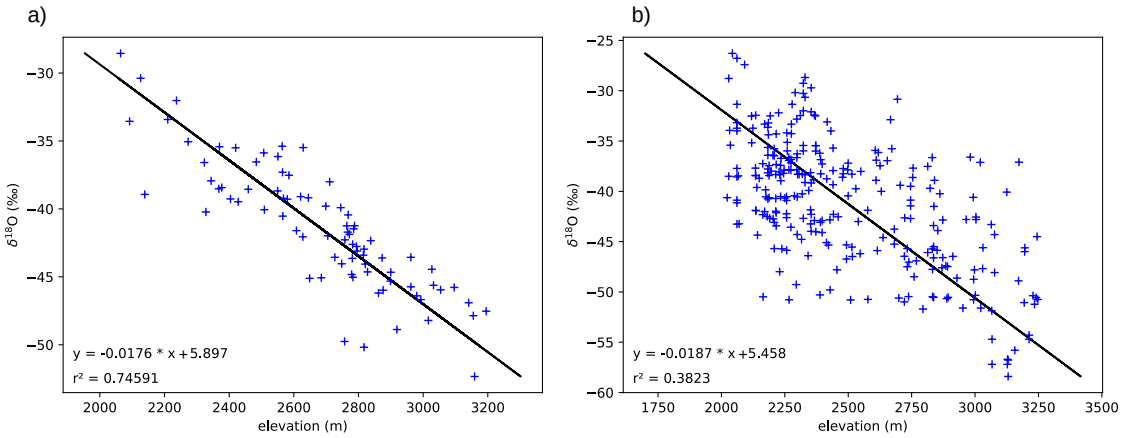

Figure 5.12. $\delta^{18}O$ – elevation slopes in surface snow studies: (**a**) Zongshan to Dome A traverses (Pang et al., 2015; Xiao et al., 2013), and (**b**) Goursaud et al. (2018), including but not restricted to the database of Masson-Delmotte et al. (2008). For both databases, we restricted our slope to sites at elevations comprised between 2000 and 3250 m.a.s.l., and longitudes from 80°E to 160°E.

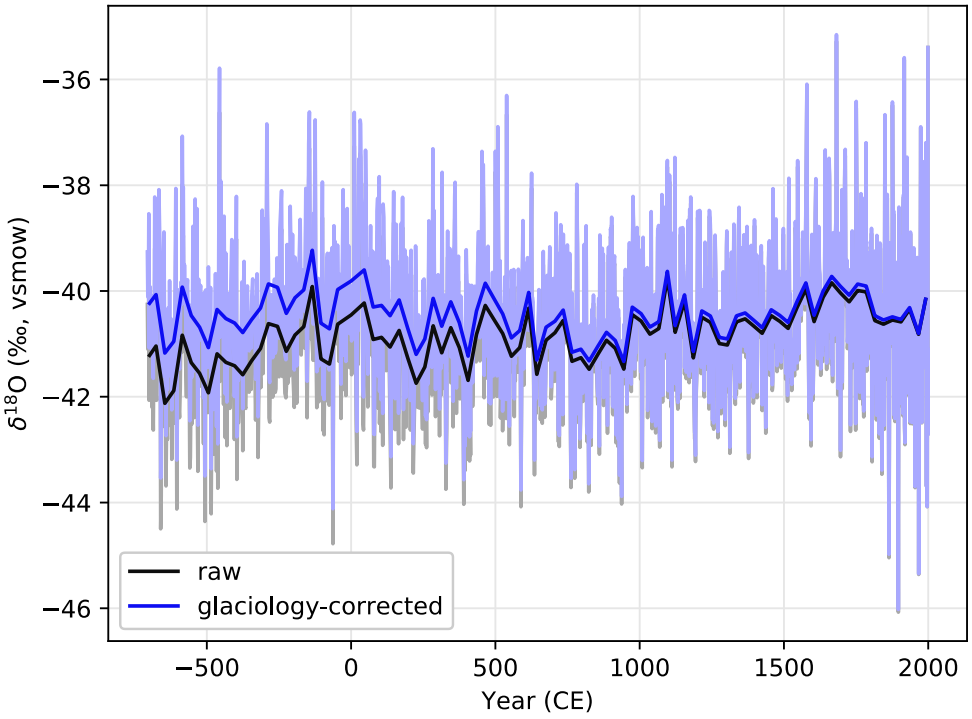

Figure 5.13. Glaciological flow correction of the $\delta^{18}O$ series

temperature correction, and a more complete database (Goursaud et al., 2018). This includes isotope data from numerous transects, stations and ice core locations. Both datasets give similar slopes of -0.0176 to -0.0187 ‰·m^{-1}, and the lower correlation of the Goursaud et al. (2018) database likely results from the more diverse transects across the region. Using an averaged slope of -0.018 ‰·m^{-1}, and the paleo-elevation described in section 5.5.2, we correct the measured $\delta^{18}O$ in ABN1314 (figure 5.13).

The correction results in a +1‰ shift in the earliest section of the record, and increases the mean value of the entire series to -40.5‰. This correction cancels out the slight positive trend in the initial $\delta^{18}O$ data, with most of the 30-year averaged values falling into a -41‰ to -40‰ range, supporting relatively stable climatic conditions over the last 2700 years.

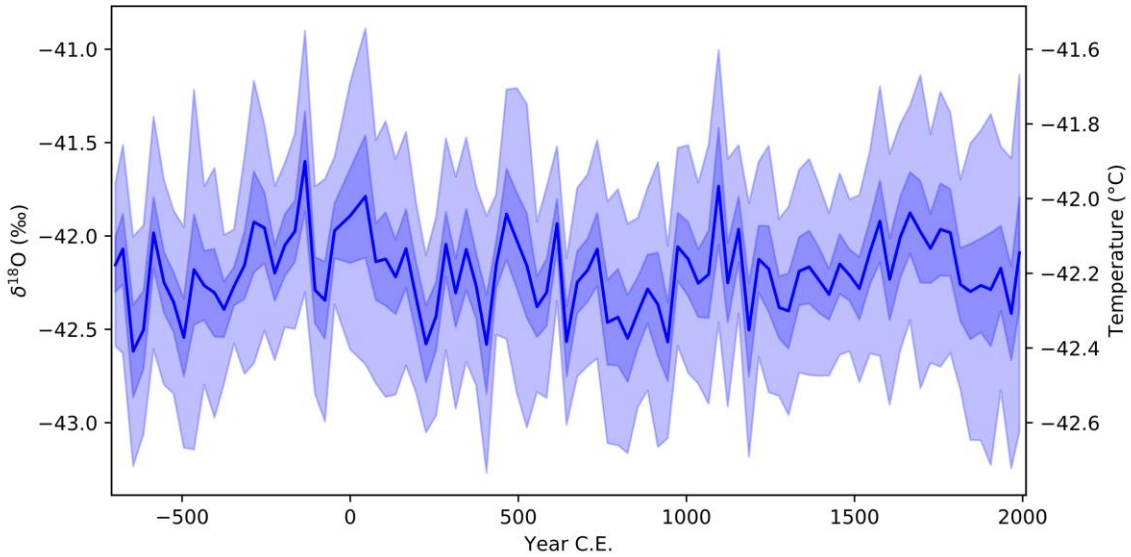

Figure 5.14. ABN $\delta^{18}O$ converted to temperature with 30-year averages. The dark shading indicates the uncertainty from the slope used for the reconstruction (main reconstruction with 0.50 °C·‰$^{-1}$, with 95% confidence intervals of 0.29 to 0.71 °C·‰$^{-1}$). The light shading depicts the standard deviation of $\delta^{18}O$ or temperature within the 30-year window (1σ).

5.6.3 Conversion to temperature

In the Chapter 4, we defined a 0.50 °C·‰$^{-1}$ slope by comparing high resolution, precisely dated short core $\delta^{18}O$ measurements with the temperature data from the Modèle Atmosphérique Régional. The slope given here is 0.50 °C·‰$^{-1}$, inversed from the 2.01 ‰·°C^{-1} given in Chapter 4. We use this slope here, to convert the $\delta^{18}O$ from ABN1314 to a temperature record (figure 5.14).

The $\delta^{18}O$-derived temperature record supports very stable conditions over the past 2700 years, with an average temperature around -42.0 °C, and likely to have remained within a 1 °C range (from -42.6 to -41.6 °C).

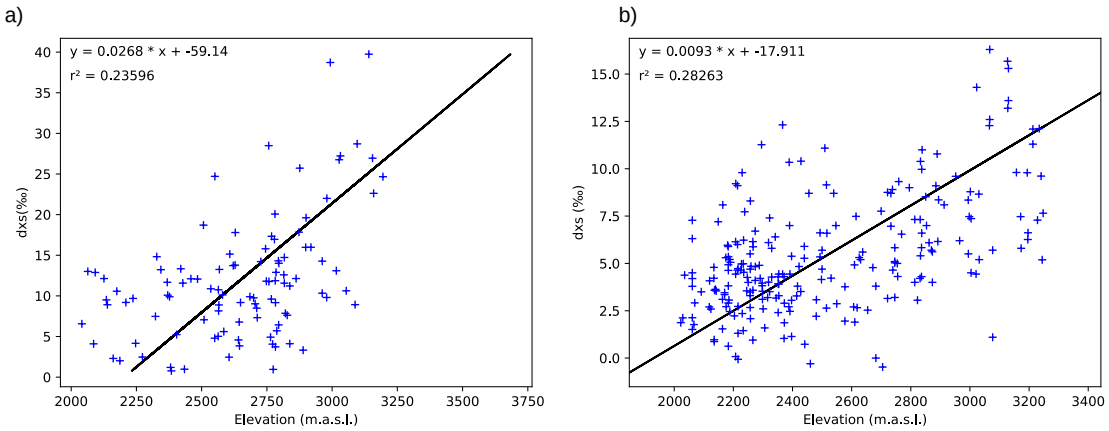

Figure 5.15. d_{excess} – elevation slopes in surface snow studies: (a) Zongshan to Dome A traverses (Pang et al., 2015; Xiao et al., 2013), and (b) Goursaud et al. (2018). For both databases, we restricted our slope to sites at elevations comprised between 2000 and 3250 m.a.s.l., and longitudes from 80°E to 160°E.

5.6.4 Deuterium excess

Although $\delta^{18}O$ and δD are roughly proportional, deviation from the standard meteoric water line of $\delta D = 8.0 \cdot \delta^{18}O + 10$ likely results from non-equilibrium processes that primarily occur during evaporation at the moisture source (Dansgaard, 1964; Uemura et al., 2008). The deuterium excess d_{excess} is defined as the difference to this linear relationship: $d_{excess} = \delta D - 8 \cdot \delta^{18}O$. On a similar fashion to the $\delta^{18}O$ correction, we used the surface snow datasets to compute a d_{excess} correction based on elevation changes (figures 5.15 and 5.16)

Given the opposite sign for the slopes compared to $\delta^{18}O$, the correction applied lowers the raw d_{excess} data by about 1‰ in the deepest part of the ABN1314 ice core, lowering the mean value from 4.4‰ to 4.0‰

The d_{excess} series is relatively constant, with most of the 30-year averaged values between 3‰ and 5‰. One of the most significant excursion at -400 CE coincides with the low accumulation feature identified with both annual layer counting and radar. A lower accumulation

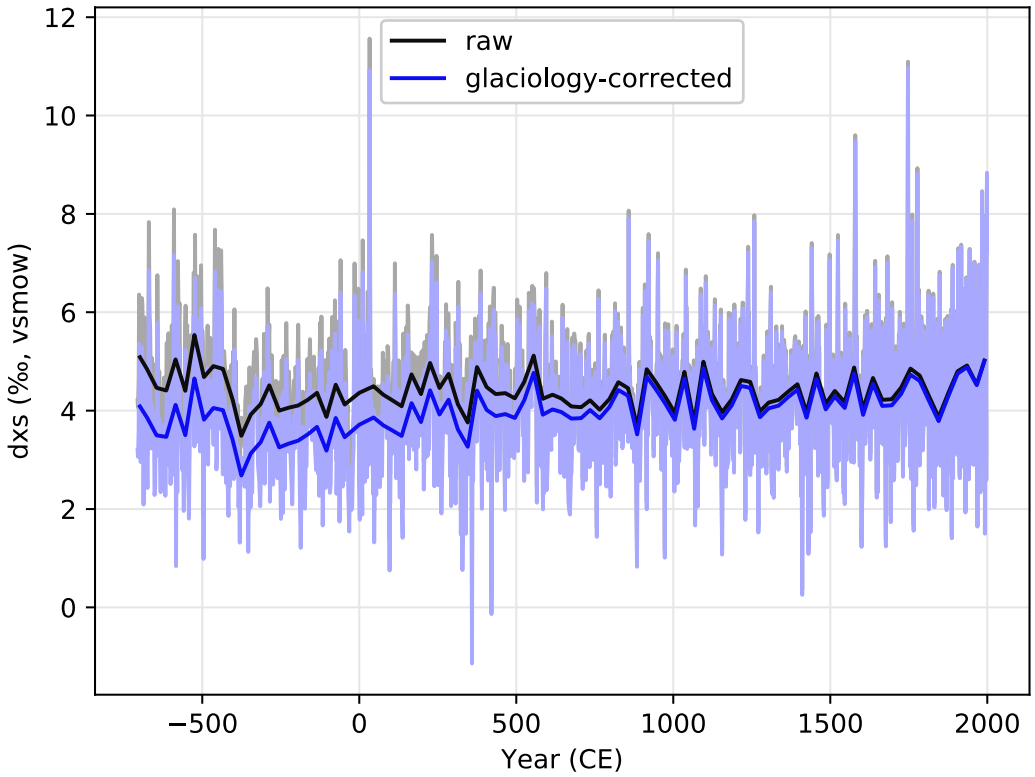

Figure 5.16. Glaciological flow correction of the d_{excess} series

would favor a longer exchange time with the atmosphere and could induce changes in post-deposition processes at this time, and/or a topographic change could cause both the low accumulation and a change in post-deposition processes by altering the surface wind conditions (Casado et al., 2018). Because post-deposition processes were shown to strongly influence the deuterium excess in the snow (Johnsen et al., 2000; Oerter et al., 2004), the observed low-excursion of d_{excess} at -400 CE could result from the changes in the site location and topography, but this hypothesis is difficult to confirm and is not the focus of this work.

5.6.5 ^{17}O-excess

With the development of a protocol of water fluorination to isolate oxygen from the water molecules, the measurement of the least abundant stable oxygen isotope with mass 17 became much simpler (Barkan & Luz, 2005), and can now be used in paleoclimate studies (e.g. Landais et al., 2008). By analogy with the d_{excess}, we define the $^{17}O_{excess}$ as the difference to the meteoric water line, using a logarithmic definition that better fits the measurements:

$$^{17}O_{excess} = \ln(\delta^{17}O + 1) - 0.528 \ln(\delta^{18}O + 1) \quad (5.3)$$

This parameter provides additional information on the moisture origin, as it is not sensitive to temperature changes over the Antarctic continent, unlike d_{excess} (Landais et al., 2008). It is primarily sensitive to changes in the relative humidity of the moisture source.

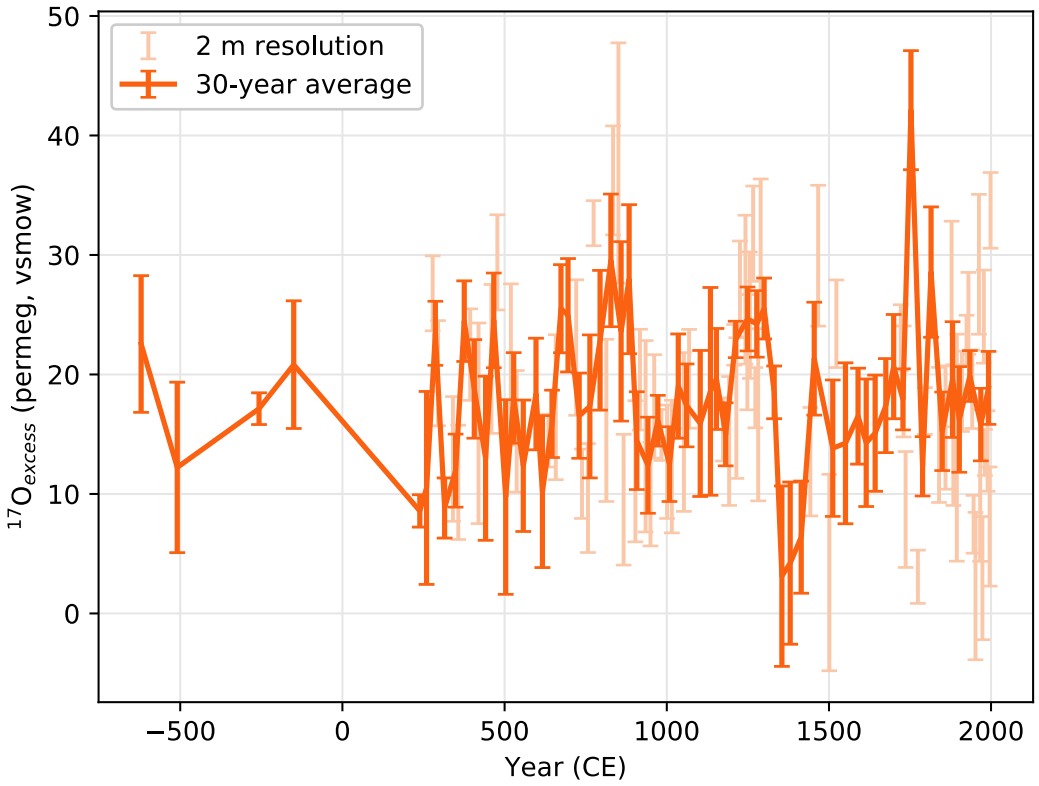

Figure 5.17. Series of $^{17}O_{excess}$ in the ice of the ABN1314 core.

With the help of Frederic Prié and Amaëlle Landais, $^{17}O_{excess}$ was measured on ABN1314. Due to the measurements of $^{17}O_{excess}$ requiring heavier experimental work that is more time consuming compared to other water stable isotope analysis we are not able to measure $^{17}O_{excess}$ at the same sample resolution as other water stable isotopes. Instead, we measured one sample every 2 m. This sample resolution enabled the measurement of 10 samples per day, which also included two melted ice samples from ABN1314 with 4 replicates each, and 2 replicates of a water standard with known isotopic composition. At the beginning of every week a full calibration with fluorination of 3 different water standards with varying isotopic composition was measured with $^{17}O_{excess}$ values around the range expected for ABN. The ABN water isotopic composition and its $^{17}O_{excess}$ values are therefore calibrated weekly, to ensure a high precision record. In total, 104 samples were measured for $^{17}O_{excess}$ with at least 4 replicates each, and the pooled standard deviation on the measurements was 10 permeg (1 permeg = 0.001‰). We averaged the samples over 30 years, to better reflect changes in climate conditions (figure 5.17).

We focused our analytical efforts on the most recent 2000 years, which is the time period that overlaps with the age of atmospheric gases in the ABN1314 core. Indeed, gas trapped in bubbles is usually more recent than ice at the same depth in an ice core by a few hundreds of years (e.g. Bender et al., 2006; ABN gas chronology is given in Chapter 6), and the deepest and oldest gas sample recovered at ABN will be significantly younger than the oldest ice sample. The gases will be used to make a second temperature reconstruction, detailed in the Chapter 6.

Similar to the glaciological corrections that were completed for water stable isotopes, we computed a slope of $^{17}O_{excess}$ – elevation, and found the correlation was not significant (figure 5.18). Only the dataset provided by Pang et al. (2015) includes measurements of $^{17}O_{excess}$ in this region. This dataset and other $^{17}O_{excess}$ – elevation from surface snow (Touzeau et al.

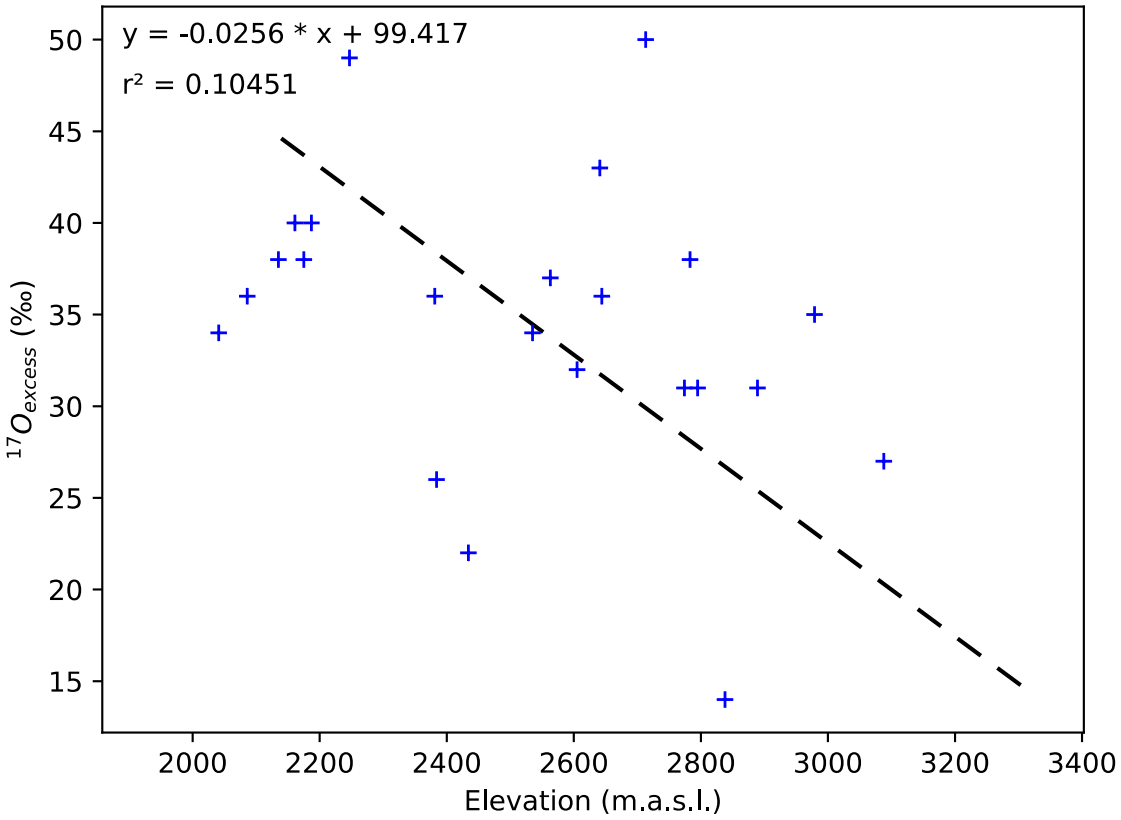

Figure 5.18. Scatter plot of $^{17}O_{excess}$ – elevation in a sub-region of the Zongshan – Dome A traverse (Pang et al., 2015). The slope identified was not significant (P value > 0.10, n =23) and is thus indicated with a dashed line.

2016) showed that there was minimal spatial variation of $^{17}O_{excess}$ in the East Antarctic Plateau. The trend was only evident on the highest elevations of the continent, possibly resulting from stratospheric air masses influence and/or increased post-deposition due to ice-air exchanges in the driest regions. Due to the ABN site being located far from these areas, the $^{17}O_{excess}$ at ABN is not corrected for the elevation at the ice origin.

Due to the origin of the ice at ABN likely originating from upstream, caution with the water isotope record should be noted, especially the second-order parameters such as d_{excess} and $^{17}O_{excess}$, as they likely reflect changes unrelated to climate condition as the site experienced different topography over time.

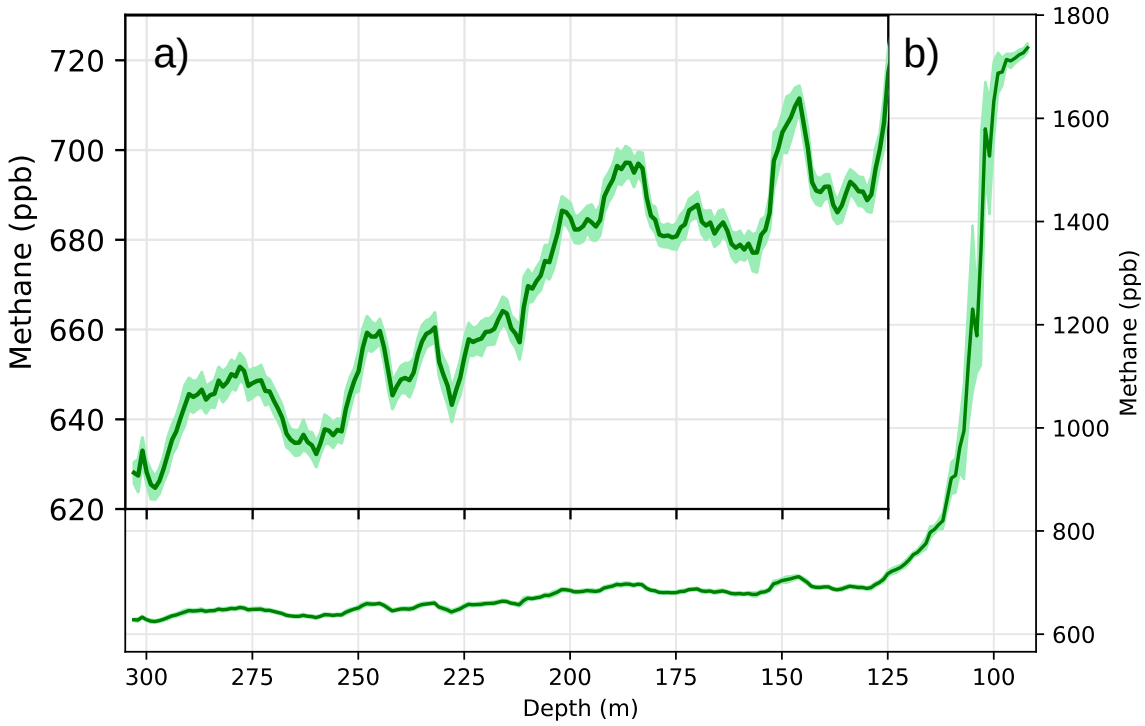

Figure 5.19. Methane record in the ABN1314 core. For clarity, the 305 to 125 m section is duplicated and shown on with different methane ranges. For **(a)** a 620 to 730 ppb range, and **(b)** a 580 to 1800 ppb range. The x-axis is shared.

5.7 Gas concentrations

Polar ice forms from porous snow that is compacted over time, and gas bubbles become trapped in the ice (see Chapter 2). Ice cores thus constitute an excellent archive that captures and preserves past atmospheric gas composition. Genthon et al. (1987) established a link between atmospheric carbon dioxide (CO_2) and climate cycles at the glacial-interglacial time scales, supporting the greenhouse feedback of atmospheric gases on global surface temperature. Other greenhouse gases, such as methane (CH_4), have been used to synchronize different ice core records (Buizert et al., 2015), due to the rapid mixing time of gases in the atmosphere, where there is a mixing time of less than a year.

The CH_4 content of gases trapped in ABN1314 were measured by Xavier Fain and Jerôme Chappelaz on the Desert Research Institute (Reno, Nevada) CFA system that was modified for gas measurement (Rhodes et al., 2013). The CH_4 record is shown on figure 5.19 against depth, as the gas age significantly differs from the ice age because the gases are trapped at the bottom of a diffusive column in the snow, where ice is older (Buizert et al., 2012). We determine precisely the gas-age in the Chapter 6, which details the gas isotope measurements we performed at LSCE.

The methane record at ABN shows variations of about 50 ppb, similar to other ice core records (Blunier et al., 1993). Above 125 m depth, there is a large increase in methane that was released in the atmosphere with industrial activities from the 19th century (Craig & Chou, 1982). We observe changes in the methane at ABN, which will be used in the next chapter to synchronize the gas record with the published age scale of WD2014 (Sigl et al., 2016).

5.8 Conclusion

In collaboration with the ABN project members, we measured various properties and proxies in the ice core, allowing us to date the ice, correct it for ice flow, and establish a temperature history from the water stable isotopes. However, we have seen in previous chapters that temperature reconstructions from $\delta^{18}O$ may be biased toward warm synoptic events. We also know that gases were preserved in the bubbles trapped in the ice, which isotopic composition may be used as another temperature proxy (Severinghaus et al., 2003, Chapter 2). Therefore, in the next Chapter, we will characterize the gases isotopic composition in the Aurora Basin North ice core to build a second temperature record, independent from the water stable isotopes.

Chapter 6

Reconstruction of temperature from $\delta^{40}Ar$, $\delta^{15}N$, and borehole temperature

While most of the Antarctic temperature reconstruction rely on water stable isotopes, a growing number of studies have shown the limits of using a proxy dependent on precipitation (Casado et al., 2020; Servettaz et al., 2020) that can be moved and mixed after deposition of snow (e. g. Nishimura & Nemoto, 2005), and which keeps exchanging with the atmosphere for an extended amount of time (Casado et al., 2018; Johnsen et al., 2000). Here we detail the reconstruction of temperature of the past 2000 years using the isotopes of inert gases argon and nitrogen, as well as borehole temperature measurements. The specific methods and calibration used in this study were adapted from the literature and will be detailed here, unlike the established methods that were generally described in chapter 2. We achieve high analytical precision thanks to cautious processing of gases and correction of isotope ratios measured with the mass spectrometer. We determine the temperature gradient in the firn with the two isotope ratios. We then use a heat diffusion model in the firn, and use an inverse method to reconstruct a temperature history that matches both the temperature gradients from gases isotopes and measurements of temperature in the borehole.

6.1 Measurement of $\delta^{15}N$ and $\delta^{40}Ar$ from air trapped in ice

To reconstruct temperature from stable isotopes of inert gases, we must extract the air from the ice and remove gases that could interfere with our measurements in the mass spectrometer. The ice extraction, measurements and corrections were presented by Severinghaus et al. (2003), and the method was improved for argon and nitrogen specifically by Kobashi et al. (2008). We describe hereafter how we processed samples from firn air and air trapped

in ice bubbles, and how we achieved the precision needed for temperature reconstructions. We introduced a new correction to account for the varying focus of the mass spectrometer, which was found to drift over weeks of measurements.

6.1.1 Wet extraction of Nitrogen and Argon gases

To analyze the inert gases contained in the ice bubbles, we must extract it. We process the extracted air to remove water vapor (H_2O), carbon dioxide (CO_2) and dioxygen (O_2), which could later interfere with the masses we want to measure. For example, dioxygen can react with steel tubing to create CO_2, which can be broken into carbon monoxide (CO) during the ionization in the mass spectrometer source, with molecular masses 28 ($^{12}C^{16}O$) and 29 ($^{13}C^{16}O$), same as dinitrogen (N_2) but in different proportions.

6.1.1.1 Ice preparation

Analysis of N_2 and Ar of air trapped in ice cores require a volume of ice of about 80 ml (~70 g). The samples of ice at our disposal were a quarter section of a 9 cm diameter core, of 20 cm length, for a volume of 300 ml. We inspect the ice for possible cracks, where gas could have diffused, which would alter the air composition in the bubble.

Argon is a small molecule that can go through thin layers of ice, especially because the ice was compressed and bubbles have a higher pressure than atmosphere. This is known to cause Argon gas loss in the freeze storage of ice cores (Kobashi et al. 2008), and is associated with a fractionation of Argon isotopes. Therefore, we shave off 3 to 5 mm of the outer layer of the ice bar. We split the remaining of ice in two ~70 g replicates, by cutting along the depth. We weight the ice of each replicate to be able to quantify the total air content later on. We then cut the ice bars into smaller parts that fit in sample vessels. We also insert glass-coated magnetic stir bars into the vessels.

6.1.1.2 Line preparation

We use an extraction line that is built around an oven that will remove O_2 from the air. It consists of three sample vessel mounts, a water trap bathing in a dewar filled with -100°C ethanol, a CO_2 trap bathing in a dewar filled with liquid nitrogen, a tubular ceramic oven filled with copper wool, a third trap also bathing in a dewar filled with liquid nitrogen, and a steel collector tube of 10 ml bathing in liquid helium. We control the opening of different circuits with manual (Swagelok) stainless steel bellows sealed valves, and keep track of the pressure in the line with a 10 mbar Baratron gauge and another 1 mbar Baratron gauge. The valve n°10 serves as a flux controller, because it can be opened gradually to limit gas flow. We use a fore-vacuum pump and a high-vacuum pump are to clean up the line.

We evacuate the line and three 10 ml steel collector tubes for at least 10 minutes on the high-vacuum pump, and make sure the pressure goes to 0 on the 1 mbar Baratron gauge, with a precision of 10^{-4} mbar. When the tubes and the line are clean, we take the ice-containing vessels out of the freezer and connect them to the line with a copper gasket. While a vessel is being connected, we keep the ice frozen by bathing the vessel in a dewar filled with -20°C

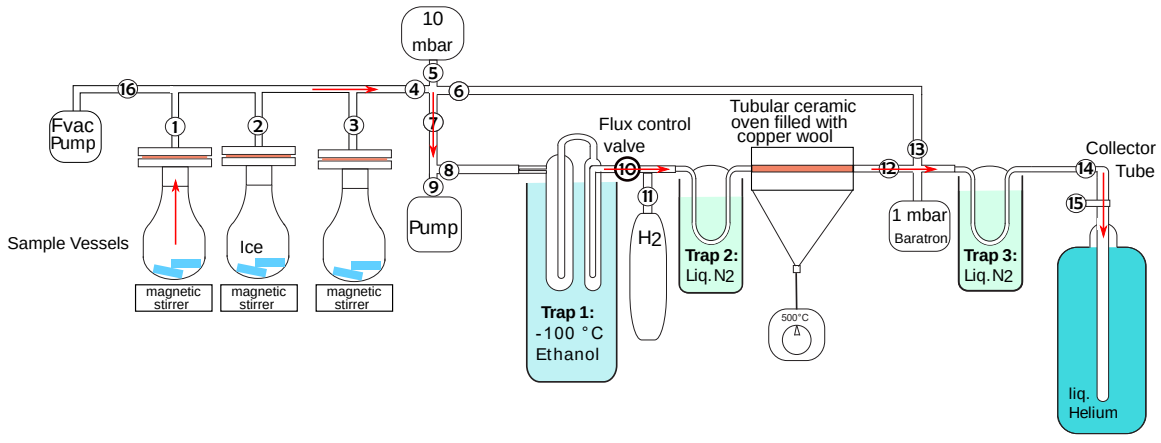

Figure 6.1. Schematic of the extraction line. The red arrows indicate the path of gas through the line.

ethanol. We then evacuate the air in the vessel, keeping the ice frozen. We make sure there is no leak in the vessel connections by closing the pump and checking if pressure plateaus at vapor pressure over ice, and the resume pumping for a total of 30 min. Vapor sublimating from the ice helps flushing the room air out of the vessel. We avoid using ethanol colder than -30°C because sublimation would be too slow.

6.1.1.3 Ice melt, oxygen removal, and transfer

After the 30 min evacuation, the vessels are isolated from the line by closing each sample valve, and left to warm up at room temperature for 1 hour. The ice melts and the content of bubbles is released into the sealed vessel. Meanwhile, we cool the steel collector tube with liquid nitrogen, insert it into the helium tank, connect it to the line, and evacuate the line to flush the air introduced and the residual water vapor. Additionally, we start heating the oven at 500°C, as the copper wool can outgas when it is brought up to temperature. We also prepare a -100°C ethanol dewar by cooling ethanol with liquid nitrogen.

When the ice is melted, we start stirring the water to help degassing, with a glass-coated magnetic stir bar. With the traps and dewars prepared, we close all valves to the pumps and we open the sample vessel valve and the collector tube valve, with the flux control valve still closed. We open the flux control valve very slowly to read a pressure lower than 0.5 mbar on the pressure gauge after the oven. Opening too fast would result in a flow too strong and insufficient reaction time with copper in the oven tube. The gases condensate in the collector tube cooled at 4 K in the helium tank. Therefore, the gases passively go through the line from the high pressure in the sample vessel to the low pressure in the collector tube. When the gases go through the oven, O_2 is adsorbed on the copper wool. The water vapor acts as a carrier gas for the first part of the line, up until the first trap at -100°C. During the transfer, we refill traps very regularly. We transfer gases for 45 min, until we read a pressure lower

than $5 \cdot 10^{-4}$ mbar on the gauge after the oven, on the collector tube side. In that case we shut closed the collector tube and the sample vessel. We label the tube and replace it with an empty one in the helium tank. We evacuate the line for at least 10 min and repeat the transfer process for the other two samples.

After the third sample is transferred, we regenerate the copper wool: we evacuate the line for a few minutes, then close the pumps and let a small amount of H_2 gas in, with the copper wool maintained at 500°C. The H_2 reacts with CuO formed at the surface of the copper wool and CuO is reduced to Cu while the H_2O released is trapped in the cold traps. Therefore, the total pressure of gas in the line diminishes. If it tends to 0 mbar, we put more H_2 gas, while if it reaches a plateau, we consider that the copper wool is regenerated. In the latter case, we slowly flush the H_2. Then, we shut down the oven, evacuate the line and remove cold traps. We heat the collector tubes and let them equilibrate overnight, in a horizontal position, so that the gas in the tube is homogeneously mixed by diffusion. By doing so, we try to avoid possible fraction of gases that would sublimate first and reach the top of the tube faster. Diffusion within the tube is expected to be quite slow, as the section in the tube is lower than 5 mm.

6.1.2 Preparation of Air samples from free Atmosphere and firn

6.1.2.1 Air standards

One day per week, we process three replicates of air standard. The air is collected on the roof of the LSCE building in Gif-sur-Yvette, France. We pump air through a water trap into a glass bottle with an inlet (on pump side) and an outlet (releasing the extra air in the atmosphere) for 5 minutes, and then close the bottle at both ends. The bottle is connected to the line as shown on figure 6.2. We take an aliquot of about 10 ml, and transfer it to the collector

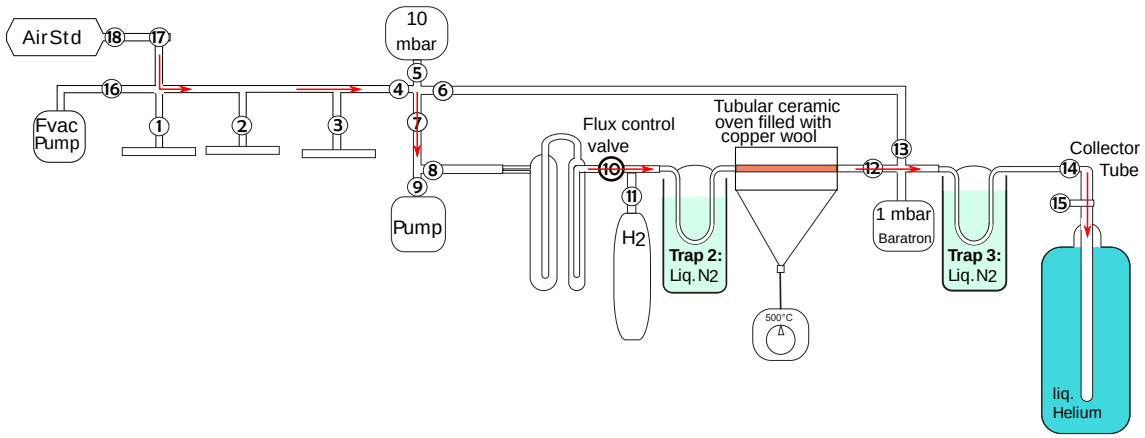

Figure 6.2. Schematic of the transfer line in air configuration. The red arrows indicate the path of gas through the line. Because the air was dried at collection, we keep the same trap 1 to conserve the line geometry but do not put a cold dewar.

tube through the line, same as described in section 1.3, except that we do not use a water trap on the line. The air standard bottle contains enough gas for about 100 aliquots. We do not observe fractionation of gases from the air standard bottle after taking multiple aliquots (figure 6.3). We verified the composition of the bottle of air standard by taking a new bottle, which had a very similar composition. Noise in the measurement is probably caused by small fractionations during the transfer.

6.1.2.2 Firn air samples

Air in the diffusive column was sampled on site with firn air sampling device in a dedicated drill hole. First, a section of ice core is drilled, and as the borehole gets progressively deeper, the drilling is stopped to sample the firn air at the bottom of the hole. The firn air sampling device is designed to fill the borehole with a bladder that is inflated to seal the borehole, to prevent contamination from the air above, while air is pumped from below into a flask. The flask is flushed with sampled air by letting the gas flow through. When the sample at the current depth is acquired, we remove the firn air sampling device and resume ice

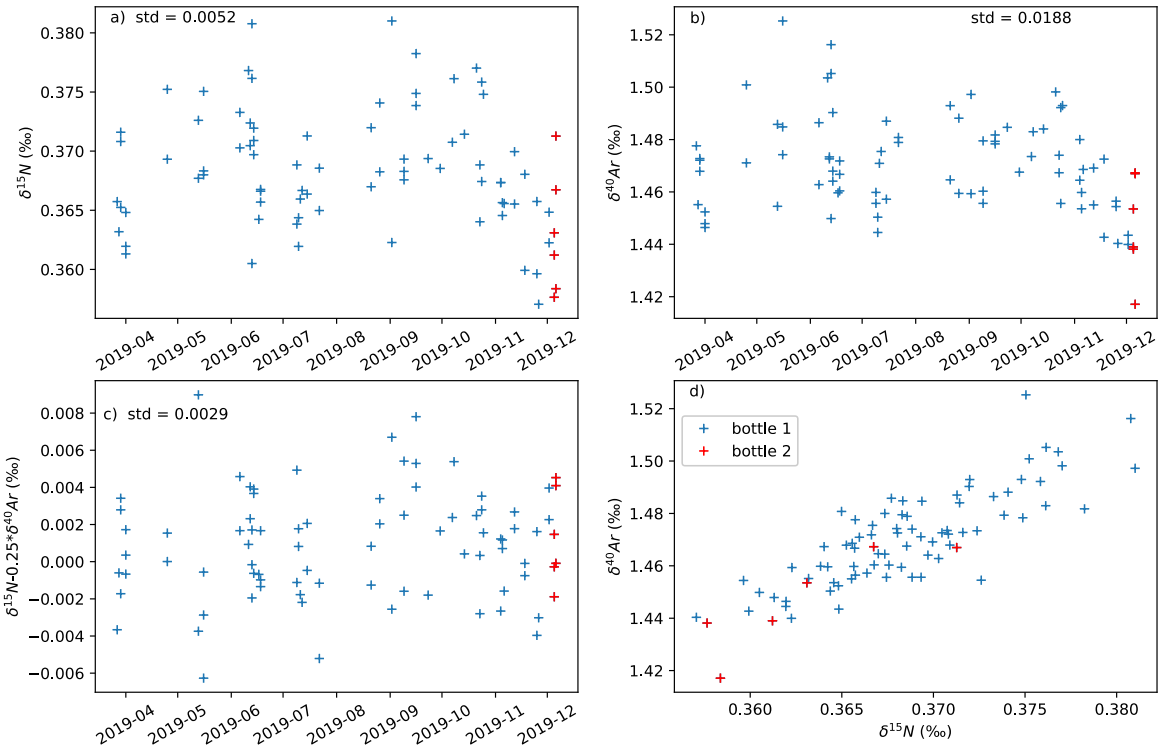

Figure 6.3. Stability in time of the composition of Air Standards normalized to the working standard, after pressure imbalance, chemical and drift corrections. The corrections are described in the section 6.1.3.

drilling to reach a greater depth. The analysis of firn air is useful to better understand the signal in gas isotopes, that will be trapped in bubbles in ice. A small aliquot of gas of about 5 mL was taken from each flask and processed in the line with the same method as for air standard.

6.1.3 Mass Spectrometry

6.1.3.1 Description of the mass spectrometer

Measurements of gas isotopes were performed on a dual inlet Thermo Fischer Scientific^{TM} 253 Plus. This mass spectrometer is equipped with a dual inlet system that allows for alternative introduction of working standard and sample (figure 6.4), with computer-controlled valves. There are two bellows connected to a switch through capillary tubes, and the

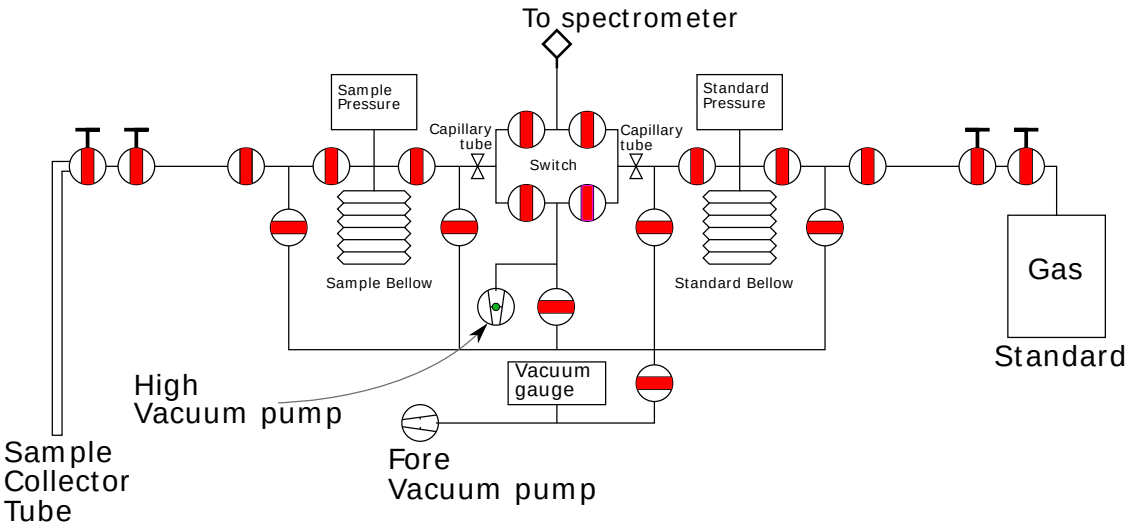

Figure 6.4. Schematic of the dual inlet system

switch lets one gas flow to the ionizer source while the other gas is kept flowing by a high vacuum pump. In a regular measurement, the switch will alternate to let by turn the sample or the standard flow in the source. The gas is ionized by a cathode filament at a 10 kV, then ions are accelerated in the electric field. The ion beam is focused in a series of lenses and then separated by the magnet in the curved part before counting in the faraday cups. Heavier ions have a trajectory with a lower curvature due to their greater inertia.

The collectors of the 253 Plus at LSCE consists of 10 cups with resistors ranging from 1×10^{11} to 1×10^{13} Ohm. It was configured to be able to measure isotopes of N_2, O_2, Ar, Kr and Xe, depending on the magnet intensity. In its Ar configuration, the spectrometer uses three Faraday cups dedicated to simultaneous collection of ^{36}Ar, ^{38}Ar, and ^{40}Ar isotopes, as well as two cups between ^{40}Ar and ^{36}Ar to monitor beam dispersion. Despite the cup dedicated to collection of ^{38}Ar beam, insufficient separation of beams causes the tail of ^{40}Ar beam to leak significantly into the ^{38}Ar cup. The shape and intensity of this tail varied through time and could not be corrected for, therefore we will not consider ^{38}Ar here. We will focus on

^{40}Ar and ^{36}Ar, which are major isotopes so they are easier to measure, and the mass difference is larger so any mass-dependent fractionation processes have a stronger signal. Under a different magnet configuration, the mass spectrometer can collect $^{28}N_2$ and $^{29}N_2$ simultaneously.

6.1.3.2 Introduction of gases

Before introducing sample and standard in their respective bellows, we connect sample tube and standard bottle with ultratorr fittings, and evacuate the lines and the bellows for at least 10 minutes. We prepare an aliquot of standard while the line is cleaning, so the aliquot volume and the standard bottle are open for about 10 minutes. Then we let the sample and standard gases flow into fully open bellows, with an equilibration time of 3 min during which the valves remain open between the tube and the bellow. We take note of the pressure on the sample side, which is used to quantify the amount of gas extracted from the ice. We then close the bellows and adjust the volume to increase the pressure closer to the injection level, in order to ease the automatic adjustment of the bellows.

6.1.3.3 Measurement

6.1.3.3.1 Integration of $\delta^{15}N$ and $\delta^{40}Ar$

A typical measurement block starts with peak centering, during which the electric field is adjusted to position the beam in the center of the Faraday cup, followed by background measurement and bellow adjustment. Next, the gas is introduced into the source from the bellow of standard for 10 s of stabilization and 16 s integration. Then, the inlet switches to sample bellow for 10 s of stabilization and 16 s integration. The standard – sample cycle is repeated 10 times and ends with a last standard integration. The mass spectrometer computes

raw delta values with the sample integration (*i*) and average of previous and following standard integrations (*i*–1, *i*+1, equation 6.1), of which it removes the background. A block takes about 20 min to complete.

$$\delta^{15}\mathrm{N_i} = \left(\frac{\left(\frac{^{15}\mathrm{N}^{14}\mathrm{N}}{^{14}\mathrm{N}^{14}\mathrm{N}}\right)_{\mathrm{sample\ i}}}{\left(\frac{0.5 \times {}^{15}\mathrm{N}^{14}\mathrm{N}_{\mathrm{standard_{i-1}}} + 0.5 \times {}^{15}\mathrm{N}^{14}\mathrm{N}_{\mathrm{standard_{i+1}}}}{0.5 \times {}^{14}\mathrm{N}^{14}\mathrm{N}_{\mathrm{standard_{i-1}}} + 0.5 \times {}^{14}\mathrm{N}^{14}\mathrm{N}_{\mathrm{standard_{i+1}}}}\right)} - 1 \right) \times 1000 \qquad (6.1)$$

We compute δ^{40}Ar similarly (equation 6.2).

$$\delta^{40}\mathrm{Ar_i} = \left(\frac{\left(\frac{^{40}\mathrm{Ar}}{^{36}\mathrm{Ar}}\right)_{\mathrm{sample\ i}}}{\left(\frac{0.5 \times {}^{40}\mathrm{Ar}_{\mathrm{standard_{i-1}}} + 0.5 \times {}^{40}\mathrm{Ar}_{\mathrm{standard_{i+1}}}}{0.5 \times {}^{36}\mathrm{Ar}_{\mathrm{standard_{i-1}}} + 0.5 \times {}^{36}\mathrm{Ar}_{\mathrm{standard_{i+1}}}}\right)} - 1 \right) \times 1000 \qquad (6.2)$$

In addition, we define $^{15}\mathrm{N_{excess}}$ as the non-gravitational fractionation of nitrogen (equation 6.3)

$$^{15}\mathrm{N_{excess}} = \delta^{15}\mathrm{N} - \frac{1}{4}\delta^{40}\mathrm{Ar} \qquad (6.3)$$

All delta values are given in permil (‰) relative to a standard: either the working standard when describing the raw measurements, or the international standard after normalization to atmosphere (from section 6.1.3.4 on).

6.1.3.3.2 Determination of elemental ratios with peak jumping

The measurement of elemental ratios ($^{36}\mathrm{Ar}/^{28}\mathrm{N_2}$, $^{84}\mathrm{Kr}/^{36}\mathrm{Ar}$ and $^{32}\mathrm{O_2}/^{36}\mathrm{Ar}$) requires a specific measurement with a change in magnet parameters to be able to measure the two different elements. For $\mathrm{Ar}/\mathrm{N_2}$ ratio for example, after peak a first centering, the spectrometer counts Ar in the sample and in the standard. Then the magnetic field is decreased to measure $\mathrm{N_2}$. After changing the magnet parameters, another peak centering is done, and the spectrometer counts the new element in sample and standard. During a block, the spectrometer measures

each element four times. Because the peak jumping and magnet change take a significant amount of time, the decrease in intensity due to the pressure decreasing over time is accounted for when computing the $\delta Ar/N_2$: the sample and standard counts are time-interpolated and the elemental ratio is computed with values at equivalent time.

6.1.3.3.3 Description of a full sequence

We repeat integration blocks for each element, in order to obtain a pooled standard deviation (PSTD) lower than 4 permeg per mass unit on both $\delta^{15}N$ and $\delta^{40}Ar$. Preliminary tests revealed that five blocks are necessary to have a PSTD lower than 16 permeg for $\delta^{40}Ar$, and three blocks to have a PSTD lower than 4 permeg for $\delta^{15}N$. Additionally, we measure elemental ratios of $^{36}Ar/^{28}N_2$, $^{84}Kr/^{36}Ar$ and $^{32}O_2/^{36}Ar$. We measure O_2/Ar ratio to verify that most of oxygen was successfully removed from the sample. Consequently, the typical sequence consists of 5 blocks of argon, 3 blocks of nitrogen, 1 peak jumping for Kr/Ar ratio, 1 peak jumping for Ar/N_2 ratio, and 1 peak jumping for O_2/Ar ratio. The full sequence takes 4 hours to complete, so we can measure a maximum of three samples in a day.

During the night, additional measurements were performed routinely to help calibrate the data: we measured the dependency of δ values versus pressure imbalance in the inlet bellows (figure 6.5). This pressure imbalance dependency will be accounted for and corrected in the next section. Pressure imbalance slopes (PIS) are determined for $\delta^{40}Ar$, $\delta^{15}N$ and $\delta Ar/N_2$. After PIS determination, the sequence resumes to measure 5 argon blocks, 3 nitrogen blocks and Ar/N_2 peak jumping until bellows run out of gas.

$$1\ \text{sequence}\begin{cases}5\ \text{argon blocks} = 5 \times \begin{cases}11\ \text{standard integrations}\\ 10\ \text{sample integrations}\end{cases}\\ 3\ \text{nitrogen blocks}\\ Ar/N_2\ \text{Peak Jumping}\\ Kr/Ar\ \text{Peak Jumping}\\ Ar/O_2\ \text{Peak Jumping}\end{cases}$$

6.1.4 Data calibration and correction

In order to achieve a better precision, we can quantify and correct several processes that induce a change in the measured isotopic ratios. We calculate the pooled standard deviation with the ice replicates (as prepared in 6.1.1.1), consequently it will include not only the analytical uncertainties but also the uncertainty due to air extraction and transfer.

6.1.4.1 Pressure imbalance correction

The dual-inlet implies that two bellows alternatively supply gas to the source, but there might be a difference in the pressure of each bellow, causing a change in the measured δ values. To account for this effect, we use the daily measurements of Pressure Imbalance Slopes (PIS), where the volume in the bellows is forced into asymmetrical state to evaluate the effect on isotope ratios (for example figure 6.5). The pressure imbalance (ΔP) is defined by the difference of intensity (*int*) between sample and standard of the main gas measured ($^{28}N_2$ in nitrogen configuration or ^{40}Ar in argon configuration).

$$\mathrm{PIS}_{^{40}\mathrm{Ar}} = \frac{\Delta\delta^{40}\mathrm{Ar}}{\Delta\mathrm{P}} \tag{6.4}$$

We can then correct the $\delta^{40}Ar$ isotope ratios using the slope and an imbalance measured as the, as shown in equation (6.5).

$$\delta^{40}\mathrm{Ar}_{\mathrm{PI\ corrected}} = \delta^{40}\mathrm{Ar}_{\mathrm{raw}} - \mathrm{PIS}_{^{40}\mathrm{Ar}} \times \Delta\mathrm{P} \tag{6.5}$$

Equivalent slopes and corrections were performed for $\delta^{15}N$. For all pressure imbalance calculations, the intensities are averaged on the entire block for standards (11 integrations) and samples (10 integrations). Pressure imbalance correction is applied block by block, and the standard deviation of 5 blocks of argon in a sequence typically decreases from 0.020‰ to 0.015‰ (0.005% improvement). The pressure imbalance corrected values are compared to raw values in figure 6.6. Note that the Pooled Standard Deviation in the figure is given for

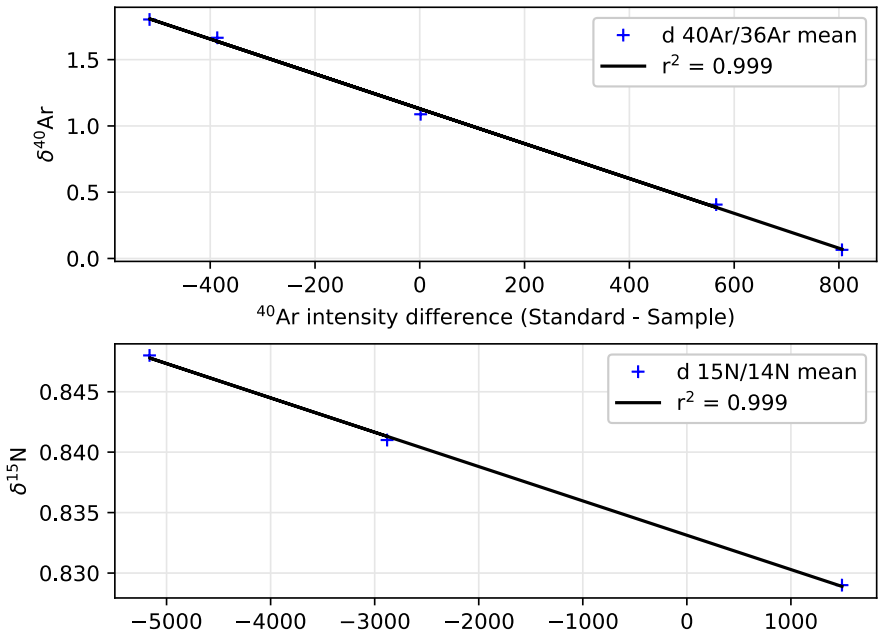

Figure 6.5. Variability of $\delta^{40}Ar$ and $\delta^{15}N$ as a function of intensity difference between sample and standard, resulting from Pressure Imbalance (PI).

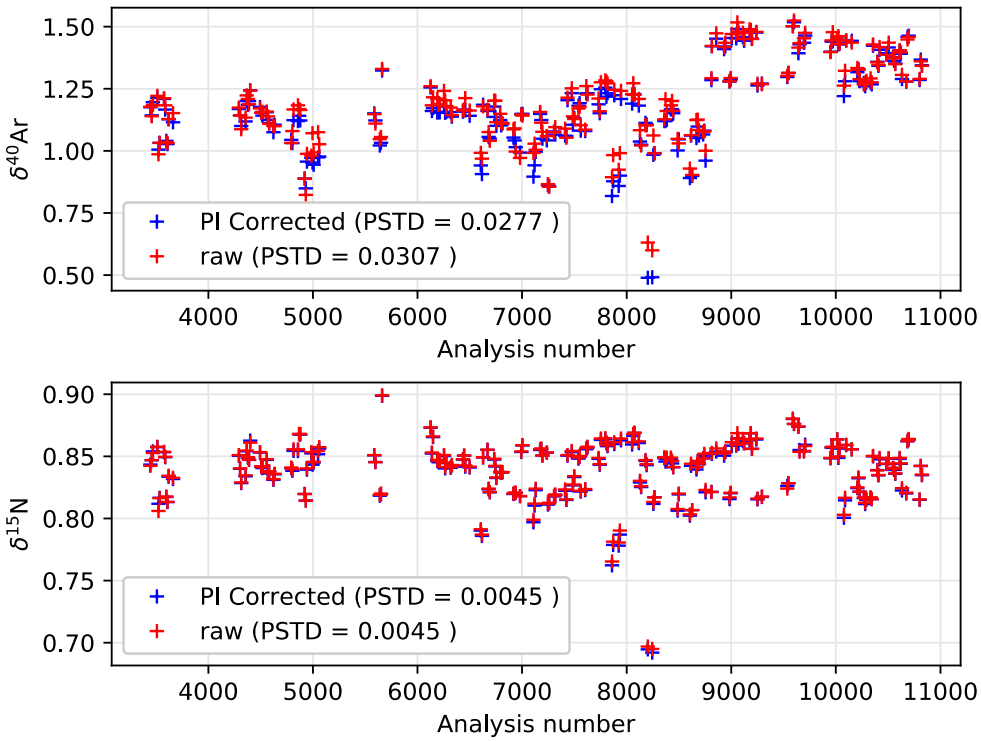

Figure 6.6. Comparison of $\delta^{40}Ar$ and $\delta^{15}N$ before and after pressure imbalance correction for all the measurements. Analysis number corresponds to the number of blocks proceeded, measurements were performed between February and December of 2019.

ice replicates, so it is higher than the standard deviation of block-averaged δ values within a sequence.

6.1.4.2 Chemical Slope correction

The gas supplied to the spectrometer and ionized by the filament is a mixture of argon (about 1%) in nitrogen (about 99%) with very few other gases. The elemental ratio of argon to nitrogen can modify how effectively the argon will be ionized, because of charge transfer in the source. Therefore, the $\delta^{40}Ar$ measured by the spectrometer depends on the relative quantity of argon. This effect is quantified by preparing collector tubes of pure nitrogen with varying amount of standard argon of known isotopic composition. We determine the ratio of Ar/N_2 with peak jumping, and measure the $\delta^{40}Ar$ over 5 blocks for each mixture. The slope is defined in equation 6.6, and illustrated by figure 6.7.

$$CS_{^{40}Ar} = \frac{\Delta\delta^{40}Ar_{\text{PI corrected}}}{\Delta\delta Ar/N_2} \tag{6.6}$$

We apply the chemical slope correction on the $\delta^{40}Ar$ values averaged on a full sequence, because the elemental mixture does not change within a sample.

$$\delta^{40}Ar_{\text{CS corrected}} = \delta^{40}Ar_{\text{PI corrected}} - CS_{^{40}Ar} \times \delta Ar/N_2 \tag{6.7}$$

The chemical slope was measured after each change in the filament and if the filament was put in contact with air, as it may cause change in the ionization rate and therefore the chemical slope. Consequently, we only have three chemical slope measurements for 8 months: at the beginning, in the middle and at the end. This correction results in a minor improvement, as shown in figure 6.8.

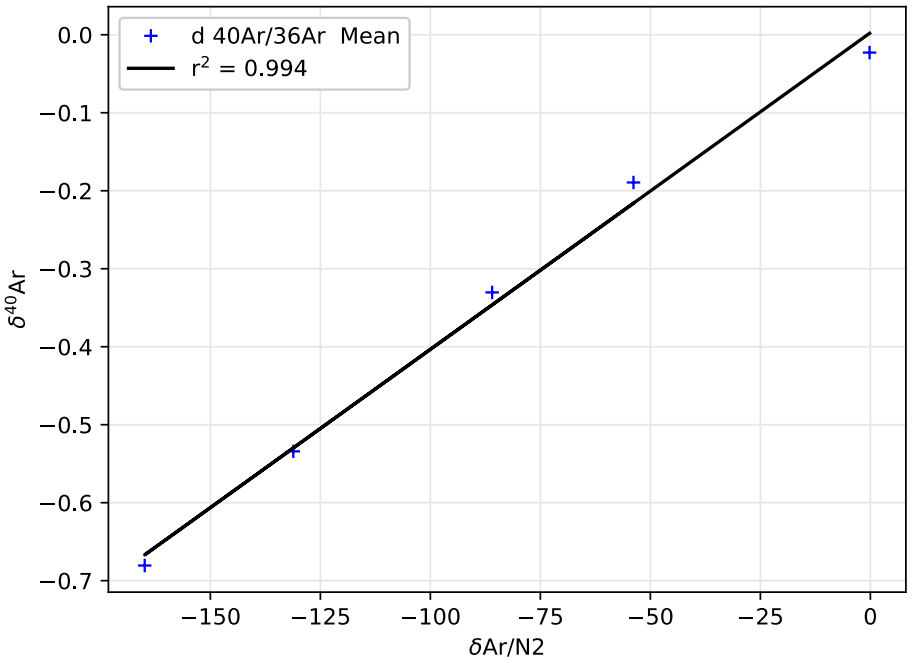

Figure 6.7. Chemical Slope: variability of $\delta^{40}Ar$ versus $\delta Ar/N_2$. Larger concentration of Ar in the gas mixture introduced into the spectrometer tend to increase the $\delta^{40}Ar$ values measured.

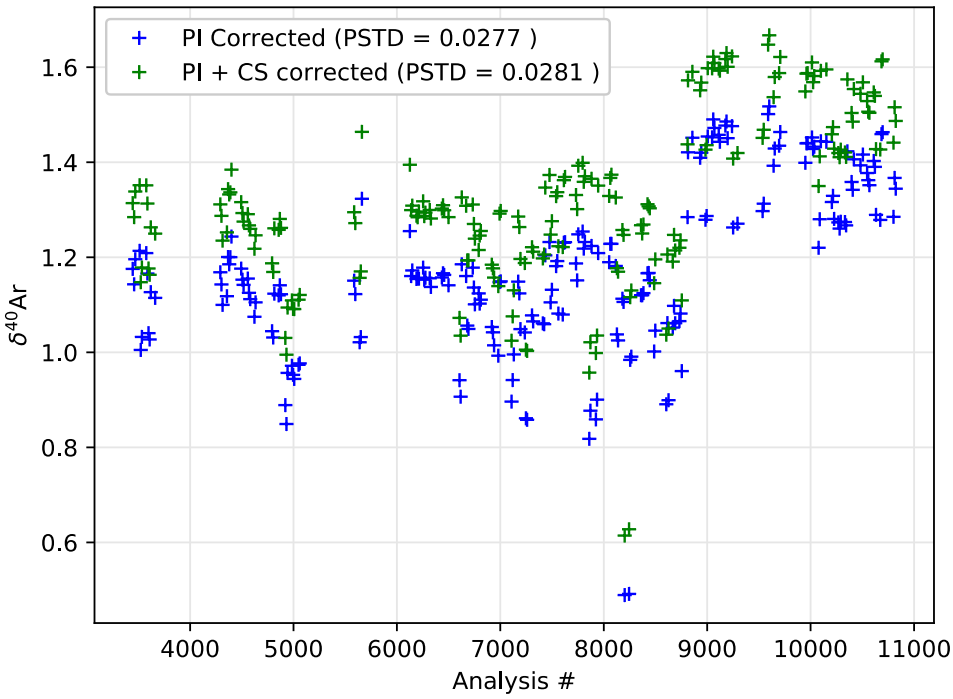

Figure 6.8. Correction of the chemical slope effect on $\delta^{40}Ar$. Because the gas trapped in ice is generally argon-depleted compared to atmosphere, the chemical slope corrected values (green) are greater than non-corrected values (blue).

6.1.4.3 Drift correction

In addition to previously published correction, we found that the spectrometer focus was changing through time, causing a strong variability of δ^{40}Ar and PIS. This is illustrated by strong drifts around analysis 5000, or 7200, and could not be easily resolved because it only appeared after weeks of measurements. This was temporarily fixed with regular autofocus, but we needed a thorough recalibration of the focus parameters to make it more stable (from the analysis number 8800). Fortunately, the focus drift was proportionally shifting the PIS and the δ^{40}Ar, and did not affect δ^{15}N values, probably because nitrogen is very abundant. To minimize our error, we removed the gravitational fractionation of δ^{40}Ar using the δ^{15}N, so the drift effect on δ^{40}Ar could be quantified against the PIS_{40Ar} as shown in figure 6.9. We define a drift slope as the non-gravitational fractionation of Ar versus the PIS_{40Ar} in equation 6.8.

$$\text{Drift}_{^{40}\text{Ar}} = \frac{\Delta(\delta^{40}\text{Ar}_{\text{CS corrected}} - 4 \cdot \delta^{15}\text{N}_{\text{PI corrected}})}{\Delta\text{PIS}_{^{40}\text{Ar}}} \quad (6.8)$$

Using the drift slope, we correct our values (equation 6.9).

$$\delta^{40}\text{Ar}_{\text{drift corrected}} = \delta^{40}\text{Ar}_{\text{CS corrected}} - \text{Drift}_{^{40}\text{Ar}} \times \text{PIS}_{^{40}\text{Ar}} \quad (6.9)$$

This resulted in a significant improvement of pooled standard deviation of δ^{40}Ar in replicates that dropped from 0.028‰ to 0.013‰ (figure 6.10). The large shift in the absolute values induced by the drift correction is not impacting the measurements, which are given relative to a working standard. The final value needs to be given relative to an international standard where the measured delta values will get their final value. This step is described in the next section. The present improvement can be seen in the continuity of the measurements: for example, the step increase around analysis number 8800, which was caused by a change of focus parameters, is corrected with this process.

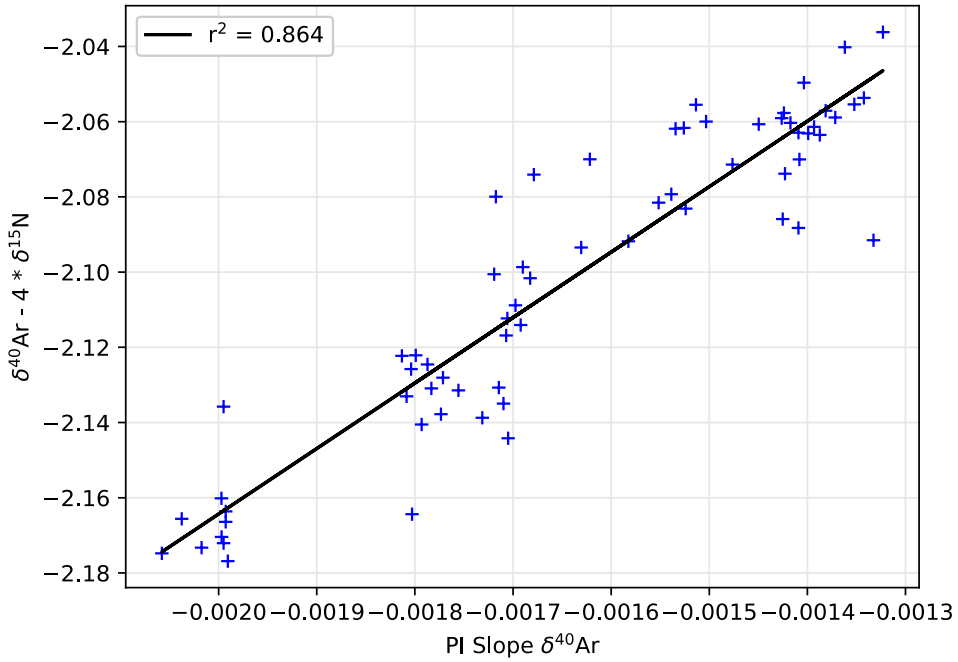

Figure 6.9. Non-gravitational fractionation of argon as a function of the PIS for argon.

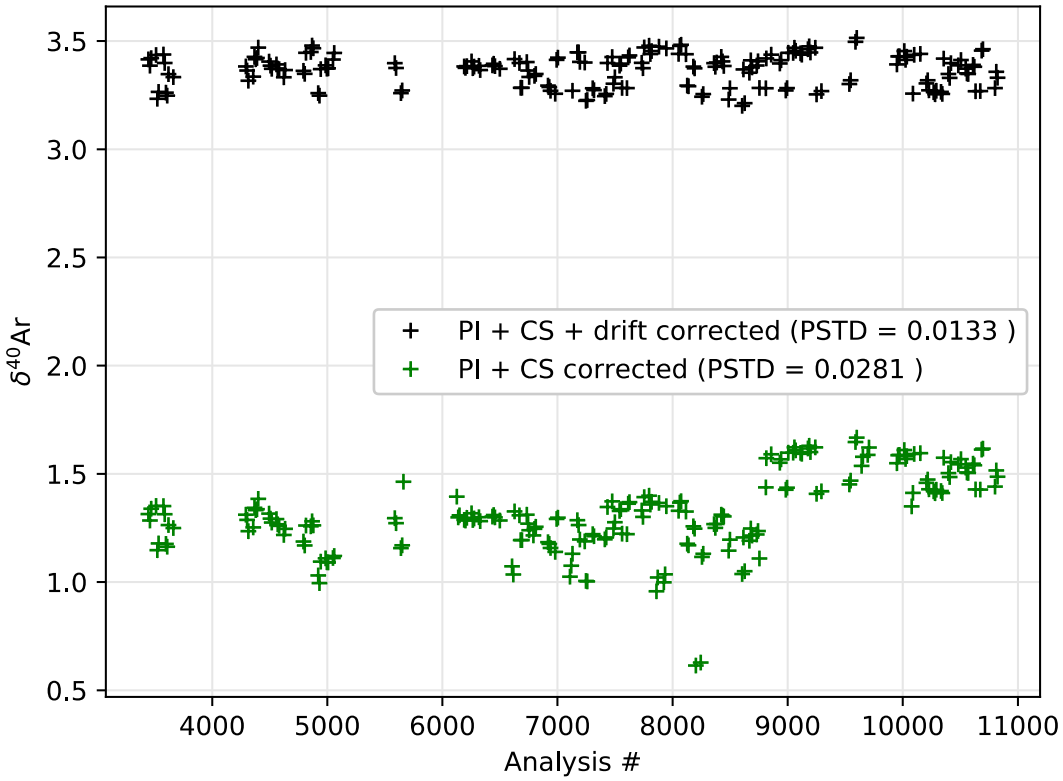

Figure 6.10. Correction of the drift effect on $\delta^{40}Ar$.

6.1.4.4 Normalization to atmosphere

All δ values measured need to be given relative to a standard. For the gases studied here, the standard is the atmospheric air. Every week, two to three Air standards were prepared from the Air bottle with the setting described in section 6.1.1.4. The same corrections are applied to the Air standard, as would be made for an ice sample. In total, 83 Air standards were measured. The standard deviation of Air standard after all correction is 0.0052‰ for $\delta^{15}N$, 0.0188‰ for $\delta^{40}Ar$, and 0.0029‰ for $^{15}N_{excess}$. We use weekly averages of two to three measurements of $\delta^{15}N$ and $\delta^{40}Ar$ in atmospheric air to normalize the measurements of the corresponding week. By doing this correction weekly, we further correct any drift that can happen, as it would affect both our gas trapped in ice and atmospheric air standards in the same manner.

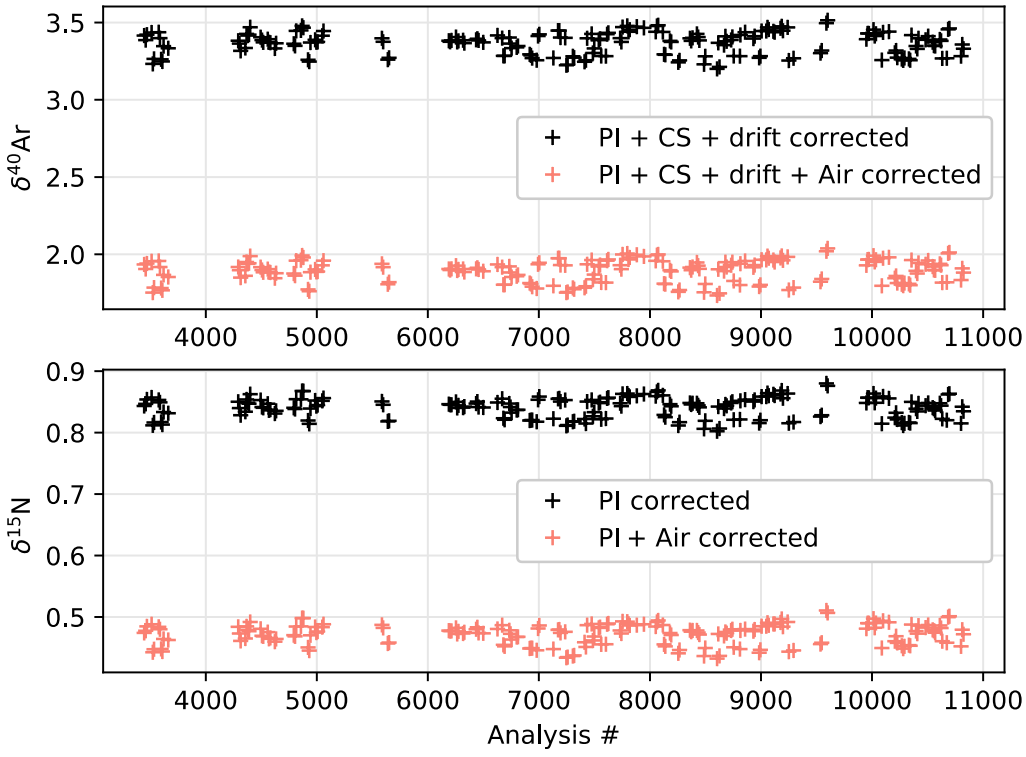

Figure 6.11. Normalization to atmosphere. The values are given in permil versus atmosphere.

Correcting the $\delta^{40}Ar$ and $\delta^{15}N$ of ice samples does not improve the pooled standard deviation, because the two replicates are corrected by the same amount. However, it corrects the absolute value needed for quantification of gravitational and thermal effects (as will be done in section 6.2.1).

6.1.4.5 Argon gas loss

6.1.4.5.1 During storage

Previous studies have shown that storage of ice in the freezer at -20°C for an extended period of time could cause the pressured gas trapped in the ice to escape through ice matrix (Kobashi et al., 2008). The argon molecule is especially small and can more easily be expelled from the bubble, causing argon loss in the ice bubbles. This process is associated with a fractionation. The ice used in this study was rather recent (5 years), and the outer layer was shaven when preparing the ice. Therefore, we do not observe a correlation between Ar depletion and the $\delta^{40}Ar$ of the gas remaining in the bubbles (figure 6.12).

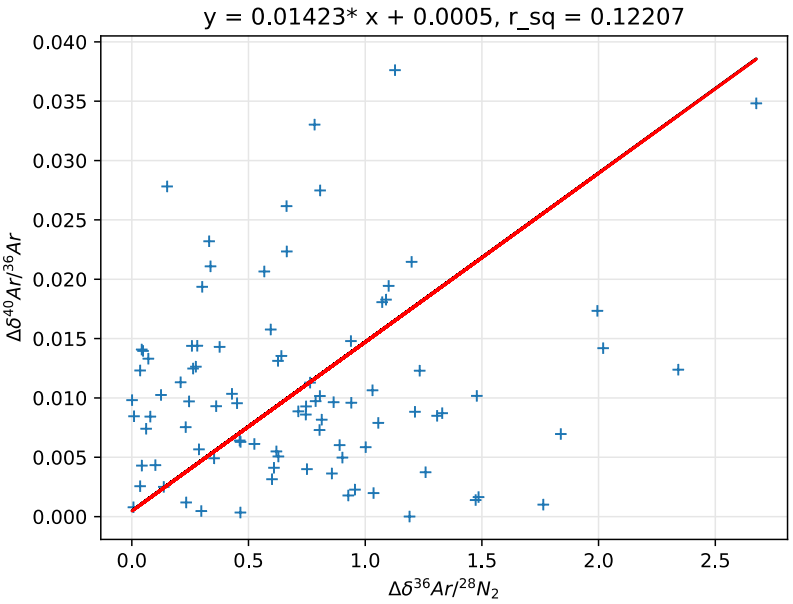

Figure 6.12. Difference of $\delta^{40}Ar$ between ice replicates as a function of the difference in Ar/N_2 ratios. The Δ notation indicates the isotopic difference between two replicates of ice taken at the same depth.

We do not observe a significant correlation (p value > 0.10), so we consider that our ice was not affected by argon loss during storage.

6.1.4.5.2 During close-off

The close-off process causes the expulsion of a small amount of gas, as the ice matrix is thin enough for some gas to go through when the bubble just closed and its pressure is increasing. This amount of gas expelled is different for argon and dinitrogen because of the difference in size of the two molecules (Severinghaus & Battle, 2006). Consequently, the Ar/N_2 ratio is lower in the ice (figure 6.13).

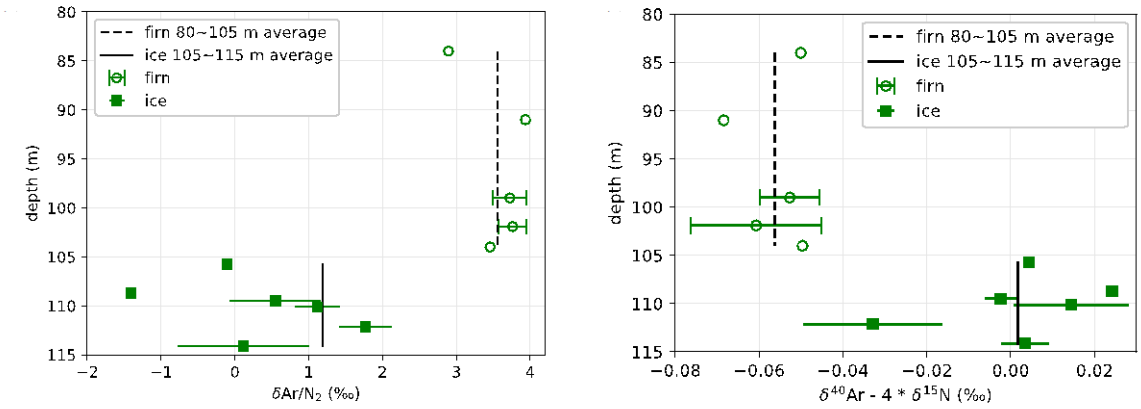

Figure 6.13. (a) $\delta Ar/N_2$ and **(b)** $\delta^{40}Ar - 4*\delta^{15}N$ in the firn-ice transition, at around 105 m depth.

Additionally, the $\delta^{40}Ar$ content of ice samples are shifted compared to the deep parts of the firn. When correcting for gravitational fractionation with $4*\delta^{15}N$, we observe a shift of $\delta^{40}Ar$ from the firn to the ice of + 58 permeg (figure 6.13b). Although the origin of this effect is not clearly understood, it is known and some corrections may be applied to account for this increase: for example Orsi (2013) observed a shift of $\delta^{40}Ar$ of 3.7 permeg per mass unit (+15 permeg for argon). This effect may be due to gas exclusion in the lock-in zone, and depend on lock-in zone thickness properties, which depend preferentially on the accumulation rate, and may indicate that the firn is not at steady state. It could also be linked to argon loss

during storage, which has a constant effect throughout the dataset (see the section above), and justifies the use of a constant shift. We will later constrain the correction for the $\delta^{40}Ar$ in the ice, with the goal to minimize error on the temperature reconstruction by adjusting to the borehole temperature (Section 6.2.7.5). For now, we will consider the $\delta^{40}Ar$ normalized to atmosphere without firn to ice correction.

6.1.4.6 Detection of Outliers

Measurements were routinely controlled. We carefully checked measurements that showed a difference of $\delta^{15}N$ or $\delta^{40}Ar$ between the two replicates larger than 2σ (pooled standard deviation), and searched for a possible cause. Of the 105 ice samples, two were too small to cut duplicates in sufficient size. One other duplicate was contaminated by a leakage during vessel mounting. Thus, 102 samples were duplicated and 3 samples were measured only once.

Due to unplanned power outage, the mass spectrometer was accidentally vented and we had to stop measuring samples although 3 duplicates were in the processing line. They were measured after two weeks, the time needed to get back to the clean vacuum conditions necessary for our measurement, but the points were flagged with high difference between duplicates, so we chose to not consider them.

Finally, one sample had exceptionally high duplicate differences. Because no particular problem was reported this day, we suppose there was a mistake in the processing or the ice quality was not good for this sample, so we did not consider any of its duplicate. Figure 6.14 shows the points measured and corrected, and the points categorized as outliers are marked with red crosses.

The shallowest ice samples may have not been completely closed, and vacuum pumping during sample preparation may have altered the bubble compositions near the close-off depth.

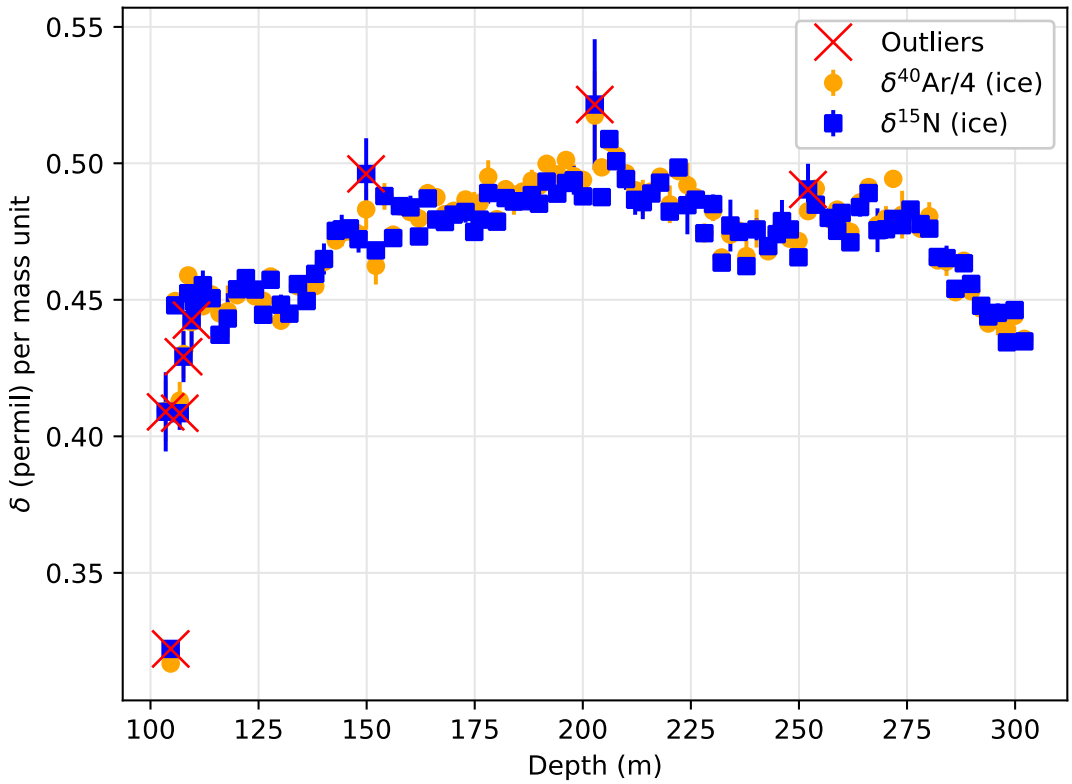

Figure 6.14. Average corrected series of δ^{40}Ar and δ^{15}N with the spread between duplicates illustrated with error bars, in permil per mass unit. The points considered as outliers are marked with red crosses.

We will also be careful and not consider the sample points that significantly differ from the 0.45‰ average that is observed for ice samples between 110 and 130 m. Alternately, the closing of new bubbles after sampling the ice may have entrapped modern air with delta values closer to zero.

When excluding the outliers, the PSTD calculated from the remaining 91 duplicates is 0.0034‰ for δ^{15}N and 0.0134‰ for δ^{40}Ar (or 0.0034‰ per mass unit). Because the two pair of isotopes where processed simultaneously, any fractionation during the extraction and transfer will likely affect both δ^{15}N and δ^{40}Ar simultaneously. Thus, the $^{15}N_{excess}$ defined as $\delta^{15}N - \frac{\delta^{40}Ar}{4}$, only has a PSTD of 0.0026‰.

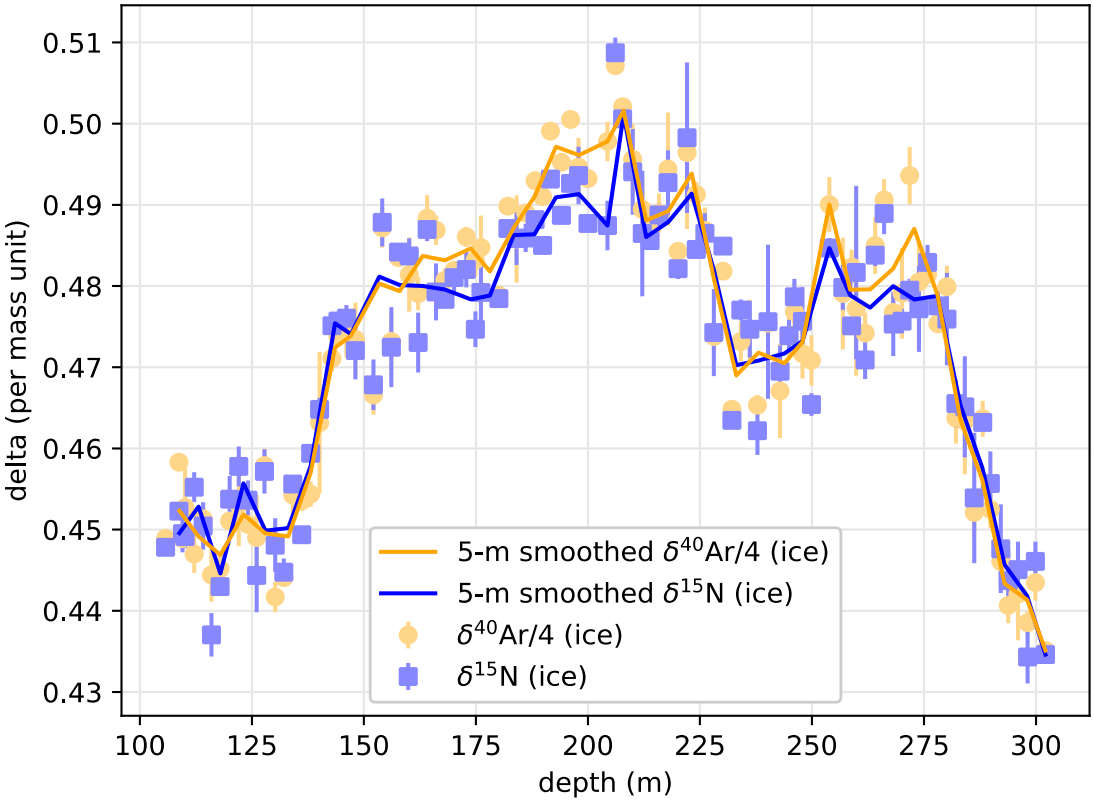

Figure 6.15. Average corrected series of $\delta^{40}Ar$ and $\delta^{15}N$ with the spread between duplicates illustrated with error bars. The 5-m smoothing is shown with continuous lines for both series. Each point was attributed uncertainty from the standard deviation of all points in the 5-m window (not shown here for clarity).

6.1.4.7 Multiple-sample-based smoothing

The bubble trapping was shown to be heterogeneous at the 10-cm scale, causing variability in the isotopic composition of the gases (Orsi, 2013). Because high frequency variability is not well understood, and we cannot relate it to climate information, we chose to smoothen the data by resampling in 5-m windows to average to both $\delta^{15}N$ and $\delta^{40}Ar$ (figure 6.15). The uncertainty on the resampled points was inferred as the standard deviation of all points in the 5-m window. Hereafter, we will use the smoothed data with a 5 m resolution.

6.2 Reconstruction of the temperature history

To achieve the objective of tracking temperature variation through time, we first need to quantify the gravitational and thermal fractionation effects on the $\delta^{40}Ar$ and $\delta^{15}N$. Thermal fractionation will inform on the temperature difference between surface and the lock-in depth, and the gravitational fractionation can be used to infer the height of the diffusive column, used in turn to determine the lock-in depth. We can thus estimate the state of the firn at different given times, and have a temperature gradient. Once we determined the temperature gradient in the firn we will run a firn evolution model with several scenarios of temperature evolution, and will combine the solutions into a temperature history that best recreates the firn conditions through time.

6.2.1 Quantification of gravitational and thermal fractionation of gases

We distinguish the gravitational effect form thermal effect using the two pair of isotopes: the gravitational effect (δ_{grav}) is mass dependent, while the thermal fractionation can be approximated as a linear function of the temperature gradient in the firn, with known fractionation coefficients for nitrogen (Ω_{15}) and argon (Ω_{40}) gases. We thus have the following system:

$$\begin{cases} \delta^{15}N = \delta_{grav} + \Omega_{15} \cdot \Delta T \\ \delta^{40}Ar = 4 \cdot \delta_{grav} + \Omega_{40} \cdot \Delta T \end{cases} \tag{6.10}$$

So δ_{grav} and ΔT can be written as a function of $\delta^{15}N$ and $\delta^{40}Ar$:

$$\begin{cases} \Delta T = \dfrac{\delta^{15}N - \frac{1}{4} \cdot \delta^{40}Ar}{\Omega_{15} - \frac{1}{4} \cdot \Omega_{40}} = \dfrac{{}^{15}N_{excess}}{\Omega_{15} - \frac{1}{4} \cdot \Omega_{40}} \\ \delta_{grav} = \dfrac{\Omega_{15} \cdot \delta^{40}Ar - \Omega_{40} \cdot \delta^{15}N}{4\Omega_{15} - \Omega_{40}} \end{cases} \tag{6.11}$$

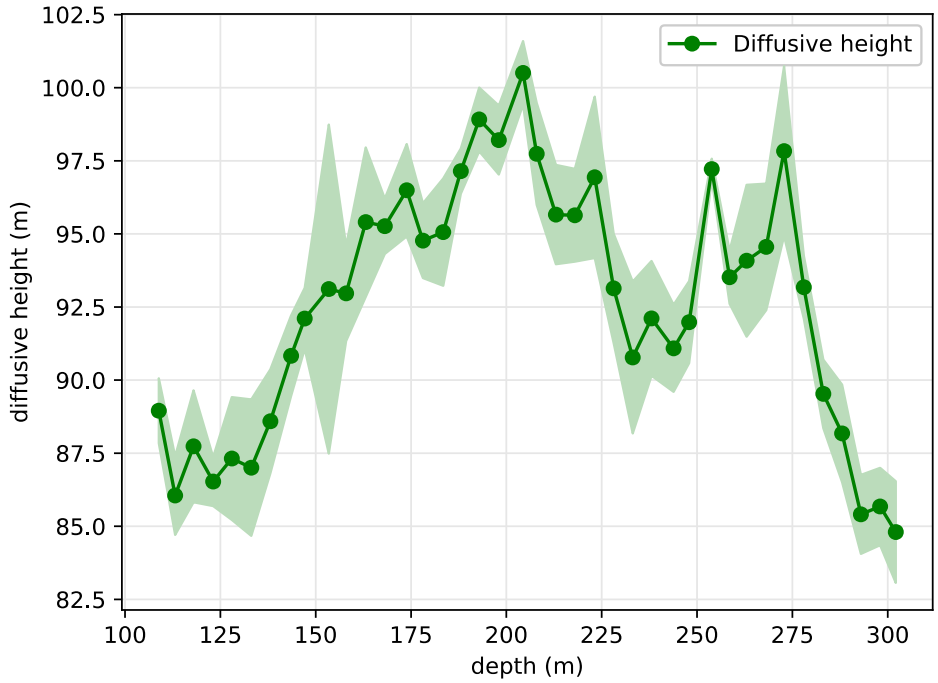

Figure 6.16. Diffusive column height, reconstructed from $\delta^{40}Ar$ and $\delta^{15}N$ of bubbles trapped in the ice.

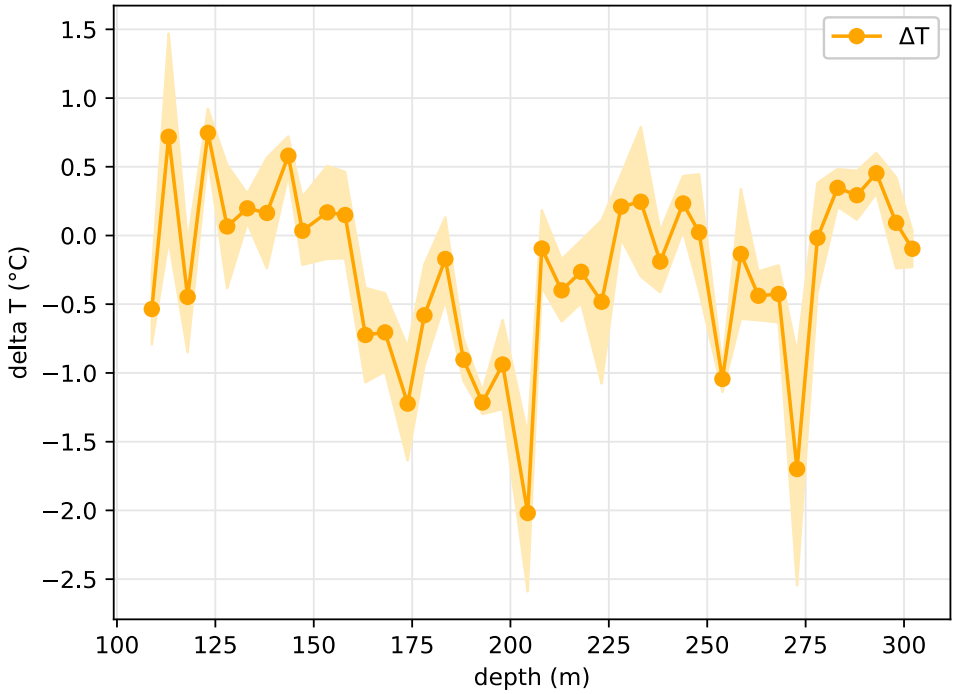

Figure 6.17. Temperature difference in the diffusive column ($T_{surface} - T_{LIZ}$), reconstructed from $\delta^{40}Ar$ and $\delta^{15}N$ of bubbles trapped in the ice. T_{LIZ} is the temperature at the lock-in zone, the bottom of the firn diffusive column.

Using the equations 6.11, we obtain an estimate of the temperature gradient and gravitational fractionation at the points of measurement. We use values of 0.0145‰·°C^{-1} for Ω_{15} and for 0.0375‰·°C^{-1} for Ω_{40}, given by Severinghaus et al., (2001) at 230K.

The gravitational fractionation can be converted in diffusive column height using the following equation (Sowers et al., 1992):

$$z_{diffusive} = \frac{R \cdot T}{g} \cdot \delta_{grav} \quad (6.12)$$

where R is the gas constant, T is the temperature, and g is the gravitational acceleration. For simplicity, and because the temperature was relatively stable during the Holocene, we used a constant temperature of 229.5 K (-43.7°C), corresponding to the observed annual mean at Aurora Basin North. The average uncertainty for the δ_{grav} is 0.008‰, resulting in a 1.5 m uncertainty in the diffusive column height. Given the analytical uncertainties on $^{15}N_{excess}$ of 2.6 permeg, mitigated by the 5-m smoothing, the uncertainty for ΔT is 0.3°C. Evolution of diffusive column height and ΔT are shown with their uncertainties in figures 6.16 and 6.17.

The diffusive column height varies between 86 and 100 m. Variations in the firn depth are primarily due to changes in accumulation, but are also affected by temperature (Goujon et al., 2003).

6.2.2 Convection in the shallow firn and evolution of the lock-in depth

To evaluate variations in the lock-in depth, we must know the convective height in addition to the diffusive height in the firn (the different processes in the firn are introduced in Chapter 2). To quantify the present convective height, we chose to fit an isotope diffusivity model to our firn air measurements, with configurable convective height, diffusive height, and temperature gradient in the model. The temperature profile was both measured with borehole logging, and estimated using the equation 6.11 and the measurements of isotopes in firn air (figure 6.18).

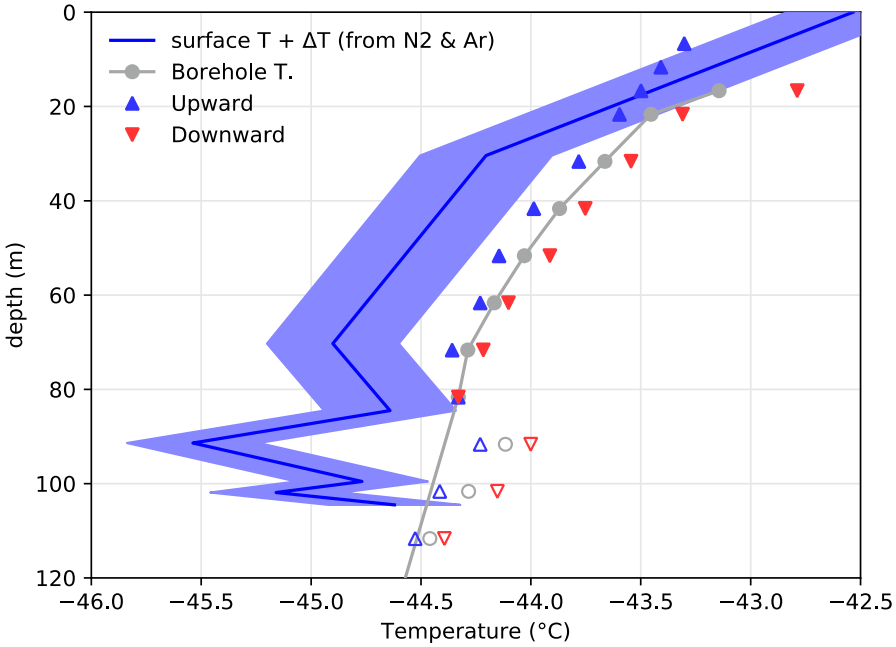

Figure 6.18. Temperature in the firn measured in borehole (triangle markers, grey line is the average) and estimated from fractionation of isotopes (blue line and shading, using equation 6.11). The open markers indicate the borehole temperature measurement that were likely biased by drilling fluid (see Chapter 5)

The temperature gradient obtained with the firn isotopes is almost twice as large as the gradient measured with on-site borehole temperature measurements, which is about 1°C·100 m^{-1}. We will test different hypothesis for the gradient in the firn in this section, but will default to measured borehole temperature later, because it is more robust to rely on real temperature measurements. The temperature spike around 90 m is due to the drilling liquid that was recently introduced in the drill hole, and is thus an artifact.

The isotope diffusion model is based on the steady state diffusion of gases in a firn column, and is detailed by Severinghaus et al. (2010). We use a simplified equation:

$$\delta(z) = \int_0^z \frac{1}{1 + \frac{D_0}{D_{mol}} \exp\left(-\frac{z'}{H}\right)} \left(\frac{\Delta m g}{RT(z')} - \Omega \frac{\partial T}{\partial z'}\right) \partial z' \qquad 6.13$$

where D_0 is the surface eddy diffusivity, D_{mol} is the diffusivity of a specific molecule, the $\frac{D_0}{D_{mol}} \exp\left(-\frac{z'}{H}\right)$ component approximates the eddy diffusivity in the first meters of the firn with H as a scale depth, Δm is the mass difference in the isotope couple, R is the gas constant, $T(z')$ is the temperature, Ω is the molecule specific thermal fractionation coefficient specific to each gas, and $\frac{\partial T}{\partial z'}$ is the temperature gradient. The integration was performed numerically with a quadratic approximation of the function, to obtain modelled δ values for each gas at different depths. The parameters relative to each gas are given in Table 6.1.

Table 6.1. Parameters used to model the isotope diffusion in the firn (source: Severinghaus et al., 2001)

Isotope ratio	Ω	D_{mol}	Δm
$\delta^{15}N$	0.0145	1.963	1
$\delta^{40}Ar$	0.0375	1.904	4
$\delta^{86}Kr$	0.011	1.465	4

We run the model with different assumptions for temperature, and with varying convective height parameter (*H*). We show the best fits (least root mean square errors), along with delta values measured in firn air, in figure 6.19. The best fitting convective heights range from 0.8 m to 1.6 m, depending on the temperature gradient assumption. We give the diffusion model based constant temperature as an example to better illustrate the temperature effect on the isotope diffusion, but the observed temperature gradient is more compatible with a *H* of 1.3 to 1.6 m.

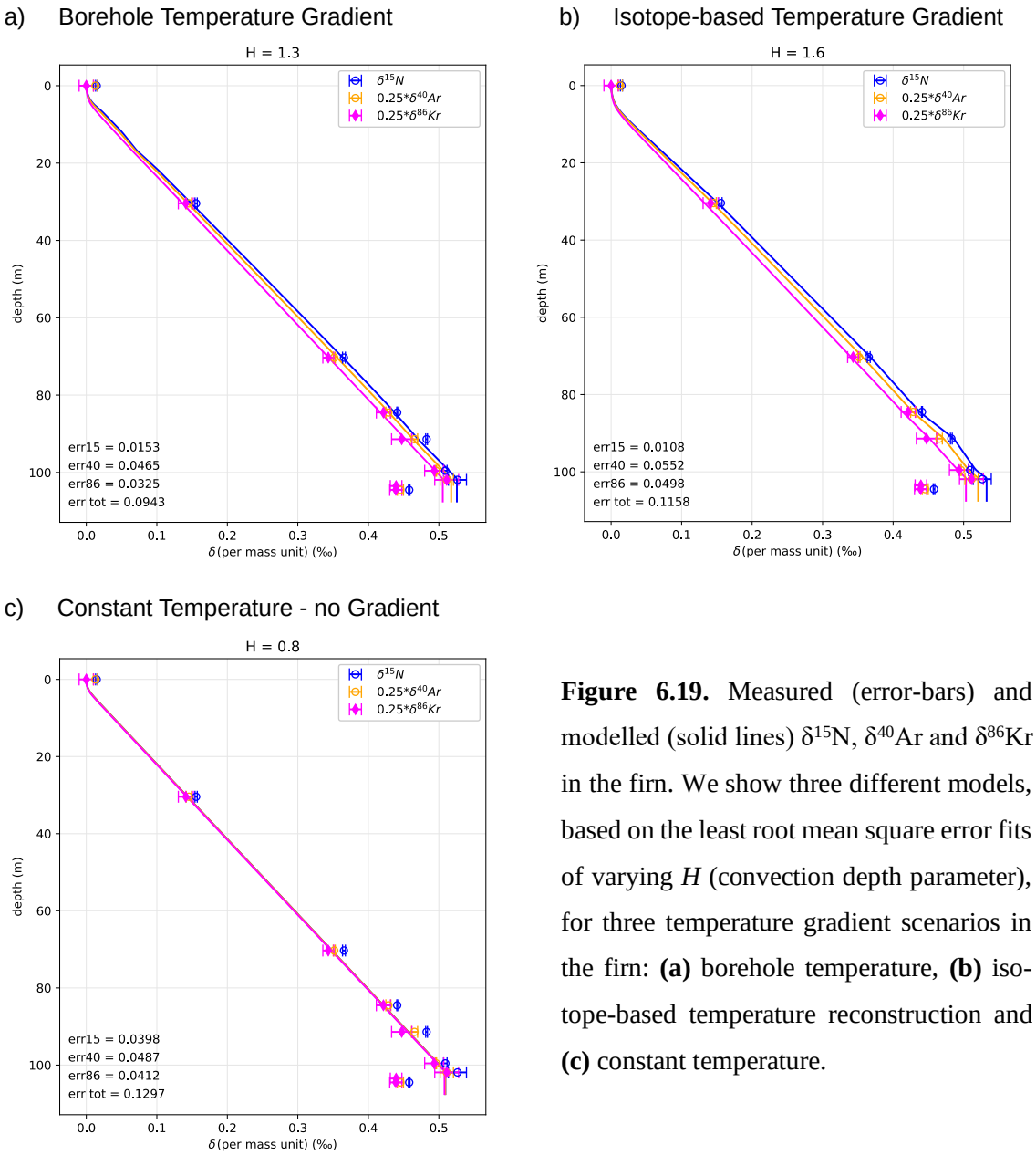

Figure 6.19. Measured (error-bars) and modelled (solid lines) $\delta^{15}N$, $\delta^{40}Ar$ and $\delta^{86}Kr$ in the firn. We show three different models, based on the least root mean square error fits of varying *H* (convection depth parameter), for three temperature gradient scenarios in the firn: **(a)** borehole temperature, **(b)** isotope-based temperature reconstruction and **(c)** constant temperature.

A convective height parameter of 1.4 m translates into a real depth difference of 4.3 m, as shown in figure 6.20. This value for convective height is consistent with other Antarctic sites with similar accumulation, and is therefore likely to have remained quite stable during the last 2000 years (Veres et al., 2013). The convective height determined here is of the same order of magnitude as the uncertainty on diffusive height of 1.5, given in section 6.2.1. In

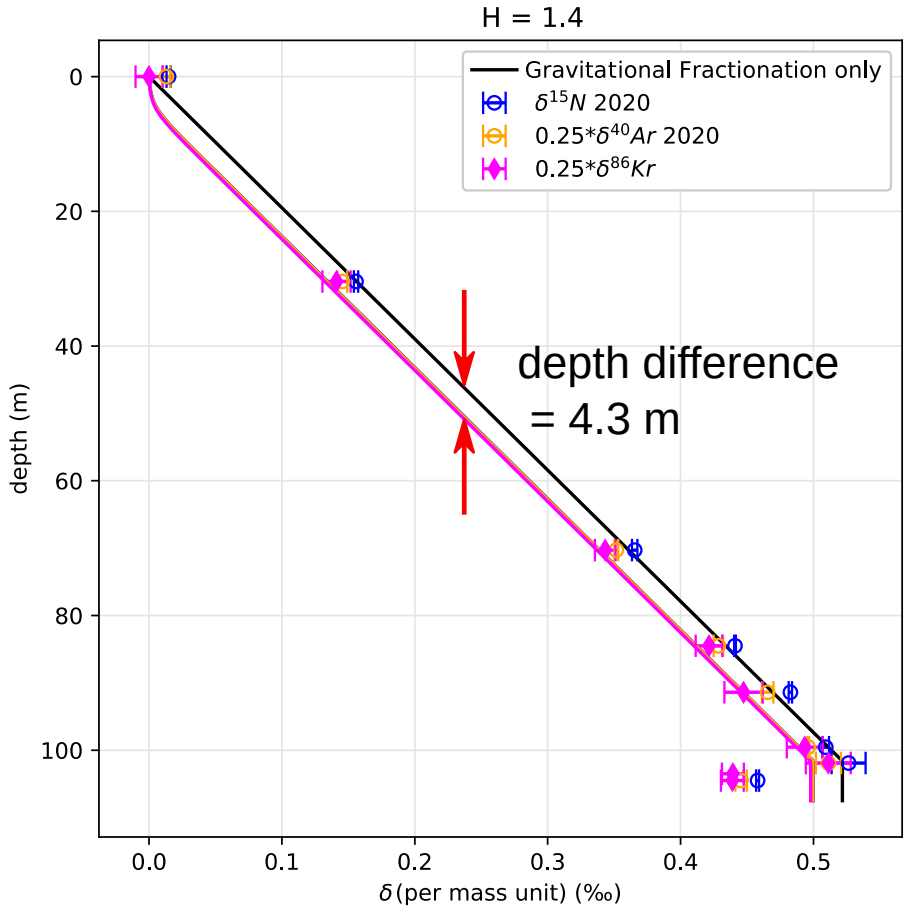

Figure 6.20. Difference between gravitational fractionation alone and modelled fractionation with a convective zone with H = 1.4 m. Both models (continuous lines) do not include thermal fractionation, as they were computed with constant temperature profile with no gradient.

summary, we will add a 4.3 m depth compensation to the diffusive height computed with isotopes to obtain the lock-in depth for ice samples.

The deltas measured in the top of the lock in zone, at 101.9 m depth in the firn, are about 0.060 ‰ higher than measured in the ice (figure 6.21). However, air in the deepest part of the firn, at 104.5 m has comparable δ values to what we measured in ice, at 0.450 ‰. This may be explained by a recent increase in firn depth of 12 m. We also observe a strong temperature gradient both recorded in the isotopes and measured in the borehole, ranging from 1 to 2°C (figure 6.18). A temperature gradient of this amplitude is rarely observed, even at

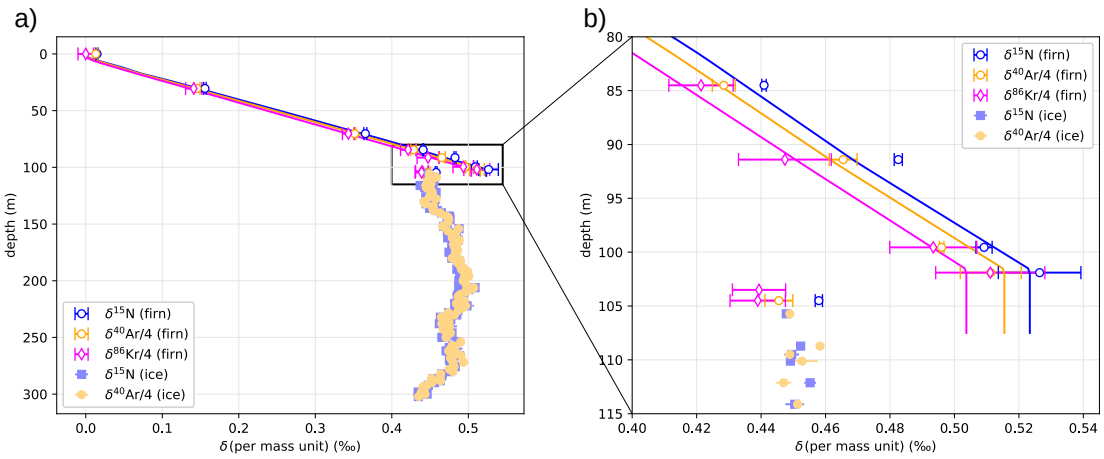

Figure 6.21. Isotopic composition of the air in the firn and in ice bubbles. Solid lines represent the diffusion model with a convective height of 1.4 m and borehole temperatures.

sites with a strong warming trend such as Greenland (Orsi et al., 2017). Such changes in firn depth is not unprecedented at ABN, as attested by the 10 m variations in the firn diffusive height (figure 6.16).

The diffusivity of argon and nitrogen are relatively similar (Table 6.1), and therefore convection will not significantly affect the $^{15}N_{excess}$. For a convective height parameter of 1.4 m, the $^{15}N_{excess}$ difference due to the convection is about 0.2 permeg, which is an order of magnitude lower than our analytical uncertainty. We thus chose not to apply a correction for the convection effect on the isotopes.

6.2.3 Gas Age model

The temperature inferred from isotope composition of gases trapped in ice is built while gases diffuse through the firn, and the definitive composition in the bubble reflects the composition at the bottom of the firn. While we have detailed the age model for ice in Chapter 5, the age of gases trapped in ice is significantly younger than the surrounding ice. Here we

determine the age of gases by using the information on lock-in depth to infer depth differences and retrieve the age of ice at the surface. We then refine the gas age model by fitting the methane composition to the published WD2014 gas age scale for Antarctica (Sigl et al., 2016).

6.2.3.1 Firn compaction

The snow and ice in the column is compacted and thins as more ice is loaded on top of it with snow accumulation at the surface. Consequently, the height difference between the past lock-in depth and the corresponding paleo surface will change due to compression. We use a simple mass conservation equation, with the density profile measured at ABN to infer compaction and retrieve the delta-depth after compaction of the lock-in depth. Under the assumption that the density profile remained constant through time, for each lock-in depth (z_{lid}) inferred from the isotopic composition of gases at a given depth, we have:

$$\int_{z_{lid}}^{z_{surface}} \rho(z)dz = \text{constant} = \int_{z_{gas}}^{z_{ice}} \rho(z)dz \qquad (6.14)$$

The paleo lock-in depth of gas at a depth of z_{gas} is thus used to get the paleo surface z_{ice} that was on top of the ice column when gases acquired their definitive composition. $\rho(z)$ is the ice density at depth z. The compaction is illustrated in figure 6.22. We hereafter call Δdepth the difference between z_{ice} and z_{gas}. Similarly, we call Δage the difference between the age of gas and the age of the surrounding ice at the same depth.

By computing the Δdepth for each gas depth and paleo lock-in depth, we obtain the corresponding depth of paleo surfaces, that have a known age from the ice age model. Assuming that the diffusion through the column is instantly equilibrated, we can infer the age at z_{gas}

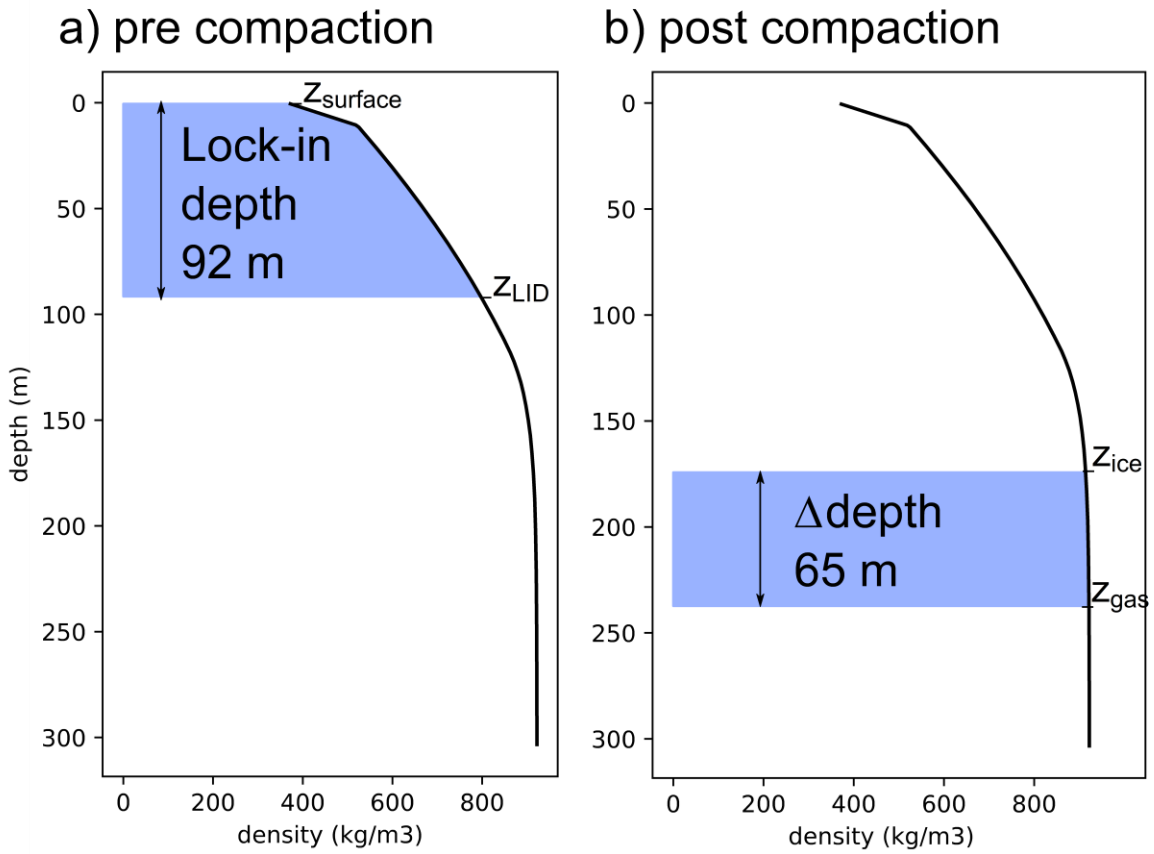

Figure 6.22. Example of the compaction of a firn with a paleo-lock in depth of 92 m, now at a depth of z_{gas} = 238 m. The paleo surface when gases were trapped is now at a depth of 173 m, so the firn has been compacted to a thickness of 65 m, but the total mass remained the same in this model.

from the ice age at z_{ice}. This implies that the diffusion of gases is rather fast compared to the ice accumulation. Gases typically diffuse through the firn in ~10 years (Buizert et al., 2012), while the Δage is about 500 years.

6.2.3.2 Adjustments with methane

Despite the high precision of the ice age model, the dating of gases with a Δdepth method introduces consequent uncertainties, resulting from the uncertainties in the lock-in depth. It is useful to give a first estimate of the gas age, but we need a more precise dating. We thus

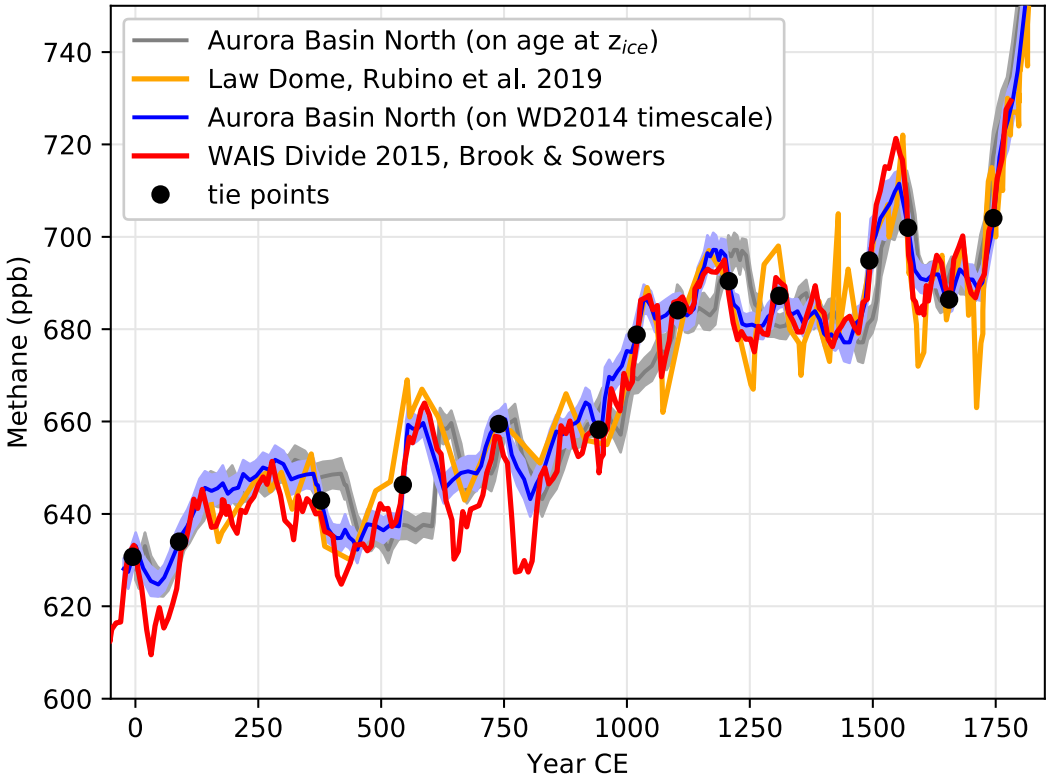

Figure 6.23. Methane concentration in trapped air at ABN (blue), West Antarctic Ice Sheet Divide (red), and Law Dome (orange, Rubino et al., 2019), on WD2014 gas timescale (Sigl et al., 2016).

refine the gas age by adjusting the age model so that the methane content in bubbles at ABN fits the published gas age scale for methane from West Antarctic Ice Sheet (WAIS) Divide ice core, named WD2014 (Sigl et al., 2016). To adjust the ages, we manually picked tie points at clear transitions or extrema on both ABN methane and WAIS Divide methane, and shifted the ABN ages to correspond to the WAIS Divide age. We then interpolated the ABN ages in between the tie points. We show the methane concentrations of the two age models for ABN, of WAIS Divide and Law dome, as well as age tie points on figure 6.23.

For the most recent part (1800 to 2000 CE, figure 6.24), we did not have data from WAIS Divide, so we tied to the revised record of Law Dome instead (Rubino et al., 2019).

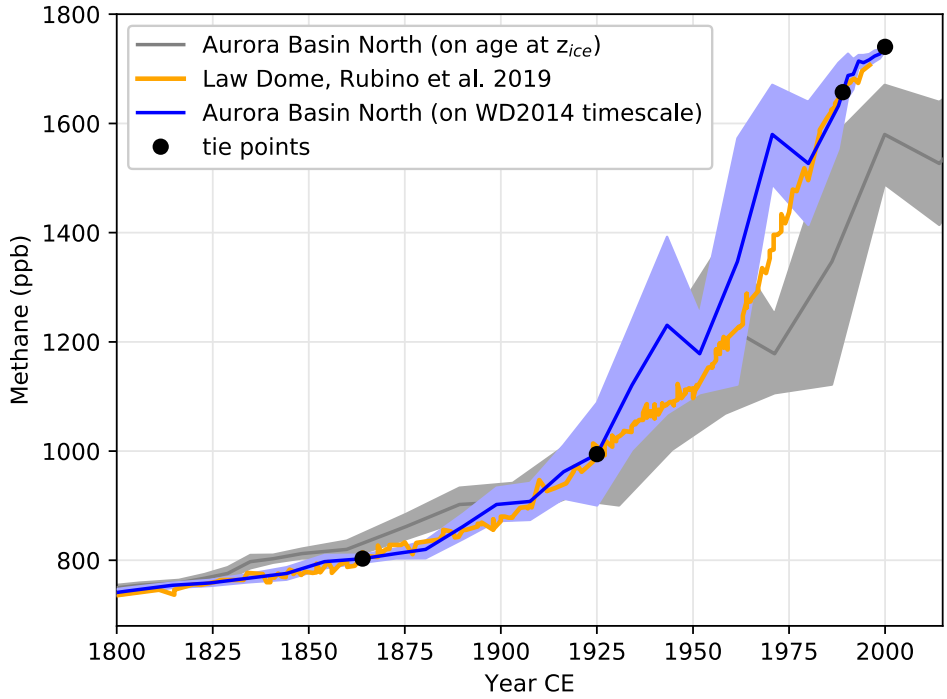

Figure 6.24. Methane concentration in trapped air at ABN (blue), and Law Dome (orange, Rubino et al., 2019), on calibrated Global Atmospheric Sampling LABoratory gas timescale. Note that the close-off depth of ~107 m below surface corresponds to the date of 1925 CE, so more recent pores were not fully closed at the time of sampling and may have been contaminated with more recent air, responsible for higher methane concentrations.

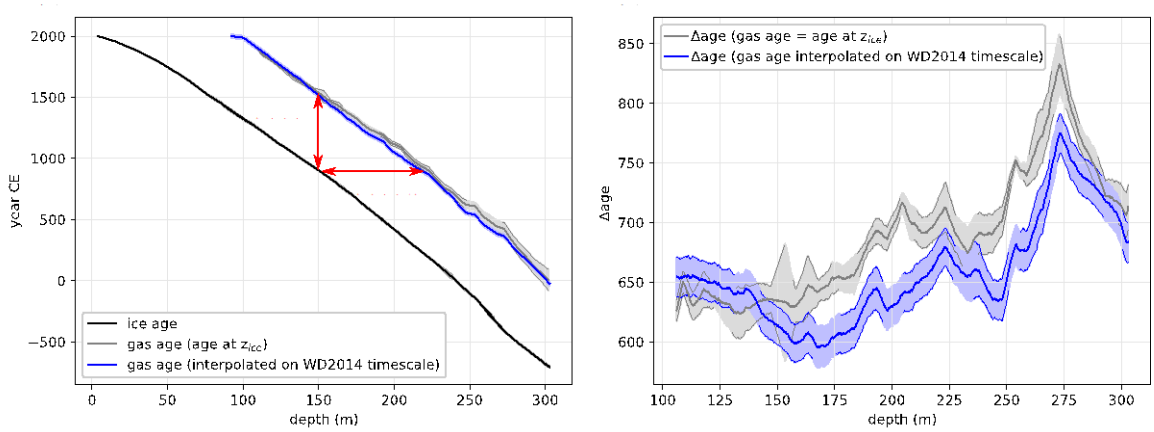

Figure 6.25. a) Age models for ice (annual layer counting, see Chapter 5), gas based on Lock-in Depth and ice age (grey) and gas on WD2014 timescale (blue) and **b)** Difference between ice and gas ages at a given depth (Δage), for the preliminary gas age model (grey) and the gas age on WD2014 timescale (blue).

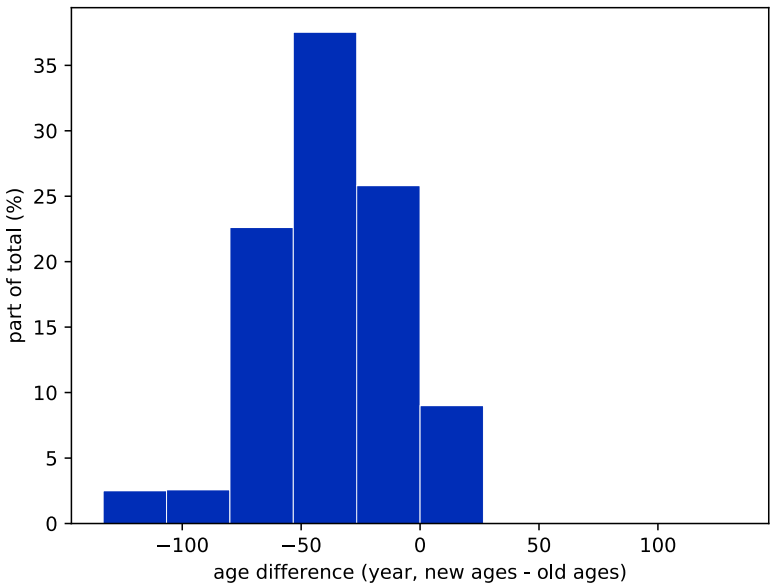

Figure 6.26. Histogram of differences between the new dating on WD2014 timescale and the preliminary dating based on ice age plus Δage inferred from the lock in depth.

The age tying mostly increased the gas ages from the first dating based on ice age and lock-in depth, thus reducing the age difference between the gas and surrounding ice, noted Δage (figure 6.25). The difference in ages between the first guess of gas ages and the gas ages tied to WD2014 is rather small, ranging from -138 to +25 years, with more than 70% of ages with an absolute difference lower than 50 years. We represent in figure 6.26 the histogram of differences between the new dating and the old dating.

Because we picked our points manually, it is difficult to quantify the uncertainty on the gas age model. A rough estimate is that we constrained transitions within a ± 15 yr confidence interval. For reference, we counted on average 79 uncertain years every 650 yr (the order of magnitude of Δage) in the ice age model (Chapter 5).

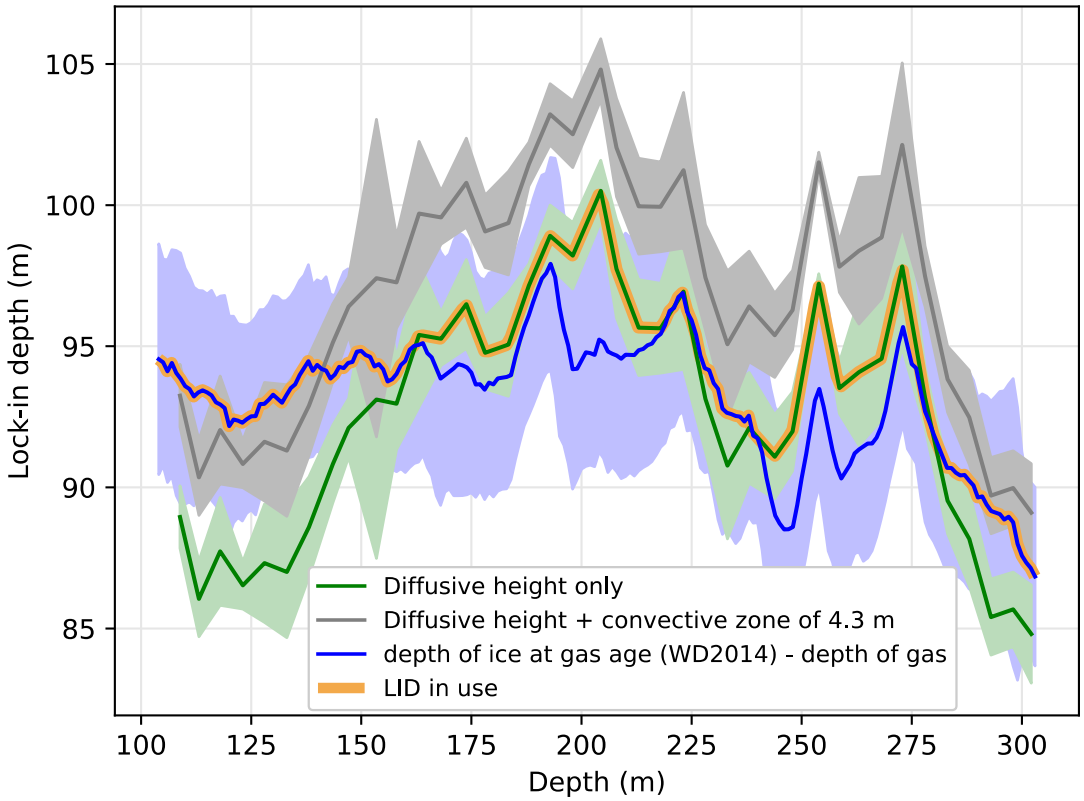

Figure 6.27. Lock in depth evaluated from δ_{grav} in the gas (green), with a convective zone of 4.3 m (grey) and adjusted between the two age models for ice and gas (blue). The definitive lock-in depth chosen is a mix of different records, and is highlighted with orange.

6.2.3.3 Implications for the Lock-in Depth

By adjusting the gas age model (6.25) we have slightly modified the Δdepth. Therefore, using the compaction model in reverse (Δdepth to Lock-in Depth, figure 6.22), we can estimate a lock-in depth pre-compaction from the gas ages on WD2014 timescale and ice age from annual layer counting. We present the resulting lock-in depth in figure 6.27, along with the previous estimates.

Even though the lock-in depth adjusted with age models (blue) matches the estimate with a convective zone of 4.3 m (grey) in the shallow part of the record (depth of 150 m and above), the adjusted lock-in depth is often lower. For most of the record, the adjusted lock-

in depth is more similar to the diffusive height only (green), suggesting that the convection was lower, if not inexistent. The adjusted lock-in depth is at most 5 m greater than diffusive height only, meaning that the estimated 4.3 m convective height calibrated on present-day firn conditions is close to the maximum convective height observed here. In two instances, around 200 m depth and 260 m depth, the adjusted lock-in depth is lower than diffusive height only, which is unrealistic. This may be due to errors in the age models, with an underestimated Δage causing the adjusted lock-in depth to be smaller than the gases isotopes recorded. Consequently, we will use a mixture of these records: we default to the adjusted lock-in depth (blue) with the minimum value of the estimated diffusive height (green). Given that the convective height was seemingly not constant, and because the adjusted lock-in depth depends on both ice and gas age models, the definitive lock-in depth will be given with a ± 6.5 m uncertainty. This uncertainty can be attributed to pooled uncertainties of the diffusive column height (± 1.5 m), the convective height (± 5 m), and the gas age model converted to delta-depth (± 3.8 m).

6.2.4 Modeling of temperature diffusion in the firn and ice

The information on temperature given by the nitrogen isotopes is a difference between the temperature at the surface and at the lock-in depth. We previously estimated the values and uncertainties of both temperature difference and lock-in depth, and precisely dated the time series on WD2014 timescale. The following step is to model the temperature diffusion in different scenarios of temperature evolution, and retrieve the best temperature history with inverse methods. The history of the temperature difference between surface and lock-in depth given by the model will be as close as possible to what we measured from the gases. Additionally, we may constrain the model temperature profile to correspond to measured borehole

temperatures, anchoring the absolute temperature to the observations. In this section, we describe the temperature diffusion model that we use.

The temperature diffusion is modelled using a heat diffusion model (Orsi et al., 2012, 2014). This one-dimensional model simulates the evolution of the temperature in the firn through time, for given temperature and snow accumulation history conditions. The surface history conditions will be detailed in the next section (6.2.5), while we use the accumulation obtained with annual layer counting (as detailed in Chapter 5) with a 20-year running average. The entire ice column is modelled, as bottom geothermal heat flux significantly influences the temperature gradient in the ice. Although the model is one-dimensional, cold ice at depth resulting from advection of ice from colder places at higher elevation can be accounted for by initializing the model with a colder temperature profile (detailed at the end of this section). For the timescale of a few centuries to millennia, we consider a constant geothermal heat flux of 65 mWm^{-2} for Aurora Basin (Maule, 2005). With these boundary conditions, the model computes the vertical heat diffusion in the ice sheet, with temperature profiles for each time-step. Specifically designed for ice sheets and firn, the model takes into account the density of the firn to adjust the thermal diffusivity at each iteration.

We use time-steps of 1 s, and implement annual cycle of temperature. We calibrate the temperature cycle using the ABN Automatic Weather Station data on the three full years of temperature measurements, from October 2014 to September 2017. We first average the temperatures per day of year, then apply a 30-day rolling mean to smooth the signal. We then use a cosinus approximation of the seasonal cycle (figure 6.28):

$$T_{season} = 13.7 \times \cos\left(\left(DOY + \frac{354}{365}\right) \times 2\pi\right) + \frac{13.7}{2.8} \times \cos\left(\left(DOY + \frac{354}{365}\right) \times 4\pi\right) - T_{annual} \qquad (6.15)$$

where DOY is the day of year, with a phase lag of 354 days to center the cosine around December 20th, and T_{annual} is the annual average temperature.

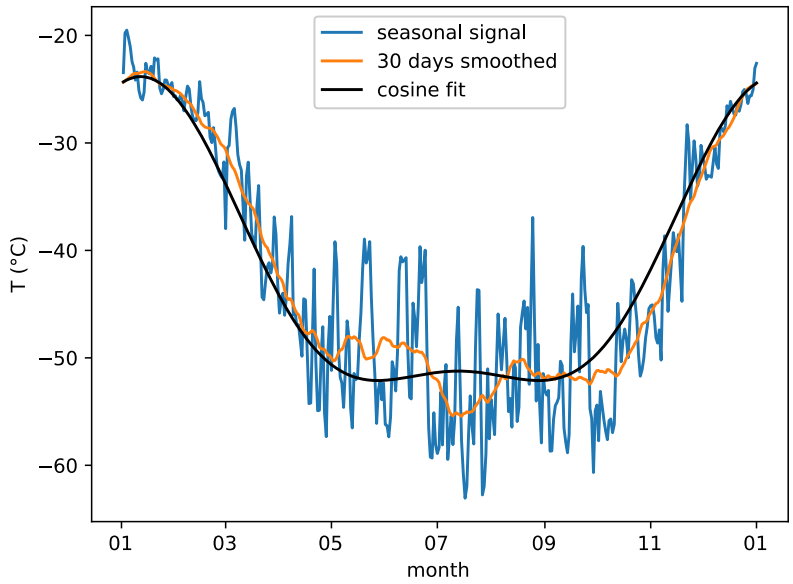

Figure 6.28. Annual amplitude cycle from the Automatic Weather Station ABN, with 30-day smoothing and cosine fit.

The variables of interest are the surface temperature forced by the given history, and the temperature difference between surface and the lock-in depth (ΔT), which will be compared to the ΔT estimated from the gas isotopes (Sections 6.1 to 6.2.1). Although the model is able to determine a lock-in depth with pore closure at a computed density, we force it to retrieve temperature at given lock-in depths, that we determined in section 6.2.3. Sensitivity tests with the uncertainty on the lock-in depth will be conducted in section 6.2.7.6

We initialize the model by running 20,000 iterations of a year with constant accumulation and seasonal cycle centered around the mean temperature. This step is necessary to reach a steady state of the temperature profile in the ice, and avoid artificial disequilibrium from initial conditions. Because we observed a temperature gradient with the borehole profile, with decreasing temperature at depth, we initialize the temperature profile with an annual cycle centered around -48°C colder than the actual mean of -42.4°C. Sensibility to the initialization temperature will be described in section 6.2.7.

The one-dimensional model does not account for ice advected from upstream, where it might have been accumulated under colder conditions. This may cause the very cold temperatures measured in the deepest part of the borehole, as temperature diffusion is rather slow

in ice. We chose to initialize with colder temperatures to account for advected ice rather than adding complexity to the diffusion model, to keep the computation time low as we decide to run numerous simulations with the model, and because the implementation of multidimensional model is not the focus of this work.

After the initialization, the stationary temperature profile is set as a starting point for the simulation. We run the model between 0 CE and 2014 CE, and specify the temperature and accumulation history scenarios that will force the surface conditions during this period. For the reference simulation, we use an assumption of a constant mean temperature at -45°C, same as the stationary profile. The accumulation is estimated from the annual layer counting in the ice core, which we smoothed with a 20-year running mean. We chose this smoothing because yearly accumulation is highly variable, and the results of the simulation will be compared with data from gas isotopes that we averaged in 5-m windows, which have thus a temporal resolution of about 50 years. Any accumulation change at a higher resolution will at best not influence the results of the heat diffusion model as we will not be able resolve between different solutions, or at worst introduce noise in the signal.

6.2.5 Linearization and inversion of temperature history

In this section we introduce the inversion method adapted from Orsi et al. (2014), used to determine temperature changes from gases isotopes. We suppose that the temperature history $T(t)$ can be expressed as the sum of a reference temperature guess T_0, plus a linear combination of simple temperature scenarios $b_i(t)$, with their respective coefficients x_i:

$$T(t) = T_0 + \sum_i x_i b_i(t) \tag{6.16}$$

The following subsections detail how we define the scenarios b_i and how we determine the weighting coefficients x_i. The general idea is that each temperature scenario is associated

with a delta-temperature record, as the difference between the surface temperature and lock-in depth temperature, which is directly comparable to the delta-temperature we determined from gases stable isotopes. We will then search for the combination of scenarios that results in the delta-temperature record that is the closest our findings. Additional constraints may be applied on the combination of scenarios, such as a combined temperature profile in the ice fitting to the measured borehole temperature profile.

6.2.5.1 Simulation of multiple scenarios b_i of temperature history: forward model

We run the heat diffusion model described in section 6.2.4 with different temperature histories. After the reference simulation with a constant temperature history, we introduce small variations on temperature histories by introducing a spike of temperature at a different date for each simulation. In these simulations the amplitude of annual cycle of temperature remains unchanged, only the mean annual temperature varies. A selection of temperature input forcings are shown in figure 6.29.

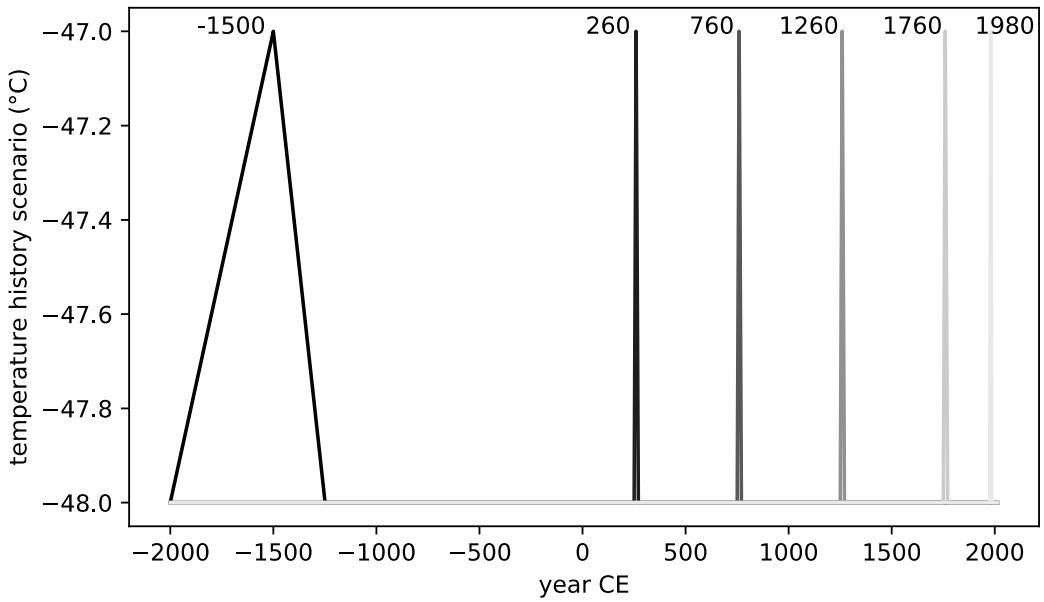

Figure 6.29. Example of six temperature history scenarios with a baseline T_0 of -48°C, each with a single temperature spike of +1°C in a triangle shape of usually 10 years, centered around

the time indicated at the top of the spikes. The spikes prior to 0 CE are asymmetric and cover longer timescale, as there is only low-resolution constraint from borehole temperature, and no constraint from gases at this time.

In total a batch of simulations included 220 temperature scenarios, with 10-year frequency during the 0 to 2000-year CE period, when we have gas-based delta-temperature data, and lower resolution Before Common Era (BCE, or negative CE) to give some flexibility to allow for long-term temperature adjustments, and match the borehole temperature profile. For each temperature scenario $T_0 + b_i$, we get a temperature profile history $y_i(z, t)$, corresponding to the evolution of the temperature profile through time. The $b_i(t)$ is used as the input of the simulation and only describes the surface temperature. The modelled temperature profile histories $y_i(z, t)$ is directly comparable with the delta-temperature estimated from the gas-based measurements, as they are the difference of temperature between the surface and the lock-in-depth.

6.2.5.2 Recombination of temperature history scenarios to match the temperature gradients estimated from gases: inversion and determination of x_i

Assuming the model is linear, the outputs of the simulations y_i can be expressed as the difference to the reference simulation with T_0 only (no b_i), noted y_0:

$$h_i(z,t) = y_i(z,t) - y_0(z,t) \tag{6.17}$$

If we generalize equation 6.16 to describe not only the surface temperature $T(t)$, but more generally the evolution of temperature profiles as captured in our data $d(z,t)$, it can be re-written as

$$d(z,t) = y_0(z,t) + \sum_i x_i h_i(z,t) + r \tag{6.18}$$

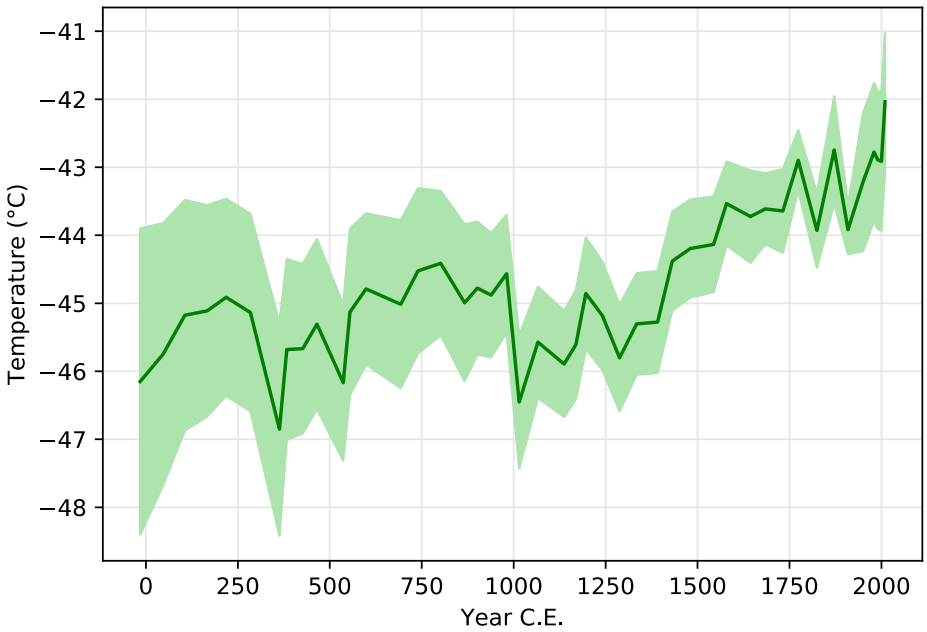

Figure 6.30. Temperature obtained from the inversion of gas delta-temperature and borehole temperature data. The shading indicates the combined uncertainty resulting from the uncertainty on original data and the temperature inversion (1σ).

where *r* are the residuals, *i.e.* the data that could not be fit with a combination of model simulations. For clarity and consistency with Orsi et al. (2014), we write equation 6.18 in a matrix notation, with the data expressed as the difference to the reference simulation:

$$\mathbf{d} - \mathbf{y_0} = \mathbf{Hx} + \mathbf{r} \tag{6.19}$$

with $\mathbf{x} = [x_1,\ x_2, \ldots\ x_n]$ and $\mathbf{H} = [h_1(z,t),\ h_2(z,t), \ldots\ h_n(z,t)]$. The goal of the inversion is to determine the vector **x** that would minimize both the variance of **x** and **r**. Reducing the residuals **r** gives a solution closer to the data, and reducing the variance of **x** gives a solution with minimal variability where we have no constraints by data. Because more information is contained in the simulations (**H**) than in the data (**d**), the system is underdetermined, and several combinations could be chosen, consequently we select the solution with the minimum **x** variability. Minimizing the residuals **r** is essential to have a temperature history as close as

possible to the reality. By a least squares optimization, Orsi et al. (2014) concluded that solving the equation 6.18 implies the minimization of the cost function *C* defined as

$$C = \frac{1}{2}\mathbf{r}^T\mathbf{R}^{-1}\mathbf{r} + \frac{1}{2}\mathbf{x}^T\mathbf{P}^{-1}\mathbf{x} \quad (6.20)$$

where **P** represents the uncertainty on the model simulations, and **R** the uncertainty on the residuals and by extent the data.

We chose to solve the equation 6.19 with the inversion given by Wunsch (1996):

$$\mathbf{x} = \mathbf{P}\mathbf{H}^T(\mathbf{H}\mathbf{P}\mathbf{H}^T + \mathbf{R})^{-1}(\mathbf{d} - \mathbf{y}_0) \quad (6.21)$$

Concretely, we only use the information of the simulations $h_i(z, t)$ outputs that is comparable with our data. They can be categorized in two sets: (1) the delta-temperature between surface and lock in depth (fixed *z*) at different times (varying *t*) as determined in sections 6.2.1 and 6.2.2, and dated in 6.2.3, and (2) the final temperature profile from borehole measurements (figure 6.17 fixed *t*, and varying *z*). The inversion can take the two sets as long as the simulation matrix **H** is shaped accordingly: we extract from each simulation $h_i(z, t)$ the points corresponding to the data $d(z, t) - y_0(z, t)$. In the case of the use of the two datasets, we just append our data varying on *z* to the data varying on *t*, as the data is weighted by the uncertainties in the inversion.

With the coefficients x_i obtained, we get back to the surface temperature history with equation 6.16. The temperature solution given in figure 6.30 was optimized after testing several parametrizations as described in the sensitivity tests (following section). The inversion method provides an estimate of the uncertainty as the square root of the diagonal elements of $\mathbf{S} = \mathbf{B}\widehat{\mathbf{P}}\mathbf{B}^{\mathbf{T}}$, where B is the matrix of surface temperature $\mathbf{B} = [b_1,\ b_2, \ldots\ b_n]$ and $\widehat{\mathbf{P}}$ is the covariance of the given uncertainty for the model parameters:

$$\widehat{\mathbf{P}} = \mathbf{P} - \mathbf{P}\mathbf{H}_\mathbf{n}^\mathbf{T}(\mathbf{H}_\mathbf{n}\mathbf{P}\mathbf{H}_\mathbf{n}^\mathbf{T} + \mathbf{R})^{-\mathbf{1}}\mathbf{H}_\mathbf{n}\mathbf{P} \quad (6.22)$$

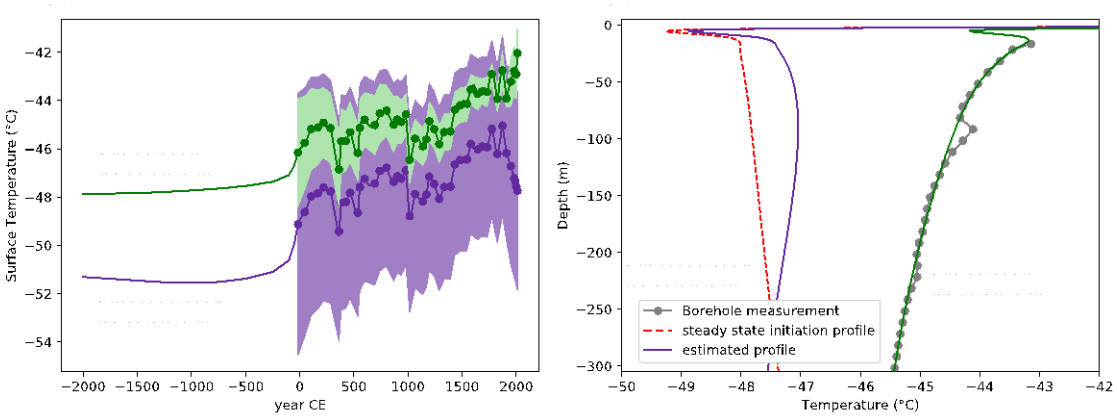

Figure 6.31. Comparison of (**a**) temperature history and (**b**) temperature profile reconstructions with (green) and without using (purple) the borehole temperature to constrain the inversion.

In short, the temperature is reconstructed by inversion of a linear advection-diffusion temperature model, so that it fits temperature data from borehole and firn gradient. The least square inversion provides both optimized solution and evaluation of the uncertainties, based on the original uncertainties of the data.

6.2.6 Sensitivity of temperature inversion

In this section we describe the limits and uncertainties on the temperature reconstruction. For this, we compare the results of inversions with different parameters, each subsection corresponding to a different parameter. The different reconstructions are compared to the reference temperature history presented in figure 6.30, which was chosen as the best temperature reconstruction we could produce, after the sensitivity tests.

6.2.6.1 Influence of Borehole Temperature in the temperature inversion

The borehole temperature allows us to constrain the long term trends in temperature, by having the simulated temperature profile in the ice to fit on-site measurements. The absolute value of the temperature is also provided by borehole measurements, whereas the delta-temperature estimated from gases only gives a relative temperature reconstruction. Moreover,

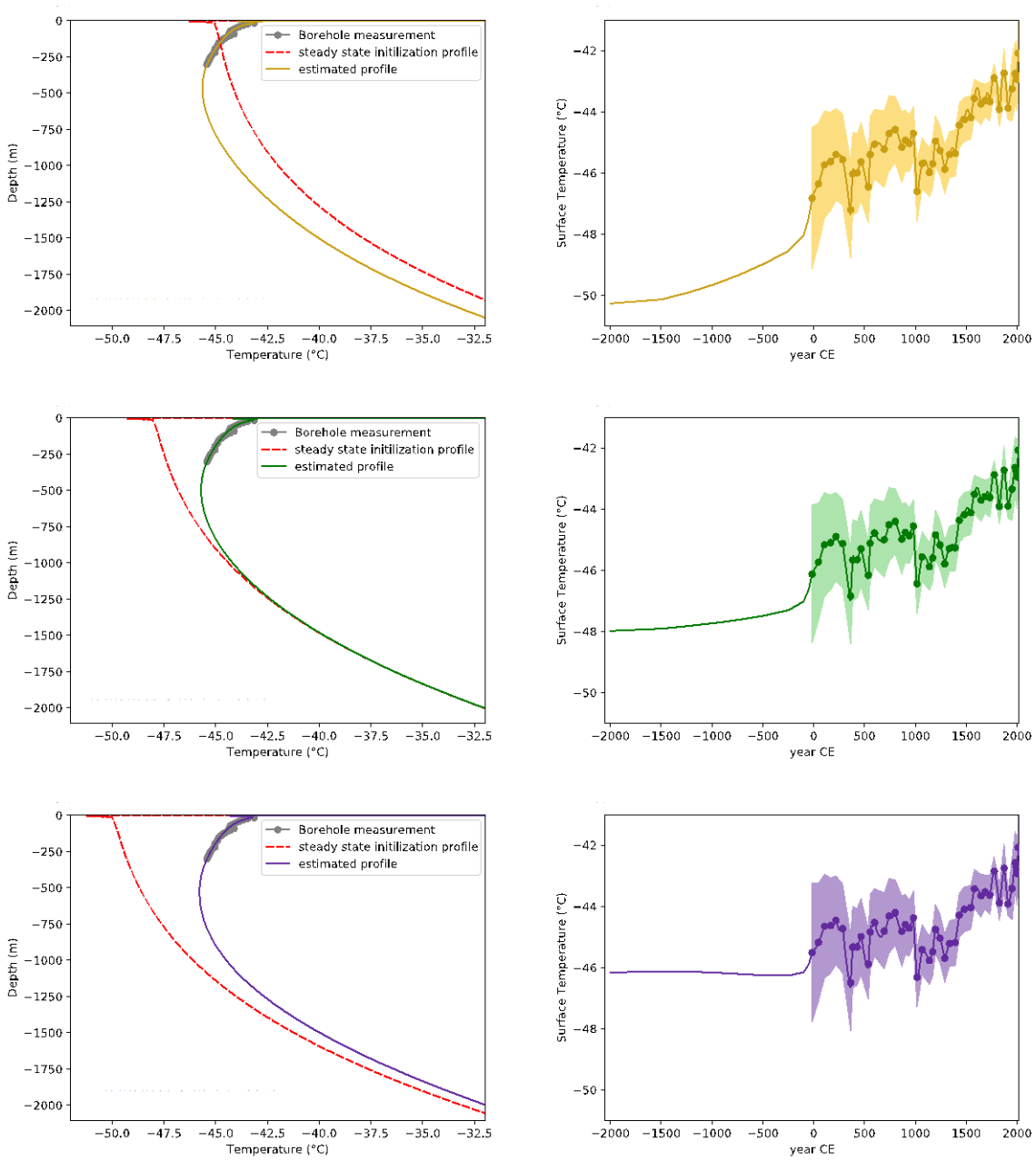

Figure 6.32. Comparison of three temperature reconstructions using different initial temperature: -45°C (a, b), -48°C (c, d), and -50°C (e, f). We show the temperature profiles in the ice (a, c, e) obtained from simulation initialized with the steady state profiles indicated in red dashed lines, and the corresponding temperature histories (b, d, f). The large dots correspond to dates when we have constraints from gases measurements, with lower resolution than the full temperature reconstruction.

the long term trend of temperature may not be reliably captured in the gases, as the diffusion of gases through the firn reaches an equilibrium in about 10 years (Buizert et al., 2012).

Figure 6.31 shows that the borehole temperature constrains the temperature evolution, and strongly reduces uncertainties. Without the borehole temperature constraint, the average temperature is closer to the initial hypothesis of -48°C, while the reconstruction obtained accounting for the borehole temperature is 3°C warmer. Consequently, the temperature in the ice is matching the measured temperature profile. It also appears that the initial hypothesis on temperature influences the temperature reconstruction.

We will use the borehole temperature as an additional constraint in the temperature reconstruction, because it lowers uncertainties and gives a better absolute temperature estimation.

6.2.6.2 Initial temperature hypothesis

We conducted simulations with different initialization of the steady state temperature profile in the ice (figure 6.32). Despite the different initialization temperature, the estimated profiles in the ice after the temperature inversion are very similar, and match the borehole temperature measurements. However, the temperature histories reveal that a simulation initialized with too high temperature in the ice result in an inversion with temperature lower than the initialization temperature on the first 2000 years of the simulation, where we have no constraint from gases (from 2000 BCE to 0 CE). Even if we introduced this accommodation period of 2000 years before the temperature reconstruction that we will describe (from 0 CE to present), we try to release constraints on the inversion and decide to use an initialization temperature with a profile as close as possible to the final temperature profile. Therefore, we selected an initialization temperature of -48°C.

The influence of colder ice advected from higher elevation locations and burried under ABN is expected to be small, as the temperature diffuses rather quickly in the ice. The deposition of ice 10°C colder (-53°C) during the Last Glacial Maximum (LGM) at a higher elevation, which is then advected under the present ABN site would only account for a -0.4°C change at 300 m depth (computed with the temperature diffusion model described in chapter 6), compared to an hypothetical case where the ice would remain at -43°C at the surface. The cold anomaly due to LGM ice alone cannot explain the positive gradient of +2°C/300 m obeserved in the borehole temperature. In fact it would "only" reduce the negative gradient from -0.7°C/300 m to -0.3°C/300 m, which naturally occurs at equilibrium between the cold surface (-43°C) and the warm ice-rock transition (about -5°C, as used in our simulation). The observed gradient is thus most likely due to a strong, recent warming in surface conditions. The temperature reconstruction from borehole temperature will be made in the next chapter, in association with gas stable isotopes.

6.2.6.3 Constant delta-temperature shift to firn-ice δ^{40}Ar correction

We saw in section 6.1.4.5.2 that the close-off could induce a shift in argon isotopes trapped in bubbles, and therefore affect the $^{15}N_{excess}$ and the delta-temperature. Here we try different δ^{40}Ar corrections and compare the influence on the temperature reconstruction (figure 6.33).

The figure 6.33 illustrates that constraints from gases (at the dates pointed with large dots) and from borehole temperature cannot be satisfied simultaneously in case of a too large or too low correction on δ^{40}Ar. For example, with no δ^{40}Ar correction (purple on figure 6.33), the gases indicate a lower temperature difference at a given time, whereas the long term trend that is only forced by the borehole temperature causes the temperature to rise sharply in the short periods where we have no gases constraints. Conversely, if the correction is too strong

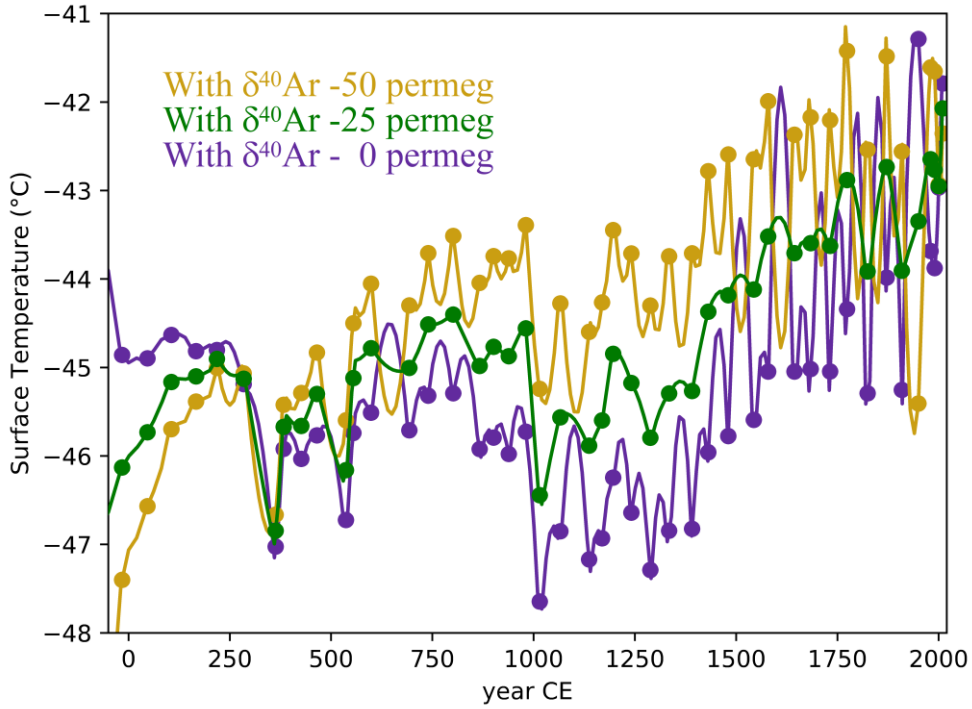

Figure 6.33. Comparison of temperature reconstructions with different δ^{40}Ar corrections in ice to account for the difference between ice and firn composition. The large dots correspond to dates when we have constraints from gases measurements, with lower resolution than the full temperature reconstruction.

(yellow), the temperature shortly decreases to compensate the too intense temperature warming forced by the gases. This jagged pattern in the temperature record is highly unlikely and is associated with strong variability in the x_i coefficients of the inversion, which is why we try to minimize the variability in between two gas points. The temperature reconstruction that better minimizes the x_i coefficients (green) was found with a δ^{40}Ar correction of -25 permeg, resulting in a delta-temperature shift of +1.2°C (the uncorrected delta-temperature was shown in figure 6.16).

6.2.6.4 Seasonal temperature cycle amplitude

We performed the temperature inversion with seasonal temperature cycle amplitude increased by 10% and decreased by 10%, and minor influence on the reconstructed temperatures, with a standard deviation of the difference to the reference simulation lower than 0.1°C. We conclude that a change in the seasonal amplitude would not significantly influence the temperature reconstruction.

6.2.6.5 Accumulation

We reconstructed the temperature histories with accumulation 10% higher and 10% lower than the accumulation record obtained with annual layer counting. The temperature history after inversion was not significantly affected by the accumulation, with standard deviation of the difference to the reference simulation lower than 0.1°C. Minor changes in accumulation, or slight errors in the estimation from annual layer counting should thus not influence the temperature reconstruction.

6.2.6.6 Lock in depth

Lock-in depth determines the depth at which the temperature is taken to compute the difference to surface temperature in the model – the delta-temperature. Therefore, errors in the lock-in depth estimation could have a repercussion on the estimated temperature changes. We performed the temperature inversion using the lock-in depth determined in section 6.2.3 with lock in depths increased by 10%, and decreased by 10%. The 10% change on the lock-in depth roughly corresponds to a ± 9 m, which is larger than the estimated uncertainties of ± 6.5 m. The reconstructed temperatures here again were not significantly affected by the change in the lock-in depth, because the temperature gradient is rather low at 90 m depth. The reported differences with the temperature of the reference run have a standard deviation

lower than 0.1°C. However, in this case where we observe a recent warming trend on temperature, a deeper lock-in depth could cause the delta-temperature to increase. A greater lock-in depth could partly compensate the delta-temperature correction described in section 6.2.6.3, although it would require an unrealistic increase of more than 100 m to cause a delta-temperature effect of 1°C. Within our error estimation on the lock-in depth of ± 6.5 m, the temperature reconstruction does not depend on the lock-in depth.

6.2.6.7 Summary

The sensitivity tests highlighted the importance of the use of both borehole temperature and delta-temperature from gases. Borehole temperature gives an absolute temperature for the reconstruction, and also helps constrain the long term trend of temperature, whereas the gases and delta-temperature record fast-changing temperatures, allowing for the identification of quick changes in the climate of ABN. In order for the delta-temperature to match the warming trend, a constant correction on the $^{15}N_{excess}$ was applied, consistently with the observed difference between ice and firn $^{15}N_{excess}$ (section 6.1.4.5.2). We could use the two constraints of borehole temperature and delta-temperature derived from gases stable isotopes to build a reliable temperature history.

6.2.7 Glaciological correction

As the ice flowed during the past 2000 years, the surface of the ABN site moved lower in elevation and closer to the coast. The surface conditions thus changed over time because of the ice flow, independently from climate changes. In order to focus on the climate changes, we corrected the temperature for the change in elevation (Chapter 5, figure 5.10). We used the temperature gradient determined on the transect from Zhongshan to Dome A (Pang et al., 2015; Xiao et al., 2012), with kriging of annual average temperature from automatic weather

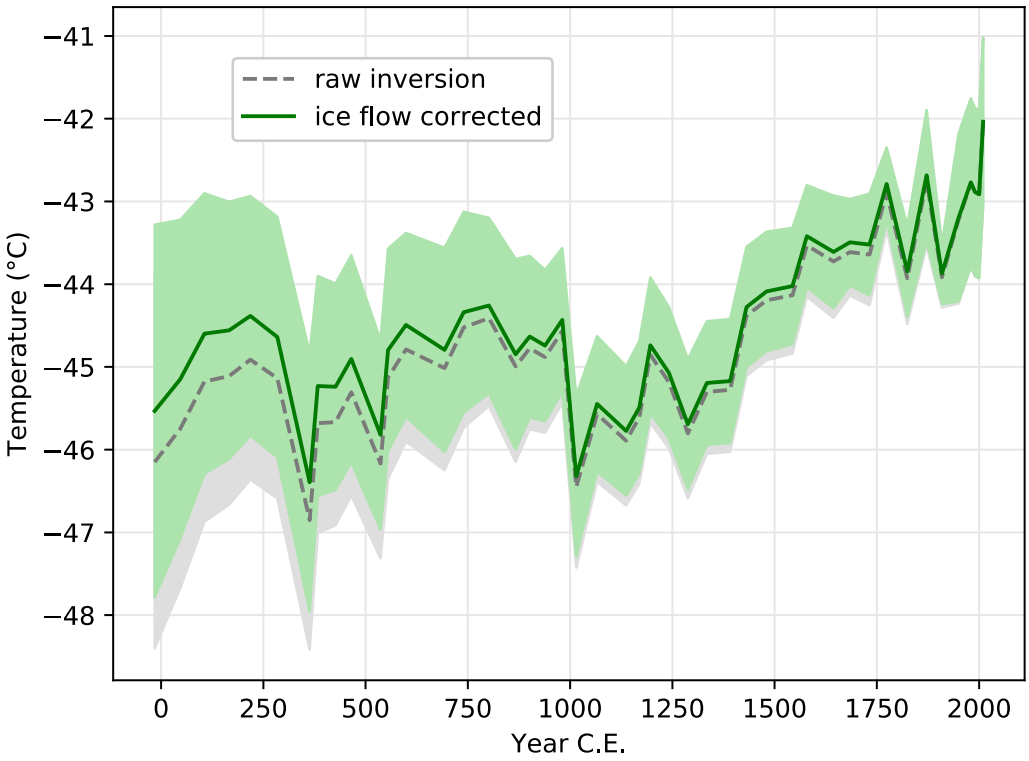

Figure 6.34. Glaciological correction of the temperature reconstructed with the inversion.

stations and borehole temperature measurements along the transect. The correction slightly reduces the warming trend on the temperature reconstructed at ABN (figure 6.34), with an adjusted temperature of +0.5°C at the beginning of the record.

6.3 Conclusions on the temperature reconstruction

We measured the isotopic ratios of $\delta^{40}Ar$ and $\delta^{15}N$ in the bubbles trapped in the ABN1314 ice core, with excellent precision. We deduced the temperature gradient in the firn from the gases stable isotopes, and combined with borehole temperature measurements, we inversed a heat diffusion model to reconstruct the evolution of the surface temperature during the last 2000 years. This temperature reconstruction comes with uncertainties resulting from both the

measurement and the inversion, but supplements the water isotope record with an independent temperature estimation, and with slightly different information as it records the temperature in the snow. In the next chapter, we will compare the two independent temperature records, and explore the implications for the climate at ABN and in the Antarctic region. This works also points that we need to better understand the changes in gas isotopic composition during bubble formation, to explain and quantify the $^{15}N_{excess}$ shift observed between air in the firn and in the bubbles.

Chapter 7

Climate interpretations of the Aurora Basin North data

Many interrogations remain on the climate of the East Antarctic Plateau, due to the uncertainties of water-isotope based temperature reconstructions. After trying to understand how the water isotope records climate at Aurora Basin North (ABN), we produced two independent temperature records, one with the water isotopes and one with the gases isotopes. Here we compare the results and discuss them in terms of climate variability at the Aurora Basin North, and the teleconnections with other regions.

7.1 Climate at ABN

7.1.1 Summary of the temperature records

Because of the uncertainties associated with each paleoclimate reconstruction, we carefully reconstructed the temperature using two different methods. The first method is the most popular approach to reconstruct temperature in glaciated areas, by calibrating the $\delta^{18}O$ against temperature during a period of observation, and extending the temperature back in time using the $\delta^{18}O$ in older ice. This record is detailed in Chapter 5, and will be named $\delta^{18}O$-temperature in this chapter. The second method takes advantage of $\delta^{40}Ar$, and $\delta^{15}N$ in the air trapped in bubbles within the ice, as well as borehole temperature, to retrieve the temperature in the snow, as explained in Chapter 6. Here, we make reference to it as the $^{15}N_{excess}$-temperature. We thus have two different insights on the temperature history at ABN, given in figure 7.1.

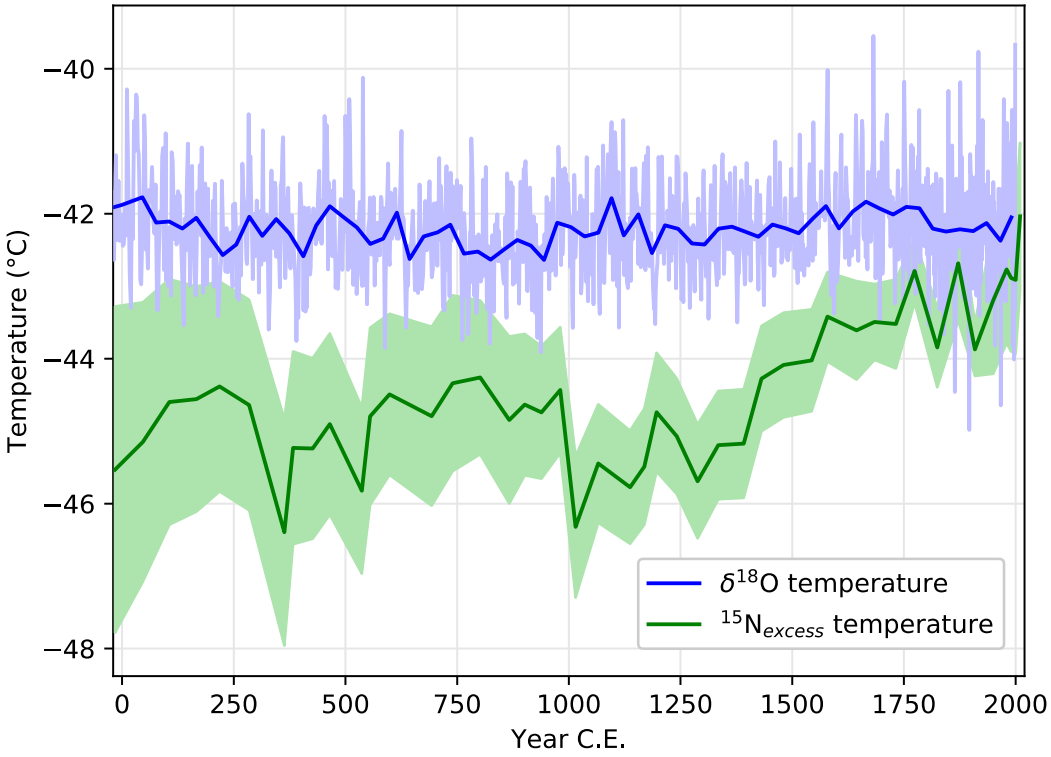

Figure 7.1. Temperature reconstructions at ABN from $\delta^{18}O$ in the ice (full resolution in light blue, 30-year average in dark blue) and $^{15}N_{excess}$ in the gases (best reconstruction is shown with dark green).

The two temperature reconstructions for ABN appear to differ significantly: while the $\delta^{18}O$-temperature suggests stable conditions with a temperature remaining close to -42 ± 1°C for the past 2000 years, the $^{15}N_{excess}$-temperature shows more variability, and a generally lower temperature. The $^{15}N_{excess}$-temperature is especially marked by cold conditions during two phases, with excursions below -45°C from 300 to 550 CE, and from 1000 to 1400 CE. After 1400 CE, the $^{15}N_{excess}$-temperature gradually increased up to the recent annual mean of -42°C.

7.1.2 Possible causes for the divergence of temperature reconstructions

There are several reasons to why the two temperature records could differ. We will explore the multiple possibilities hereafter.

7.1.2.1 Moisture source effect on the $\delta^{18}O$

The $\delta^{18}O$ not only depends on the site temperature, but is also sensitive to the moisture source and conditions during evaporation (Jouzel et al., 2003). As detailed in Chapter 2, the second order water isotope proxies d_{excess} and $^{17}O_{excess}$ track the changes of conditions at the moisture source. Here, both d_{excess} and $^{17}O_{excess}$ shown in figure 7.2 remained relatively stable over the last 2000 years, arguing for consistence in the source conditions as well. The long term trend over the past 2000 years is +1.1 ‰ in d_{excess} (the 95% confidence interval is +0.9 to +1.4 ‰·2000 yr^{-1}), while the trend is not significant for $^{17}O_{excess}$. The d_{excess} signal has a detrended variability of ± 0.36 ‰ (1σ), and we do not identify notable extreme events outside of this range. This evidence argues for stable air mass pathways through the past 2000 years.

The $^{17}O_{excess}$ signal has a mean value of 18 ppm, and a standard deviation of 7 ppm. Variations of $^{17}O_{excess}$ at ABN are in the range of what has been observed in snow pits and surface snow on the Antarctic Plateau (Winkler et al, 2013; Touzeau et al., 2016). We identify some events with distinct $^{17}O_{excess}$ signature (outside of mean value, ±1σ): a more positive phase of $^{17}O_{excess}$ at 30 ppm from 800 to 900 CE, and a very low phase around 5 ppm from 1340 to 1440 CE. These changes may be related to changes in the location of the moisture source, with changing storm tracks. The short temporal extent and low number of points during these $^{17}O_{excess}$ excursions limit our interpretations, and would need additional high resolution measurements for confirmation. On the long term, the data suggest that the moisture source remained roughly similar during the last 2000 years.

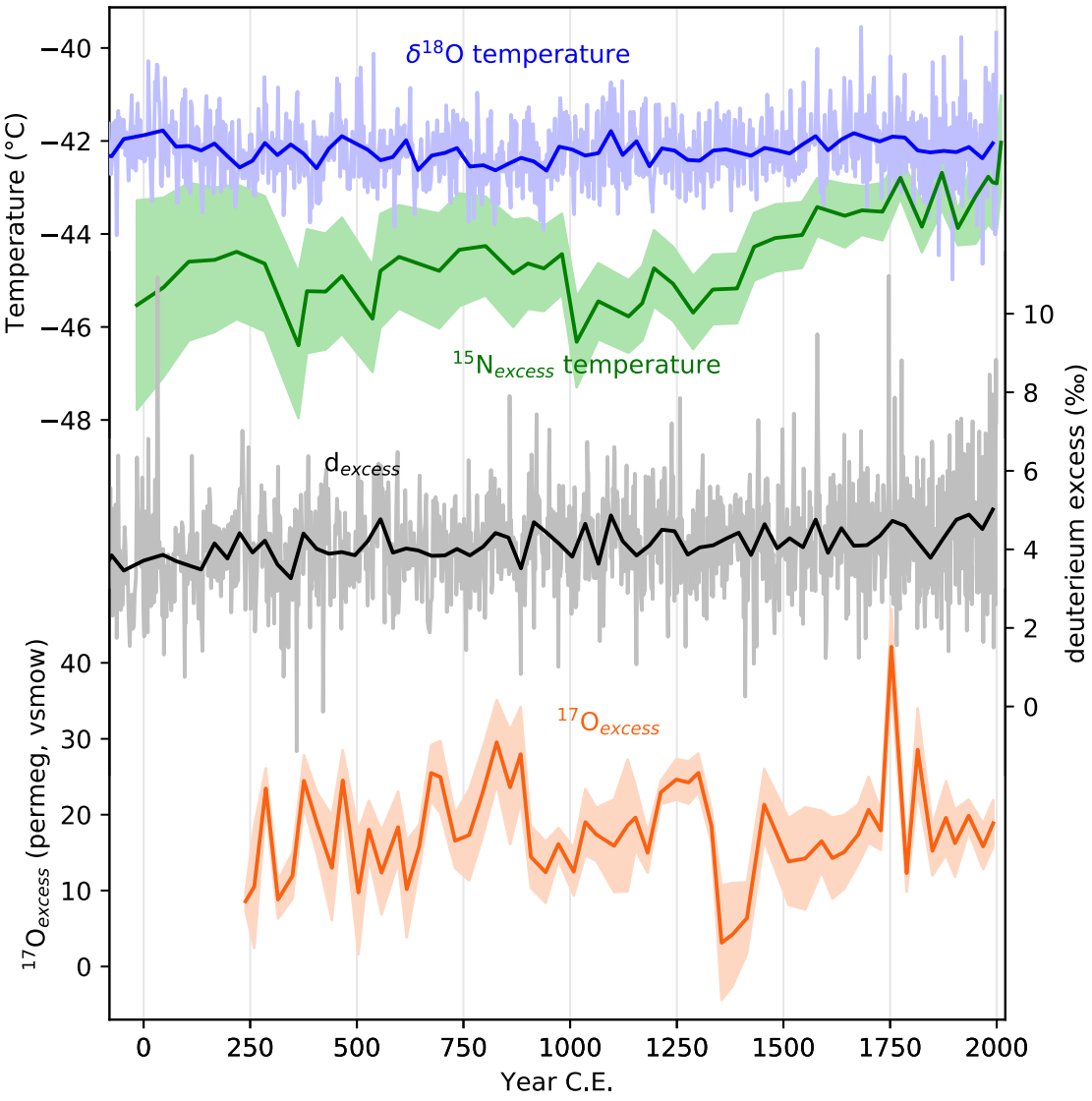

Figure 7.2. Comparison of (**a**) $\delta^{18}O$-temperature, (**b**) $^{15}N_{excess}$-temperature, (**c**) d_{excess}, and (**d**) $^{17}O_{excess}$ from the ABN1314 core.

Consequently, water isotopes generally support that the pathways and conditions during precipitations reaching the East Antarctic Plateau and ABN did not change significantly, and while we see variations in the $^{17}O_{excess}$, they do not fully cover the periods of lower surface

temperature. It is unlikely that a moisture source change alone would explain the difference in the temperature records.

7.1.2.2 Boundary layer changes

The $\delta^{18}O$ of precipitation primarily depends on cloud temperature, as described in isotopic models (Ciais & Jouzel, 1994; Jouzel & Merlivat, 1984) and on-site studies (Stenni et al., 2016). On the other hand, the $^{15}N_{excess}$-temperature tracks changes in the snow, at the surface. However, there is a large temperature gradient in the atmospheric column over the Antarctic Plateau, with a temperature inversion especially strong during the coldest months (Hudson & Brandt, 2005). Variations of the temperature inversion in the stable boundary layer, and by extent the gradient between cloud level and surface, could cause the discrepancy between the two temperature reconstructions at ABN. If this hypothesis is valid, it would indicate that the recent period is associated with a reduction of the surface temperature inversion, inducing more turbulence in the boundary layer. The surface temperature inversion is frequently larger than 10°C between the surface and the top of the boundary layer, and larger than 2°C for the top 20m (Hudson & Brandt, 2005), so a change on the order of 2°C is plausible.

There is a dual influence of katabatic surface winds on surface temperature: on one hand they bring dry and cold air from the higher elevations on the plateau to the ABN site reducing the surface temperature and increasing the surface temperature inversion. On the other hand, stronger winds could be associated with increased turbulence that would tend to reduce the temperature inversion and warm the surface (Van Den Broeke & Van Lipzig, 2003). Analysis of aerosol ions and dust in the ice core may help clarify the origin of air masses reaching ABN, and thus inform on the wind regimes that are related to turbulence and the intensity of

the temperature inversion. This work is currently ongoing at the Australian Antarctic Division.

7.1.2.3 Change in seasonality of the precipitation events

A change in the seasonality of precipitation could also explain the increased temperature difference between surface and cloud temperatures: because the precipitations are intermittent, they do not necessarily represent equally the warm and cold seasons. This is particularly true for Antarctica, where a few extreme precipitation events can account for most of the yearly precipitations (Turner et al., 2019; see Chapter 3).

The temperature inversion, causing the difference between surface temperature and cloud-level temperature, is larger in winter. It could be responsible for a greater difference in the two records if more precipitation occurred in winter. In addition, we showed in Chapter 3 that there is a positive temperature anomaly during precipitation events that is more important during the winter at ABN. These two mechanisms point that a redistribution of precipitation events toward winter precipitations would cause the $\delta^{18}O$-temperature to be significantly warmer than the surface temperature as recorded in $^{15}N_{excess}$. However, the increase of winter precipitation would also be associated with colder temperature recorded in the $\delta^{18}O$, because the precipitation would mainly occur in the cold months. As a general rule, we would expect a greater difference between $\delta^{18}O$ (cloud) temperature and $^{15}N_{excess}$ (surface) temperature when both records indicate colder conditions, which is not clearly happening here.

Alternatively, the suppression of winter precipitation as temperature gets colder would cause $\delta^{18}O$ to stay elevated, even if the mean annual temperature would drop. Similarly, the decreased d_{excess} in the late winter months inferred from ECHAM5-wiso would not be recorded in absence of winter precipitation. Generally speaking, multiple lines of evidence indicate a sensitivity of precipitation to temperature of 5% $°C^{-1}$ over Antarctica as a whole

(Frieler et al., 2015). This hypothesis is compatible with the reduction of meridional moisture flux over the Indian Ocean during positive SAM anomalies, and related reduction in precipitation over Wilkes land (Marshall et al., 2017).

7.1.2.4 Post deposition effects on water stable isotopes

The snow isotopic composition is not definitively acquired in the cloud during precipitation. Indeed, the snow keeps exchanging isotopes with the atmosphere by sublimation – condensation processes, as the saturation pressure of vapor may vary with daily and annual cycles (Casado et al., 2018; Stenni et al., 2016). Winkler et al. (2013) estimated that sublimation at warmer temperature and recondensation could increase the $\delta^{18}O$ content of the snow, and reduce the $^{17}O_{excess}$ and the d_{excess}, especially for sites with strong katabatic winds and relatively warm temperature. Furthermore, the snow may be reworked and each snowfall event causes a patch of accumulation with horizontal heterogeneities in its thickness (Picard et al., 2019). Those patterns of accumulation cause some events to be overrepresented at a single point, thus shifting the average isotopic composition in a single core location, and was described as stratigraphic noise in the isotopic series (Münch et al., 2016). Finally, sublimation, diffusion and recondensation processes may also occur in the firn, where the vapor can move in the diffusive column, especially with the seasonal cycle that changes the temperature in the top 20 m of the firn (Johnsen et al., 2000). This diffusion results in a loss of high frequency signal, and may cause an artificial d_{excess} signal due to the differential diffusive speed of deuterium and oxygen (Jones et al., 2017).

Overall, most of these effect tend to homogenize the water stable isotopic composition of the snow column, which result in a lower variability and a lower sensibility to initial climate conditions (Casado et al., 2018). Even though the variability reduction is more evident

at higher frequencies, post-deposition processes could account for the lower temperature variability suggested by the $\delta^{18}O$ temperature $\delta^{18}O$-temperature. Despite this loss of signal on the shorter periods, it is possible to identify most annual layers in the ABN1314 ice core chemistry record, suggesting that the snow is not entirely mixed on the scale of a year. While the water stable isotopes have diffused and show less clear annual cycles, the signal is much clearer than high-plateau sites with lower accumulation, suggesting that the climate information may be better preserved at ABN than cores at Dome C, Vostok or Dome F, while depicting the climate variability of the East Antarctic plateau.

7.2 Teleconnections and climate variability in the southern hemisphere during the last 2000 years

7.2.1 Comparison with other ice cores in the region

We put the ABN $\delta^{18}O$ record in perspective with nearby ice core records covering the same time period in East Antarctica (figure 7.3). The three other ice core records introduced here, from Dome C (Jouzel et al., 2001; Masson-Delmotte et al., 2011), Talos Dome (Stenni et al., 2011) and Law Dome (PAGES 2k Consortium, 2013; Plummer et al., 2012) have very different average $\delta^{18}O$ values, owing to the different mean temperature and continentality of the sites where these ice cores were drilled. All the cores presented here were analyzed at a high vertical resolution, but ABN and Law Dome cores having higher accumulation provide a much higher temporal resolution. To be able to compare the $\delta^{18}O$ between the different sites, we computed 30-year averages for each site. The first similarity between all these ice core records is that they show relatively stable conditions over the last 2000 years, as the 30-year averages of $\delta^{18}O$ remain in a ± 1‰ range around the mean value.

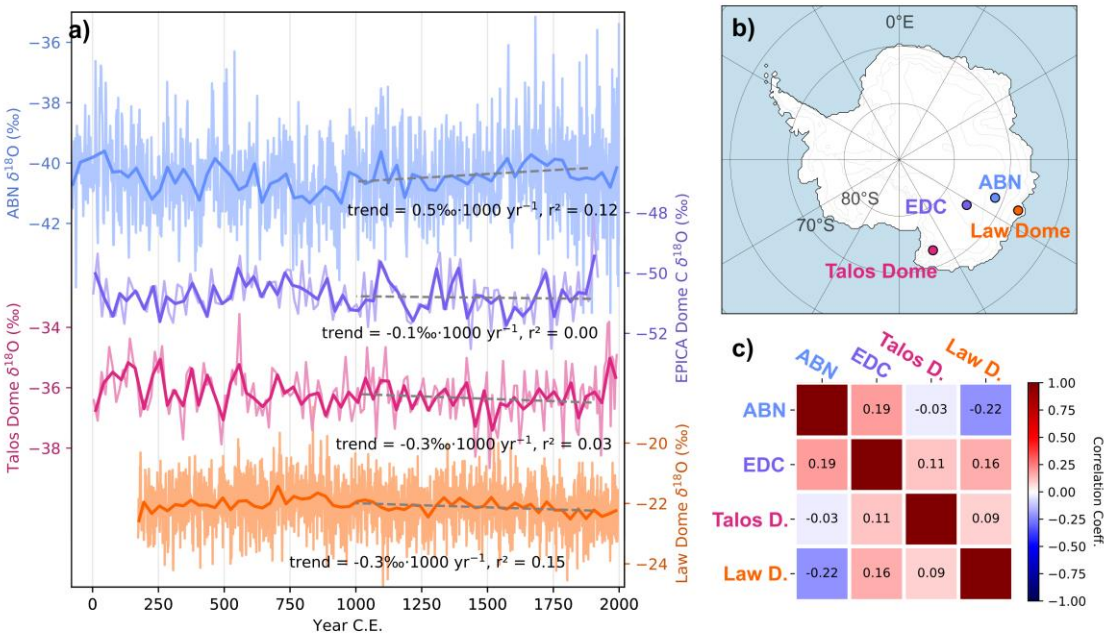

Figure 7.3. (**a**) Comparison of $\delta^{18}O$ in ice cores in East Antarctica, analyzed with a high resolution covering the last 2000 years. Thin lines show the full resolution on the original data, and thick dark lines represent 30-year averages. Dashed grey lines highlight the trend on the 1000 to 1900 CE period. (**b**) Map with the ice core locations. Thin lines indicate elevation levels every 1000 m. (**c**) Pearson correlation between the 30-year averaged $\delta^{18}O$ series. Data collected from Antarctica2k (Stenni et al., 2017), except for ABN.

The low correlation coefficients (figure 7.3c) between the different 30-year averaged $\delta^{18}O$ series suggest that the short term climate variability is not consistent across the continent. The synoptic events dominating the climate variability at shorter scales are not large enough to reach all the sites simultaneously (figure 7.4 and the corresponding discussion in section 4.4.2). Furthermore, the sites presented here have very different meteorological characteristics. Law Dome is a coastal site with high accumulation, and is influenced by nearby sea ice cover (Souney et al., 2002) as well as larger scale atmospheric circulation patterns (Schneider et al., 2006; Vance et al., 2015; Vance et al., 2013; see also the discussion in 7.2.3). At Dome C, the low accumulation allows for post-deposition processes to modify the

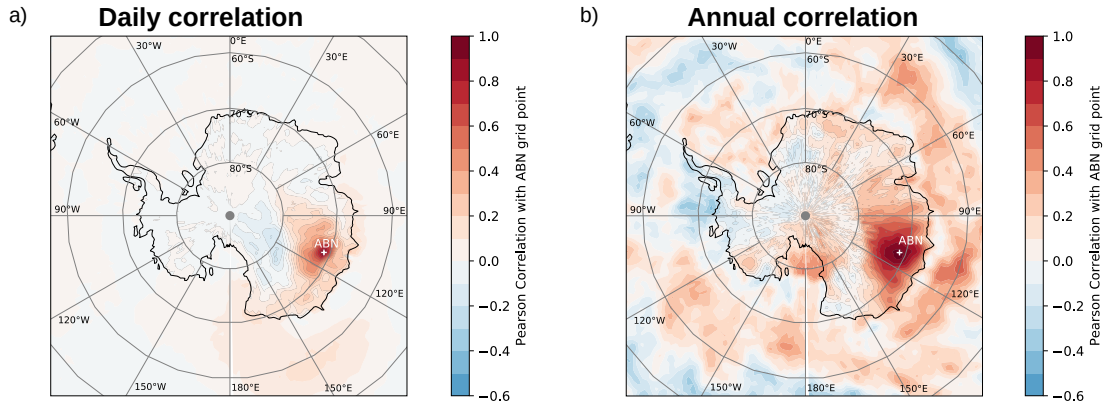

Figure 7.4. (a) Daily precipitation $\delta^{18}O$ correlation map with Aurora Basin North (white cross). (b) Yearly snowfall-weighted mean $\delta^{18}O$ correlation map with Aurora Basin North (white cross). The statistics have been computed from ECHAM5-wiso outputs on the 1979-2015 period. $\delta^{18}O$ of the precipitation only takes non-null value when there is precipitation on the site, so the correlation is constrained by the occurrence of precipitations. This figure is presented and fully discussed in section 4.4.2.

snow isotopic composition as it keeps exchanging with the atmosphere for an extended period of time (Masson-Delmotte et al., 2008; Stenni et al., 2016). In addition, clear sky precipitation (diamond dust) can represent a significant amount of the annual accumulation and have a very different isotopic signature than that of synoptic precipitation (Stenni et al., 2016). Talos Dome is a very singular site with moisture sources from both Indian and Pacific Oceans, and the relative contribution of each of these sources may significantly influence the $\delta^{18}O$ composition (Scarchilli et al., 2011). We observe no consistent excursion of $\delta^{18}O$ featured in the four records simultaneously at the centennial scale or below. This may be due to the distance between the coring sites, larger than the scale of synoptic events.

The comparison of temperature inferred from $\delta^{18}O$ in the Antarctica2k database, covering all the Antarctic continent showed that most regions were cooling during the last millennium, with decreasing $\delta^{18}O$ in ice cores through time (Stenni et al., 2017). The trends are computed on the 1000 to 1900 CE period to exclude any possible influence of recent warming

related to anthropogenic forcings. In the four records chosen here, ABN stands out by its weak positive trend of + 0.5‰ 1000 yr^{-1} ($r^2 = 0.12$, $p = 0.05$), while EPICA Dome C shows no significant trend ($r^2 = 0.0$), and Talos Dome and Law Dome have a decreasing $\delta^{18}O$ in the ice cores, of -0.3‰/1000 yr for Talos Dome ($r^2 = 0.03$, $p > 0.05$, not significant) and also -0.3‰1000 yr^{-1} for Law Dome ($r^2 = 0.15$, $p < 0.05$, significant). The opposite signs in the $\delta^{18}O$ trends at ABN and Law Dome for example may happen if these two sites respond differently to large-scale atmospheric variability.

This observation indicates that the large scale negative isotope trend is modulated locally by other influences that can dominate the signal, and that it remains difficult to extract common variability among the different records, even at millennial scale.

7.2.2 Influence of the Southern Annular Mode

In the southern Hemisphere, the atmospheric variability is dominated by the Southern Annular Mode (SAM), the first empirical orthogonal function of geopotential height, which shows the variation of the latitudinal pressure gradient (Gong & Wang, 1999; Marshall, 2003). Over the span of the satellite era (1979 onwards), the SAM was shown to influence the surface temperature and accumulation of many regions of Antarctica (Marshall et al., 2017; Marshall & Thompson, 2016). At ABN, and generally in East Antarctica, positive phases of the SAM tend to isolate the continent and cool the surface temperature by reducing meridional heat advection from warmer lower latitudes.

There is a complex interaction between the SAM and surface winds in Antarctica. Positive phases of the SAM enhance westerly flow and reduce the surface easterlies in some coastal regions, which leads to decreased turbulent heat flux in the inversion layer, resulting in a surface cooling (Marshall et al., 2013; Van Den Broeke & Van Lipzig, 2003). However, colder surface generally enhances katabatic flow, advecting cold air from plateau regions,

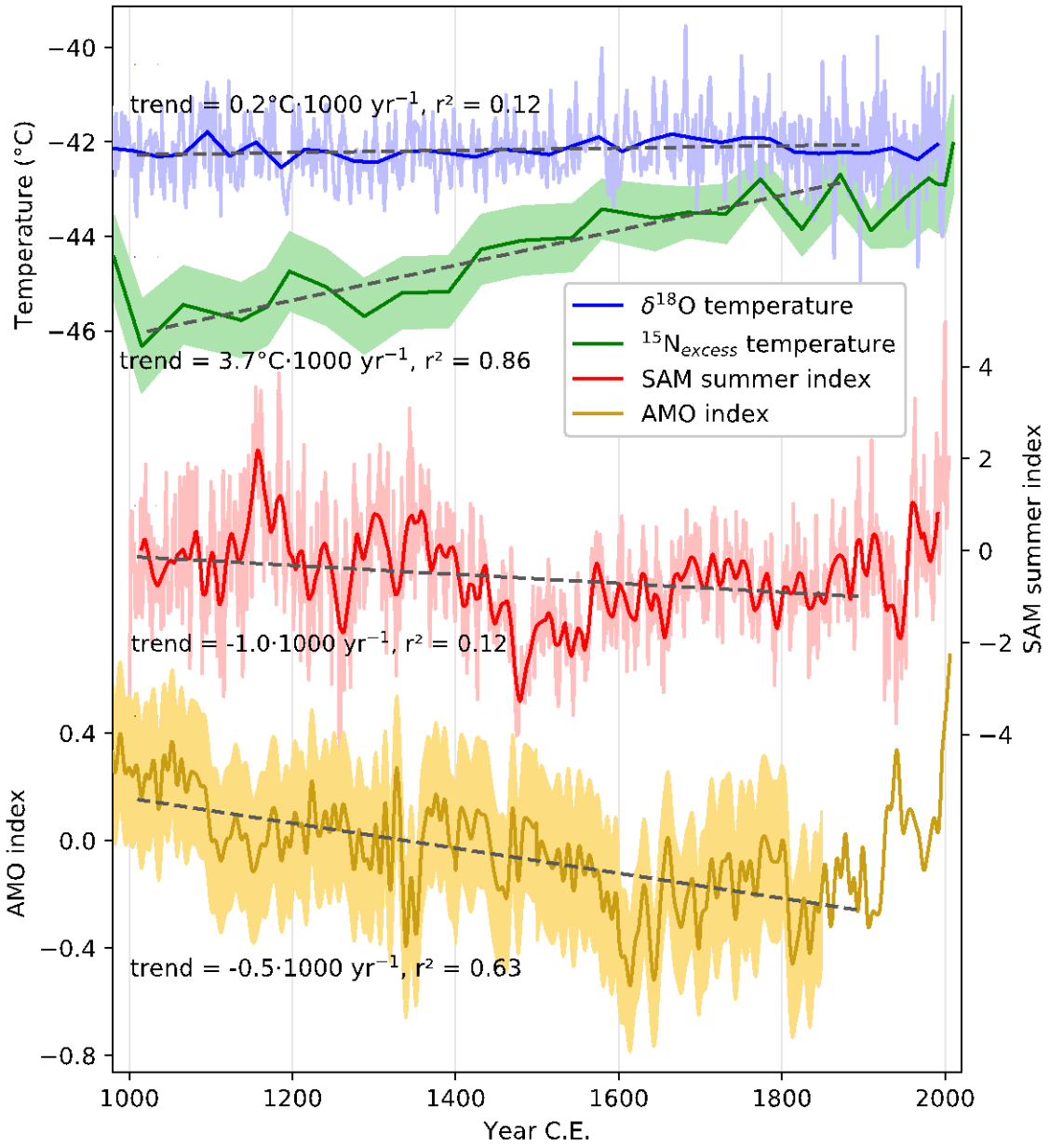

Figure 7.5. (**a**) $\delta^{18}O$-temperature and (**b**) $^{15}N_{excess}$-temperature records at ABN. Thin lines for $\delta^{18}O$ temperature show the full resolution, and thick blue line represent 30-year averages. The green shading on $^{15}N_{excess}$-temperature shows the confidence intervals of the reconstruction (this work). (**c**) SAM summer index reconstructed from a variety of proxies in the southern high latitudes (Dätwyler et al., 2018) at full resolution (light red) and 30-year filtered (red). (**d**) Atlantic Multidecadal Oscillation index reconstruction (Mann et al., 2009), discussed in section 7.2.5. For each record, the 1000 – 1900 CE trend is shown with dashed grey lines, with slope values and correlation with the record indicated below.

with a negative feedback on temperature. In the ABN region, the changes in wind regimes are negligible, with no impact on turbulent flux. Cooling related to reduced meridional flow will be the dominant effect on temperature at ABN (Van Den Broeke & Van Lipzig, 2003). Because meridional flow is also responsible for precipitations at ABN, the SAM is only weakly correlated with water stable isotopes, even though it is significantly correlated with average temperature (Abram et al., 2014; Chapter 4).

Dätwyler et al., (2018) used the paleo temperature data collection of Pages2k to estimate the past variability of the SAM during the last 1000 years. By carefully selecting sites in the medium to high southern latitudes, and proxies that show significant correlation with SAM indexes (Fogt et al., 2009; Marshall, 2003) on historical periods, they used a Correlation Plus Stationarity method to extend the time period covered by SAM index. The Dätwyler SAM reconstruction (shown in figure 7.5) improves previous SAM reconstructions (e.g. Abram et al., 2014) by including records from Australasian region. This is particularly important as SAM depicts a roughly zonally symmetric variability pattern, and the ABN site is particularly sensitive to pressure on the Indian sector of the Southern Ocean (Chapter 3), which should be better recorded in Australian sites.

The SAM index shows important variations during the past 1000 years. While it was at a near-present level during the 1000 to 1400 CE period, it decreased by about 2 points in 100 years and remained below zero during second half of the record, up until 1900 CE. During the most recent 100 years, the SAM index increased again to reach 1 in 2000 CE.

The variations of surface temperature recorded in the $^{15}N_{excess}$ mirror the SAM changes prior to 1900 CE. The positive phase of the SAM from 1000 to 1400 CE is concurrent with low snow temperature at ABN, and the subsequent decrease of the SAM index corresponds to the onset of a surface warming. Consequently, the 1000 to 1900 CE trends in $^{15}N_{excess}$ temperature and SAM have opposite signs. This negative correlation is consistent with the

observations on the recent period presented above: an extended positive phase of the SAM at the beginning of the record matches with low surface temperature. The $\delta^{18}O$-temperature shows much lower temperature variability during the large SAM changes of the last millenium. Stronger temperature gradient between surface and cloud level could be favored by strong radiative cooling of the surface during the positive SAM phase in the 1000 to 1400 period. Conversely, the more negative phase of the SAM from 1400 to 1900 corresponds to a reduced temperature inversion in ABN temperature. The variability of the SAM is consistent with the hypothesis of a change in temperature gradient between surface and cloud levels.

However, the most negative phase of the SAM index centered around 1500 CE is not matched by at temperature minimum at ABN. This points to the complexity of atmospheric circulation around Antarctica, and we don't expect that the excursions of one zonally symmetric index would map precisely on the temperature, or temperature gradient at ABN.

For the most recent part of the record, after 1900 CE, we observe an increase in surface temperature at ABN as well as a more positive SAM index. This apparent correlation results from anthropogenic forcings: first, the increase in greenhouse gases tends to generally warm the atmosphere, and second, ozone depletion has forced the SAM in a more positive phase (Roscoe & Haigh, 2007).

Because the $\delta^{18}O$-temperature remained very stable over the last 1000 years, it does not show consistent changes during the large shifts in SAM. Indeed, changes in the SAM also affect the blockings that are necessary for large precipitation events to reach the ABN site (Chapter 3, Servettaz et al., 2020). Atmospheric reanalyzes show that a positive SAM index favors reduced meridional moisture transport, and reduced precipitation in some regions of the East Antarctic Plateau (Marshall et al. 2017). By reducing the blockings, it is possible that more positive phases of the SAM become underrepresented in the precipitation proxy,

exacerbating the isotopic signal of warm events. A glaciology-corrected accumulation record could help clarify whether more positive phases of the SAM would lower the accumulation in East Antarctica, as this is the case for Law Dome in observations (Marshall et al., 2017). However, reconstructing accumulation from a single ice core with clear influence of spatial variations (section 5.5) would require dedicated work with ice flow model, and is beyond the scope of this study. As a general rule, it seems that the $\delta^{18}O$-temperature does not respond as intensely as $^{15}N_{excess}$-temperature to changes in the SAM, consistently with the results discussed in Chapter 4. The difference between the two temperature reconstructions is compatible with a reduction of winter precipitation during positive SAM periods.

To sum up, the snow temperature record indicates cooler surface temperature and a stronger temperature inversion during the period 1000 to 1400 CE, which is consistent with the positive SAM index, and associated reduced meridional heat and moisture advection.

7.2.3 Relationship with sea ice records

In addition to Antarctic surface temperature, the Southern Annular Mode (SAM) regulates many processes in both the Antarctic continent but also the mid latitudes through the influence of the Southern Westerly Winds (Thompson & Solomon, 2002).

The SAM influences sea-ice extent as more poleward cyclones favor the opening of ice-forming polynyas and sea-ice equatorward export (Pezza et al., 2012). Although the current paleo sea ice records do not allow for a millennial-length reconstruction of sea-ice extent around the entire Antarctic continent (Thomas et al., 2019), recent studies of diatom assemblages support an extended duration of the winter sea-ice coverage offshore the Adélie Coast in the more positive phases of the SAM, before 1500 CE (Crosta, 2020, personal communication). Ongoing analyses of methanesulfonic acid in the Law Dome ice core, a proxy that showed good correlation with sea-ice extent (Curran et al., 2003) may help clarify the past

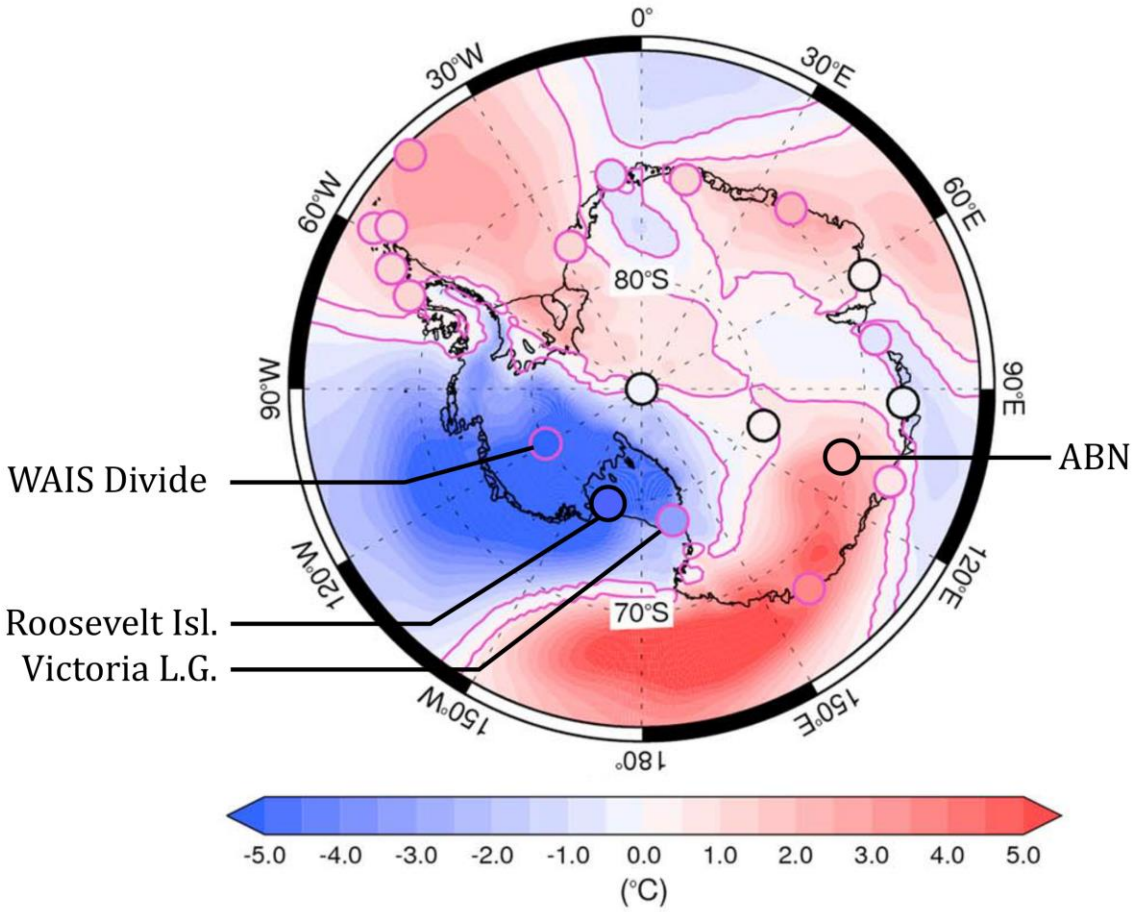

Figure 7.6. Differences in mean daily Surface Air Temperature anomalies between the positive and negative polarities of PSA2 pattern. The purple contour represents regions where the difference is significant at the $p<0.05$ level. Similarly, stations where the difference is significant at the $p<0.05$ level are represented as a purple circle. Locations discussed in the text are indicated: ABN – Aurora Basin North, WAIS – West Antarctic Ice Sheet, Victoria L. G. – Victoria lower Glacier. Figure modified from (Marshall & Thompson, 2016).

changes in sea-ice coverage during the past 2000 years (Curran, 2020, personal communication). Together, these observations indicating larger sea ice extent complement our record of cold temperature and strong surface temperature inversion before 1500 CE. Sea ice extent can influence the water isotope record, by limiting local sources of moisture during large sea ice extent excursions, but this effect is mostly important for coastal cores (e.g. Bertler et al., 2018). Although we do not expect sea ice to influence temperature or isotopes at ABN, it

further supports the signature of positive SAM phase in the Wilkes Land region. Upcoming analyses of sea ice proxies in the ABN cores will provide additional constraints on sea ice.

7.2.4 Relationship with Pacific South America patterns

Antarctic variability is also affected by the Pacific-South America patterns (PSA). They are characterized by a pressure dipole over the South Pacific, centered over the Amundsen sea for PSA1, and the Ross sea for PSA2. Both these patterns are linked to the central tropical pacific connection via Rossby wave trains, and are associated with ENSO variability (Ding et al., 2011). The strongest effect is felt in West Antarctica, but PSA2 also exhibits a dipole between West Antarctica including the Ross sea, and Wilkes land (Marshall et al., 2017; Marshall & Thompson, 2016). The positive phase of PSA2 is associated with the anticyclonic center positioned at 150°W, over the Ross sea, creating a dipole over the Ross Ice shelf, with increased marine air masses over the Indian Ocean facing Victoria Land, on East Antarctica, and increased katabatic drainage over the Eastern side and West Antarctica (Marshall & Thompson, 2016, figure 7.6).

Both the West Antarctic Ice Sheet Divide site (79°S, 112°W) and Victoria Lower Glacier (77.2°S, 166.5°E) experienced warmer conditions during 1000 – 1400 CE, and colder conditions thereafter, in contrast with ABN. These observations indicate that the PSA2 pattern may have been in a more negative phase during 1000 – 1400 CE, which means that the Amundsen sea low pressure system was more towards the Amundsen sea than the Ross sea. Lower sea ice extent during this period is thought to cause the increased accumulation observed in Roosevelt Island ice core in Eastern Ross Sea (Bertler et al., 2018) which supports the hypothesis of a negative PSA2 pattern.

During the period of most negative SAM (1400 – 1700 CE), cold conditions prevailed over the whole Ross Sea region (Bertler et al., 2011; Rhodes et al., 2012; Steig et al., 1998;

Stenni et al., 2011), with more extensive sea ice and more intense katabatic flow in the Western Ross sea (Bertler et al., 2011). Both West Antarctica and Victoria Land show below average accumulation (Bertler et al., 2011), while the accumulation at Roosevelt Island starts a decreasing trend. This homogeneity points to a neutral phase of the PSA2 pattern, and generally weaker cyclonic activity (Bertler et al., 2018). At ABN, surface temperature continues to rise, and the difference between surface and cloud temperature reduces. Both positive PSA2 and negative SAM trends support the warming trend at ABN.

7.2.5. Inter-hemispheric coupling

Recent studies of the Atlantic Multidecadal Oscillation (AMO), a large scale pattern of North Atlantic sea surface temperature (SST) variability with an estimated period of 60-80 years, have shown linkages between North Atlantic SST variability and Southern Ocean SST (Chylek et al., 2010; Wang et al., 2015). The AMO is thought to be related to modes of variability of the Atlantic Meridional Overturning circulation (AMOC), and to solar forcing (e.g. Delworth & Mann, 2000; Drinkwater et al., 2014). The AMO has an impact on the latitudinal position of the Inter Tropical Convergence Zone, influencing tropical rainfall (Knight et al., 2006), and the latitudinal position of the Westerly wind belt. It is thus expected to have impact on Antarctic temperature related to SAM variability. Specifically, Li et al. (2015) have shown that elevated temperature in the tropical Atlantic related to the AMO triggers Rossby waves that propagate to the Southern high latitudes, and cause a strengthening of the Amundsen sea low, as well as an elevated SAM index, with warming on the Antarctic peninsula, and cooling over the Antarctic continent.

Interhemispheric coupling has been discussed in light of Antarctic ice core data during Greenland abrupt warming events in the last glacial period, named Dansgaard-Oeschger events (Buizert et al., 2018; Markle et al., 2017). Similarly here, the low temperature at ABN

and positive phase of the SAM between 1000 and 1400 CE are concurrent to an extended positive phase of the Atlantic Multidecadal Oscillation and a warm period in the North Atlantic, which gradually decreases until 1600 CE (figure 7.5, Diaz et al., 2011; Graham et al., 2011). Even with low intensity, our data support the role of inter-hemispheric teleconnections in the most recent 2000 years.

7.3 Conclusions

We presented two temperature reconstructions from the Aurora Basin North (ABN) ice core. The $\delta^{18}O$-temperature, sensitive to temperature at the cloud level remained relatively stable over the last 2000 years with a very low trend increase during the 1000 – 1900 CE period. On the other hand, the $^{15}N_{excess}$-temperature shows much more variability with cold period when the average temperature was 3°C cooler than present, especially between 1000 and 1400 CE. Among other hypothesis, the strengthening of near-surface temperature inversion and suppression of winter precipitation are the most probable causes for the lowering of snow surface temperature recorded in the $^{15}N_{excess}$, while the temperature at the cloud level influencing the $\delta^{18}O$ did not vary as much in amplitude. These hypotheses are further supported by southern annular mode (SAM) reconstructions, which show an extended positive phase during the same period: it has been shown from recent climate re-analyses that positive phases of the SAM tend to isolate the Antarctic continent by reducing the meridional transport of heat and moisture.

The water stable isotopes, used to trace local temperature ($\delta^{18}O$) and moisture source conditions (d_{excess}, $^{17}O_{excess}$), showed no millennial trend, arguing for consistent moisture source and transport to the site during the last 2000 years. The temperature of the source ocean and the atmosphere, above the surface inversion remained mostly similar during precipitation throughout the entire record. Synoptic events causing precipitation on the plateau

may have become less frequent during positive phases of the SAM, but kept their temperature characteristics.

The atmospheric teleconnections between Antarctica and North Atlantic described for present day observations (Li et al., 2014) and for the last glacial period (Markle et al., 2017) are consistent with the reconstructions on the last 1000 years, as low temperature in East Antarctica related to a positive SAM phase coincide with warm North Atlantic phase (Diaz et al., 2011; PAGES 2k Consortium, 2013). The period 1000 – 1400 CE was particularly cold at ABN, which is in contrast to the Ross sea and West Antarctic records, which were warmer during the first millennium. These observations indicate a low PSA2 pattern during that time.

The warm period from 1000 to 1400 CE in the North Atlantic favored a high AMO index and teleconnections to a positive SAM, which favored cold conditions on the Antarctic continent. A negative PSA2 pattern further enhanced the cooling trend at ABN compared to the Ross sea and West Antarctica. The following period (1400 – 1700) was characterized by decreasing SAM index and a more neutral phase of the PSA2, and the surface temperature at ABN increased progressively, to stable conditions after 1800.

This work highlights the importance of using diverse paleoclimate reconstructions in ice covered regions, as the most used water isotope proxy may be spatially restricted to the cloud level, and temporally restricted to the precipitation events, and therefore miss large surface temperature changes in East Antarctica. Understanding of the causes of surface temperature changes at ABN may be improved with reconstructions of wind conditions and air mass influences with distinct aerosol signatures, which are currently undergoing analysis.

Chapter 8

Conclusion and perspectives

8.1 The Aurora Basin North temperature record

Antarctic climate is closely interacting with the Southern Ocean, which is critically important for the global climate (Jones et al., 2016). Ice cores can provide additional information on past climate and help reconstruct the evolution of climate parameters on longer timescales. Yet, the uneven distribution of ice cores covering the last 2000 years do not allow for understanding of past temperature variability in East Antarctica. The last 2000 years are particularly important to provide a baseline of natural climate variability to compare with the recent warming observed in most regions around the globe (Abram et al., 2016). A new ice core drilled at Aurora Basin North (ABN, 71°S, 111°E) aims at increasing the coverage of 2000 year-long ice cores with an unprecedented temporal resolution on the East Antarctic Plateau.

Ice sheets are formed by accumulated snow that transformed to ice with increasing pressure, and can trap impurities and gases. Drilling ice cores gives access to ice formed in the past, and can provide information on past climates. The water constituting the ice comports stable isotopes that can be used as tracers of the hydrological cycle. The temperature in the cloud during precipitation formation is particularly important and will strongly influence the $\delta^{18}O$ in the snow and ice (Ciais & Jouzel, 1994; Dansgaard, 1964). However, processes altering the snow $\delta^{18}O$ may occur after its deposition (Casado et al., 2018; Steen-Larsen et al., 2014).

We use the polar-oriented atmospheric model MAR to characterize the temperature and precipitation variability at ABN. This site is highly correlated in temperature with most of continental Wilkes Land, and will be representative of the lower part of the East Antarctic

plateau. A few large precipitation events are responsible for most of the snow accumulation at ABN, but do not represent average conditions. We evidence a warm anomaly of about +2°C when ABN receives precipitations, because the moisture flux is associated with an atmospheric warming. We show that large events respond to regional climate variability, and occur during a blocking North-East of ABN, on the Wilkes Land Coast. This blocking in turn is favored during negative phases of the Southern Annular Mode (SAM), the main mode of variability in the southern hemisphere.

The co-occurrence of precipitations and warm anomalies may bias the water stable isotopes $\delta^{18}O$ and δD, usually measured in ice cores and used as a temperature proxy. We compare simulations of the isotope-enabled atmospheric general circulation model ECHAM5-wiso with three precisely dated, high-resolution snow records from ABN, and we evidence that warm phases with summer-like temperature in winter are well-recorded in the snow $\delta^{18}O$. However, the cold phases, when little to no precipitation occurs, in the absence of coastal blocking, may be underrepresented. While warm phases at ABN, coincident with negative SAM mode, leave their footprint in the snow $\delta^{18}O$, the cold phases with positive SAM mode are muffled; this is seen in the lower correlation between SAM and $\delta^{18}O$ than between SAM and temperature. We define a $\delta^{18}O$ – temperature slope based on the model surface temperature and local snow $\delta^{18}O$, at inter-annual scale, but keep in mind the possible bias towards warm events.

A 300-m-deep ice core was drilled at ABN to investigate past climate variability. We present the measurements performed on the ice core. The ice was dated back to 2700 years by annual layer counting and tied to West Antarctic ice sheet divide ice core chronology, with the sulfur signature of volcanic events. Using the age model and density measurements, we estimate the accumulation at the ABN coring site and show that it primarily varied because of the change in location of the coring site with ice flow: the temporal accumulation

record in the ice core mirrors recent accumulation patterns upstream from the coring location. During the past 2700 years, the site was displaced by 42 km. We estimate the impact of glaciological displacement on elevation and average site temperature. We also present measurements of water isotopes $\delta^{18}O$, $\delta^{17}O$ and δD, and their corresponding glaciological corrections. We propose a temperature history from the $\delta^{18}O$ record and the $\delta^{18}O$ – temperature slope established previously.

The $\delta^{18}O$ is hampered by high uncertainties and bias towards warm conditions. We present an alternative temperature reconstruction based on the measurement of argon and nitrogen stable isotopes in the ice core. We describe the extraction and deoxygenation protocol, and detail the measurement procedure on the mass spectrometer, with a number of corrections needed to achieve a very high analytical precision on $^{15}N_{excess}$ of 3 permeg. We use the isotopes thermal diffusion properties to estimate past temperature gradients in the firn. Finally, we inverse a firn advection-diffusion model to reconstruct the evolution of surface temperature, by combining the present day borehole temperature profile and past firn gradients. After glaciological correction on temperature, we have a second, independent temperature history recording changes in surface snow temperature.

The ABN ice core was used to reconstruct past temperature history using two different methods. The $\delta^{18}O$ is representative of the temperature at the cloud level and mostly during precipitation events ($\delta^{18}O$-temperature), whereas the temperature inversion from $^{15}N_{excess}$ and borehole temperature ($^{15}N_{excess}$-temperature) integrates temperature changes in the surface snow over timescales of about a decade. While the $\delta^{18}O$-temperature remained within a ± 1 °C range of variability with no significant changes during the last 2000 years, the $^{15}N_{excess}$-temperature suggests that phases with colder surface temperature at ABN prevailed around 300 – 500 CE and 1000 – 1400 CE, with temperature 3°C colder than present days. We discuss the possible causes for the temperature discrepancy, and suggest that suppression of

winter precipitation could further bias the $\delta^{18}O$-temperature towards warm summer conditions, while the average conditions were actually colder. This hypothesis is discussed against past SAM reconstructions for the last 1000 years (Dätwyler et al., 2018). An extended positive SAM phase during the 1000 – 1400 CE period supports the colder surface temperature and reduction of coastal blockings necessary to funnel precipitations inland East Antarctica. The cold temperature at ABN and a positive SAM phase are concurrent with a warm phase in the North Atlantic Ocean (Diaz et al., 2011; Graham et al., 2011), supporting interhemispheric coupling during the 1000 – 1400 CE period.

8.2 Perspectives

8.2.1 Explore the influence of other climate modes on ABN temperature

In the Chapter 7, we briefly compared the temperature at ABN with the temperature records in the Ross Sea and West Antarctic regions, where the climate is strongly influenced by Pacific-South America modes of variability (Marshall et al., 2017; Marshall & Thompson, 2016). This sensitivity to other atmospheric modes would require further investigation, on a similar level to the analysis of SAM influence on precipitations and temperature performed with MAR and ECHAM5-wiso models. These modes are comparatively under-documented and a better knowledge of their variability could help understand the past changes in Antarctic climate.

8.2.2 Confirm our interpretations with further analyses

The cold surface temperature during the 1000 – 1400 CE period at ABN, while little variation was found in $\delta^{18}O$ supports the hypothesis that winter precipitations were reduced under a more positive SAM phase. This hypothesis would require further confirmation.

A first possibility would be to characterize the signature of continental and oceanic air masses in the winter time, with signature in the aerosol composition and the chemistry of the ice. The aerosol signal could be compared with back-trajectories on the recent period to link the origin of air masses with their aerosol composition.

A second option is to evaluate the changes of conditions during precipitation under different SAM phases, with model simulations. It would be interesting to quantify changes in the warm bias associated with precipitations, and estimate the impact of SAM or other modes on the warm bias. Changes in precipitation seasonality and frequency cause the warm bias at ABN and should receive particular attention.

8.2.3 Further explore moisture source variability

We presented data of d_{excess} and $^{17}O_{excess}$, which did not show long-term trends in concordance with temperature changes at ABN. However, short-term changes in $^{17}O_{excess}$ were observed, which could indicate changes in the moisture source conditions. Analysis of the sources with atmospheric back-trajectories and improvement of the resolution of the $^{17}O_{excess}$ record could inform us on changes in the hydrological cycle.

8.2.4 Reproduce the $^{15}N_{excess}$ and borehole temperature inversion at other ice core locations

The new temperature record from ABN challenges the understanding of the climate history of the past 2000 years, indicating a cold medieval climate anomaly inland East Antarctica. We demonstrated that water isotope proxies under-estimate the temperature variability, but this results needs to be confirmed with measurements in other locations, where the $^{15}N_{excess}$ and borehole temperature inversion method can be applied. A good candidate would be a

short core in Droning Maud Land, the Atlantic region of East Antarctica, where we expect to get a clear signal from interhemispheric teleconnections.

This work presents a new temperature record, at Aurora Basin North, on the East Antarctic plateau, with high resolution over the last 2000 years. The good understanding of water stable isotopes, commonly measured as a temperature proxy, and the precise measurement of inert gases stable isotopes allowed us to characterize the variations of temperature in East Antarctica. In particular, our results suggest a cold medieval climate anomaly in continental Wilkes Land, driven by a positive phase of the Southern Annular Mode. This interpretation needs further study, and could be confirmed with other measurements in the same core and in the region.

References

Abram, N. J., McGregor, H. V., Tierney, J. E., Evans, M. N., McKay, N. P., & Kaufman, D. S. (2016). Early onset of industrial-era warming across the oceans and continents. *Nature*, *536*(7617), 411-418. https://doi.org/10.1038/nature19082

Abram, N. J., Mulvaney, R., Vimeux, F., Phipps, S. J., Turner, J., & England, M. H. (2014). Evolution of the Southern Annular Mode during the past millennium. *Nature Climate Change*, *4*(7), 564-569. https://doi.org/10.1038/nclimate2235

Agosta, C., Amory, C., Kittel, C., Orsi, A. J., Favier, V., Gallée, H., van den Broeke, M. R., Lenaerts, J. T. M., van Wessem, J. M., van de Berg, W. J., & Fettweis, X. (2019). Estimation of the Antarctic surface mass balance using the regional climate model MAR (1979–2015) and identification of dominant processes. *The Cryosphere*, *13*(1), 281-296. https://doi.org/10.5194/tc-13-281-2019

Alley, R. B., & Koci, B. R. (1990). Recent Warming in Central Greenland? *Annals of Glaciology*, *14*, 6-8. https://doi.org/10.3189/S0260305500008144

Altnau, S., Schlosser, E., Isaksson, E., & Divine, D. (2015). Climatic signals from 76 shallow firn cores in Dronning Maud Land, East Antarctica. *The Cryosphere*, *9*(3), 925-944. https://doi.org/10.5194/tc-9-925-2015

Angert, A., Cappa, C. D., & DePaolo, D. J. (2004). Kinetic 17O effects in the hydrologic cycle: Indirect evidence and implications1 1Associate editor: J. Horita. *Geochimica et Cosmochimica Acta*, *68*(17), 3487-3495. https://doi.org/10.1016/j.gca.2004.02.010

Arthern, R. J., Vaughan, D. G., Rankin, A. M., Mulvaney, R., & Thomas, E. R. (2010). In situ measurements of Antarctic snow compaction compared with predictions of models. *Journal of Geophysical Research: Earth Surface*, *115*(F3). https://doi.org/10.1029/2009JF001306

Aurora Basin: drilling ice cores in the heart of Antarctica. (s. d.). [5 january 2021] https://www.antarctica.gov.au/science/climate-processes-and-change/antarctic-palaeoclimate/aurora-basin/

Bader, H. (1964). Density of ice as a function of temperature and stress. *This Digital Resource Was Created from Scans of the Print Resource*. https://erdc-library.erdc.dren.mil/jspui/handle/11681/11579

Barkan, E., & Luz, B. (2005). High precision measurements of17O/16O and18O/16O ratios in H2O. *Rapid Communications in Mass Spectrometry*, *19*(24), 3737-3742. https://doi.org/10.1002/rcm.2250

Bender, M. L., Floch, G., Chappellaz, J., Suwa, M., Barnola, J.-M., Blunier, T., Dreyfus, G., Jouzel, J., & Parrenin, F. (2006). Gas age–ice age differences and the chronology of the Vostok ice core, 0–100 ka. *Journal of Geophysical Research: Atmospheres*, *111*(D21). https://doi.org/10.1029/2005JD006488

Bertler, N.A.N., Mayewski, P. A., & Carter, L. (2011). Cold conditions in Antarctica during the Little Ice Age — Implications for abrupt climate change mechanisms. *Earth and Planetary Science Letters*, *308*(1-2), 41-51. https://doi.org/10.1016/j.epsl.2011.05.021

Bertler, Nancy A. N., Conway, H., Dahl-Jensen, D., Emanuelsson, D. B., Winstrup, M., Vallelonga, P. T., Lee, J. E., Brook, E. J., Severinghaus, J. P., Fudge, T. J., Keller, E. D., Baisden, W. T., Hindmarsh, R. C. A., Neff, P. D., Blunier, T., Edwards, R., Mayewski, P. A., Kipfstuhl, S., Buizert, C., … Zhang, X. (2018). The Ross Sea Dipole – temperature, snow accumulation and sea ice variability in the Ross Sea region, Antarctica, over the past 2700 years. *Climate of the Past*, *14*(2), 193-214. https://doi.org/10.5194/cp-14-193-2018

Bigg, G. R., & Rohling, E. J. (2000). An oxygen isotope data set for marine waters. *Journal of Geophysical Research: Oceans*, *105*(C4), 8527-8535. https://doi.org/10.1029/2000JC900005

Blunier, T., Chappellaz, J. A., Schwander, J., Barnola, J.-M., Desperts, T., Stauffer, B., & Raynaud, D. (1993). Atmospheric methane, record from a Greenland Ice Core over the last 1000 year. *Geophysical Research Letters*, *20*(20), 2219-2222. https://doi.org/10.1029/93GL02414

Boggs, P. T., Byrd, R. H., Rogers, J. E., & Schnabel, R. B. (1992). *User's reference guide for odrpack version 2.01: Software for weighted orthogonal distance regression*. https://doi.org/10.6028/NIST.IR.4834

Bonne, J.-L., Behrens, M., Meyer, H., Kipfstuhl, S., Rabe, B., Schönicke, L., Steen-Larsen, H. C., & Werner, M. (2019). Resolving the controls of water vapour isotopes in the Atlantic sector. *Nature Communications*, *10*(1), 1632. https://doi.org/10.1038/s41467-019-09242-6

Bony, S., Risi, C., & Vimeux, F. (2008). Influence of convective processes on the isotopic composition (δ18O and δD) of precipitation and water vapor in the tropics: 1. Radiative-convective equilibrium and Tropical Ocean–Global Atmosphere–Coupled Ocean-Atmosphere Response Experiment (TOGA-COARE) simulations. *Journal of Geophysical Research: Atmospheres*, *113*(D19). https://doi.org/10.1029/2008JD009942

Boyle, E. A. (1997). Cool tropical temperatures shift the global δ18O-T relationship: An explanation for the ice core δ18O - borehole thermometry conflict? *Geophysical Research Letters*, *24*(3), 273-276. https://doi.org/10.1029/97GL00081

Bromwich, D. H., Nicolas, J. P., & Monaghan, A. J. (2011). An Assessment of Precipitation Changes over Antarctica and the Southern Ocean since 1989 in Contemporary Global

Reanalyses. *Journal of Climate*, *24*(16), 4189-4209. https://doi.org/10.1175/2011JCLI4074.1

Buizert, C., Cuffey, K. M., Severinghaus, J. P., Baggenstos, D., Fudge, T. J., Steig, E. J., Markle, B. R., Winstrup, M., Rhodes, R. H., Brook, E. J., Sowers, T. A., Clow, G. D., Cheng, H., Edwards, R. L., Sigl, M., McConnell, J. R., & Taylor, K. C. (2015). The WAIS Divide deep ice core WD2014 chronology – Part 1: Methane synchronization (68–31 ka BP) and the gas age–ice age difference. *Climate of the Past*, *11*(2), 153-173. https://doi.org/10.5194/cp-11-153-2015

Buizert, C., Martinerie, P., Petrenko, V. V., Severinghaus, J. P., Trudinger, C. M., Witrant, E., Rosen, J. L., Orsi, A. J., Rubino, M., Etheridge, D. M., Steele, L. P., Hogan, C., Laube, J. C., Sturges, W. T., Levchenko, V. A., Smith, A. M., Levin, I., Conway, T. J., Dlugokencky, E. J., … Blunier, T. (2012). Gas transport in firn: multiple-tracer characterisation and model intercomparison for NEEM, Northern Greenland. *Atmospheric Chemistry and Physics*, *12*(9), 4259-4277. https://doi.org/10.5194/acp-12-4259-2012

Buizert, C., Sigl, M., Severi, M., Markle, B. R., Wettstein, J. J., McConnell, J. R., Pedro, J. B., Sodemann, H., Goto-Azuma, K., Kawamura, K., Fujita, S., Motoyama, H., Hirabayashi, M., Uemura, R., Stenni, B., Parrenin, F., He, F., Fudge, T. J., & Steig, E. J. (2018). Abrupt ice-age shifts in southern westerly winds and Antarctic climate forced from the north. *Nature*, *563*(7733), 681-685. https://doi.org/10.1038/s41586-018-0727-5

Casado, M., Landais, A., Picard, G., Münch, T., Laepple, T., Stenni, B., Dreossi, G., Ekaykin, A., Arnaud, L., Genthon, C., Touzeau, A., Masson-Delmotte, V., & Jouzel, J. (2018). Archival processes of the water stable isotope signal in East Antarctic ice cores. *The Cryosphere*, *12*(5), 1745-1766. https://doi.org/10.5194/tc-12-1745-2018

Casado, M., Münch, T., & Laepple, T. (2020). Climatic information archived in ice cores: impact of intermittency and diffusion on the recorded isotopic signal in Antarctica. *Climate of the Past*, *16*(4), 1581-1598. https://doi.org/10.5194/cp-16-1581-2020

Casado, M., Orsi, A. J., & Landais, A. (2017). On the limits of climate reconstruction from water stable isotopes in polar ice cores. *Past Global Changes Magazine*, *25*(3), 146-147. https://doi.org/10.22498/pages.25.3.146

Christiansen, B., & Ljungqvist, F. C. (2017). Challenges and perspectives for large-scale temperature reconstructions of the past two millennia. *Reviews of Geophysics*, *55*(1), 40-96. https://doi.org/10.1002/2016RG000521

Chylek, P., Folland, C. K., Lesins, G., & Dubey, M. K. (2010). Twentieth century bipolar seesaw of the Arctic and Antarctic surface air temperatures. *Geophysical Research Letters*, *37*(8). https://doi.org/10.1029/2010GL042793

Ciais, P., & Jouzel, J. (1994). Deuterium and oxygen 18 in precipitation: Isotopic model, including mixed cloud processes. *Journal of Geophysical Research*, *99*(D8), 16793. https://doi.org/10.1029/94JD00412

Climate Models | NOAA Climate.gov. (s. d.). [9 january 2021] https://www.climate.gov/maps-data/primer/climate-models

Clow, G. D. (2008). *USGS polar temperature logging system, description and measurement uncertainties* (US Department of the Interior, US Geological Survey).

Colbeck, S. C. (1982). An overview of seasonal snow metamorphism. *Reviews of Geophysics*, *20*(1), 45-61. https://doi.org/10.1029/RG020i001p00045

Cole-Dai, J., & Mosley-Thompson, E. (1999). The Pinatubo eruption in South Pole snow and its potential value to ice-core paleovolcanic records. *Annals of Glaciology*, *29*, 99-105. https://doi.org/10.3189/172756499781821319

Cole-Dai, J., Mosley-Thompson, E., Wight, S. P., & Thompson, L. G. (2000). A 4100-year record of explosive volcanism from an East Antarctica ice core. *Journal of Geophysical Research: Atmospheres*, *105*(D19), 24431-24441. https://doi.org/10.1029/2000JD900254

Craig, H., & Chou, C. C. (1982). Methane: The record in polar ice cores. *Geophysical Research Letters*, *9*(11), 1221-1224. https://doi.org/10.1029/GL009i011p01221

Craig, H., Horibe, Y., & Sowers, T. (1988). Gravitational Separation of Gases and Isotopes in Polar Ice Caps. *Science*, *242*(4886), 1675-1678. https://doi.org/10.1126/science.242.4886.1675

Craig, Harmon. (1961). Isotopic Variations in Meteoric Waters. *Science, New Series*, *133*(3465), 1702-1703.

Craig, Harmon, & Gordon, L. I. (1965). *Deuterium and oxygen 18 variations in the ocean and the marine atmosphere* (Conference on Stable Isotopes in Oceanographic Studies and Paleotemperatures, Éd.). Conference on Stable Isotopes in Oceanographic Studies and Paleotemperatures.

Criss, R. E. (1999). *Principles of Stable Isotope Distribution*. Oxford University Press, USA.

Cuffey, K. M., Clow, G. D., Alley, R. B., Stuiver, M., Waddington, E. D., & Saltus, R. W. (1995). Large Arctic Temperature Change at the Wisconsin-Holocene Glacial Transition. *Science*, *270*(5235), 455-458. https://doi.org/10.1126/science.270.5235.455

Cuffey, K. M., Clow, G. D., Steig, E. J., Buizert, C., Fudge, T. J., Koutnik, M., Waddington, E. D., Alley, R. B., & Severinghaus, J. P. (2016). Deglacial temperature history of West Antarctica. *Proceedings of the National Academy of Sciences*, *113*(50), 14249-14254. https://doi.org/10.1073/pnas.1609132113

Curran, M. (2015, avril 1). *Aurora Basin North (ABN) - a new 2000 year ice core record from East Antarctica*. EGU2015, Vienna, Austria. http://adsabs.harvard.edu/abs/2015EGUGA..17.3153C

Curran, M. A. J. (2014, février 27). *Aurora Basin: science and logistics*. Australian Antarctic Program. https://www.antarctica.gov.au/science/climate-processes-and-change/antarctic-palaeoclimate/aurora-basin/aurora-basin-science-and-logistics/

Curran, M. A. J., Ommen, T. D. van, Morgan, V. I., Phillips, K. L., & Palmer, A. S. (2003). Ice Core Evidence for Antarctic Sea Ice Decline Since the 1950s. *Science*, *302*(5648), 1203-1206. https://doi.org/10.1126/science.1087888

Dahl-Jensen, D., Mosegaard, K., Gundestrup, N., Clow, G. D., Johnsen, S. J., Hansen, A. W., & Balling, N. (1998). Past Temperatures Directly from the Greenland Ice Sheet. *Science*, *282*(5387), 268-271. https://doi.org/10.1126/science.282.5387.268

Dahl-Jensen, Dorthe, Morgan, V. I., & Elcheikh, A. (1999). Monte Carlo inverse modelling of the Law Dome (Antarctica) temperature profile. *Annals of Glaciology*, *29*, 145-150. https://doi.org/10.3189/172756499781821102

Dansgaard, W. (1964). Stable isotopes in precipitation. *Tellus*, *16*(4), 436-468. https://doi.org/10.1111/j.2153-3490.1964.tb00181.x

Dätwyler, C., Neukom, R., Abram, N. J., Gallant, A. J. E., Grosjean, M., Jacques-Coper, M., Karoly, D. J., & Villalba, R. (2018). Teleconnection stationarity, variability and trends of the Southern Annular Mode (SAM) during the last millennium. *Climate Dynamics*, *51*(5-6), 2321-2339. https://doi.org/10.1007/s00382-017-4015-0

Dee, D. P., Uppala, S. M., Simmons, A. J., Berrisford, P., Poli, P., Kobayashi, S., Andrae, U., Balmaseda, M. A., Balsamo, G., Bauer, P., Bechtold, P., Beljaars, A. C. M., Berg, L. van de, Bidlot, J., Bormann, N., Delsol, C., Dragani, R., Fuentes, M., Geer, A. J., … Vitart, F. (2011). The ERA-Interim reanalysis: configuration and performance of

the data assimilation system. *Quarterly Journal of the Royal Meteorological Society*, *137*(656), 553-597. https://doi.org/10.1002/qj.828

Delworth, T. L., & Mann, M. E. (2000). Observed and simulated multidecadal variability in the Northern Hemisphere. *Climate Dynamics*, *16*(9), 661-676. https://doi.org/10.1007/s003820000075

Diaz, H. F., Trigo, R., Hughes, M. K., Mann, M. E., Xoplaki, E., & Barriopedro, D. (2011). Spatial and Temporal Characteristics of Climate in Medieval Times Revisited. *Bulletin of the American Meteorological Society*, *92*(11), 1487-1500. https://doi.org/10.1175/BAMS-D-10-05003.1

Ding, Q., Steig, E. J., Battisti, D. S., & Küttel, M. (2011). Winter warming in West Antarctica caused by central tropical Pacific warming. *Nature Geoscience*, *4*(6), 398-403. https://doi.org/10.1038/ngeo1129

Drinkwater, K. F., Miles, M., Medhaug, I., Otterå, O. H., Kristiansen, T., Sundby, S., & Gao, Y. (2014). The Atlantic Multidecadal Oscillation: Its manifestations and impacts with special emphasis on the Atlantic region north of 60°N. *Journal of Marine Systems*, *133*, 117-130. https://doi.org/10.1016/j.jmarsys.2013.11.001

Edwards, T. L., Brandon, M. A., Durand, G., Edwards, N. R., Golledge, N. R., Holden, P. B., Nias, I. J., Payne, A. J., Ritz, C., & Wernecke, A. (2019). Revisiting Antarctic ice loss due to marine ice-cliff instability. *Nature*, *566*(7742), 58-64. https://doi.org/10.1038/s41586-019-0901-4

Ekaykin, A. A., Vladimirova, D. O., Lipenkov, V. Y., & Masson-Delmotte, V. (2017). Climatic variability in Princess Elizabeth Land (East Antarctica) over the last 350 years. *Climate of the Past*, *13*(1), 61-71. https://doi.org/10.5194/cp-13-61-2017

EPICA community members. (2004). Eight glacial cycles from an Antarctic ice core. *Nature*, *429*(6992), 623-628. https://doi.org/10.1038/nature02599

Fogt, R. L., Goergens, C. A., Jones, J. M., Schneider, D. P., Nicolas, J. P., Bromwich, D. H., & Dusselier, H. E. (2017). A twentieth century perspective on summer Antarctic pressure change and variability and contributions from tropical SSTs and ozone depletion. *Geophysical Research Letters*, *44*(19), 9918-9927. https://doi.org/10.1002/2017GL075079

Fogt, R. L., Perlwitz, J., Monaghan, A. J., Bromwich, D. H., Jones, J. M., & Marshall, G. J. (2009). Historical SAM Variability. Part II: Twentieth-Century Variability and Trends from Reconstructions, Observations, and the IPCC AR4 Models. *Journal of Climate*, *22*(20), 5346-5365. https://doi.org/10.1175/2009JCLI2786.1

Fourteau, K., Martinerie, P., Fain, X., Schaller, C. F., Tuckwell, R. J., Löwe, H., Arnaud, L., Magand, O., Thomas, E. R., Freitag, J. H., Mulvaney, R., Schneebeli, M., & Lipenkov, V. Y. (2019). Multi-tracer study of gas trapping in an East Antarctic ice core. *The Cryosphere*, *13*(12), 3383-3403. https://doi.org/10.5194/tc-2019-89

Fréville, H., Brun, E., Picard, G., Tatarinova, N., Arnaud, L., Lanconelli, C., Reijmer, C., & van den Broeke, M. (2014). Using MODIS land surface temperatures and the Crocus snow model to understand the warm bias of ERA-Interim reanalyses at the surface in Antarctica. *The Cryosphere*, *8*(4), 1361-1373. https://doi.org/10.5194/tc-8-1361-2014

Frieler, K., Clark, P. U., He, F., Buizert, C., Reese, R., Ligtenberg, S. R. M., van den Broeke, M. R., Winkelmann, R., & Levermann, A. (2015). Consistent evidence of increasing Antarctic accumulation with warming. *Nature Climate Change*, *5*(4), 348-352. https://doi.org/10.1038/nclimate2574

Galewsky, J., Steen-Larsen, H. C., Field, R. D., Worden, J., Risi, C., & Schneider, M. (2016). Stable isotopes in atmospheric water vapor and applications to the hydrologic cycle. *Reviews of Geophysics*, *54*(4), 809-865. https://doi.org/10.1002/2015RG000512

Gallée, H., Preunkert, S., Argentini, S., Frey, M. M., Genthon, C., Jourdain, B., Pietroni, I., Casasanta, G., Barral, H., Vignon, E., Amory, C., & Legrand, M. (2015). Characterization of the boundary layer at Dome C (East Antarctica) during the OPALE summer campaign. *Atmospheric Chemistry and Physics*, *15*(11), 6225-6236. https://doi.org/10.5194/acp-15-6225-2015

Genthon, C., Barnolat, J. M., Raynaudt, D., Loriust, C., Jouzel, J., Barkov, N. I., Korotkevich, Y. S., & Kotlyakov, V. M. (1987). *Vostok ice core: climatic response to C02 and orbital forcing changes over the last climatic cycle*. 5.

Gill, A. E. (1982). *Atmosphere—Ocean Dynamics*. Elsevier.

Ginot, P., Dumont, M., Lim, S., Patris, N., Taupin, J.-D., Wagnon, P., Gilbert, A., Arnaud, Y., Marinoni, A., Bonasoni, P., & Laj, P. (2014). A 10 year record of black carbon and dust from a Mera Peak ice core (Nepal): variability and potential impact on melting of Himalayan glaciers. *The Cryosphere*, *8*(4), 1479-1496. https://doi.org/10.5194/tc-8-1479-2014

Gkinis, V., Popp, T. J., Blunier, T., Bigler, M., Schüpbach, S., Kettner, E., & Johnsen, S. J. (2011). Water isotopic ratios from a continuously melted ice core sample. *Atmospheric Measurement Techniques*, *4*(11), 2531-2542. https://doi.org/10.5194/amt-4-2531-2011

Gong, D., & Wang, S. (1999). Definition of Antarctic Oscillation index. *Geophysical Research Letters*, *26*(4), 459-462. https://doi.org/10.1029/1999GL900003

Goujon, C., Barnola, J.-M., & Ritz, C. (2003). Modeling the densification of polar firn including heat diffusion: Application to close-off characteristics and gas isotopic fractionation for Antarctica and Greenland sites: A NEW FIRN DENSIFICATION MODEL. *Journal of Geophysical Research: Atmospheres*, *108*(D24), n/a-n/a. https://doi.org/10.1029/2002JD003319

Goursaud, S., Masson-Delmotte, V., Favier, V., Orsi, A. J., & Werner, M. (2018). Water stable isotope spatio-temporal variability in Antarctica in 1960–2013: observations and simulations from the ECHAM5-wiso atmospheric general circulation model. *Climate of the Past*, *14*(6), 923-946. https://doi.org/10.5194/cp-14-923-2018

Grachev, A. M., & Severinghaus, J. P. (2003a). Laboratory determination of thermal diffusion constants for 29N2/28N2 in air at temperatures from −60 to 0°C for reconstruction of magnitudes of abrupt climate changes using the ice core fossil–air paleothermometer. *Geochimica et Cosmochimica Acta*, *67*(3), 345-360. https://doi.org/10.1016/S0016-7037(02)01115-8

Grachev, A. M., & Severinghaus, J. P. (2003b). Determining the Thermal Diffusion Factor for 40Ar/36Ar in Air To Aid Paleoreconstruction of Abrupt Climate Change. *The Journal of Physical Chemistry A*, *107*(23), 4636-4642. https://doi.org/10.1021/jp027817u

Graf, W., Oerter, H., Reinwarth, O., Stichler, W., Wilhelms, F., Miller, H., & Mulvaney, R. (2002). Stable-isotope records from Dronning Maud Land, Antarctica. *Annals of Glaciology*, *35*, 195-201. https://doi.org/10.3189/172756402781816492

Graham, N. E., Ammann, C. M., Fleitmann, D., Cobb, K. M., & Luterbacher, J. (2011). Support for global climate reorganization during the “Medieval Climate Anomaly”. *Climate Dynamics*, *37*(5), 1217-1245. https://doi.org/10.1007/s00382-010-0914-z

Gupta, P., Noone, D., Galewsky, J., Sweeney, C., & Vaughn, B. H. (2009). Demonstration of high-precision continuous measurements of water vapor isotopologues in laboratory and remote field deployments using wavelength-scanned cavity ring-down spectroscopy (WS-CRDS) technology. *Rapid Communications in Mass Spectrometry*, *23*(16), 2534-2542. https://doi.org/10.1002/rcm.4100

Herron, M., M., & Langway, C., C. (1980). Firn Densification: An Empirical Model | Journal of Glaciology | Cambridge Core. *Journal of Glaciology*, *25*(93), 373-385. https://doi.org/doi.org/10.3189/S0022143000015239

Holme, C., Gkinis, V., & Vinther, B. M. (2018). Molecular diffusion of stable water isotopes in polar firn as a proxy for past temperatures. *Geochimica et Cosmochimica Acta*, *225*, 128-145. https://doi.org/10.1016/j.gca.2018.01.015

Hudson, S. R., & Brandt, R. E. (2005). A Look at the Surface-Based Temperature Inversion on the Antarctic Plateau. *Journal of Climate*, *18*(11), 1673-1696. https://doi.org/10.1175/JCLI3360.1

IAEA, I. A. E. A. (1995). *Reference and intercomparison materials for stable isotopes of light elements. Proceedings of a consultants meeting held in Vienna, 1-3 December 1993* (IAEA-TECDOC--825). International Atomic Energy Agency. http://inis.iaea.org/Search/search.aspx?orig_q=RN:27021327

Johnsen, S J. (1977). Stable isotope homogenization of polar firn and ice. *Isotopes and Impurities in Snow and Ice*, *118*, 210-219.

Johnsen, Sigfus J., Clausen, H. B., Cuffey, K. M., Hoffmann, G., Schwander, J., & Creyts, T. (2000). Diffusion of stable isotopes in polar firn and ice : the isotope effect in firn diffusion. *Physics of Ice Core Records*, 121-140.

Johnsen, Sigfus J., Dahl-Jensen, D., Dansgaard, W., & Gundestrup, N. (1995). Greenland palaeotemperatures derived from GRIP bore hole temperature and ice core isotope profiles. *Tellus B*, *47*(5), 624-629. https://doi.org/10.1034/j.1600-0889.47.issue5.9.x

Jones, J. M., Gille, S. T., Goosse, H., Abram, N. J., Canziani, P. O., Charman, D. J., Clem, K. R., Crosta, X., de Lavergne, C., Eisenman, I., England, M. H., Fogt, R. L., Frankcombe, L. M., Marshall, G. J., Masson-Delmotte, V., Morrison, A. K., Orsi, A. J., Raphael, M. N., Renwick, J. A., … Vance, T. R. (2016). Assessing recent trends

in high-latitude Southern Hemisphere surface climate. *Nature Climate Change*, *6*(10), 917-926. https://doi.org/10.1038/nclimate3103

Jones, T. R., Cuffey, K. M., White, J. W. C., Steig, E. J., Buizert, C., Markle, B. R., McConnell, J. R., & Sigl, M. (2017). Water isotope diffusion in the WAIS Divide ice core during the Holocene and last glacial. *Journal of Geophysical Research: Earth Surface*, *122*(1), 290-309. https://doi.org/10.1002/2016JF003938

Jouzel, J. (2003). Magnitude of isotope/temperature scaling for interpretation of central Antarctic ice cores. *Journal of Geophysical Research*, *108*(D12), 4361. https://doi.org/10.1029/2002JD002677

Jouzel, J., Masson, V., Cattani, O., Falourd, S., Stievenard, M., Stenni, B., Longinelli, A., Johnsen, S. J., Steffenssen, J. P., Petit, J. R., Schwander, J., Souchez, R., & Barkov, N. I. (2001). A new 27 ky high resolution East Antarctic climate record. *Geophysical Research Letters*, *28*(16), 3199-3202. https://doi.org/10.1029/2000GL012243

Jouzel, J., Masson-Delmotte, V., Cattani, O., Dreyfus, G., Falourd, S., Hoffmann, G., Minster, B., Nouet, J., Barnola, J. M., Chappellaz, J., Fischer, H., Gallet, J. C., Johnsen, S. J., Leuenberger, M., Loulergue, L., Luethi, D., Oerter, H., Parrenin, F., Raisbeck, G., … Wolff, E. W. (2007). Orbital and Millennial Antarctic Climate Variability over the Past 800,000 Years. *Science*, *317*(5839), 793-796. https://doi.org/10.1126/science.1141038

Jouzel, J., Vimeux, F., Caillon, N., Delaygue, G., Hoffmann, G., Masson-Delmotte, V., & Parrenin, F. (2003). Magnitude of isotope/temperature scaling for interpretation of central Antarctic ice cores. *Journal of Geophysical Research: Atmospheres*, *108*(D12), 4361-4372. https://doi.org/10.1029/2002JD002677

Jouzel, Jean, & Masson-Delmotte, V. (2010). Paleoclimates: what do we learn from deep ice cores? *Wiley Interdisciplinary Reviews: Climate Change*, *1*(5), 654-669. https://doi.org/10.1002/wcc.72

Jouzel, Jean, & Merlivat, L. (1984). Deuterium and oxygen 18 in precipitation: Modeling of the isotopic effects during snow formation. *Journal of Geophysical Research*, *89*(D7), 11749. https://doi.org/10.1029/JD089iD07p11749

Jullien, N., Vignon, É., Sprenger, M., Aemisegger, F., & Berne, A. (2020). Synoptic conditions and atmospheric moisture pathways associated with virga and precipitation over coastal Adélie Land in Antarctica. *The Cryosphere*, *14*(5), 1685-1702. https://doi.org/10.5194/tc-14-1685-2020

Kawamura, K., Severinghaus, J. P., Albert, M. R., Courville, Z. R., Fahnestock, M. A., Scambos, T., Shields, E., & Shuman, C. A. (2013). Kinetic fractionation of gases by deep air convection in polar firn. *Atmospheric Chemistry and Physics*, *13*(21), 11141-11155. https://doi.org/10.5194/acp-13-11141-2013

Keeley, S. (2013, décembre 17). *Climate reanalysis* [Text]. ECMWF. https://www.ecmwf.int/en/research/climate-reanalysis

Knight, J. R., Folland, C. K., & Scaife, A. A. (2006). Climate impacts of the Atlantic Multidecadal Oscillation. *Geophysical Research Letters*, *33*(17). https://doi.org/10.1029/2006GL026242

Kobashi, T., Severinghaus, J. P., & Kawamura, K. (2008). Argon and nitrogen isotopes of trapped air in the GISP2 ice core during the Holocene epoch (0–11,500 B.P.): Methodology and implications for gas loss processes. *Geochimica et Cosmochimica Acta*, *72*(19), 4675-4686. https://doi.org/10.1016/j.gca.2008.07.006

Laepple, T., Münch, T., Casado, M., Hoerhold, M., Landais, A., & Kipfstuhl, S. (2018). On the similarity and apparent cycles of isotopic variations in East Antarctic snow pits. *The Cryosphere*, *12*(1), 169-187. https://doi.org/10.5194/tc-12-169-2018

Landais, A., Barkan, E., & Luz, B. (2008). Record of δ18O and 17O-excess in ice from Vostok Antarctica during the last 150,000 years. *Geophysical Research Letters*, *35*(2), L02709. https://doi.org/10.1029/2007GL032096

Law, R., Christoffersen, P., Hubbard, B., Doyle, S., Chudley, T., Bougamont, M., & Schoonman, C. (2020). *Distributed fibre-optic temperature sensing in a 1 km borehole drilled on a fast-flowing glacier in Greenland* (N^{o} EGU2020-2433). Copernicus Meetings. https://doi.org/10.5194/egusphere-egu2020-2433

Li, X., Gerber, E. P., Holland, D. M., & Yoo, C. (2015). A Rossby Wave Bridge from the Tropical Atlantic to West Antarctica. *Journal of Climate*, *28*(6), 2256-2273. https://doi.org/10.1175/JCLI-D-14-00450.1

Li, X., Holland, D. M., Gerber, E. P., & Yoo, C. (2014). Impacts of the north and tropical Atlantic Ocean on the Antarctic Peninsula and sea ice. *Nature*, *505*(7484), 538-542. https://doi.org/10.1038/nature12945

Lorius, C., & Merlivat, L. (1975). *Distribution of mean surface stable isotopes values in east Antarctica; observed changes with depth in coastal area* (CEA-CONF--3397). CEA Centre d'Etudes Nucleaires de Saclay. http://inis.iaea.org/Search/search.aspx?orig_q=RN:7242101

Mann, M. E., Zhang, Z., Rutherford, S., Bradley, R. S., Hughes, M. K., Shindell, D., Ammann, C., Faluvegi, G., & Ni, F. (2009). Global Signatures and Dynamical Origins of the Little Ice Age and Medieval Climate Anomaly. *Science*, *326*(5957), 1256-1260. https://doi.org/10.1126/science.1177303

Mariotti, A. (1983). Atmospheric nitrogen is a reliable standard for natural 15N abundance measurements. *Nature*, *303*(5919), 685-687. https://doi.org/10.1038/303685a0

Markle, B. R., Steig, E. J., Buizert, C., Schoenemann, S. W., Bitz, C. M., Fudge, T. J., Pedro, J. B., Ding, Q., Jones, T. R., White, J. W. C., & Sowers, T. (2017). Global atmospheric teleconnections during Dansgaard–Oeschger events. *NATURE GEOSCIENCE*, *10*, 7.

Marshall, G. J. (2003). Trends in the Southern Annular Mode from Observations and Reanalyses. *Journal of Climate*, *16*(24), 4134-4143. https://doi.org/10.1175/1520-0442(2003)016<4134:TITSAM>2.0.CO;2

Marshall, G. J. (2004). Causes of exceptional atmospheric circulation changes in the Southern Hemisphere. *Geophysical Research Letters*, *31*(14), L14205. https://doi.org/10.1029/2004GL019952

Marshall, G. J. (2007). Half-century seasonal relationships between the Southern Annular mode and Antarctic temperatures. *International Journal of Climatology*, *27*(3), 373-383. https://doi.org/10.1002/joc.1407

Marshall, G. J., Orr, A., & Turner, J. (2013). A Predominant Reversal in the Relationship between the SAM and East Antarctic Temperatures during the Twenty-First Century. *Journal of Climate*, *26*(14), 5196-5204. https://doi.org/10.1175/JCLI-D-12-00671.1

Marshall, G. J., & Thompson, D. W. J. (2016). The signatures of large-scale patterns of atmospheric variability in Antarctic surface temperatures: Antarctic Temperatures. *Journal of Geophysical Research: Atmospheres*, *121*(7), 3276-3289. https://doi.org/10.1002/2015JD024665

Marshall, G. J., Thompson, D. W. J., & Broeke, M. R. (2017). The Signature of Southern Hemisphere Atmospheric Circulation Patterns in Antarctic Precipitation. *Geophysical Research Letters*, *44*(22), 11,580-11,589. https://doi.org/10.1002/2017GL075998

Maselli, O. J., Fritzsche, D., Layman, L., McConnell, J. R., & Meyer, H. (2013). Comparison of water isotope-ratio determinations using two cavity ring-down instruments and classical mass spectrometry in continuous ice-core analysis. *Isotopes in Environmental and Health Studies*, *49*(3), 387-398. https://doi.org/10.1080/10256016.2013.781598

Masson, V., Vimeux, F., Jouzel, J., Morgan, V., Delmotte, M., Ciais, P., Hammer, C., Johnsen, S. J., Lipenkov, V. Ya., Mosley-Thompson, E., Petit, J.-R., Steig, E. J., Stievenard, M., & Vaikmae, R. (2000). Holocene Climate Variability in Antarctica Based on 11 Ice-Core Isotopic Records. *Quaternary Research*, *54*(3), 348-358. https://doi.org/10.1006/qres.2000.2172

Masson-Delmotte, V., Buiron, D., Ekaykin, A., Frezzotti, M., Gallée, H., Jouzel, J., Krinner, G., Landais, A., Motoyama, H., Oerter, H., Pol, K., Pollard, D., Ritz, C., Schlosser, E., Sime, L. C., Sodemann, H., Stenni, B., Uemura, R., & Vimeux, F. (2011). A comparison of the present and last interglacial periods in six Antarctic ice cores. *Climate of the Past*, *7*(2), 397-423. https://doi.org/10.5194/cp-7-397-2011

Masson-Delmotte, Valerie, Hou, S., Ekaykin, A., Jouzel, J., Aristarain, A., Bernardo, R. T., Bromwich, D., Cattani, O., Delmotte, M., Falourd, S., Frezzotti, M., Gallée, H., Genoni, L., Isaksson, E., Landais, A., Helsen, M. M., Hoffmann, G., Lopez, J., Morgan, V., … White, J. W. C. (2008). A Review of Antarctic Surface Snow Isotopic Composition: Observations, Atmospheric Circulation, and Isotopic Modeling*. *Journal of Climate*, *21*(13), 3359-3387. https://doi.org/10.1175/2007JCLI2139.1

Masson-Delmotte, Valérie, Schulz, M., Abe-Ouchi, A., Beer, J., Ganopolski, A., Fidel, J., Rouco, G., Jansen, E., Lambeck, K., Luterbacher, J., Naish, T., Ramesh, R., Rojas, M., Shao, X., Anchukaitis, K., Arblaster, J., Bartlein, P. J., Benito, G., Clark, P., … Wanner, H. (2013). *Information from Paleoclimate Archives*. 82.

Maule, C. F. (2005). Heat Flux Anomalies in Antarctica Revealed by Satellite Magnetic Data. *Science*, *309*(5733), 464-467. https://doi.org/10.1126/science.1106888

McConnell, J. R., Lamorey, G. W., Lambert, S. W., & Taylor, K. C. (2002). Continuous Ice-Core Chemical Analyses Using Inductively Coupled Plasma Mass Spectrometry. *Environmental Science & Technology*, *36*(1), 7-11. https://doi.org/10.1021/es011088z

Meur, E. L., Magand, O., Arnaud, L., Fily, M., Frezzotti, M., Cavitte, M., Mulvaney, R., & Urbini, S. (2018). Spatial and temporal distributions of surface mass balance between Concordia and Vostok stations, Antarctica, from combined radar and ice core data: first results and detailed error analysis. *The Cryosphere*, 20.

Mouginot, J., Rignot, E., & Scheuchl, B. (2019). Continent-Wide, Interferometric SAR Phase, Mapping of Antarctic Ice Velocity. *Geophysical Research Letters*, *46*(16), 9710-9718. https://doi.org/10.1029/2019GL083826

Münch, T., Kipfstuhl, S., Freitag, J., Meyer, H., & Laepple, T. (2016). Regional climate signal vs. local noise: a two-dimensional view of water isotopes in Antarctic firn at Kohnen Station, Dronning Maud Land. *Climate of the Past*, *12*, 1565–1581. https://doi.org/10.5194/cp-12-1565-2016

Münch, T., & Laepple, T. (2018). What climate signal is contained in decadal- to centennial-scale isotope variations from Antarctic ice cores? *Climate of the Past*, *14*(12), 2053-2070. https://doi.org/10.5194/cp-14-2053-2018

Muto, A., Scambos, T. A., Steffen, K., Slater, A. G., & Clow, G. D. (2011). Recent surface temperature trends in the interior of East Antarctica from borehole firn temperature measurements and geophysical inverse methods. *Geophysical Research Letters*, *38*(15). https://doi.org/10.1029/2011GL048086

NASA. (s. d.). *NASA - Top Story - ICESAT'S LASERS MEASURE ICE, CLOUDS AND LAND ELEVATIONS - October 06, 2003*. Consulté 11 janvier 2021, à l'adresse https://www.nasa.gov/centers/goddard/news/topstory/2003/0920icesatfirst.html

Nicolas, J. P., & Bromwich, D. H. (2014). New Reconstruction of Antarctic Near-Surface Temperatures: Multidecadal Trends and Reliability of Global Reanalyses. *Journal of Climate*, *27*(21), 8070-8093. https://doi.org/10.1175/JCLI-D-13-00733.1

Nishimura, K., & Nemoto, M. (2005). Blowing snow at Mizuho station, Antarctica. *Philosophical Transactions of the Royal Society A: Mathematical, Physical and Engineering Sciences*. https://doi.org/10.1098/rsta.2005.1599

Oerter, H., Graf, W., Meyer, H., & Wilhelms, F. (2004). The EPICA ice core from Dronning Maud Land: first results from stable-isotope measurements. *Annals of Glaciology*, *39*, 307-312. https://doi.org/10.3189/172756404781814032

Orsi, Anaïs J. (2013). *Temperature reconstruction at the West Antarctic Ice Sheet Divide, for the last millennium, from the combination of borehole temperature and inert gas isotope measurements* [University of California, San Diego]. https://escholarship.org/uc/item/02g3c5fq

Orsi, Anais J., Cornuelle, B. D., & Severinghaus, J. P. (2012). Little Ice Age cold interval in West Antarctica: Evidence from borehole temperature at the West Antarctic Ice Sheet (WAIS) Divide: WAIS DIVIDE TEMPERATURE. *Geophysical Research Letters*, *39*(9), n/a-n/a. https://doi.org/10.1029/2012GL051260

Orsi, Anais J., Cornuelle, B. D., & Severinghaus, J. P. (2014). Magnitude and temporal evolution of Dansgaard–Oeschger event 8 abrupt temperature change inferred from nitrogen and argon isotopes in GISP2 ice using a new least-squares inversion. *Earth and Planetary Science Letters*, *395*, 81-90. https://doi.org/10.1016/j.epsl.2014.03.030

Orsi, Anais J., Kawamura, K., Masson-Delmotte, V., Fettweis, X., Box, J. E., Dahl-Jensen, D., Clow, G. D., Landais, A., & Severinghaus, J. P. (2017). The recent warming trend in North Greenland: RECENT WARMING TREND IN NORTH GREENLAND. *Geophysical Research Letters*, *44*(12), 6235-6243. https://doi.org/10.1002/2016GL072212

PAGES 2k Consortium. (2013). Continental-scale temperature variability during the past two millennia. *Nature Geoscience*, *6*(5), 339-346. https://doi.org/10.1038/ngeo1797

Pang, H., Hou, S., Landais, A., Masson-Delmotte, V., Prie, F., Steen-Larsen, H. C., Risi, C., Li, Y., Jouzel, J., Wang, Y., He, J., Minster, B., & Falourd, S. (2015). Spatial distribution of 17O-excess in surface snow along a traverse from Zhongshan station to Dome A, East Antarctica. *Earth and Planetary Science Letters*, *414*, 126-133. https://doi.org/10.1016/j.epsl.2015.01.014

Parsons, S., Renwick, J. A., & McDonald, A. J. (2016). An Assessment of Future Southern Hemisphere Blocking Using CMIP5 Projections from Four GCMs. *Journal of Climate*, *29*(21), 7599-7611. https://doi.org/10.1175/JCLI-D-15-0754.1

Persson, A., Langen, P. L., Ditlevsen, P., & Vinther, B. M. (2011). The influence of precipitation weighting on interannual variability of stable water isotopes in Greenland. *Journal of Geophysical Research*, *116*(D20), D20120. https://doi.org/10.1029/2010JD015517

Pezza, A. B., Rashid, H. A., & Simmonds, I. (2012). Climate links and recent extremes in antarctic sea ice, high-latitude cyclones, Southern Annular Mode and ENSO. *Climate Dynamics*, *38*(1), 57-73. https://doi.org/10.1007/s00382-011-1044-y

Picard, G., Arnaud, L., Caneil, R., Lefebvre, E., & Lamare, M. (2019). *Observation of the process of snow accumulation on the Antarctic Plateau by time lapse laserscanning* [Preprint]. Snow/Antarctic. https://doi.org/10.5194/tc-2019-4

Picard, G., Arnaud, L., Caneill, R., Lefebvre, E., & Lamare, M. (2019). Observation of the process of snow accumulation on the Antarctic Plateau by time lapse laser scanning. *The Cryosphere*, *13*(7), 1983-1999. https://doi.org/10.5194/tc-13-1983-2019

Picarro. (s. d.). Consulté 31 décembre 2020, à l'adresse https://www.picarro.com/company/technology/crds

Plummer, C. T., Curran, M. a. J., van Ommen, T. D., Rasmussen, S. O., Moy, A. D., Vance, T. R., Clausen, H. B., Vinther, B. M., & Mayewski, P. A. (2012). An independently dated 2000-yr volcanic record from Law Dome, East Antarctica, including a new perspective on the dating of the 1450s CE eruption of Kuwae, Vanuatu. *Climate of the Past*, *8*(6), 1929-1940. https://doi.org/10.5194/cp-8-1929-2012

Pozzi, F., Di Matteo, T., & Aste, T. (2012). Exponential smoothing weighted correlations. *The European Physical Journal B*, *85*(6), 175. https://doi.org/10.1140/epjb/e2012-20697-x

Radu, R., Déqué, M., & Somot, S. (2008). Spectral nudging in a spectral regional climate model. *Tellus A: Dynamic Meteorology and Oceanography*, *60*(5), 898-910. https://doi.org/10.1111/j.1600-0870.2008.00341.x

Rhodes, R. H., Bertler, N. A. N., Baker, J. A., Steen-Larsen, H. C., Sneed, S. B., Morgenstern, U., & Johnsen, S. J. (2012). Little Ice Age climate and oceanic conditions of the Ross Sea, Antarctica from a coastal ice core record. *Climate of the Past*, *8*(4), 1223-1238. https://doi.org/10.5194/cp-8-1223-2012

Rhodes, Rachael H., Faïn, X., Stowasser, C., Blunier, T., Chappellaz, J., McConnell, J. R., Romanini, D., Mitchell, L. E., & Brook, E. J. (2013). Continuous methane measurements from a late Holocene Greenland ice core: Atmospheric and in-situ signals. *Earth and Planetary Science Letters*, *368*, 9-19. https://doi.org/10.1016/j.epsl.2013.02.034

Ritter, F., Steen-Larsen, H. C., Werner, M., Masson-Delmotte, V., Orsi, A. J., Behrens, M., Birnbaum, G., Freitag, J., Risi, C., & Kipfstuhl, S. (2016). Isotopic exchange on the diurnal scale between near-surface snow and lower atmospheric water vapor at Kohnen station, East Antarctica. *The Cryosphere*, *10*(4), 1647-1663. https://doi.org/10.5194/tc-10-1647-2016

Ritz, C. (1987). Time dependent boundary conditions for calculation of temperature fields in ice sheets. *IAHS Publ*, *170*, 207-216.

Roberts, J. L., Moy, A. D., van Ommen, T. D., Curran, M. a. J., Worby, A. P., Goodwin, I. D., & Inoue, M. (2013). Borehole temperatures reveal a changed energy budget at Mill Island, East Antarctica, over recent decades. *The Cryosphere*, *7*(1), 263-273. https://doi.org/10.5194/tc-7-263-2013

Roscoe, H. K., & Haigh, J. D. (2007). Influences of ozone depletion, the solar cycle and the QBO on the Southern Annular Mode. *Quarterly Journal of the Royal Meteorological Society*, *133*(628), 1855-1864. https://doi.org/10.1002/qj.153

Rubino, M., Etheridge, D. M., Thornton, D. P., Howden, R., Allison, C. E., Francey, R. J., Langenfelds, R. L., Steele, L. P., Trudinger, C. M., Spencer, D. A., Curran, M. A. J., van Ommen, T. D., & Smith, A. M. (2019). Revised records of atmospheric trace gases CO₂, CH₄, N₂O, and <i>δ</i>¹³C-CO₂ over the last 2000 years from Law Dome, Antarctica. *Earth System Science Data*, *11*(2), 473-492. https://doi.org/10.5194/essd-11-473-2019

Scarchilli, C., Frezzotti, M., & Ruti, P. M. (2011). Snow precipitation at four ice core sites in East Antarctica: provenance, seasonality and blocking factors. *Climate Dynamics*, *37*(9-10), 2107-2125. https://doi.org/10.1007/s00382-010-0946-4

Schlosser, E., Manning, K. W., Powers, J. G., Duda, M. G., Birnbaum, G., & Fujita, K. (2010). Characteristics of high-precipitation events in Dronning Maud Land, Antarctica. *Journal of Geophysical Research*, *115*(D14), D14107. https://doi.org/10.1029/2009JD013410

Schneider, D. P., Steig, E. J., Ommen, T. D. van, Dixon, D. A., Mayewski, P. A., Jones, J. M., & Bitz, C. M. (2006). Antarctic temperatures over the past two centuries from ice cores. *Geophysical Research Letters*, *33*(16). https://doi.org/10.1029/2006GL027057

Schwander, J., Barnola, J.-M., Andrié, C., Leuenberger, M., Ludin, A., Raynaud, D., & Stauffer, B. (1993). The age of the air in the firn and the ice at Summit, Greenland. *Journal of Geophysical Research: Atmospheres*, *98*(D2), 2831-2838. https://doi.org/10.1029/92JD02383

Servettaz, A. P. M., Orsi, A. J., Curran, M. A. J., Moy, A. D., Landais, A., Agosta, C., Winton, V. H. L., Touzeau, A., McConnell, J. R., Werner, M., & Baroni, M. (2020). Snowfall and Water Stable Isotope Variability in East Antarctica Controlled by Warm Synoptic Events. *Journal of Geophysical Research: Atmospheres*, *125*(17). https://doi.org/10.1029/2020JD032863

Severinghaus, J., & Battle, M. (2006). Fractionation of gases in polar ice during bubble close-off: New constraints from firn air Ne, Kr and Xe observations. *Earth and Planetary Science Letters*, *244*(1-2), 474-500. https://doi.org/10.1016/j.epsl.2006.01.032

Severinghaus, J. P., Albert, M. R., Courville, Z. R., Fahnestock, M. A., Kawamura, K., Montzka, S. A., Mühle, J., Scambos, T. A., Shields, E., Shuman, C. A., Suwa, M., Tans, P., & Weiss, R. F. (2010). Deep air convection in the firn at a zero-accumulation site, central Antarctica. *Earth and Planetary Science Letters*, *293*(3-4), 359-367. https://doi.org/10.1016/j.epsl.2010.03.003

Severinghaus, J. P., Grachev, A., & Battle, M. (2001). Thermal fractionation of air in polar firn by seasonal temperature gradients: THERMAL FRACTIONATION OF AIR. *Geochemistry, Geophysics, Geosystems*, *2*(7), n/a-n/a. https://doi.org/10.1029/2000GC000146

Severinghaus, J. P., Grachev, A., Luz, B., & Caillon, N. (2003). A method for precise measurement of argon 40/36 and krypton/argon ratios in trapped air in polar ice with applications to past firn thickness and abrupt climate change in Greenland and at Siple Dome, Antarctica. *Geochimica et Cosmochimica Acta*, *67*(3), 325-343. https://doi.org/10.1016/S0016-7037(02)00965-1

Severinghaus, J. P., Sowers, T., Brook, E. J., Alley, R. B., & Bender, M. L. (1998). Timing of abrupt climate change at the end of the Younger Dryas interval from thermally fractionated gases in polar ice. *Nature*, *391*(6663), 141-146. https://doi.org/10.1038/34346

Sigl, M., Fudge, T., Winstrup, M., Cole-Dai, J., Ferris, D., Mcconnell, J., Taylor, K., Welten, K., Woodruff, T., Adolphi, F., Bisiaux, M., Brook, E., Buizert, C., Caffee, M., Dunbar, N., Edwards, R., Geng, L., Iverson, N., Koffman, B., … Sowers, T. (2016). The WAIS Divide deep ice core WD2014 chronology - Part 2: Annual-layer counting (0-31 ka BP). *Clim. Past*, 19.

Sigl, M., McConnell, J. R., Layman, L., Maselli, O., McGwire, K., Pasteris, D., Dahl-Jensen, D., Steffensen, J. P., Vinther, B., Edwards, R., Mulvaney, R., & Kipfstuhl, S. (2013). A new bipolar ice core record of volcanism from WAIS Divide and NEEM and implications for climate forcing of the last 2000 years. *Journal of Geophysical Research: Atmospheres*, *118*(3), 1151-1169. https://doi.org/10.1029/2012JD018603

Sigl, M., Winstrup, M., McConnell, J. R., Welten, K. C., Plunkett, G., Ludlow, F., Büntgen, U., Caffee, M., Chellman, N., Dahl-Jensen, D., Fischer, H., Kipfstuhl, S., Kostick, C.,

Maselli, O. J., Mekhaldi, F., Mulvaney, R., Muscheler, R., Pasteris, D. R., Pilcher, J. R., … Woodruff, T. E. (2015). Timing and climate forcing of volcanic eruptions for the past 2,500 years. *Nature*, *523*(7562), 543-549. https://doi.org/10.1038/nature14565

Sodemann, H., & Stohl, A. (2009). Asymmetries in the moisture origin of Antarctic precipitation. *Geophysical Research Letters*, *36*(22), L22803. https://doi.org/10.1029/2009GL040242

Souney, J. M., Mayewski, P. A., Goodwin, I. D., Meeker, L. D., Morgan, V., Curran, M. A. J., Ommen, T. D. van, & Palmer, A. S. (2002). A 700-year record of atmospheric circulation developed from the Law Dome ice core, East Antarctica. *Journal of Geophysical Research: Atmospheres*, *107*(D22), ACL 1-1-ACL 1-9. https://doi.org/10.1029/2002JD002104

Sowers, T., Bender, M., Raynaud, D., & Korotkevich, Y. S. (1992). δ15N of N2 in air trapped in polar ice: A tracer of gas transport in the firn and a possible constraint on ice age-gas age differences. *Journal of Geophysical Research: Atmospheres*, *97*(D14), 15683-15697. https://doi.org/10.1029/92JD01297

Steen-Larsen, H. C., Masson-Delmotte, V., Hirabayashi, M., Winkler, R., Satow, K., Prié, F., Bayou, N., Brun, E., Cuffey, K. M., Dahl-Jensen, D., Dumont, M., Guillevic, M., Kipfstuhl, S., Landais, A., Popp, T., Risi, C., Steffen, K., Stenni, B., & Sveinbjörnsdottír, A. E. (2014). What controls the isotopic composition of Greenland surface snow? *Climate of the Past*, *10*(1), 377-392. https://doi.org/10.5194/CP-10-377-2014

Steen-Larsen, H. C., Risi, C., Werner, M., Yoshimura, K., & Masson-Delmotte, V. (2017). Evaluating the skills of isotope-enabled general circulation models against in situ atmospheric water vapor isotope observations. *Journal of Geophysical Research: Atmospheres*, *122*(1), 246-263. https://doi.org/10.1002/2016JD025443

Steig, E. J., Fitzpatrick, J. J., Noel Potter, jr., & Clark, D. H. (1998). The geochemical record in rock glaciers. *Geografiska Annaler: Series A, Physical Geography*, *80*(3-4), 277-286. https://doi.org/10.1111/j.0435-3676.1998.00043.x

Stenni, B., Buiron, D., Frezzotti, M., Albani, S., Barbante, C., Bard, E., Barnola, J. M., Baroni, M., Baumgartner, M., Bonazza, M., Capron, E., Castellano, E., Chappellaz, J., Delmonte, B., Falourd, S., Genoni, L., Iacumin, P., Jouzel, J., Kipfstuhl, S., … Udisti, R. (2011). Expression of the bipolar see-saw in Antarctic climate records during the last deglaciation. *Nature Geoscience*, *4*(1), 46-49. https://doi.org/10.1038/ngeo1026

Stenni, Barbara, Curran, M. A. J., Abram, N. J., Orsi, A. J., Goursaud, S., Masson-Delmotte, V., Neukom, R., Goosse, H., Divine, D., van Ommen, T., Steig, E. J., Dixon, D. A., Thomas, E. R., Bertler, N. A. N., Isaksson, E., Ekaykin, A., Werner, M., & Frezzotti, M. (2017). Antarctic climate variability on regional and continental scales over the last 2000 years. *Climate of the Past*, *13*(11), 1609-1634. https://doi.org/10.5194/cp-13-1609-2017

Stenni, Barbara, Scarchilli, C., Masson-Delmotte, V., Schlosser, E., Ciardini, V., Dreossi, G., Grigioni, P., Bonazza, M., Cagnati, A., Karlicek, D., Risi, C., Udisti, R., & Valt, M. (2016). Three-year monitoring of stable isotopes of precipitation at Concordia Station, East Antarctica. *The Cryosphere*, *10*(5), 2415-2428. https://doi.org/10.5194/tc-10-2415-2016

Telford, P., & Dalvi, M. (2010, août). *Nudging - UKCA*. https://www.ukca.ac.uk/wiki/index.php/Nudging

Thomas, E. R., Allen, C. S., Etourneau, J., King, A. C. F., Severi, M., Winton, V. H. L., Mueller, J., Crosta, X., & Peck, V. L. (2019). Antarctic Sea Ice Proxies from Marine and Ice Core Archives Suitable for Reconstructing Sea Ice over the Past 2000 Years. *Geosciences*, *9*(12), 506. https://doi.org/10.3390/geosciences9120506

Thompson, D. W. J., & Solomon, S. (2002). Interpretation of Recent Southern Hemisphere Climate Change. *Science*, *296*(5569), 895-899. https://doi.org/10.1126/science.1069270

Tierney, J. E., Abram, N. J., Anchukaitis, K. J., Evans, M. N., Giry, C., Kilbourne, K. H., Saenger, C. P., Wu, H. C., & Zinke, J. (2015). Tropical sea surface temperatures for the past four centuries reconstructed from coral archives. *Paleoceanography*, *30*(3), 226-252. https://doi.org/10.1002/2014PA002717

Tiwari, M., Singh, A. K., & Sinha, D. K. (2015). Chapter 3 - Stable Isotopes: Tools for Understanding Past Climatic Conditions and Their Applications in Chemostratigraphy. In Mu. Ramkumar (Éd.), *Chemostratigraphy* (p. 65-92). Elsevier. https://doi.org/10.1016/B978-0-12-419968-2.00003-0

Touzeau, A., Landais, A., Stenni, B., Uemura, R., Fukui, K., Fujita, S., Guilbaud, S., Ekaykin, A., Casado, M., Barkan, E., Luz, B., Magand, O., Teste, G., Meur, E. L., Baroni, M., Savarino, J., Bourgeois, I., & Risi, C. (2016). Acquisition of isotopic composition for surface snow in East Antarctica and the links to climatic parameters. *The Cryosphere*, *10*, 837-852. https://doi.org/doi:10.5194/tc-10-837-2016

Turner, J., Phillips, T., Thamban, M., Rahaman, W., Marshall, G. J., Wille, J. D., Favier, V., Winton, V. H. L., Thomas, E., Wang, Z., Broeke, M. van den, Hosking, J. S., & Lachlan-Cope, T. (2019). The Dominant Role of Extreme Precipitation Events in Antarctic

Snowfall Variability. *Geophysical Research Letters*, *46*(6), 3502-3511. https://doi.org/10.1029/2018GL081517

Uechi, Y., & Uemura, R. (2019). Dominant influence of the humidity in the moisture source region on the 17O-excess in precipitation on a subtropical island. *Earth and Planetary Science Letters*, *513*, 20-28. https://doi.org/10.1016/j.epsl.2019.02.012

Uemura, R., Barkan, E., Abe, O., & Luz, B. (2010). Triple isotope composition of oxygen in atmospheric water vapor. *Geophysical Research Letters*, *37*(4). https://doi.org/10.1029/2009GL041960

Uemura, R., Matsui, Y., Yoshimura, K., Motoyama, H., & Yoshida, N. (2008). Evidence of deuterium excess in water vapor as an indicator of ocean surface conditions. *Journal of Geophysical Research*, *113*(D19), D19114. https://doi.org/10.1029/2008JD010209

Van Den Broeke, M. R., & Van Lipzig, N. P. M. (2003). Response of Wintertime Antarctic Temperatures to the Antarctic Oscillation: Results of a Regional Climate Model. In E. Domack, A. Levente, A. Burnet, R. Bindschadler, P. Convey, & M. Kirby (Éds.), *Antarctic Research Series* (p. 43-58). American Geophysical Union. https://doi.org/10.1029/AR079p0043

Vance, T. R., Roberts, J. L., Plummer, C. T., Kiem, A. S., & van Ommen, T. D. (2015). Interdecadal Pacific variability and eastern Australian megadroughts over the last millennium. *Geophysical Research Letters*, *42*(1), 129-137. https://doi.org/10.1002/2014GL062447

Vance, T. R., van Ommen, T. D., Curran, M. A. J., Plummer, C. T., & Moy, A. D. (2013). A Millennial Proxy Record of ENSO and Eastern Australian Rainfall from the Law Dome Ice Core, East Antarctica. *Journal of Climate*, *26*(3), 710-725. https://doi.org/10.1175/JCLI-D-12-00003.1

Veres, D., Bazin, L., Landais, A., Toyé Mahamadou Kele, H., Lemieux-Dudon, B., Parrenin, F., Martinerie, P., Blayo, E., Blunier, T., Capron, E., Chappellaz, J., Rasmussen, S. O., Severi, M., Svensson, A., Vinther, B., & Wolff, E. W. (2013). The Antarctic ice core chronology (AICC2012): an optimized multi-parameter and multi-site dating approach for the last 120 thousand years. *Climate of the Past*, *9*(4), 1733-1748. https://doi.org/10.5194/cp-9-1733-2013

WAIS Divide Ice Core. (s. d.). Consulté 23 décembre 2020, à l'adresse https://waisdivide.unh.edu/

Wang, Z., Zhang, X., Guan, Z., Sun, B., Yang, X., & Liu, C. (2015). An atmospheric origin of the multi-decadal bipolar seesaw. *Scientific Reports*, *5*(1), 8909. https://doi.org/10.1038/srep08909

Werner, M., Langebroek, P. M., Carlsen, T., Herold, M., & Lohmann, G. (2011). Stable water isotopes in the ECHAM5 general circulation model: Toward high-resolution isotope modeling on a global scale. *Journal of Geophysical Research*, *116*(D15), D15109. https://doi.org/10.1029/2011JD015681

Winkler, R., Landais, A., Risi, C., Baroni, M., Ekaykin, A., Jouzel, J., Petit, J. R., Prie, F., Minster, B., & Falourd, S. (2013). Interannual variation of water isotopologues at Vostok indicates a contribution from stratospheric water vapor. *Proceedings of the National Academy of Sciences*, *110*(44), 17674-17679. https://doi.org/10.1073/pnas.1215209110

Winstrup, M., Svensson, A., Rasmussen, S., Winther, O., Steig, E., & Axelrod, A. (2012). An automated approach for annual layer counting in ice cores. *Climate of the Past*, *8*, 1881-1895. https://doi.org/10.5194/cp-8-1881-2012

Woodruff, F., & Savin, S. M. (1989). Miocene deepwater oceanography. *Paleoceanography*, *4*(1), 87-140. https://doi.org/10.1029/PA004i001p00087

Wunsch, C. (1996, juin). *The Ocean Circulation Inverse Problem*. Cambridge Core. https://doi.org/10.1017/CBO9780511629570

Xiao, C., Ding, M., Masson-Delmotte, V., Zhang, R., Jin, B., Ren, J., Li, C., Werner, M., Wang, Y., Cui, X., & Wang, X. (s. d.). *Stable isotopes in surface snow along a traverse route from Zhongshan station to Dome A, East Antarctica*. 12.

Xiao, C., Ding, M., Masson-Delmotte, V., Zhang, R., Jin, B., Ren, J., Li, C., Werner, M., Wang, Y., Cui, X., & Wang, X. (2013). Stable isotopes in surface snow along a traverse route from Zhongshan station to Dome A, East Antarctica. *Climate Dynamics, 41*(9), 2427-2438. https://doi.org/10.1007/s00382-012-1580-0

Zachos, J., Pagani, M., Sloan, L., Thomas, E., & Billups, K. (2001). Trends, Rhythms, and Aberrations in Global Climate 65 Ma to Present. *Science*, *292*(5517), 686-693. https://doi.org/10.1126/science.1059412

List of abbreviations

AAD: Australian Antarctic Division (Kingston, Tasmania)

ABN: Aurora Basin North

ABN1314: designation of the ABN main core

ALC01112018: Annual Layer Counting, 01 November 2018

CE: common era

CFA: continuous flow analysis

CS chemical slope

DRI: Desert Research Institute (Reno, Nevada)

ECHAM5-wiso: European Centre Hamburg Model

ERA-interim: European Centre for Medium-Range Weather Forecasts re-analysis (Dee et al. 2011)

LID: lock-in depth

LSCE: Laboratoire des Sciences du Climat et de l'Environnement (Gif-sur-Yvette, France)

MAR: Modèle Atmospherique Régional

PSA: Pacific South American pattern (Marshall & Thompson, 2016)

PIS: pressure imbalance sensitivity

SAM: Southern Annular Mode

SMB: Surface Mass Balance

WD: West Antarctic Ice Sheet Divide ice core

WD2014 chronology: chronology based on the WAIS-Divide ice core (Sigl et al., 2016)

Table of figures

Résumé en français

Le climat Antarctique est étroitement lié à l'océan austral, un composant majeur du climat global et du cycle du carbone (Jones et al., 2016). Les carottes de glace peuvent fournir des indications sur le climat passé dans les zones polaires et aident à reconstruire l'évolution de paramètres climatiques sur des échelles de temps plus longues que la période historique au cours de laquelle des observations ont été réalisées. Cependant, la répartition inégale des carottes de glace couvrant les 2000 dernières années ne permet pas de comprendre la variabilité de la température en Antarctique de l'Est (Stenni et al., 2017). Ces derniers 2000 ans sont particulièrement importants car ils établissent une référence de la variabilité climatique naturelle, à laquelle on peut comparer le réchauffement récent observé dans la plupart des régions du globe (Abram et al., 2016). Une nouvelle carotte de glace de 300 m forée à Aurora Basin North (ABN, 71°S, 111°E) a pour but de renseigner sur le climat des 2000 dernières années avec une haute résolution temporelle pour le plateau Est-Antarctique, de l'ordre d'une décennie.

Les calottes de glaces sont formées par accumulation de neige, qui se transforme en glace avec la pression, et peut piéger des impuretés et des gaz. Forer des carottes de glaces permet d'accéder à de la glace formée antérieurement qui comporte des informations sur ses conditions de formation dans le passé. Les molécules d'eau constituant la glace comprennent différents isotopes stables qui peuvent être utilisés comme traceurs du cycle hydrologique. La température dans le nuage lors de la formation des précipitations est particulièrement importante car elle influence fortement le $\delta^{18}O$ dans la neige puis dans la glace archivée (Ciais et Jouzel, 1994 ; Dansgaard, 1964). Cependant, des processus tels que la diffusion ou l'évaporation partielle peuvent modifier le $\delta^{18}O$ de la neige après sa déposition sur la calotte (Casado et al., 2018 ; Steen-Larsen et al., 2014). Afin de caractériser l'évolution de la température sur le site d'ABN, nous chercherons à comprendre le signal de température enregistré dans le

$\delta^{18}O$, et comparerons à une seconde reconstruction de température basée sur l'analyse des gaz et du profil de température dans la glace.

Dans un premier chapitre, nous évaluons la variabilité de la température et des précipitations à ABN sur les derniers 40 ans (couvertes par les observations satellites), une étape indispensable pour ensuite interpréter correctement les traceurs contenus dans les carottes de glace. Dans ce but, nous avons utilisé le modèle atmosphérique régional MAR avec une physique adaptée aux processus polaires et obtenu les résultats suivants (Servettaz et al., 2020). Le climat au site d'ABN est fortement corrélé avec le climat sur une large partie de la Terre de Wilkes, et est représentatif de la partie basse du plateau Est-Antarctique. La majorité de la neige accumulée à ABN provient d'un nombre restreint d'événements de précipitation, qui diffèrent des conditions moyennes : nous mettons en évidence une anomalie de l'ordre de +2°C lorsqu'il neige à ABN, car le flux d'humidité est associé à un réchauffement de l'atmosphère. Nous montrons que les événements de forte précipitation répondent à la variabilité climatique régionale, avec davantage d'événements lorsqu'un blocage se forme au nord-est d'ABN, sur la côte de la Terre de Wilkes. Ce blocage est lui-même favorisé par une phase négative du Southern Annular Mode (SAM), le principal mode de variabilité climatique dans l'hémisphère Sud.

L'anomalie chaude lors de précipitation peut se traduire par un biais dans les isotopes stables de l'eau $\delta^{18}O$ et δD, qui sont habituellement mesurés dans les carottes de glace et utilisés comme indicateur de la température. Nous comparons des simulations réalisées avec le modèle de circulation générale ECHAM5-wiso, qui simule également les isotopes de l'eau, avec trois enregistrements de neige à très haute résolution et précisément datés. Nous montrons que des événements hivernaux chauds avec une température comparable à la température en été sont bien enregistrés dans le $\delta^{18}O$ de la neige. Cependant, les phases froides avec

peu de précipitation, en l'absence d'un blocage atmosphérique, peuvent être sous-représentées. Alors que les phases chaudes à ABN, principalement associées à un SAM négatif, laissent leur trace dans le $\delta^{18}O$ de la neige, les phases froides sont moins marquées. Cela se traduit par une plus faible corrélation entre le SAM et le $\delta^{18}O$ qu'entre le SAM et la température. Nous définissons une relation entre $\delta^{18}O$ et la température en utilisant la température de surface du modèle MAR et le $\delta^{18}O$ de la neige précisément datée, à l'échelle interannuelle. Nous gardons à l'esprit que les isotopes peuvent être biaisés en enregistrant préférentiellement les événements de précipitation chauds.

Afin de reconstruire les variations passées de température, nous avons mesuré divers paramètres sur la carotte de glace de 300 m. Nous présentons les mesures effectuées sur la carotte de glace d'ABN, forée pour étudier la variabilité du climat. La glace a été datée à 2700 ans par comptage de couches annuelles et comparaison d'horizons volcaniques sulfurés avec la chronologie de WAIS Divide en Antarctique Ouest. En utilisant le modèle d'âge et des mesures de densité de la glace, nous estimons l'accumulation sur le site de carottage d'ABN, et montrons qu'elle est influencée par le changement de la position du site de forage, à cause de l'écoulement de la glace. La variation temporelle d'accumulation dans la carotte de glace reflète la variation spatiale d'accumulation en amont du site de forage. Le site d'ABN s'est déplacé de 42 km en 2700 ans. Nous estimons l'impact de l'écoulement de la glace sur l'altitude et la température moyenne du site au cours du temps. Nous présentons également les mesures des isotopes de l'eau $\delta^{18}O$, $\delta^{17}O$ et δD, et leurs corrections glaciologiques respectives. Nous proposons une reconstruction de température à partir du $\delta^{18}O$ et de la calibration entre température et $\delta^{18}O$ établie précédemment sur les enregistrements récents.

La reconstruction de température à partir du $\delta^{18}O$ de la glace est attachée à de larges incertitudes car la relation entre $\delta^{18}O$ et température n'est pas bien connue dans le passé et elle est affectée par un possible biais vers les événements chauds. Nous présentons donc

également une reconstruction alternative, basée sur la mesure des isotopes stables de l'argon et de l'azote dans la carotte de glace. Nous décrivons le protocole d'extraction et de désoxygénation, et détaillons la mesure avec le spectromètre de masse et les corrections nécessaires pour obtenir une précision analytique de 3 ppm sur le $^{15}N_{excess}$. Nous utilisons les propriétés de diffusion thermique des isotopes des gaz pour estimer les gradients de température passés dans le névé. Enfin, nous inversons un modèle d'advection-diffusion dans le névé pour reconstruire l'évolution de la température de surface, en combinant le profil actuel de température dans le trou de forage et les gradients de température passés dans le névé. Après correction de l'effet de l'écoulement de la glace, nous obtenons une deuxième reconstruction de température indépendante, qui enregistre les changements dans la neige de surface.

La carotte de glace d'ABN a donc été utilisée pour reconstruire l'historique de la température par deux méthodes différentes ne donnant pas accès exactement aux mêmes paramètres climatiques. Le $\delta^{18}O$ de l'eau est représentatif de la température au niveau des nuages et surtout lors des événements de précipitation (« température $\delta^{18}O$ »), tandis que l'inversion de température à partir du $^{15}N_{excess}$ de l'air atmosphérique (« température $^{15}N_{excess}$ ») intègre les changements de température dans la neige de surface sur des échelles de temps d'environ une décennie. Alors que la « température $\delta^{18}O$ » est restée dans une plage de variabilité de ± 1 ° C sans changement notable au cours des 2000 dernières années, la « température $^{15}N_{excess}$ » suggère que des phases avec une température de surface plus froide à ABN ont prévalu autour de 300 – 500 EC (Ere Commune) et 1000 – 1400 EC, avec une température 3 ° C plus froide qu'à l'actuel. Nous comparons les causes potentielles de l'écart entre les deux reconstructions de température, et suggérons que la diminution des précipitations hivernales pourrait davantage biaiser la « température $\delta^{18}O$ » vers des conditions estivales chaudes, alors que les conditions moyennes étaient plus froides. Cette hypothèse est discutée en regard d'une reconstruction du SAM au cours des 1000 dernières années (Dätwyler et al., 2018). Une

longue phase positive du SAM au cours de la période de 1000 à 1400 EC est en accord avec une température de surface plus froide et la réduction des blocages côtiers nécessaires pour canaliser les précipitations à l'intérieur des terres de l'Antarctique de l'Est. La température froide à ABN et la phase SAM positive sont concomitantes avec une phase chaude dans l'océan Atlantique Nord (Diaz et al., 2011 ; Graham et al., 2011), ce qui suggère un couplage inter-hémisphérique pendant la période 1000 – 1400 EC.

Ce travail présente un nouvel enregistrement de température, à Aurora Basin North, sur le plateau Est-Antarctique, avec une haute résolution au cours des 2000 dernières années. La bonne compréhension des isotopes stables dans l'eau, couramment mesurés comme indicateur de température, et la mesure précise des isotopes stables des gaz inertes nous ont permis de caractériser les variations de température en Antarctique de l'Est. En particulier, nos résultats suggèrent un climat médiéval froid dans la Terre de Wilkes, entraîné par une phase positive du SAM. Cette interprétation nécessite une étude plus approfondie et pourrait être confirmée par d'autres mesures sur la même carotte de glace, et par d'autres carottes dans la région.